

UNIVERSITY OF BIRMINGHAM

Engineering of Interfaces in Sodium-ion Batteries for Long Cycle Life

By

Tengfei Song

A thesis submitted to the University of Birmingham for the degree of

DOCTOR OF PHILOSOPHY

School of Metallurgy and Materials

College of Engineering and Physical Sciences

University of Birmingham

September 2023

UNIVERSITY OF
BIRMINGHAM

University of Birmingham Research Archive

e-theses repository

This unpublished thesis/dissertation is copyright of the author and/or third parties. The intellectual property rights of the author or third parties in respect of this work are as defined by The Copyright Designs and Patents Act 1988 or as modified by any successor legislation.

Any use made of information contained in this thesis/dissertation must be in accordance with that legislation and must be properly acknowledged. Further distribution or reproduction in any format is prohibited without the permission of the copyright holder.

Abstract

Sodium-ion Batteries (SIBs) present a wealth of possibilities for cost-effective and environmentally friendly energy storage solutions. One challenge to close the gap is the insufficient cycling lifetime.

To maximize their potential, new cathode materials with high specific capacity and stable structures are required. Cobalt-free sodium transition metal oxides of O3 type are promising candidates as cathodes for use in SIBs, owing to their high specific capacity, appropriate operating potential, wide availability of transition metals, and facile synthesis methods that can be inherited from lithium-ion batteries. However, layered oxides suffer from irreversible phase transitions and structural instability, hindering long-term cycling stability. In this work, innovative approaches for improving the cycle life of layered oxides (O3-type $NaNi_{1/3}Fe_{1/3}Mn_{1/3}O_2$ in specific) and the final full-cell battery are investigated through structure tailoring, morphology engineering, and full-cell design. Through in-depth analysis and experimentation, this research aims to establish an effective path toward the practical utilization of enhanced sodium-ion batteries.

Firstly, the flexibility of Sn^{4+} dopant, a non-transition metal, was explored, with the aim of modifying the material's bulk structure by suppressing the host rearrangement and TMO_2 gliding. A series of Sn-modified $NaNi_{1/3}Fe_{1/3}Mn_{1/3}O_2$ cathode was synthesized and characterized, and 8%Sn-modified $NaNi_{1/3}Fe_{1/3}Mn_{1/3}O_2$ cathode exhibited outstanding cycling performance owed to the simultaneously stabilized bulk structure and interface. The underlying mechanism was studied through an extensive analysis (Chapter 4).

Secondly, the physical properties of the synthesized materials are significantly dependent on the synthetic conditions, which in turn affect the final electrochemical performance. Here, the effect of synthesis conditions (pH, molar ratio of ammonia/metal precursor salt, and stirring speed) upon the particle size and morphology of $NaNi_{1/3}Fe_{1/3}Mn_{1/3}O_2$ particles was investigated for the first time. Statistical methods and regression analysis were employed to provide valuable insights into the relationship between synthesis parameters and materials properties. Optimized conditions were derived from the obtained regression models, and particles synthesized with optimum parameters displayed uniformly distributed particle size together with a threefold increase in cycling performance (Chapter 5).

Finally, the optimized $NaNi_{1/3}Fe_{1/3}Mn_{1/3}O_2$ cathode synthesized under the optimum parameters together with 8% Sn modification was fabricated into 8%Sn-$NaNi_{1/3}Fe_{1/3}Mn_{1/3}O_2$ || Hard carbon full cells to verify the practical application. The effects of the N/P ratio on the material utilization, initial capacity, first Coulombic efficiency, and cycling performance were investigated by using three-electrode cells. The failure mechanisms under different N/P levels (areal capacity ratio between negative and positive electrode) were preliminary discussed. The fundamental reason for battery failure is that the electrode potential of the positive or negative electrode exceeds the critical window. Cells with an N/P ratio of 0.9 perform the best cycling performance due to the suppression of irreversible phase transition and sluggish kinetic reactions in the cathode at voltages above 4.1 V (Chapter 6).

Table of Contents

Table of Contents i

Table of Tables vii

Table of Figures ix

Publications xvii

Acknowledgements xix

Definitions and Abbreviations xx

Chapter 1 Introduction and background 23

1.1 Motivation 23

1.2 The Na-ion batteries 25

1.2.1 Development history of sodium-ion batteries 26

1.2.2 Working principle of sodium-ion batteries 28

1.2.3 Cathode material for sodium-ion batteries 29

1.2.4 Anode material for sodium-ion batteries 36

1.3 Challenges for sodium-ion batteries 38

1.4 Research aims and thesis outline 39

1.5 References 42

Chapter 2 Literature review- Strategies to improve the high-voltage stability of layered-oxide cathode materials 53

2.1 Introduction 53

2.2 Main causes of failure under high-voltage operation 54

2.2.1 Phase transitions and induced bulk degradation 54

2.2.2 Surface-related chemical degradation 54

2.2.2.1 Surface instability in air and moisture 55

2.2.2.2 Interfacial reactions between deep-charged cathode and electrolyte 55

2.3 Strategies for high voltage stabilization 57

2.3.1 Selective cationic doping into the crystal framework 57

2.3.2 Particle surface coating and modifications 62

2.3.2.1 Mechanical coating methods 64

2.3.2.2 Chemical coating processes 66

2.3.3 Combined composition and coating strategies 68

2.3.4 Particle morphology and material structure design 70

2.3.4.1 Multi and bi-phasic hybrid materials 70

2.3.4.2 Core-shell particles 73

2.3.4.3 Concentration gradient particles 74

2.3.5 Morphology and particle engineering 76

2.3.5.1 Grain boundary engineering 76

2.3.5.2 Single crystal particles 77

2.4 Conclusion and critical opinions 79

2.5 References 81

Chapter 3 Experimental and characterisation techniques 87

3.1 Experimental techniques 87

3.1.1 Co-precipitation synthesis 87

3.1.2 Electrode preparation 89

3.1.3 Coin Cell assembly 91

3.1.4 Swagelok Cell assembly 91

3.2 Characterisation techniques 92

3.2.1 Physical characterisation 92

3.2.1.1 Powder X-ray diffraction (XRD) 92

3.2.1.2 Scanning electron microscopy (SEM) 95

3.2.1.3 Transmission electron microscopy (TEM) 96
3.2.1.4 Transmission electron inductively coupled plasma atomic emission spectrometry (ICP-AES) 96
3.2.1.5 Raman spectroscopy (Raman) 98
3.2.1.6 X-ray photoelectron spectroscopy (XPS) 98
3.2.2 Electrochemical characterisation 99
3.2.2.1 Galvanostatic charge/discharge 99
3.2.2.2 Electrochemical impedance spectroscopy (EIS) 100
3.2.2.3 Differential Capacity (dQ/dV) 103
3.2.2.4 Galvanostatic intermittent titration technique (GITT) 105
3.3 References 107

Chapter 4 High-voltage stabilization of O3-type layered oxide for sodium-ion batteries by simultaneous Tin dual modification 109

4.1 Introduction 110
4.2 Experimental section 111
4.2.1 Materials synthesis 111
4.2.2 Analytical techniques 113
4.3 Results and discussion 113
4.3.1 Materials characterization 113
4.3.2 Electrochemical performance 124
4.3.3 Mechanism investigation 130
4.4 Conclusion 134
4.5 References 138

Chapter 5 Informed synthesis and particle design of $NaNi_{1/3}Fe_{1/3}Mn_{1/3}O_2$ cathode materials for sodium-ion batteries 142

5.1 Introduction 143

5.2 Experimental and methods 145

5.2.1 Experimental design and analysis 145

5.2.2 Material synthesis 148

5.2.3 Analytical techniques 148

5.3 Results and discussion 149

5.3.1 Physical properties 149

5.3.2 Electrochemical properties 155

5.3.3 Response analysis and results of ANOVA 157

5.4 Validation experiments 163

5.5 Conclusions 165

5.6 References 167

Chapter 6 Optimize areal capacity balance to maximize the lifetime of sodium-ion batteries 169

6.1 Introduction 170

6.2 Experimental 172

6.2.1 Materials preparation 172

6.2.2 Electrochemical performance tests 173

6.3 Results and discussion 173

6.3.1 Active materials characterization 173

6.3.2 Formation with different areal capacity balances 175

6.3.3 Cycling performance with different areal capacity balances 179

6.3.4 Capacity fading mechanisms with different areal capacity balances 180

6.4 Conclusion 184

6.5 References 185

Chapter 7 Conclusions and Outlook 187

7.1 Conclusions 187

7.2 Outlook 189

Table of Tables

Table 1-1 Comparison of the Primary materials used for LIBs and SIBs. 29

Table 1-2 Comparison of properties of commonly used cathode materials for sodium-ion battery. 35

Table 1-3 Comparison of the physicochemical characteristics of Li^+ and Na^+..... 38

Table 4-1 The chemical compositions of the as-prepared samples measured by inductively coupled plasma mass spectroscopy (ICP-AES)..... 113

Table 4-2 Summary of the refined parameters and the R factors. 135

Table 4-3 Summary of the further refined parameters and the R factors considering the sodium vacancy. 136

Table 4-4 Summary of cell parameters used for GITT calculation 137

Table 5-1 Experimental design matrix for the $Ni_{1/3}Fe_{1/3}Mn_{1/3}(OH)_2$ co-precipitation reactions with different pH, ammonium hydroxide quantity and stirring speed. 147

Table 5-2 Summary of experimental design and measured physical response results. 149

Table 5-3 Summary of the refined parameters and the R factors. 154

Table 5-4 Summary of fitted models with coded coefficients and corresponding confidence levels for the prediction of the selected responses. 159

Table 5-5 Comparison of experimental and predicted values for selected responses. 165

Table 6-1 Details of Sn-NFM111 || Hard carbon full cells with different N/P ratios. 172

Table of Figures

Figure 1.1 a) Global forecast demand for LIBs from 2020 to 2026[7]. b) The annual and total lithium consumption forecast from 2015–2050 under the assumption that only the demand for electric vehicles will increase, while other uses remain constant[12]. 24

Figure 1.2 (a) Element abundance in Earth's crust; (b) The world distribution of lithium resource[13].. 25

Figure 1.3 Comparison of the development history of LIBs and SIBs[41]..... 27

Figure 1.4 Working principle of SIBs. 28

Figure 1.5 Number of publications regarding cathodes for SIBs in the past decade. 30

Figure 1.6 Scheme representation of the structure of $Na_3V_2(PO_4)_2F_3$. 31

Figure 1.7 Scheme representation of the structure of PB. 33

Figure 1.8 Schematic illustration of typical structural evolution during charge/discharge of (a) O3-, and (b) P2-phase layered oxides[84]. 35

Figure 1.9 Summary of the proposed sodium-storage models in hard carbon[170]. 37

Figure 1.10 Overview of the thesis..... 41

Figure 2.1 Overview on proposed degradation mechanisms for sodium layered oxide materials under high voltage operations. 56

Figure 2.2 (a) In situ XRD patterns of (a1) $NaNi_{0.5}Mn_{0.5}O2$ and (a2) $NaNi_{0.5}Sn_{0.5}O2$ cycled between 4.2 and 2.8 V in the first cycle showing the largely delayed O3⇔P3 phase transition[35]. (b) Schematic illustration shows the dual-stabilization effect (stabilization of bulk structure and interphase) of Li doping. 59

Figure 2.3 (a) Rough particulate surface coating synthesized via mechanical mixing, with example (b) TEM images of Al_2O_3-coated $Na(Ni_{0.6}Co_{0.2}Mn_{0.2})O_2$ and TEM EDX mapping. (c) Schematic diagram showing the effects ofAl_2O_3 coating on the thickness of electrically insulating surface and the Na^+ transport during cycling. (d) the schematic of a complete coating, synthesized by chemical processes and an example (e) of a

$NaPO_3$ coating layer on $Na_{2/3}(Ni_{1/3}Mn_{2/3})O_2$ formed via reaction with residual NaOH and Na_2CO_3 on the surface, and a schematic illustration ofby-products at the surface ofbare-$Na_{2/3}Ni_{1/3}Mn_{2/3}O_2$ (top) and $NaPO_3$-coated $Na_{2/3}Ni_{1/3}Mn_{2/3}O_2$ (bottom). 65

Figure 2.4 (a) Example ofdual effect from a one-step synthesis process for fabricating the MgO coated and Mg doped $Na(Ni_{0.5}Mn_{0.5})O_2$ (MgO–NM55) cathode. EPMA results of (a1) NM55 and (a2) MgO–NM55 cathodes. (b1) 3D structural model of the NMTN samples composed of a Ti-rich spinel-like interface (green shell) and Mn-rich layered bulk (brown core). (b2–5) EELS chemical mapping of the NMTN samples and corresponding chemical compositions (white rectangle) for b2 Ti, b3 Na, b4 Mn, and b5 Ni elements showing that the interface 2 nm from the particle edge is enriched by titanium rather than other elements.. 69

Figure 2.5 (a) X-ray diffraction patterns of $Na_{1-x}Li_xNi_{0.5}Mn_{0.5}O_{2+d}$ with different Li content, x ($0 \leqslant x \leqslant 1$) showing phase evolution as a function of Li content. (b) High-resolution TEM images directly showing the intergrowth stacking of the P2 and O3 lattices of $Na_{0.7}Li_{0.3}Ni_{0.5}Mn_{0.5}O_{2+d.}$ [69] (c1, c2) Representative plan-view and cross-sectional SEM images of the pristine O3/O′ 3 material. (c3, c4) Representative plan-view and cross-sectional SEM images of the pristine O3/O′ 3 – P2 material. Comparison of cross-sectional SEM image of the (c5) pristine O3/O′ 3 and the (c6) O3/O′ 3 – P2 electrode after 50 cycles. (d) Scheme illustration of the composition and structure for a typical RAHC particle. 71

Figure 2.6 (a) Schematic illustration shows the evolution of the Li_3PO_4 coating layer on the secondary particle following coating and annealing. (b1) Low- and (b2) high-magnification FESEM images of $Na_{0.7}MnO_2$ nanoplates. (c) Capacity–voltage plots of the very first 20 cycles obtained from a single-crystal and polycrystalline Na_2IrO_3 electrodes in the voltage window 1.5–4.2 V. 78

Figure 2.7 Overview on corresponding modifying strategies for sodium layered oxide materials under high voltage operation. 80

Figure 3.1 Diagrams of the sample calcination procedure. 89

Figure 3.2 Structure diagrams of two-electrode coin cell. 91

Figure 3.3 Structure diagrams of three-electrode Swagelok cell. 92

Figure 3.4 Diagram of an X-ray diffractometer 93

Figure 3.5 A example refinement profile with observed, calculated and difference profile of an O3 type layered material, R_{wp} = 2.34%. 94

Figure 3.6 Real photos of In situ X-ray diffraction coin cell. 95

Figure 3.7 Simple Diagram of ICP-AES. 97

Figure 3.8 (a) A typical impedance spectrum of sodium-ion cells, inserted is the equivalent circuit model. (b) A diagram shows that a battery system can be understood as a circuit system. (c) The symbols and corresponding figures in the EIS complex plane of the basic electrical elements used for equivalent circuits. 103

Figure 3.9 (a) Example of Voltage vs. Q charge/discharge curves of different cycles for an O3-type layered oxide. (b) dQ/dV curves derived from (a) showing the varies of peaks with cycling. 104

Figure 3.10 The schematic diagram of a single sequence for GITT. 105

Figure 4.1 The colour of the different Sn stoichiometry doped layered oxides. 112

Figure 4.2 Structural characterization of the as-synthesized materials. (a) XRD patterns of all samples; Detailed Rietveld refinements of XRD patterns. 116

Figure 4.3 (a) Variation of lattice parameters and the I003/I104 value as a function of SnO_2 content; (b, c) Na−O−TM structure evolution before and after 8% Sn modification. (d) Raman spectra of NaNFMO and Sn8%-NaNFMO. 117

Figure 4.4 SEM images of (a) NaNFMO and (b) Sn8%-NaNFMO. (c) Corresponding EDS elemental mapping for Sn8%-NaNFMO. 118

Figure 4.5 (a) Cross-sectional SEM image and EDS element mappings of the as-prepared Sn8%-NaNFMO acquired by FIB, and (b) corresponding counts content distribution of elements along the arrow; HRTEM and the corresponding FFT of (c) NaNFMO and (d) Sn8%-NaNFMO; and (e, f) STEM/EDS mapping and corresponding count content of element distribution in a single primary particle of the Sn8%-NaNFMO. 120

Figure 4.6 XPS spectra from the surface of NaNFMO particles with 0%, 3% and 8% Sn additions (a) Survey XPS spectra, (b) Sn 3d5/2 spectra, (c) Ni 2p, (d) Fe 2p, (e) Mn 2p, (f) C 1s, (g) O 1s , and (h) Na KLL and Sn 3d XPS spectra. 122

Figure 4.7 (a) Room temperature ^{57}Fe Mössbauer spectra recorded from pristine NaNFMO, Sn3%-NaNFMO, and Sn8%-NaNFMO. (b) Quadrupole splitting distributions obtained from the fit of the spectra presented on (a)..... 124

Figure 4.8 Electrochemical performance of the as-synthesized materials. (a) Initial charge-discharge curves at room temperature; (b-c) The cycling performance and capacity retention of all the electrodes after 150 cycles at 75 mA/g (0.5C); (d) The average discharge voltage of NaNFMO and and Sn8%-NaNFMO at 0.5C; Charge/discharge curves of different cycles for (e) NaNFMO and (f) Sn8%-NaNFMO (g) Comparison of initial differential capacity (dQ/dV) curves of NaNFMO and Sn8%-NaNFMO at 0.1C; dQ/dV curves of (h) NaNFMO and (i) Sn8%-NaNFMO cathodes under various cycles at 0.5C. 125

Figure 4.9 (a) GITT curves of NaNFMO and Sn-NaNFMO cathode material in the first cycle within 2.0-4.1V; Na diffusivity versus state of charge and discharge calculated by GITT of (b) NaNFMO and (c) Sn8%-NaNFMO. 127

Figure 4.10 Nyquist plots of (a) NaNFMO and (b) Sn8%-NaNFMO after different cycles. (c) Comparison of fitted impedance for NaNFMO and Sn8%-NaNFMO. (d) Liner fitting of Z' vs. $\omega^{-0.5}$ in the low-frequency region for NaNFMO and Sn8%-NaNFMO samples after 100 cycles. 129

Figure 4.11 Operando XRD patterns and corresponding 2D contour maps showing the evolution of the main characteristic peaks for (a) Sn8%-NaNFMO and (b) NaNFMO cathodes during the first charge/discharge process between 2.0 V and 4.1 V at 0.1 C. (c) EX-situ XRD patterns during the first charge/discharge of Sn8%-NaNFMO electrodes between 2.0 V and 4.2 V at 0.1 C. (d) Lattice parameters a, c and V evolution during charge process. 130

Figure 4.12 (a) XRD patterns and (b) Raman spectra of NaNFMO and Sn8%-NaNFMO after 100cycles..... 132

Figure 4.13 SEM images of NaNFMO (a, b) and Sn8%-NaNFMO (c, d) after 150 cycles. Cross-section images of NaNFMO (e) and Sn8%-NaNFMO (f) after 150 cycles. 133

Figure 5.1 Design matrix with three operating conditions. 147

Figure 5.2 Illustration of the synthesis and optimization process. 148

Figure 5.3 SEM images of the as-prepared hydroxide precursors (top) and final layered oxide particles (bottom) prepared at DoE1 (a), DoE2 (b), DoE3 (c), DoE4 (d), DoE5 (e), DoE6 (f), DoE7 (g), and DoE8 (h). 150

Figure 5.4 Particle size distribution (a,b) and tap density (c) of the synthesized final particles.150

Figure 5.5 Schematic illustration of effects of synthetic factors on the precursor morphology and the physical properties of the final particles. 152

Figure 5.6 (a) XRD patterns of NaNFMO samples obtained under different conditions. (b) Crystallite size calculated from 003 and 104 peaks. 152

Figure 5.7 Detailed Rietveld refinements of XRD pattern of the as-prepared cathode powdered materials 153

Figure 5.8 Variation of lattice parameters and the lattice spacing d003 value as a function of DoE number. 154

Figure 5.9 (a-h) Charge and discharge curves of the initial 3 formation cycles for the synthesized materials. Comparison of the formation capacity (i) and capacity retention after 50 cycles (j) for the as-synthesized materials. 155

Figure 5.10 Comparison of differential capacity (dQ/dV) curves of the first 3 cycles. The peak around 3.0 V (*vs*. Na^+/Na) is named as Peak A, and the peak around 4.0 V (*vs*. Na^+/Na) is named as Peak B. The intensity ratios of peak B to peak A were calculated and used in Figure 5.11. 157

Figure 5.11 Linear fitting between the capacity retention and the peak ratio B/A(a) and I003/I104(b). 157

Figure 5.12 Pareto charts of effective parameters for the regression model (a) Particle size D50, (b) Tap Density, (c) Crystallite Size, and (d) Capacity Retention..... 158

Figure 5.13 The distribution of the predicted versus actual values of the Particle size D50 (a), Tap Density (b), Crystallite Size (c), and Capacity Retention (d)..... 160

Figure 5.14 Contour plots of the relationship between input factors and output responses, (a) particle size D50, (b) tap density, and (c) crystallite size. 161

Figure 5.15 Interaction effect plots (a-c) and corresponding contour plots (d-f) for capacity retention. 162

Figure 6.1 SEM images of (a) Sn-NFM111 cathode and (b) commercial HC anode material; Voltage profiles of (c) cathode material in the first 2 cycles at 10 mA g^{-1} and 2.0 – 4.1 V vs Na/Na^+ and (d) hard carbon anode material in the first 2 cycles at 10 mA g^{-1} and 0.01–2.0 V vs Na/Na^+; the cycling performance of (e) cathode and (f) anode material at 0.5 C. The areal capacities for both cathode and anode tested in half-cell are 1 mAh cm^{-2}. 174

Figure 6.2 dQ/dV curves of hard carbon anode. 175

Figure 6.3 (a-b) First charge/discharge voltage/potential profile for the three-electrode cells within a controlled full cell voltage range of 1.5 – 4.1 V at 0.1C. Comparison of the end-off potentials of (c) cathode and (d) anode in the first charge process. 176

Figure 6.4 Comparison of (a) initial voltage profiles and (b) differential capacity (dQ/dV) curves of Sn-NFM111 when charged to different cut-off potentials. (c) GITT curves of Sn-NFM111 within voltage range of 2.0 – 4.2 V vs. Na^+/Na. 177

Figure 6.5 The variation of the first charge/discharge specific capacity (based on the weight of cathode material) and initial coulombic efficiency as a function of N/P ratio. 178

Figure 6.6 Cycling performance of cells with various N/P ratios within a controlled full cell voltage range of 1.5 – 4.1 V. Data were averaged from 3 cells for each condition. 179

Figure 6.7 Optical image (left) and SEM images (right) of HC after cycling tests (a) N/P=0.8, (b) N/P= 1.0, and (c) N/P=1.3. 181

Figure 6.8 Cell voltage, together with the electrode potentials over time during cycling of Sn-NFM111 || Hard carbon cell with N/P ratio of 1.0 cycles between 1.5-4.1 V. 182

Figure 6.9 Variations of cathode and anode cut-off potentials while cycling with N/P ratios of 0.8, 1.0, and 1.3. 182

Figure 6.10 Differential voltage profiles of full cell, cathode, and anode of cells with N/P ratios of 0.8, 1.0, and 1.3. 183

Publications

This thesis incorporates the four following papers, which are either published or submitted for publication:

- **Song, T**.; Kendrick, E., Recent progress on strategies to improve the high-voltage stability of layered-oxide cathode materials for sodium-ion batteries. *Journal of Physics: Materials* **2021,** 4, (3).
- **Song, T**.; Chen, L.; Gastol, D.; Dong, B.; Marco, J. F.; Berry, F.; Slater, P.; Reed, D.; Kendrick, E., High-Voltage Stabilization of O3-Type Layered Oxide for Sodium-Ion Batteries by Simultaneous Tin Dual Modification. *Chemistry of Materials* **2022**, 34, 9, 4153–4165
- **Song, T**.; Zhang, Q.; Chen, Y.; Zhu, P.; Kendrick, E., Synthesis and Design of $NaNi_{1/3}Fe_{1/3}Mn_{1/3}O_2$ Cathode Materials for Long-life Sodium-Ion Batteries. *Chemical Engineering Journal Advances* **2023**.
- **Song, T**.; Chen, Y.; Chen, L.; Kendrick, E., Optimize full-cell design parameters to maximize the lifetime of layered oxide/Hard Carbon sodium-ion batteries (In submission to *Journal of Power Sources*).

In addition, the following papers were published as co-authors during the period of postgraduate study.

- Zorin, A.; **Song, T.**; Gastol, D.; Kendrick, E., Acid-Assisted Separation of Cathodic Material from Spent Electric Vehicle Batteries for Recycling. *Metals* **2023**, 13, (7).
- Chen, L.; Kishore, B.; **Song, T.**; Walker, M.; Dancer, C.; Kendrick, E., Improved Lifetime of Na-Ion Batteries With a Water-Scavenging Electrolyte Additive. *Frontiers in Energy Research* **2022**, 10.
- Chen, Y.; Key, J.; O'Regan, K.; **Song, T.**; Han, Y.; Kendrick, E., Revealing the rate-limiting electrode of lithium batteries at high rates and mass loadings. *Chemical Engineering Journal* **2022**, 450.
- Gastol, D.; Marshall, J.; Cooper, E.; Mitchell, C.; Burnett, D.; **Song, T.**; Sommerville, R.; Middleton, B.; Crozier, M.; Smith, R.; Haig, S.; McElroy, C. R.; van Dijk, N.; Croft, P.; Goodship, V.; Kendrick, E., Reclaimed and Up-Cycled Cathodes for Lithium-Ion Batteries. *Glob Chall* **2022**, 6, (12), 2200046.

Acknowledgements

First and foremost, I want to extend my heartfelt appreciation to my supervisor, Professor Emma Kendrick. Her patient guidance and unwavering support have been a constant throughout the entire research process. She has fostered a rich academic atmosphere, a relaxed research environment, and ensured access to well-equipped laboratory facilities, all of which have significantly bolstered my academic pursuits.

I would also like to thank Dr. Daniel Reed and Amy Jade Newell, who have provided great assistance with the XRD, Raman, PSA, and SEM characterization facilities.

I would like to acknowledge Dr. Lin Chen who supported me with the experiments at the beginning of my Ph.D. study. I am also grateful to all members of the Energy Materials Group at the University of Birmingham, for the help, support, encouragement, and kindness during my Ph.D.

To my parents, your years of hard work raised me and taught me independence. In times of discouragement, your unwavering support and words of encouragement have been a constant source of strength.

I wish to place profound emphasis on the immeasurable contributions of my beloved wife, Ms. Wei Lin. Her unwavering support, boundless encouragement, and unwavering belief in my potential have been the driving force behind my academic achievements. It is her courageous spirit that gave me the courage to leave my original job position at the age of 30 and reengage in academic research, exploring and discovering more of my potential. Throughout this demanding journey, she stood by my side, providing not only emotional support but also practical assistance in countless ways.

During this period, we welcomed our first child, Eileen, who brought us much joy amidst our busy lives. We hope that she grows up happily and steps into the academic world of her dreams.

Finally, I want to thank myself. Thank you for your perseverance and for completing a doctoral degree while balancing family responsibilities. This has been a long and fulfilling journey, and I step into the next chapter with gratitude in my heart.

Definitions and Abbreviations

CC-CV	Constant Current-Constant Voltage
CEI	Cathode Electrolyte Interface
CE	Counter Electrode
CMC	Carboxymethyl Cellulose
CNTs	Carbon Nanotubes
DEC	Diethyl carbonate
DoE	Design of Experiment
EC	Ethylene Carbonate
EDS	Energy Dispersive Spectroscopy
EIS	Electrochemical Impedance Spectroscopy
EOC	End of Charge
EOD	End of Discharge
FEC	Fluoroethylene Carbonate
GITT	Galvanostatic Intermittent Titration Technique
HC	Hard Carbon
ICP-AES	Inductively Coupled Plasma Atomic Emission Spectronetry
Ksp	Precipitation Equilibrium Constant
LIBs	Lithium-ion batteries

N/P	Area Capacity Ratio between Negative and Positive electrode
NaNFMO	$NaNi_{1/3}Fe_{1/3}Mn_{1/3}O_2$
NMP	Nmethyl-2-Pyrrolidine
PA	Prussian Blue
PBA	Prussian Blue Analogues
PVDF	Polyvinylidene Fluoride
RE	Reference Electrode
SEI	Solid Electrolyte Interphase
SEM	Scanning Electron Microscopy
SHE	Standard Electrode Potential
SIBs	Sodium-ion batteries
TM	Transition Metals
TEM	Transmission Electron Microscopy
XRD	X-ray Diffraction
XPS	X-ray Photoelectron Spectroscopy

Chapter 1 Introduction and background

1.1 Motivation

With the increasing energy crisis and environmental pollution, countries are competing to develop new clean, non-polluting, and renewable energy sources, such as solar, hydro, wind, nuclear, geothermal, and other new energy sources[1]. However, the output of these renewable energy sources is intermittent, seasonal, and geographical in nature. How to maximize the use of these clean energy sources and reduce wind and power abandonment is a critical issue. Large-scale energy storage systems are an effective means to solve this problem and have been a global priority. Energy storage, as part of the electrical grid infrastructure, can enable reliable, flexible, and residential access to electricity, which is essential to the "carbon neutral"[2, 3].

Electrochemical energy storage is flexible, convenient, easy to maintain, and has high conversion efficiency leading to its share in the energy storage market gradually increasing over the last 20 years[4]. Secondary batteries are devices that can reversibly convert chemical energy into electrical energy. In modern society where electricity is an important energy source, batteries play an irreplaceable and important role. Lead acid batteries and Lithium-ion batteries (LIBs) are two dominant technologies used for electrochemical energy storage. While lead acid batteries do well in back-up power for communication towers, Internet data centers, and two-wheeled small vehicles, its application for large-scale energy storage is inhibited by low energy density, short cycle life, and hazard concerns associated with lead and sulfuric acid. Benefitting from high energy density, long service life, and high charge/discharge efficiency, LIBs are extensively used in applications ranging from portable devices to large energy grids. In recent years, the rapid development of the electric vehicle industry has opened up a much broader development space for the lithium-ion battery industry. Countries have released timetables for combustion car bans, with plans to stop selling 100% combustion vehicles by the mid-2030s and fully promote vehicle electrification. Amid the tremendous development of electric vehicles, the total global production of LIBs swelled to 116.6 GWh in 2019, and it is predicted that the global LIBs demand will reach around 700 GWh by 2025[5-7] (Figure 1.1a). Numerous lithium raw materials are needed to meet the demand, as shown in Figure 1.1b.

The relatively low abundance and non-uniform global distribution of resources needed for LIBs (Figure 1.2) present concerns about the sustainable supply to meet the future global market demand, especially with the rapid development of electric vehicles combined with the uptake of large and local stationary energy storage[8, 9]. As of 2020, the EU has defined Li as one of the 24 national strategic mineral resources. One notable issue is that 91% of lithium comes from three regions: Australia, South America, and China, which puts the lithium supply chain at high risk. In fact, the relatively limited lithium reserves and uneven geographical distribution have already led to a strong increase as well as wide fluctuations in the price of Li_2CO_3 in recent years[10]. In addition to lithium, other elements used in lithium-ion batteries, such as cobalt, nickel, and graphite have recently been identified as critical elements that also face sustainable supply issues. This could limit the suitability of LIBs in large-scale energy storage in the future. Therefore, the development of alternative energy storage batteries based on abundant resources is required to enhance the supply chain of raw materials and release the strain on global resources[11].

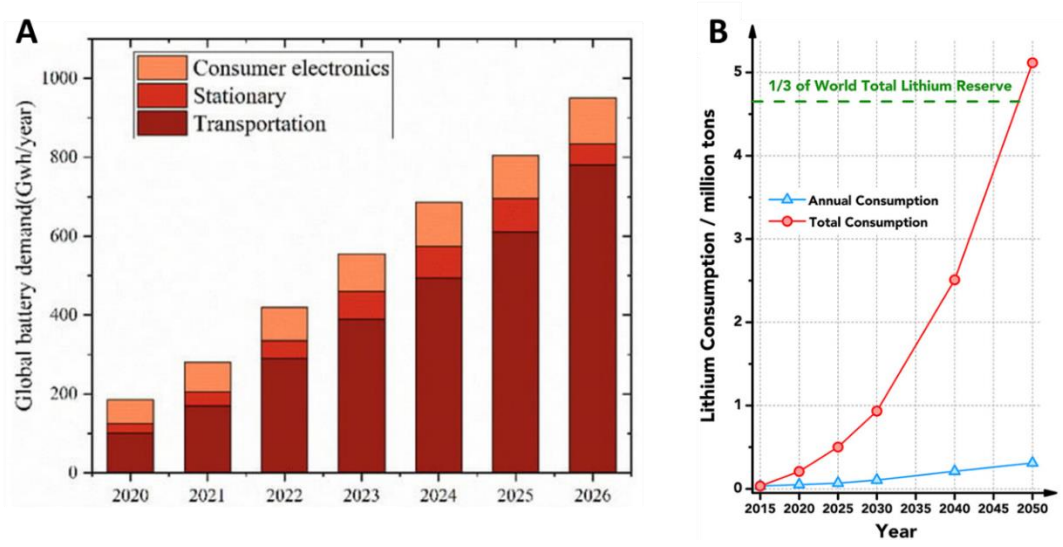


Figure 1.1 a) Global forecast demand for LIBs from 2020 to 2026[7]. b) The annual and total lithium consumption forecast from 2015–2050 under the assumption that only the demand for electric vehicles will increase, while other uses remain constant[12]. Copyright (2018), with permission from Elsevier.

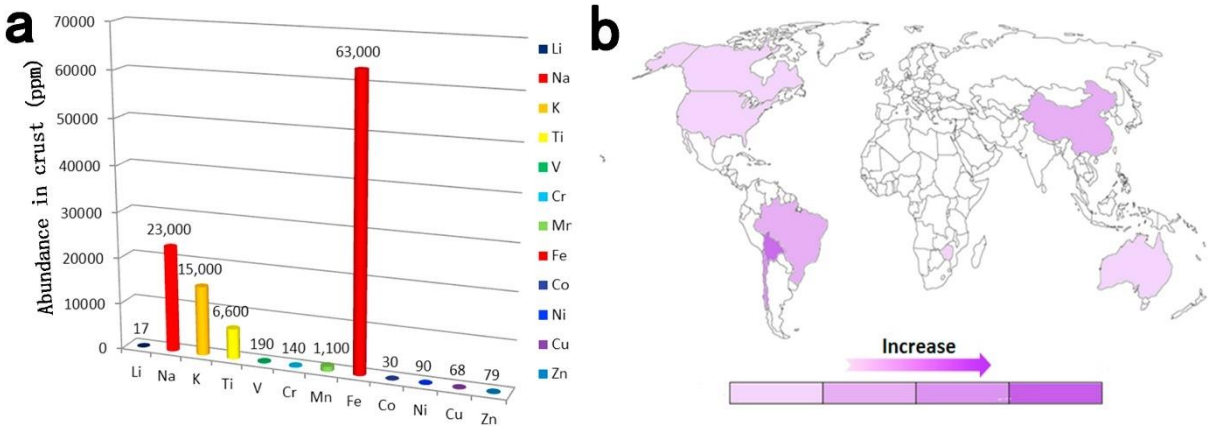


Figure 1.2 (a) Element abundance in Earth's crust; (b) The world distribution of lithium resource[13]. Copyright (2017), with permission from Elsevier.

1.2 The Na-ion batteries

Sodium-ion batteries (SIBs) offer one such solution. SIBs have intrinsic advantages on materials sustainability, as sodium is geographically widespread and is significantly more abundant than lithium (Na: 23 000 ppm *vs.* Li: 17 ppm in the Earth's crust as shown in Figure 1.2a)[14-17]. The cost of Na_2CO_3 is about 25~30 times lower than that of Li_2CO_3[18].

In addition, alternative transition metals, such as Mn[19-21], Fe[22-24], Cu[25, 26], Ti[27], Cr[28-31], V[32-34], can be utilized, instead of cobalt for the cathode, endowed with numerous unexplored opportunities in SIBs. Sodium is positioned below by lithium on the periodic table, leading to many chemical similarities between sodium and lithium. These shared characteristics facilitate the use of the same cell design and manufacturing processes for both SIBs and LIBs[14]. Given these similarities, SIBs hold the potential to serve as a 'drop-in' or direct substitute technology for LIBs in large-scale energy storage applications[35].

Sodium metal batteries such as the Sodium–sulphur and sodium–metal-halide batteries have been considered for stationary storage applications for some time[36]. However, these batteries need to operate around 300 °C, requiring expensive heating and temperature management facilities, and also causing safety issues[37]. Therefore, new types of SIBs that can operate at room temperature have been regarded as the most promising alternative to current LIBs and attracted great research attention.

1.2.1 Development history of sodium-ion batteries

Sodium-ion batteries were studied almost simultaneously with lithium-ion batteries in the late 1970s[38]. However, due to no suitable anode materials for sodium stable insertion/de-insertion found at that time and the successful commercial application of LIBs, the attention toward SIBs subsided. No successful data with satisfactory cycle life of nonaqueous Na cells was reported until 2009 when Komaba *et al* first demonstrated a satisfying long cycle life with hard carbon as anode[39].

In the early 21st century, the application of LIBs expanded further from electronics to electric vehicles. The rapid development of LIBs raised concerns about the security of the lithium supply chain. In this light, SIBs re-emerged in the researchers' view and led to a fresh wave of research. Over the past decade, more than ten start-up companies have been established worldwide to boost the commercialization of SIBs, like UK-based Faradion Ltd founded in 2011(https://faradion.co.uk/), French-based Tiamat in 2012 (http://www.tiamat-energy.com/), US-based Natron Energy in 2012 (https://natron.energy/), and Chinese-based HiNa Battery Technology in 2017 (http://www.hinabattery.com/en/). The application of SIBs in energy storage has been verified in a 30 kW/100 kW·h SIBs energy storage system by HiNa[40] in 2019, which is the largest SIB system to date. Figure 1.3 compares the development history of LIBs and SIBs.

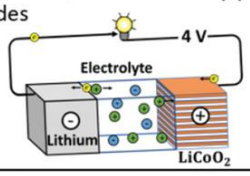
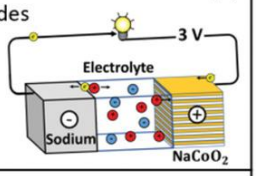
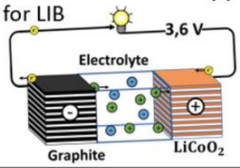
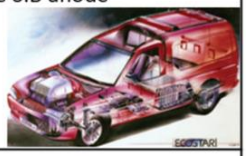
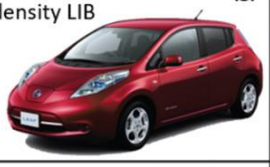
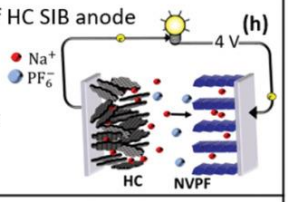
Period	Li-ion Batteries	Na-ion Batteries
1970 - 1980	- Goodenough's battery - $LiMeO_2$ cathodes (a) ***Applications:*** Research 	- Na/S batteries - $NaMeO_2$ cathodes (b) ***Applications:*** Research 
1980-1990	- The "rocking chair" battery - Graphite anode for LIB (c) ***Applications:*** Research 	- High temperature Na batteries - Lack of a suitable SIB anode (d) ***Applications***: e-Mobility, Grid 
1990-2000	- First commercial LIB by SONY - Mixed metal oxides (research) (e) ***Applications***: Portable electronic devices 	- SIB research decline - Development of ZEBRA cells (f) ***Applications***: Grid 
2000-2010	- Si anodes - High energy density LIB (g) ***Applications***: e-Mobility 	- Discovery of HC SIB anode (h) ***Applications***: Research 
2010-2020	- Large scale LIB factories - Li supply concerns (i) ***Applications***: e-Mobility, Grid 	- Revival of SIB research - SIB start-ups (j) ***Applications***: e-Mobility, Grid 

Figure 1.3 Comparison of the development history of LIBs and SIBs[41].

1.2.2 Working principle of sodium-ion batteries

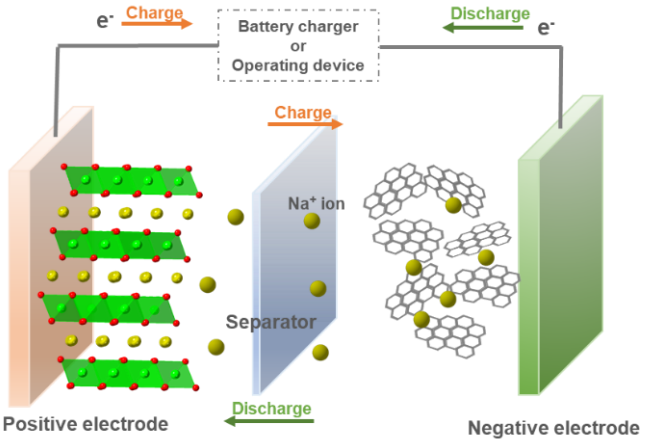


Figure 1.4 Working principle of SIBs.

The electrochemical equation for SIBs is: (-) C_n |electrolyte| $NaTMO_2$ (+)

Positive electrode: $NaTMO_2 - xe^- \underset{\text{discharge}}{\overset{\text{charge}}{\rightleftharpoons}} xNa^+ + Na_{1-x}TMO_2$ (1-1)

Negative electrode: $nC + xNa^+ + xe^- \underset{\text{discharge}}{\overset{\text{charge}}{\rightleftharpoons}} Na_xC_n$ (1-2)

Overall: $NaTMO_2 + nC \underset{\text{discharge}}{\overset{\text{charge}}{\rightleftharpoons}} Na_xC_n + Na_{1-x}TMO_2$ (1-3)

SIBs have a similar working principle to current LIBs, which can also be called "Rocking chair battery", consisting of a positive electrode, negative electrode, electrolyte, and electrically insulated separator, as illustrated in Figure 1.4 and Table 1.1. When charging, Na^+ is extracted from the positive electrode and then transported into the negative electrode through the ion-conducting electrolyte, while electrons are transferred to the negative side via the external circuit to maintain the overall charge balance[42]. The process is reversed when discharged, with Na^+ being extracted from the negative electrode and inserted into the positive side via electrolyte.

Cathode materials are typically compounds with relatively high potential *vs.* Na^+/Na and are able to stably extract/embed Na^+ ions. Anode materials are generally those with potentials higher than the sodium metal precipitation potential and capable of reversible Na^+ ion extract/embedding, such as hard carbon (HC). The electrolyte is usually an organic carbonate solution with sodium salts (e.g., $NaPF_6$ and $NaClO_4$) as solute. As for the collector, in LIBs, Al

foil is generally used as the metal collector on the positive side, while Cu foil is used for the negative side. As sodium aluminium would not react like lithium and aluminium to form a lithium-aluminum alloy, aluminium foil can be used as the collector both for the positive and negative electrodes for SIBs, which can significantly reduce the cost of sodium-ion batteries[43, 44].

Table 1-1 Comparison of the Primary materials used for LIBs and SIBs.

Component	LIBs	SIBs
Cathode	***Layered metal oxides***: $LiTMO_2$ (TM=Ni, Co, Mn, Al) ***Spinel oxides***: $LiMn_2O_4$ ***Olivine oxides***: $LiFePO_4$	***Layered metal oxides***: $NaTMO_2$ ***Polyanionic compounds:*** $Na_xTM_y(PO_4)_zX$ (X=F) ***Prussian analogues****:* $Na_xTM_y[Fe(CN)_6]$ (TM=Fe, Ni, Co, Mn, Cu, etc)
Anode	Graphite	Hard carbon
Electrolyte	EC, DEC， DMC	EC, DEC， DMC
Salts	$LiPF_6$	$NaPF_6$、$NaBF_4$、$NaClO_4$
Separator	PP/PE	PP/PE
Current collector	Al (cathode) Cu (Anode)	Al (cathode and anode)

1.2.3 Cathode material for sodium-ion batteries

The advancement of SIBs is significantly reliant on the development of new cathode materials. This is because critical battery attributes like energy density, cycling performance, and cost are predominantly shaped by the properties of the cathode materials. Therefore, the quest for cathode materials that possess high capacity, extended service life, and cost-effectiveness is critical to drive the progress of SIBs technology. During cycling, the cathode material not only needs to supply the Na^+ required for repeated insertion/de-insertion, but also needs to provide

the Na^+ required for irreversible capacity loss of the anode electrode. An ideal cathode material must possess the following characteristics:

(1) The ability to hold as much Na^+ as possible to obtain a high capacity.

(2) High structural stability and reversibility: little change in the body structure during the insertion/extraction of Na^+, which ensures that the battery has a long service life.

(3) Good chemical stability throughout the operating voltage range, no reaction with electrolyte, and high thermal chemical stability.

(4) High electronic conductivity and Na^+ diffusion coefficient, enabling the battery to be charged and discharged rapidly.

(5) Cheap, environmentally friendly, non-toxic, light in mass, and easy to prepare.

In the past decades, huge efforts have been made to explore new sodium insertion host, and various cathode materials with promising performance has been demonstrated[45-64].

Generally speaking, cathode materials for SIBs can be divided into three categories: polyanionic compounds, Prussian blue analogues (PBA/PWA), and layered metal oxides [65].

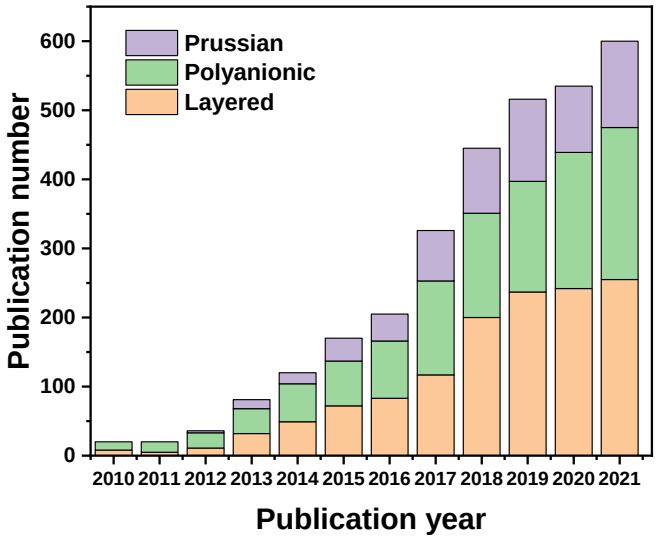


Figure 1.5 Number of publications regarding cathodes for SIBs in the past decade. Based upon sodium layered oxide cathodes, sodium polyanionic cathode (including sodium phosphates cathode and sodium NASICON cathode), and sodium Prussian cathode, web of science (March 2022).

***Polyanionic compounds**:*

Owing to the widespread use of $LiFePO_4$ in LIBs, the analogue polyanionic compounds have also been evaluated as potential cathode materials for SIBs. Polyanionic compounds, with the general chemical formula $Na_xTM_y(PO_4)_zX$ (TM=Fe, Ti, V, Cr, et al; X=F), typically exhibit high thermal and structural stability, long lifetimes, as well as good air stability. These characteristics arise from the 3D open-framework structure, formed by polyanionic polyhedra and transition metal ion polyhedra through strong covalent bonds.

Based on channels for Na-ion transportation within the crystal lattice, polyanionic compounds can be sorted into One-dimensional phosphates-type and 3D open framework NASICON (Na^+ superionic conductor)-type. $NaFePO_4$ is a representative of phosphate-type cathode with a theoretical capacity of 154 mAh g^{-1} and working voltage of 2.9 V (*vs.* Na^+/Na)[66, 67]. However, the practical capacity of $NaFePO_4$ is normally lower than the theoretical capacity in its most thermodynamically stable phase due to the limitations of 1D Na^+ transportation channel[68, 69].

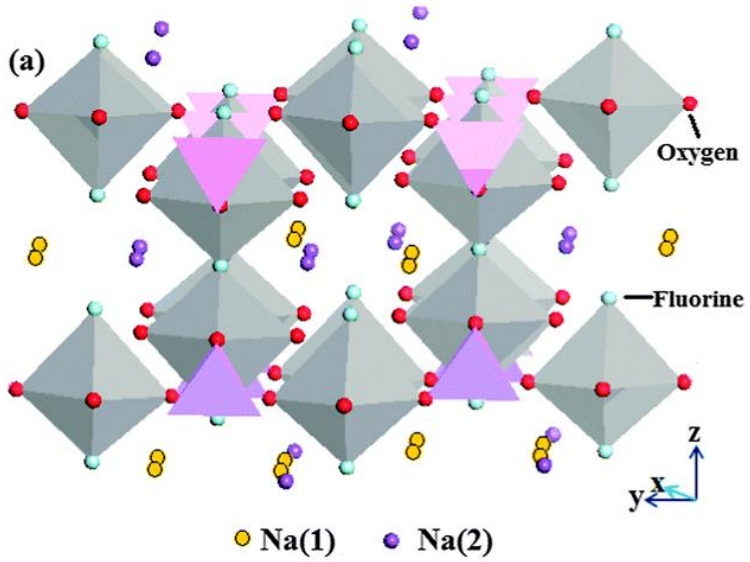


Figure 1.6 Scheme representation of the structure of $Na_3V_2(PO_4)_2F_3$. Reproduced from [70] with permission of The Royal Society of Chemistry.

To overcome this limitation, NASICON (Sodium Super Ionic Conductor)-structured compounds with 3D Na^+ channel (Figure 1.6) have demonstrated excellent rate performance. A representative material of this class is $Na_3V_2(PO4)_3$ (NVP), which contains two pairs of RedOx occurring at 1.63 and 3.4 V (*vs.* Na/Na^+) related to V^{2+}/V^{3+} and V^{3+}/V^{4+} RedOx couples, giving a theoretical capacity of 117.6 mAh g^{-1}[71]. When introducing three F^- instead of one PO_4^{3-},

an improved average working voltage of 3.9 V can be achieved giving an energy density of 507 Wh Kg^{-1} based on the mass of cathode material $Na_3V_2(PO_4)_2F_3$[70, 72].

However, polyanionic compounds generally suffer from poor electrical conductivity and need to be modified by carbon coating or nanosizing the particle[73, 74].

***Prussian analogues**:*

Another alternatives to be considered as potential cathodes for SIBs are Prussian blue (PB) and its analogues (PBA), with the general chemical formula $Na_xTM_y[Fe(CN)_6]$ (TM=Fe, Ni, Co, Mn, Cu, etc)[74-76]. These compounds have a cubic centroid structure, as shown in Figure 1.7, where the metal and ferricyanide in the lattice are arranged into a three-dimensional structural skeleton according to Fe-C=N-TM, in which Fe ions and metal ions are located at the apex according to the cubic array, C=N is located on the cubic prongs, and Na^+ and lattice HO_2 occupy the cubic voids. Such a cubic framework structure is well stabilized, and the lattice varies little before and after charging and discharging, thus offering a long cycle life. Both transition metal ions (Fe and TM) in the structure could be involved in the redox reaction, so that up to 2 Na^+ can be theoretically removed, corresponding to a capacity of 170 mAh g^{-1}, making it a very promising class of cathode materials for SIBs[77].

PB and PBAs compounds usually contain a certain amount of coordinated H_2O, introduced during the synthesis process, which is difficult to remove and results in security concerns[78, 79]. Therefore, these compounds are ideally to be used with aqueous electrolytes instead of non-aqueous[80-82].

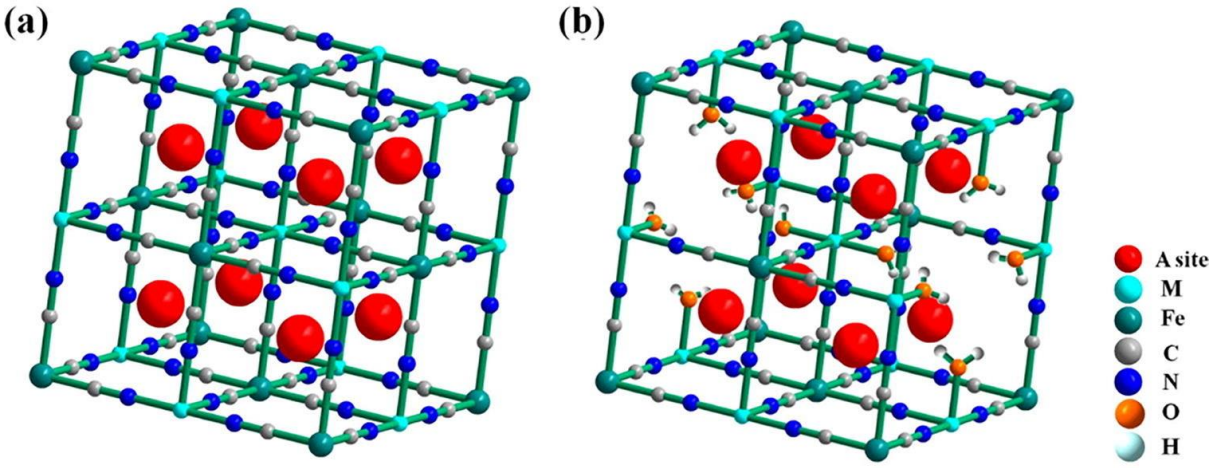


Figure 1.7 Scheme representation of the structure of PB, (a) an intact framework without structural defects, and (b) a defective framework with $Fe(CN)_6$ vacancies randomly existing in unit cells formed during the material synthesis process. Reproduced with permission [83]. Copyright 2016, American Chemical Society.

***Layered metal oxides**:*

Na_xTMO_2 ($0 < x \leq 1$, TM represents transition metal)-layered oxides are considered as the most appealing candidates for SIBs and are the most extensively studied (as shown in Figure 1.5 and Table 1.2), due to their low cost, high theoretical capacity, appropriate operating potential and relatively facile synthesis processes[84-89]. Inspired by the successful application of $LiTMO_2$ in LIBs, $NaCoO_2$[90, 91], $NaMnO_2$[92], $NaNiO_2$[93], and their mixed-cation oxides, like $Na_{2/3}[Ni_{1/3}Mn_{2/3}]O_2$[94] have been widely investigated as Na-insertion oxides. Recent studies even demonstrated that Ti[95], Cr[31], V[96], and earth-abundant Cu[97], Fe[98], which are inactive in LIBs, can act as the Na intercalation host. These interesting findings provide researchers with a wide scope for developing novel cathodes with excellent electrochemical performance by using a broad range of transition metals.

However, this type of material undergoes a series of phase transformations during the Na^+ extraction/insertion process due to slab-gliding, especially when charged to higher cut-off voltage[84, 99-101]. Depending on the Na^+ coordination environment and stacking sequence of $(MO_2)_n$ sheets, typical layered oxides can be grouped into O3-type (Na dominating the octahedral sites with ABCABC stacking sequence, Figure 1.8 a) and P2-type (Na dominating the trigonal prismatic sites with ABBA stacking sequence, Figure 1.8 b) structures[102]. P2 layered materials generally exhibit good structural stability and long cycling performance when operating under 4.0 V *vs.* Na^+/Na. This is due to the open Na^+ transport channel in the structure with low Na^+ diffusion barriers. However, a poorly reversible P2-O2 phase transition may occur when charged to 4.2 V *vs.* Na/Na^+ (Figure 1.8 b), leading to raid capacity fading[84, 103-106]. Furthermore, owing to the low Na content (≤0.85) in the unit cell, P2-type materials typically exhibit a lower first charge capacity but a higher first discharge capacity, resulting in an abnormal initial Coulombic efficiency (>100%). This discrepancy poses challenges in achieving an adequate balance in areal capacity for full cell design. O3-type oxides offer a higher reversible capacity due to the sufficient Na content in the unit cell but commonly undergo more complex phase transitions than the P2-type oxides due to the sluggish kinetics.

Most of the studied O3-type materials experience two major phase transitions, namely (Figure 1.8 a) (I) reversible O3 $NaTMO_2$ ⇔P3 $Na_{\sim 0.5}TMO_2$ and (II) irreversible P3 $Na_{\sim 0.5}TMO_2$ - X Na_yTMO_2, where y and the high voltage phase X vary with the nature of TM (transition metal) and the voltage window[84, 107]. Such irreversible phase transitions occurring under high voltage will easily lead to crystal structural collapse and thus display a rapid capacity degradation upon cycling[84]. As a compromise measure, only 0.5-0.6 Na^+ per formula unit could be removed to maintain the crystal structural stability, leading to an unsatisfactory specific energy for Na-ion battery applications[84, 108]. ***(Note: The content of this paragraph is partly derived from my published paper https://iopscience.iop.org/article/10.1088/2515-7639/abf545, with reasonable integration and citation.)***

In the pursuit of narrowing the energy density gap between SIBs and LIBs, researchers have explored various modification strategies. These strategies include doping[109-125], surface coating[126-135], doping integrated with coating[136-142], as well as the design of particle morphology [143-147]. These efforts aim to enhance the structural stability and electrochemical performance of layered materials, particularly at higher operating voltages. A comprehensive review about the role and progress of modification strategies will be discussed in Chapter 2.

The capacity and cycling stability of Na_xTMO_2-layered oxide materials are currently not achieving the desired performance, requiring further improvements. This Ph.D. project will take O3-type layered as an example and focus on the optimization of interface via crystal structure, morphology, and full cell design engineering to improve the cycle life of SIBs.

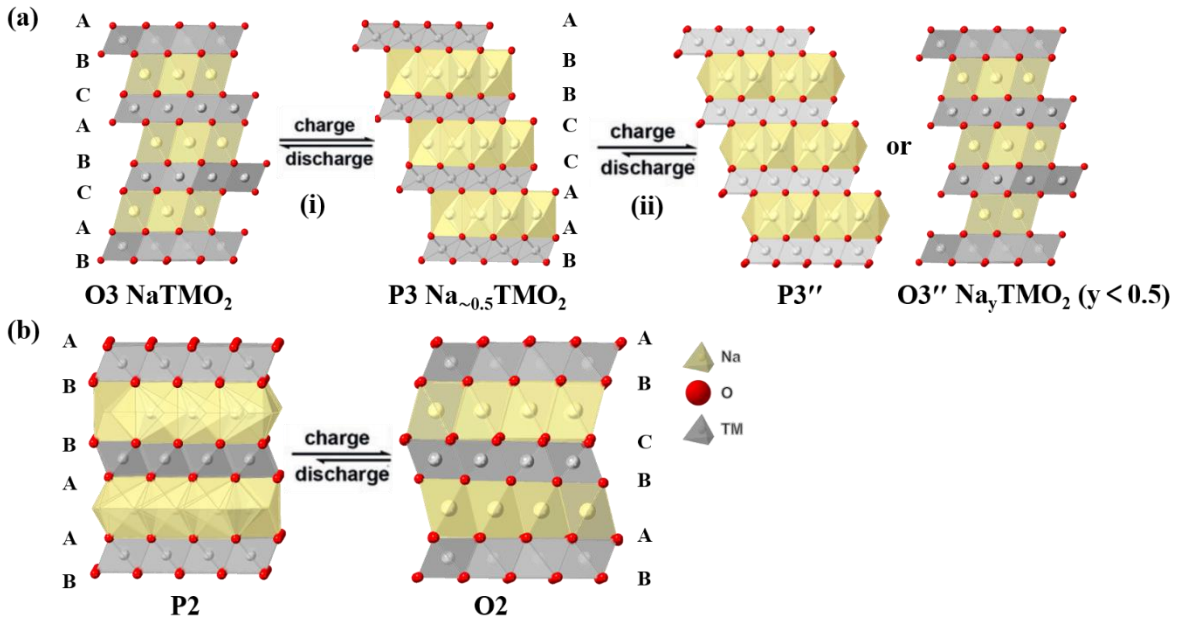


Figure 1.8 Schematic illustration of typical structural evolution during charge/discharge of (a) O3-, and (b) P2-phase layered oxides[84].

Table 1-2 Comparison of properties of commonly used cathode materials for sodium-ion battery.

	Polyanionic compounds	***Prussian analogues***	***Sodium Layered Oxides***
Major Advantages	✓ Good structure stability ✓ Good lifetime ✓ Air stable ✓ Moderate cost	✓ Moderate reversible capacity ~140 (mAh/g) ✓ Low synthesis temperature ✓ Low cost ✓ Good lifetime	✓ High reversible capacity ~160 (mAh/g) ✓ Facile synthesis ✓ High tap density ✓ Moderate cost
Major Disadvantages	✓ Low reversible capacity ~120 (mAh/g) ✓ Low tap density ✓ Poor electrical conductivity	✓ Low tap density ✓ Security concern (HCN) ✓ Crystal defects and coordinated water	✓ Multiple phase transition ✓ Poor cyclability ✓ Moisture sensitive

1.2.4 Anode material for sodium-ion batteries

Negative electrode materials in general can be divided into two main categories: carbon-based materials such as graphite, hard carbon, and non-carbon-based materials such as silicon-based materials, alloy materials, titanium-based materials, etc[148-150].

Hard carbon:

Carbon-based materials have the advantages of being widely sourced and environmentally friendly, and the most representative graphite with a theoretical capacity of 372 mAh g^{-1} has been widely used in lithium-ion batteries since 1991. However, the active sites suitable for Li^+ embedding are not necessarily suitable for Na^+ embedding due to the lattice mismatch between the graphite layers and Na ion [151, 152]. Although research has shown that a small amount of Na^+ could be inserted into the graphite layers under particular conditions[151], the reversible capacity is considerably smaller than that of Li^+, and the lack of suitable anode material also indeed hindered the development progress of SIBs. Hard carbon (HC), the most commonly used anode material in SIBs nowadays, began to catch researchers' attention in 2000 when Stevens and Dahn first reported a reversible capacity of 300 mAh g^{-1} at a low current density of C/80 rate[153].

Different from graphite, hard carbon is a kind of carbon that cannot be graphitized even at high temperatures, which has a disordered structure with expanded graphene sheet spacing compared to graphite[149, 154-156]. Hard carbon possesses the benefits of low-cost and sustainability, as it can be derived from biomass and biowastes[157]. However, the structure, specific surface area, and pores distribution are sensitive to the carbon sources and synthesis conditions[158-162], making it difficult in large-scale production with controlled physiochemical properties. Besides, the detailed structure and sodium storage mechanism of HC is still a debated topic, though several Na-storage models have been proposed (Figure 1.9)[163-169].

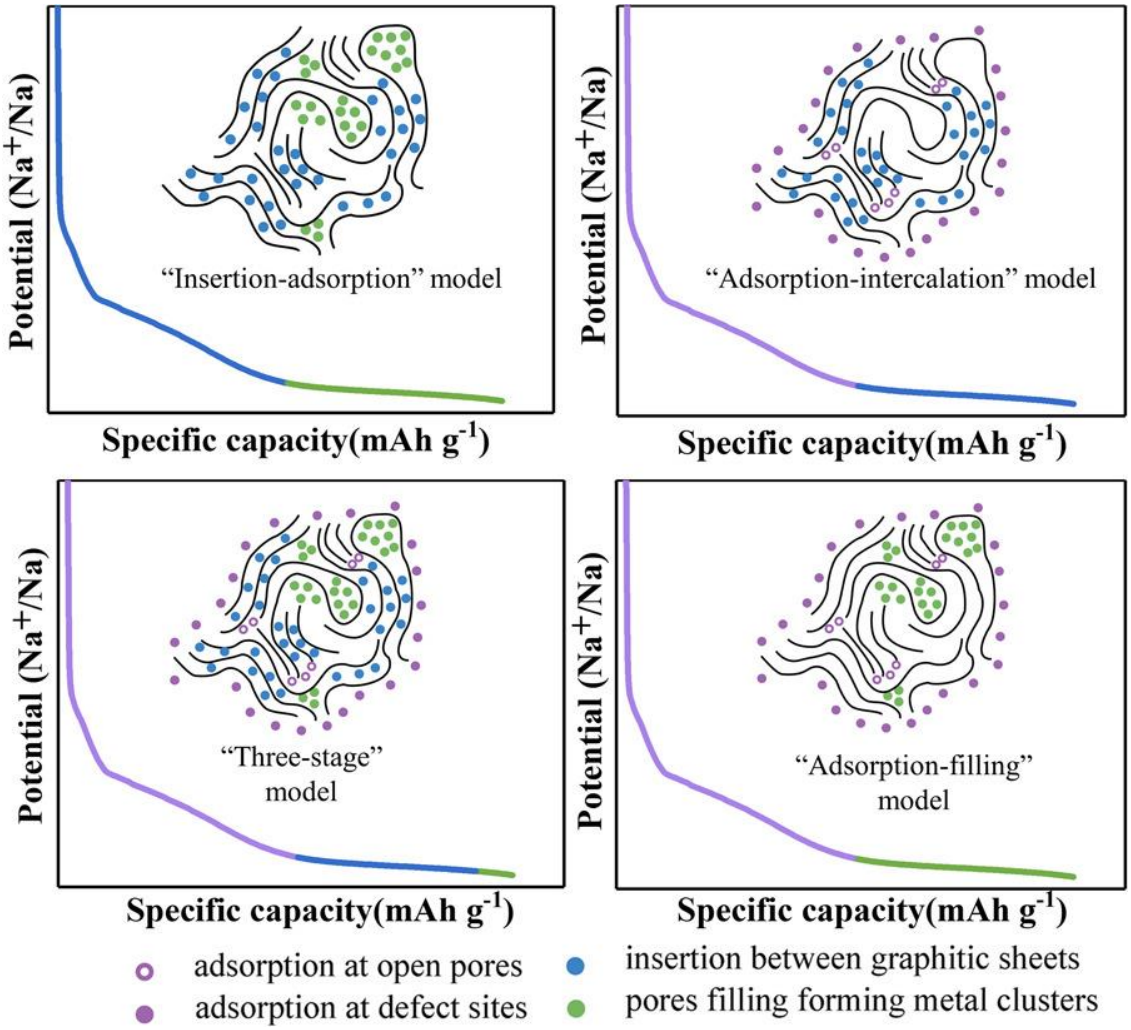


Figure 1.9 Summary of the proposed sodium-storage models in hard carbon[170].

Na alloy compounds:

Alloy materials are another promising candidate for SIBs owing to their high theoretical specific capacity and excellent electrical conductivity. Different from the sodium-insertion/adsorption mechanism in hard carbon, sodium can react with certain metals in Group 14 and Group 15 to form sodium-metal alloys (Na_nX, X= Si, Sn, Pb, Sb, etc.) based on the alloying reaction[171-180]. Sn and Sb-based alloys are the most attracted ones. For tin-metal alloys, 4 Na atoms can be inserted into tin to form $Na_{15}Sn_4$ alloy, and a capacity of 500 mA h g^{-1} can be achieved below 1V[181, 182]. However, alloy anodes generally suffer from large volume changes during the Na^+ insertion/extraction process, resulting in low Coulombic efficiency and poor cyclic performance [183-185].

1.3 Challenges for sodium-ion batteries

Despite the fact that sodium-ion batteries have been a key objective in the new energy roadmaps of countries in recent years, progress in the sector does not seem to be as fast as expected, mainly due to existing technical limitations, especially in cathode materials, which hinder their commercial application.

Table 1-3 Comparison of the physicochemical characteristics of Li^+ and Na^+.

Category	Lithium	Sodium
Atomic weight (g mol^{-1})	6.94	23
Ionic radius (Å)	0.76	1.02
Standard electrode potential (*vs.* SHE)	-3.04	-2.71
Standard electrode potential (*vs.* Li/Li+)	0	0.33
Theoretical capacity (mAh g^{-1})	3861	1166
Percentage in the crust	0.01%	2.83%

Note: SHE: standard hydrogen electrode

The main limitation in the application of sodium-ion batteries is their theoretically lower energy density compared to LIBs. The energy density of the state-of-art SIBs is 100-160 Wh/Kg, which is lower than that of 160-180 Wh/Kg for $LiFePO_4$, the most widely used LIBs in energy storage at present. Table 1.3 summarizes the physicochemical properties of Li and Na. The standard electrochemical potential of Na^+ /Na is 0.33 V higher than that of Li^+ /Li (Na -2.71 V vs. Li -3.04 V with respect to standard hydrogen electrode SHE), and the atomic mass of Na is three times heavier than Li (Na 23 g mol^{-1} vs Li 6.9 g mol^{-1}). As a result, the gravimetric energy density of electrode materials based on Na is innately much lower than that of Li.

Another challenge is the insufficient cycling durability, typically hundreds of cycles on a lab scale, which is also below the practical usage requirements, typically in thousands[186]. Therefore,

though the SIBs present the advantage of raw materials cost, this advantage is offset by their lower energy density and insufficient cycling stability[84], making the actual cost of SIBs in terms of per watt-hour even higher than that of LIBs.

In order to gain adoption into the existing and novel applications, SIBs with higher energy density and longer cycle life are required, and this can be achieved in part through the development of new cathode materials with improved specific capacity and structure stability combined with optimizing the full cell design. This will effectively reduce the cost of energy (Wh) per cycle and further aid adoption into new markets.

1.4 Research aims and thesis outline

This project will focus on the O3-layered oxides, as currently, this type of material offers the most competitive chemistry in terms of working voltage and specific capacity, which makes its electrochemical performance comparable to $LiFePO_4$ cells when incorporated into a full cell. However, O3-layered oxides typically suffer from irreversible phase transition of host structure under higher operation voltage, resulting in crystal structural collapse and rapid capacity degradation upon cycling. These materials are particularly difficult to handle and process due to the formation of carbonate surface species on the surface.

This project aims to engineer cathode and interfaces in sodium-ion batteries through doping integrated coating, particle morphology optimization, and rational full-cell design approaches in order to enhance the capacity and cycle life of O3-layered oxides. Cobalt-free O3-type layered $NaNi_{1/3}Fe_{1/3}Mn_{1/3}O_2$ oxide was specifically focused due to the use of earth-abundant and non-critical elements. The objectives of this project are:

- To investigate new doping and surface coating strategies to suppress the irreversible high voltage phase transition and lattice structure degradation of $NaNi_{1/3}Fe_{1/3}Mn_{1/3}O_2$ oxide.
- To optimize the synthetic parameters of $NaNi_{1/3}Fe_{1/3}Mn_{1/3}O_2$ oxide to get uniformly distributed spherical particles, minimize the surface side reactions, and prolong lifetime, aiming to establish a controllable scale-up process.
- Further evaluating and optimizing the performance of the above scalable material in a full-cell configuration to promote the process of practical use of $NaNi_{1/3}Fe_{1/3}Mn_{1/3}O_2$ oxide.

Initially, the failure and degradation processes associated with the layered oxide cathode materials under higher voltage are clarified, and an extensive summary of prior work on optimization strategies to overcome these degradation processes is summarised in Chapter 2. Then, three modification strategies are focused on and studied in detail as shown in Figure 1.10:

(1) Bulk structure and surface engineering: Chapter 4 explores the ways of suppressing bulk structural changes and interfacial degradation under higher voltage. Sn was selected as a foreign element. The effects of Sn contents on the bulk structure, particle surface, as well as electrochemical performance, were evaluated, and the mechanism was studied through an extensive analysis by in situ XRD, HRTEM, FIB-SEM, XPS, and Mössbauer spectroscopy.

(2) Particle Morphology Engineering: Chapter 5 focuses on optimizing the synthetic conditions. The influence of synthesis conditions (pH, amount of chelating agent, and stirring speed) on the particle size, shape, tap density, and electrochemical properties of $NaNi_{1/3}Fe_{1/3}Mn_{1/3}O_2$ was investigated. Design of Experiments (DoE) methodology was used to identify the connection between the synthesis parameters and the morphology as well as the electrochemical properties.

(3) Full cell optimization: finally, in Chapter 6, the optimized cathode material was used to make full cells to verify the practical application with hard carbon as an anode. The negative/positive capacity ratio (N/P ratio) and working voltage window were studied and optimized to maximum the cycling lifetime.

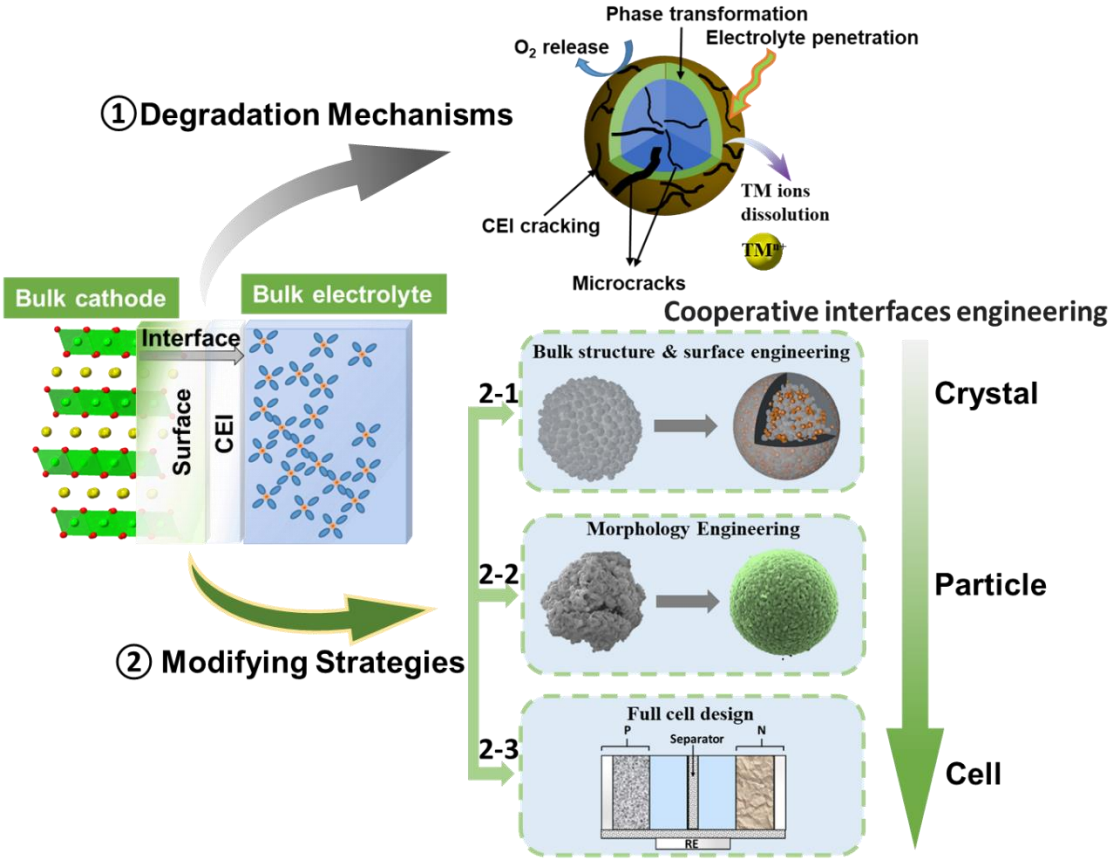


Figure 1.10 Overview of the thesis.

1.5 References

1. Wei, F.; Zhang, Q.; Zhang, P.; Tian, W.; Dai, K.; Zhang, L.; Mao, J.; Shao, G., Review—Research Progress on Layered Transition Metal Oxide Cathode Materials for Sodium Ion Batteries. *Journal of The Electrochemical Society* **2021,** 168, (5).
2. *Energy Storage Grand Challenge Roadmap*; 2020.
3. Net Zero by 2050 A Roadmap for the Global Energy Sector. **2021**.
4. Worku, M. Y., Recent Advances in Energy Storage Systems for Renewable Source Grid Integration: A Comprehensive Review. *Sustainability* **2022,** 14, (10).
5. R.A. Markets, 2020a, Global and China Li-ion Power Battery Industry Report, 2019-2025.
6. Miao, Y.; Liu, L.; Zhang, Y.; Tan, Q.; Li, J., An overview of global power lithium-ion batteries and associated critical metal recycling. *J Hazard Mater* **2022,** 425, 127900.
7. Peng, J.; Meng, J.; Chen, D.; Liu, H.; Hao, S.; Sui, X.; Du, X., A Review of Lithium-Ion Battery Capacity Estimation Methods for Onboard Battery Management Systems: Recent Progress and Perspectives. *Batteries* **2022,** 8, (11).
8. Yabuuchi, N.; Kubota, K.; Dahbi, M.; Komaba, S., Research development on sodium-ion batteries. *Chem Rev* **2014,** 114, (23), 11636-82.
9. Slater, M. D.; Kim, D.; Lee, E.; Johnson, C. S., Sodium-Ion Batteries. *Advanced Functional Materials* **2013,** 23, (8), 947-958.
10. Murdock, B. E.; Toghill, K. E.; Tapia‐Ruiz, N., A Perspective on the Sustainability of Cathode Materials used in Lithium‐Ion Batteries. *Advanced Energy Materials* **2021,** 11, (39).
11. Larcher, D.; Tarascon, J. M., Towards greener and more sustainable batteries for electrical energy storage. *Nat Chem* **2015,** 7, (1), 19-29.
12. Yang, S.; Zhang, F.; Ding, H.; He, P.; Zhou, H., Lithium Metal Extraction from Seawater. *Joule* **2018,** 2, (9), 1648-1651.
13. Li, Y.; Lu, Y.; Zhao, C.; Hu, Y.-S.; Titirici, M.-M.; Li, H.; Huang, X.; Chen, L., Recent advances of electrode materials for low-cost sodium-ion batteries towards practical application for grid energy storage. *Energy Storage Materials* **2017,** 7, 130-151.
14. Song, T.; Chen, L.; Gastol, D.; Dong, B.; Marco, J. F.; Berry, F.; Slater, P.; Reed, D.; Kendrick, E., High-Voltage Stabilization of O3-Type Layered Oxide for Sodium-Ion Batteries by Simultaneous Tin Dual Modification. *Chemistry of Materials* **2022**.
15. Pan, H.; Hu, Y.-S.; Chen, L., Room-temperature stationary sodium-ion batteries for large-scale electric energy storage. *Energy & Environmental Science* **2013,** 6, (8).
16. Jin, Y.; Xu, Y.; Le, P. M. L.; Vo, T. D.; Zhou, Q.; Qi, X.; Engelhard, M. H.; Matthews, B. E.; Jia, H.; Nie, Z.; Niu, C.; Wang, C.; Hu, Y.; Pan, H.; Zhang, J.-G., Highly Reversible Sodium Ion Batteries Enabled by Stable Electrolyte-Electrode Interphases. *ACS Energy Letters* **2020,** 5, (10), 3212-3220.
17. Liu, Q.; Hu, Z.; Chen, M.; Zou, C.; Jin, H.; Wang, S.; Chou, S. L.; Dou, S. X., Recent Progress of Layered Transition Metal Oxide Cathodes for Sodium-Ion Batteries. *Small* **2019,** 15, (32), 1805381.
18. *Mineral commodity summaries 2023*; U.S. Geological Survey: 2023.
19. Komaba, S.; Yabuuchi, N.; Nakayama, T.; Ogata, A.; Ishikawa, T.; Nakai, I., Study on the reversible electrode reaction of $Na_{(1-x)}Ni_{(0.5)}Mn_{(0.5)}O_2$ for a rechargeable sodium-ion battery. *Inorg Chem* **2012,** 51, (11), 6211-20.
20. Yu, T. Y.; Ryu, H. H.; Han, G.; Sun, Y. K., Understanding the Capacity Fading Mechanisms of O3‐Type $Na[Ni_{0.5}Mn_{0.5}]O_2$ Cathode for Sodium‐Ion Batteries. *Advanced Energy Materials* **2020,** 10, (37).
21. Mendiboure, A.; Delmas, C.; Hagenmuller, P., Electrochemical intercalation and deintercalation of Na_xMnO_2 bronzes. *J. Solid State Chem.* **1985,** 57, (3), 323-331.

22. Yuan, D. D.; Wang, Y. X.; Cao, Y. L.; Ai, X. P.; Yang, H. X., Improved Electrochemical Performance of Fe-Substituted $NaNi_{0.5}Mn_{0.5}O_2$ Cathode Materials for Sodium-Ion Batteries. *ACS Appl Mater Interfaces* **2015,** 7, (16), 8585-91.
23. Kim, D.; Lee, E.; Slater, M.; Lu, W.; Rood, S.; Johnson, C. S., Layered $Na[Ni_{1/3}Fe_{1/3}Mn_{1/3}]O_2$ cathodes for Na-ion battery application. *Electrochemistry Communications* **2012,** 18, 66-69.
24. Fang, Y.; Chen, Z.; Xiao, L.; Ai, X.; Cao, Y.; Yang, H., Recent Progress in Iron-Based Electrode Materials for Grid-Scale Sodium-Ion Batteries. *Small* **2018,** 14, (9).
25. Chen, T. R.; Sheng, T.; Wu, Z. G.; Li, J. T.; Wang, E. H.; Wu, C. J.; Li, H. T.; Guo, X. D.; Zhong, B. H.; Huang, L.; Sun, S. G., Cu^{2+} Dual-Doped Layer-Tunnel Hybrid $Na_{0.6}Mn_{1-x}Cu_xO_2$ as a Cathode of Sodium-Ion Battery with Enhanced Structure Stability, Electrochemical Property, and Air Stability. *ACS Appl Mater Interfaces* **2018,** 10, (12), 10147-10156.
26. Zheng, L.; Li, J.; Obrovac, M. N., Crystal Structures and Electrochemical Performance of Air-Stable $Na_{2/3}Ni_{1/3-x}Cu_xMn_{2/3}O_2$ in Sodium Cells. *Chemistry of Materials* **2017,** 29, (4), 1623-1631.
27. Zheng, L.; Obrovac, M. N., Investigation of O3-type $Na_{0.9}Ni_{0.45}Mn_xTi_{0.55-x}O_2$ ($0 \leqslant x \leqslant 0.55$) as positive electrode materials for sodium-ion batteries. *Electrochimica Acta* **2017,** 233, 284-291.
28. Yu, C.-Y.; Park, J.-S.; Jung, H.-G.; Chung, K.-Y.; Aurbach, D.; Sun, Y.-K.; Myung, S.-T., $NaCrO_2$ cathode for high-rate sodium-ion batteries. *Energy & Environmental Science* **2015,** 8, (7), 2019-2026.
29. Yabuuchi, N.; Ikeuchi, I.; Kubota, K.; Komaba, S., Thermal Stability of Na(x)CrO(2) for Rechargeable Sodium Batteries; Studies by High-Temperature Synchrotron X-ray Diffraction. *ACS Appl Mater Interfaces* **2016,** 8, (47), 32292-32299.
30. Kubota, K.; Ikeuchi, I.; Nakayama, T.; Takei, C.; Yabuuchi, N.; Shiiba, H.; Nakayama, M.; Komaba, S., New Insight into Structural Evolution in Layered $NaCrO_2$ during Electrochemical Sodium Extraction. *The Journal of Physical Chemistry C* **2014,** 119, (1), 166-175.
31. Komaba, S.; Takei, C.; Nakayama, T.; Ogata, A.; Yabuuchi, N., Electrochemical intercalation activity of layered $NaCrO_2$ vs. $LiCrO_2$. *Electrochemistry Communications* **2010,** 12, (3), 355-358.
32. Wang, Q.; Xu, J.; Zhang, W.; Mao, M.; Wei, Z.; Wang, L.; Cui, C.; Zhu, Y.; Ma, J., Research progress on vanadium-based cathode materials for sodium ion batteries. *Journal of Materials Chemistry A* **2018,** 6, (19), 8815-8838.
33. Hamani, D.; Ati, M.; Tarascon, J.-M.; Rozier, P., Na_xVO_2 as possible electrode for Na-ion batteries. *Electrochemistry Communications* **2011,** 13, (9), 938-941.
34. Guignard, M.; Didier, C.; Darriet, J.; Bordet, P.; Elkaim, E.; Delmas, C., P2-Na_xVO_2 system as electrodes for batteries and electron-correlated materials. *Nat Mater* **2013,** 12, (1), 74-80.
35. Roberts, S.; Kendrick, E., The re-emergence of sodium ion batteries: testing, processing, and manufacturability. *Nanotechnol Sci Appl* **2018,** 11, 23-33.
36. Patrick T. Moseley, D. A. J. R., High-Temperature Sodium Batteries for Energy Storage. *Electrochemical Energy Storage for Renewable Sources and Grid Balancing* **2015**, 253-268.
37. Kundu, D.; Talaie, E.; Duffort, V.; Nazar, L. F., The emerging chemistry of sodium ion batteries for electrochemical energy storage. *Angew Chem Int Ed Engl* **2015,** 54, (11), 3431-48.
38. Johnson, W. B.; Worrell, W. L., Lithium and sodium intercalated dichalcogenides: Properties and electrode applications. *Synth. Met.* **1982,** 4, (3), 225-248.
39. Komaba, S.; Murata, W.; Ishikawa, T.; Yabuuchi, N.; Ozeki, T.; Nakayama, T.; Ogata, A.; Gotoh, K.; Fujiwara, K., Electrochemical Na Insertion and Solid Electrolyte Interphase for Hard-Carbon Electrodes and Application to Na-Ion Batteries. *Advanced Functional Materials* **2011,** 21, (20), 3859-3867.
40. Hu, Y. S.; Komaba, S.; Forsyth, M.; Johnson, C.; Rojo, T., A New Emerging Technology: Na‐Ion Batteries. *Small Methods* **2019,** 3, (4).
41. Chayambuka, K.; Mulder, G.; Danilov, D. L.; Notten, P. H. L., From Li‐Ion Batteries toward Na‐Ion Chemistries: Challenges and Opportunities. *Advanced Energy Materials* **2020,** 10, (38).

42. Huang, Q.; Hu, Z.; Chen, K.; Zeng, Z.; Sun, Y.; Kong, Q.; Feng, W.; Wang, K.; Li, Z.; Wu, Z.; Chen, T.; Guo, X., Partial Modification Strategies of NASICON-Type Na3V2(PO4)3 Materials for Cathodes of Sodium-Ion Batteries: Progress and Perspectives. *ACS Applied Energy Materials* **2023,** 6, (5), 2657-2679.
43. Zhao, L.; Zhang, T.; Li, W.; Li, T.; Zhang, L.; Zhang, X.; Wang, Z., Engineering of Sodium-Ion Batteries: Opportunities and Challenges. *Engineering* **2022**.
44. Fan, T.-E.; Xie, H.-F., Sb_2S_3-rGO for high-performance sodium-ion battery anodes on Al and Cu foil current collector. *Journal of Alloys and Compounds* **2019,** 775, 549-553.
45. Ellis, B. L.; Nazar, L. F., Sodium and sodium-ion energy storage batteries. *Curr. Opin. Solid State Mater. Sci.* **2012,** 16, (4), 168-177.
46. Eftekhari, A.; Kim, D.-W., Sodium-ion batteries: New opportunities beyond energy storage by lithium. *Journal of Power Sources* **2018,** 395, 336-348.
47. Yabuuchi, N.; Yano, M.; Yoshida, H.; Kuze, S.; Komaba, S., Synthesis and Electrode Performance of O3-Type $NaFeO_2$-$NaNi_{1/2}Mn_{1/2}O_2$ Solid Solution for Rechargeable Sodium Batteries. *Journal of The Electrochemical Society* **2013,** 160, (5), A3131-A3137.
48. D'Arienzo, M.; Ruffo, R.; Scotti, R.; Morazzoni, F.; Mari, C. M.; Polizzi, S., Layered Na(0.71)CoO(2): a powerful candidate for viable and high performance Na-batteries. *Phys Chem Chem Phys* **2012,** 14, (17), 5945-52.
49. Li, Z.-Y.; Gao, R.; Zhang, J.; Zhang, X.; Hu, Z.; Liu, X., New insights into designing high-rate performance cathode materials for sodium ion batteries by enlarging the slab-spacing of the Na-ion diffusion layer. *Journal of Materials Chemistry A* **2016,** 4, (9), 3453-3461.
50. Ding, F.; Zhao, C.; Zhou, D.; Meng, Q.; Xiao, D.; Zhang, Q.; Niu, Y.; Li, Y.; Rong, X.; Lu, Y.; Chen, L.; Hu, Y.-S., A Novel Ni-rich O3-$Na[Ni_{0.60}Fe_{0.25}Mn_{0.15}]O_2$ Cathode for Na-ion Batteries. *Energy Storage Materials* **2020,** 30, 420-430.
51. Van Nguyen, H.; Nguyen, H. T. N.; Huynh, N. L. T.; Phan, A. L. B.; Van Tran, M.; Le, P. M. L., A study of the electrochemical kinetics of sodium intercalation in P2/O1/O3-$NaNi_{1/3}Mn_{1/3}Co_{1/3}O_2$. *J. Solid State Electrochem.* **2019,** 24, (1), 57-67.
52. Yoshida, H.; Yabuuchi, N.; Kubota, K.; Ikeuchi, I.; Garsuch, A.; Schulz-Dobrick, M.; Komaba, S., P2-type $Na_{2/3}Ni_{1/3}Mn_{2/3-x}Ti_xO_2$ as a new positive electrode for higher energy Na-ion batteries. *Chem Commun (Camb)* **2014,** 50, (28), 3677-80.
53. Yabuuchi, N.; Kajiyama, M.; Iwatate, J.; Nishikawa, H.; Hitomi, S.; Okuyama, R.; Usui, R.; Yamada, Y.; Komaba, S., P2-type $Na_x[Fe_{1/2}Mn_{1/2}]O_2$ made from earth-abundant elements for rechargeable Na batteries. *Nat Mater* **2012,** 11, (6), 512-7.
54. Barpanda, P.; Lander, L.; Nishimura, S.-i.; Yamada, A., Polyanionic Insertion Materials for Sodium-Ion Batteries. *Advanced Energy Materials* **2018,** 8, (17).
55. Barpanda, P.; Oyama, G.; Ling, C. D.; Yamada, A., Kröhnkite-Type $Na_2Fe(SO_4)_2{\cdot}2H_2O$ as a Novel 3.25 V Insertion Compound for Na-Ion Batteries. *Chemistry of Materials* **2014,** 26, (3), 1297-1299.
56. Zhang, X.; Rui, X.; Chen, D.; Tan, H.; Yang, D.; Huang, S.; Yu, Y., $Na_3V_2(PO_4)_3$: an advanced cathode for sodium-ion batteries. *Nanoscale* **2019,** 11, (6), 2556-2576.
57. Song, W.; Ji, X.; Wu, Z.; Yang, Y.; Zhou, Z.; Li, F.; Chen, Q.; Banks, C. E., Exploration of ion migration mechanism and diffusion capability for Na3V2(PO4)2F3 cathode utilized in rechargeable sodium-ion batteries. *Journal of Power Sources* **2014,** 256, 258-263.
58. Ni, Q.; Bai, Y.; Wu, F.; Wu, C., Polyanion-Type Electrode Materials for Sodium-Ion Batteries. *Adv Sci (Weinh)* **2017,** 4, (3), 1600275.
59. Li, H.; Xu, M.; Zhang, Z.; Lai, Y.; Ma, J., Engineering of Polyanion Type Cathode Materials for Sodium‐Ion Batteries: Toward Higher Energy/Power Density. *Advanced Functional Materials* **2020,** 30, (28).

60. Song, T.; Yao, W.; Kiadkhunthod, P.; Zheng, Y.; Wu, N.; Zhou, X.; Tunmee, S.; Sattayaporn, S.; Tang, Y., A Low-Cost and Environmentally Friendly Mixed Polyanionic Cathode for Sodium-Ion Storage. *Angew Chem Int Ed Engl* **2020,** 59, (2), 740-745.
61. You, Y.; Wu, X.-L.; Yin, Y.-X.; Guo, Y.-G., High-quality Prussian blue crystals as superior cathode materials for room-temperature sodium-ion batteries. *Energy Environ. Sci.* **2014,** 7, (5), 1643-1647.
62. Wang, L.; Song, J.; Qiao, R.; Wray, L. A.; Hossain, M. A.; Chuang, Y. D.; Yang, W.; Lu, Y.; Evans, D.; Lee, J. J.; Vail, S.; Zhao, X.; Nishijima, M.; Kakimoto, S.; Goodenough, J. B., Rhombohedral prussian white as cathode for rechargeable sodium-ion batteries. *J Am Chem Soc* **2015,** 137, (7), 2548-54.
63. Zhao, Q.; Lu, Y.; Chen, J., Advanced Organic Electrode Materials for Rechargeable Sodium-Ion Batteries. *Advanced Energy Materials* **2017,** 7, (8).
64. Rudola, A.; Rennie, A. J. R.; Heap, R.; Meysami, S. S.; Lowbridge, A.; Mazzali, F.; Sayers, R.; Wright, C. J.; Barker, J., Commercialisation of high energy density sodium-ion batteries: Faradion's journey and outlook. *Journal of Materials Chemistry A* **2021,** 9, (13), 8279-8302.
65. Hwang, J. Y.; Myung, S. T.; Sun, Y. K., Sodium-ion batteries: present and future. *Chem Soc Rev* **2017,** 46, (12), 3529-3614.
66. Oh, S.-M.; Myung, S.-T.; Hassoun, J.; Scrosati, B.; Sun, Y.-K., Reversible $NaFePO_4$ electrode for sodium secondary batteries. *Electrochemistry Communications* **2012,** 22, 149-152.
67. Tang, W.; Song, X.; Du, Y.; Peng, C.; Lin, M.; Xi, S.; Tian, B.; Zheng, J.; Wu, Y.; Pan, F.; Loh, K. P., High-performance $NaFePO_4$ formed by aqueous ion-exchange and its mechanism for advanced sodium ion batteries. *Journal of Materials Chemistry A* **2016,** 4, (13), 4882-4892.
68. Fang, Y.; Liu, Q.; Xiao, L.; Ai, X.; Yang, H.; Cao, Y., High-Performance Olivine $NaFePO_4$ Microsphere Cathode Synthesized by Aqueous Electrochemical Displacement Method for Sodium Ion Batteries. *ACS Appl Mater Interfaces* **2015,** 7, (32), 17977-84.
69. Zhu, Y.; Xu, Y.; Liu, Y.; Luo, C.; Wang, C., Comparison of electrochemical performances of olivine $NaFePO_4$ in sodium-ion batteries and olivine $LiFePO_4$ in lithium-ion batteries. *Nanoscale* **2013,** 5, (2), 780-7.
70. Song, W.; Ji, X.; Chen, J.; Wu, Z.; Zhu, Y.; Ye, K.; Hou, H.; Jing, M.; Banks, C. E., Mechanistic investigation of ion migration in $Na_3V_2(PO_4)_2F_3$ hybrid-ion batteries. *Phys Chem Chem Phys* **2015,** 17, (1), 159-65.
71. Song, W.; Ji, X.; Yao, Y.; Zhu, H.; Chen, Q.; Sun, Q.; Banks, C. E., A promising $Na_3V_2(PO_4)_3$ cathode for use in the construction of high energy batteries. *Phys Chem Chem Phys* **2014,** 16, (7), 3055-61.
72. Dacek, S. T.; Richards, W. D.; Kitchaev, D. A.; Ceder, G., Structure and Dynamics of Fluorophosphate Na-Ion Battery Cathodes. *Chemistry of Materials* **2016,** 28, (15), 5450-5460.
73. Jung, Y. H.; Lim, C. H.; Kim, D. K., Graphene-supported $Na_3V_2(PO_4)_3$ as a high rate cathode material for sodium-ion batteries. *Journal of Materials Chemistry A* **2013,** 1, (37).
74. Pasta, M.; Wessells, C. D.; Huggins, R. A.; Cui, Y., A high-rate and long cycle life aqueous electrolyte battery for grid-scale energy storage. *Nat Commun* **2012,** 3, 1149.
75. Wessells, C. D.; Huggins, R. A.; Cui, Y., Copper hexacyanoferrate battery electrodes with long cycle life and high power. *Nat Commun* **2011,** 2, 550.
76. Wang, L.; Lu, Y.; Liu, J.; Xu, M.; Cheng, J.; Zhang, D.; Goodenough, J. B., A superior low-cost cathode for a Na-ion battery. *Angew Chem Int Ed Engl* **2013,** 52, (7), 1964-7.
77. Song, J.; Wang, L.; Lu, Y.; Liu, J.; Guo, B.; Xiao, P.; Lee, J. J.; Yang, X. Q.; Henkelman, G.; Goodenough, J. B., Removal of interstitial H_2O in hexacyanometallates for a superior cathode of a sodium-ion battery. *J Am Chem Soc* **2015,** 137, (7), 2658-64.
78. Liu, Q.; Hu, Z.; Chen, M.; Zou, C.; Jin, H.; Wang, S.; Chou, S. L.; Liu, Y.; Dou, S. X., The Cathode Choice for Commercialization of Sodium‐Ion Batteries: Layered Transition Metal Oxides versus Prussian Blue Analogs. *Advanced Functional Materials* **2020,** 30, (14).
79. Lu, Y.; Wang, L.; Cheng, J.; Goodenough, J. B., Prussian blue: a new framework of electrode materials for sodium batteries. *Chem Commun (Camb)* **2012,** 48, (52), 6544-6.

80. Shen, L.; Jiang, Y.; Liu, Y.; Ma, J.; Sun, T.; Zhu, N., High-stability monoclinic nickel hexacyanoferrate cathode materials for ultrafast aqueous sodium ion battery. *Chemical Engineering Journal* **2020,** 388.
81. Jiang, P.; Shao, H.; Chen, L.; Feng, J.; Liu, Z., Ion-selective copper hexacyanoferrate with an open-framework structure enables high-voltage aqueous mixed-ion batteries. *Journal of Materials Chemistry A* **2017,** 5, (32), 16740-16747.
82. Qian, J.; Wu, C.; Cao, Y.; Ma, Z.; Huang, Y.; Ai, X.; Yang, H., Prussian Blue Cathode Materials for Sodium-Ion Batteries and Other Ion Batteries. *Advanced Energy Materials* **2018,** 8, (17).
83. Wu, X.; Wu, C.; Wei, C.; Hu, L.; Qian, J.; Cao, Y.; Ai, X.; Wang, J.; Yang, H., Highly Crystallized $Na_2CoFe(CN)_6$ with Suppressed Lattice Defects as Superior Cathode Material for Sodium-Ion Batteries. *ACS Appl Mater Interfaces* **2016,** 8, (8), 5393-9.
84. Song, T.; Kendrick, E., Recent progress on strategies to improve the high-voltage stability of layered-oxide cathode materials for sodium-ion batteries. *Journal of Physics: Materials* **2021,** 4, (3).
85. Kubota, K.; Komaba, S., Review—Practical Issues and Future Perspective for Na-Ion Batteries. *Journal of The Electrochemical Society* **2015,** 162, (14), A2538-A2550.
86. Li, W.-J.; Han, C.; Wang, W.; Gebert, F.; Chou, S.-L.; Liu, H.-K.; Zhang, X.; Dou, S.-X., Commercial Prospects of Existing Cathode Materials for Sodium Ion Storage. *Advanced Energy Materials* **2017,** 7, (24).
87. Liu, T.; Zhang, Y.; Jiang, Z.; Zeng, X.; Ji, J.; Li, Z.; Gao, X.; Sun, M.; Lin, Z.; Ling, M.; Zheng, J.; Liang, C., Exploring competitive features of stationary sodium ion batteries for electrochemical energy storage. *Energy & Environmental Science* **2019,** 12, (5), 1512-1533.
88. Han, M. H.; Gonzalo, E.; Singh, G.; Rojo, T., A comprehensive review of sodium layered oxides: powerful cathodes for Na-ion batteries. *Energy & Environmental Science* **2015,** 8, (1), 81-102.
89. Liang, X.; Hwang, J. Y.; Sun, Y. K., Practical Cathodes for Sodium‐Ion Batteries: Who Will Take The Crown? *Advanced Energy Materials* **2023**.
90. Fouassier, C.; Matejka, G.; Reau, J.-M.; Hagenmuller, P., Sur de nouveaux bronzes oxygénés de formule Na_xCoO_2 (x<1). Le système cobalt-oxygène-sodium. *J. Solid State Chem.* **1973,** 6, (4), 532-537.
91. Shiprath, K.; Manjunatha, H.; Venkata Nadh, R.; Anil Babu, T.; Ramesh, S.; Chandra Babu Naidu, K.; Ramesha, M., Synthesis and Electrochemical Characterization of $NaCoO_2$ as Cathode Material in 2 M NaOH Aqueous Electrolyte. *ChemistrySelect* **2021,** 6, (8), 1874-1881.
92. Billaud, J.; Clement, R. J.; Armstrong, A. R.; Canales-Vazquez, J.; Rozier, P.; Grey, C. P.; Bruce, P. G., beta-$NaMnO_2$: a high-performance cathode for sodium-ion batteries. *J Am Chem Soc* **2014,** 136, (49), 17243-8.
93. Vassilaras, P.; Ma, X.; Li, X.; Ceder, G., Electrochemical Properties of Monoclinic $NaNiO_2$. *Journal of The Electrochemical Society* **2012,** 160, (2), A207-A211.
94. Zhang, J.; Wang, W.; Wang, W.; Wang, S.; Li, B., Comprehensive Review of P2-Type $Na_{2/3}Ni_{1/3}Mn_{2/3}O_2$, a Potential Cathode for Practical Application of Na-Ion Batteries. *ACS Appl Mater Interfaces* **2019,** 11, (25), 22051-22066.
95. Wu, D.; Li, X.; Xu, B.; Twu, N.; Liu, L.; Ceder, G., $NaTiO_2$: a layered anode material for sodium-ion batteries. *Energy & Environmental Science* **2015,** 8, (1), 195-202.
96. Iermakova, D.; Rozier, P.; Chane-Ching, J.-Y.; Taberna, P.-L.; Simon, P., Non - electrochemical Na – deintercalation from O3 $NaVO_2$. *Mater. Res. Bull.* **2020,** 121.
97. Ono, Y.; Yui, Y.; Hayashi, M.; Asakura, K.; Kitabayashi, H.; Takahashi, K. I., Electrochemical Properties of $NaCuO_2$ for Sodium-Ion Secondary Batteries. *ECS Transactions* **2014,** 58, (12), 33-39.
98. Yabuuchi, N.; Yoshida, H.; Komaba, S., Crystal Structures and Electrode Performance of Alpha-$NaFeO_2$ for Rechargeable Sodium Batteries. *Electrochemistry* **2012,** 80, (10), 716-719.
99. Han, M. H.; Gonzalo, E.; Casas-Cabanas, M.; Rojo, T., Structural evolution and electrochemistry of monoclinic $NaNiO_2$ upon the first cycling process. *Journal of Power Sources* **2014,** 258, 266-271.

100. Wang, L.; Wang, J.; Zhang, X.; Ren, Y.; Zuo, P.; Yin, G.; Wang, J., Unravelling the origin of irreversible capacity loss in $NaNiO_2$ for high voltage sodium ion batteries. *Nano Energy* **2017,** 34, 215-223.
101. Wang, P. F.; You, Y.; Yin, Y. X.; Wang, Y. S.; Wan, L. J.; Gu, L.; Guo, Y. G., Suppressing the P2-O2 Phase Transition of $Na_{0.67}$ $Mn_{0.67}$ $Ni_{0.33}$ O_2 by Magnesium Substitution for Improved Sodium-Ion Batteries. *Angew Chem Int Ed Engl* **2016,** 55, (26), 7445-7449.
102. Delmas, C.; Fouassier, C.; Hagenmuller, P., Structural classification and properties of the layered oxides. *Physica B+C* **1980,** 99, (1-4), 81-85.
103. Wang, H.; Yang, B.; Liao, X.-Z.; Xu, J.; Yang, D.; He, Y.-S.; Ma, Z.-F., Electrochemical properties of P2-$Na_{2/3}[Ni_{1/3}Mn_{2/3}]O_2$ cathode material for sodium ion batteries when cycled in different voltage ranges. *Electrochimica Acta* **2013,** 113, 200-204.
104. Yabuuchi, N.; Kajiyama, M.; Iwatate, J.; Nishikawa, H.; Hitomi, S.; Okuyama, R.; Usui, R.; Yamada, Y.; Komaba, S., P2-type $Na_x[Fe_{1/2}Mn_{1/2}]O_2$ made from earth-abundant elements for rechargeable Na batteries. *Nat Mater* **2012,** 11, (6), 512-517.
105. Pahari, D.; Puravankara, S., On controlling the P2-O2 phase transition by optimal Ti-substitution on Ni- site in P2-type $Na_{0.67}Ni_{0.33}Mn_{0.67}O_2$ (NNMO) cathode for Na-ion batteries. *Journal of Power Sources* **2020,** 455.
106. Lee, D. H.; Xu, J.; Meng, Y. S., An advanced cathode for Na-ion batteries with high rate and excellent structural stability. *Phys Chem Chem Phys* **2013,** 15, (9), 3304-12.
107. Mariyappan, S.; Wang, Q.; Tarascon, J. M., Will Sodium Layered Oxides Ever Be Competitive for Sodium Ion Battery Applications? *Journal of The Electrochemical Society* **2018,** 165, (16), A3714-A3722.
108. Mariyappan, S.; Marchandier, T.; Rabuel, F.; Iadecola, A.; Rousse, G.; Morozov, A. V.; Abakumov, A. M.; Tarascon, J.-M., The Role of Divalent (Zn^{2+}/Mg^{2+}/Cu^{2+}) Substituents in Achieving Full Capacity of Sodium Layered Oxides for Na-Ion Battery Applications. *Chemistry of Materials* **2020,** 32, (4), 1657-1666.
109. Fu, J.; Huang, H.; Shi, K.; Chen, F.; Yang, Z.; Zhang, W., Al-doped walnut-shell-like P2-type $Na_{2/3}Ni_{1/3}Co_{(1/3-x)}Mn_{1/3}Al_xO_2$ as advanced sodium ion battery cathode materials with enhanced rate and cycling performance. *Electrochimica Acta* **2020,** 349.
110. Li, X.; Shen, X.; Zhao, J.; Yang, Y.; Zhang, Q.; Ding, F.; Han, M.; Xu, C.; Yang, C.; Liu, H.; Hu, Y. S., O3-$NaFe_{(1/3-x)}Ni_{1/3}Mn_{1/3}Al_xO_2$ Cathodes with Improved Air Stability for Na-Ion Batteries. *ACS Appl Mater Interfaces* **2021**.
111. Ma, A.; Yin, Z.; Wang, J.; Wang, Z.; Guo, H.; Yan, G., Al-doped $NaNi_{1/3}Mn_{1/3}Fe_{1/3}O_2$ for high performance of sodium ion batteries. *Ionics* **2020,** 26, (4), 1797-1804.
112. Deng, J.; Luo, W.-B.; Lu, X.; Yao, Q.; Wang, Z.; Liu, H.-K.; Zhou, H.; Dou, S.-X., High Energy Density Sodium-Ion Battery with Industrially Feasible and Air-Stable O3-Type Layered Oxide Cathode. *Advanced Energy Materials* **2018,** 8, (5).
113. Wang, J.; Zhou, Z.; Li, Y.; Li, M.; Wang, F.; Yao, Q.; Wang, Z.; Zhou, H.; Deng, J., High-rate performance O3-$NaNi_{0.4}Mn_{0.4}Cu_{0.1}Ti_{0.1}O_2$ as a cathode for sodium ion batteries. *Journal of Alloys and Compounds* **2019,** 792, 1054-1060.
114. Tang, W.; Duan, J.; Xie, J.; Qian, Y.; Li, J.; Zhang, Y., Dual-Site Doping Strategy for Enhancing the Structural Stability of Lithium-Rich Layered Oxides. *ACS Appl Mater Interfaces* **2021,** 13, (14), 16407-16417.
115. Chen, T.; Guo, J.; Zhuo, Y.; Hu, H.; Liu, W.; Liu, F.; Liu, P.; Yan, J.; Liu, K., An inactive metal supported oxide cathode material with high rate capability for sodium ion batteries. *Energy Storage Materials* **2019,** 20, 263-268.
116. Oh, S.-M.; Myung, S.-T.; Hwang, J.-Y.; Scrosati, B.; Amine, K.; Sun, Y.-K., High Capacity O3-Type $Na[Li_{0.05}(Ni_{0.25}Fe_{0.25}Mn_{0.5})_{0.95}]O_2$ Cathode for Sodium Ion Batteries. *Chemistry of Materials* **2014,** 26, (21), 6165-6171.

117. Xu, J.; Lee, D. H.; Clément, R. J.; Yu, X.; Leskes, M.; Pell, A. J.; Pintacuda, G.; Yang, X.-Q.; Grey, C. P.; Meng, Y. S., Identifying the Critical Role of Li Substitution in P2–$Na_x[Li_yNi_zMn_{1-y-z}]O_2$ ($0 < x, y, z < 1$) Intercalation Cathode Materials for High-Energy Na-Ion Batteries. *Chemistry of Materials* **2014,** 26, (2), 1260-1269.
118. Xu, J.; Liu, H.; Meng, Y. S., Exploring Li substituted O3-structured layered oxides $NaLi_xNi_{1/3-x}Mn_{1/3+x}Co_{1/3-x}O_2$ (x = 0.07, 0.13, and 0.2) as promising cathode materials for rechargeable Na batteries. *Electrochemistry Communications* **2015,** 60, 13-16.
119. Zhang, C.; Gao, R.; Zheng, L.; Hao, Y.; Liu, X., New Insights into the Roles of Mg in Improving the Rate Capability and Cycling Stability of O3-$NaMn_{0.48}Ni_{0.2}Fe_{0.3}Mg_{0.02}O_2$ for Sodium-Ion Batteries. *ACS Appl Mater Interfaces* **2018,** 10, (13), 10819-10827.
120. Li, J.; Risthaus, T.; Wang, J.; Zhou, D.; He, X.; Ehteshami, N.; Murzin, V.; Friesen, A.; Liu, H.; Hou, X.; Diehl, M.; Paillard, E.; Winter, M.; Li, J., The effect of Sn substitution on the structure and oxygen activity of $Na_{0.67}Ni_{0.33}Mn_{0.67}O_2$ cathode materials for sodium ion batteries. *Journal of Power Sources* **2020,** 449.
121. Meng, Y.; An, J.; Chen, L.; Chen, G.; Shi, L.; Lu, M.; Zhang, D., A $NaNi_{0.5}Mn_{0.5}Sn_xO_2$ cathode with anti-structural deformation enhancing long lifespan and super power for a sodium ion battery. *Chem Commun (Camb)* **2020,** 56, (58), 8079-8082.
122. Rong, X.; Gao, F.; Ding, F.; Lu, Y.; Yang, K.; Li, H.; Huang, X.; Chen, L.; Hu, Y.-S., Triple effects of Sn-substitution on $Na_{0.67}Ni_{0.33}Mn_{0.67}O_2$. *Journal of Materials Science & Technology* **2019,** 35, (7), 1250-1254.
123. Bao, S.; Luo, S. H.; Wang, Z. Y.; Yan, S. X.; Wang, Q., Improving the electrochemical performance of layered cathode oxide for sodium-ion batteries by optimizing the titanium content. *J Colloid Interface Sci* **2019,** 544, 164-171.
124. Hwang, T.; Lee, J. H.; Choi, S. H.; Oh, R. G.; Kim, D.; Cho, M.; Cho, W.; Park, M. S., Critical Role of Titanium in O3-Type Layered Cathode Materials for Sodium-Ion Batteries. *ACS Appl Mater Interfaces* **2019,** 11, (34), 30894-30901.
125. Mao, Q.; Zhang, C.; Yang, W.; Yang, J.; Sun, L.; Hao, Y.; Liu, X., Mitigating the voltage fading and lattice cell variations of O3-$NaNi_{0.2}Fe_{0.35}Mn_{0.45}O_2$ for high performance Na-ion battery cathode by Zn doping. *Journal of Alloys and Compounds* **2019,** 794, 509-517.
126. Alvarado, J.; Ma, C.; Wang, S.; Nguyen, K.; Kodur, M.; Meng, Y. S., Improvement of the Cathode Electrolyte Interphase on P2-$Na_{2/3}Ni_{1/3}Mn_{2/3}O_2$ by Atomic Layer Deposition. *ACS Appl Mater Interfaces* **2017,** 9, (31), 26518-26530.
127. Dang, R.; Chen, M.; Li, Q.; Wu, K.; Lee, Y. L.; Hu, Z.; Xiao, X., Na^+-Conductive $Na_2Ti_3O_7$-Modified P2-type $Na_{2/3}Ni_{1/3}Mn_{2/3}O_2$ via a Smart in Situ Coating Approach: Suppressing Na^+/Vacancy Ordering and P2-O2 Phase Transition. *ACS Appl Mater Interfaces* **2019,** 11, (1), 856-864.
128. Jo, C.-H.; Jo, J.-H.; Yashiro, H.; Kim, S.-J.; Sun, Y.-K.; Myung, S.-T., Bioinspired Surface Layer for the Cathode Material of High-Energy-Density Sodium-Ion Batteries. *Advanced Energy Materials* **2018,** 8, (13).
129. Jo, J. H.; Choi, J. U.; Konarov, A.; Yashiro, H.; Yuan, S.; Shi, L.; Sun, Y.-K.; Myung, S.-T., Sodium-Ion Batteries: Building Effective Layered Cathode Materials with Long-Term Cycling by Modifying the Surface via Sodium Phosphate. *Advanced Functional Materials* **2018,** 28, (14).
130. Li, N.; Ren, J.; Dang, R.; Wu, K.; Lee, Y. L.; Hu, Z.; Xiao, X., Suppressing phase transition and improving electrochemical performances of O3-$NaNi_{1/3}Mn_{1/3}Fe_{1/3}O_2$ through ionic conductive Na_2SiO_3 coating. *Journal of Power Sources* **2019,** 429, 38-45.
131. Liu, Y.; Fang, X.; Zhang, A.; Shen, C.; Liu, Q.; Enaya, H. A.; Zhou, C., Layered P2-$Na_{2/3}[Ni_{1/3}Mn_{2/3}]O_2$ as high-voltage cathode for sodium-ion batteries: The capacity decay mechanism and Al_2O_3 surface modification. *Nano Energy* **2016,** 27, 27-34.
132. Tang, K.; Huang, Y.; Xie, X.; Cao, S.; Liu, L.; Liu, M.; Huang, Y.; Chang, B.; Luo, Z.; Wang, X., The effects of dual modification on structure and performance of P2-type layered oxide cathode for sodium-ion batteries. *Chemical Engineering Journal* **2020,** 384.

133. Xia, J.; Wu, W.; Fang, K.; Wu, X., Enhancing the interfacial stability of P2-type cathodes by polydopamine-derived carbon coating for achieving performance improvement. *Carbon* **2020,** 157, 693-702.
134. Zhang, Q.; Gu, Q. F.; Li, Y.; Fan, H. N.; Luo, W. B.; Liu, H. K.; Dou, S. X., Surface Stabilization of O3-type Layered Oxide Cathode to Protect the Anode of Sodium Ion Batteries for Superior Lifespan. *iScience* **2019,** 19, 244-254.
135. Zhang, Y.; Pei, Y.; Liu, W.; Zhang, S.; Xie, J.; Xia, J.; Nie, S.; Liu, L.; Wang, X., $AlPO_4$-coated P2-type hexagonal $Na_{0.7}MnO_{2.05}$ as high stability cathode for sodium ion battery. *Chemical Engineering Journal* **2020,** 382.
136. Feng, Z.; Huang, X.; Rajagopalan, R.; Tang, Y.; Peng, Z.; Wang, H., Enhanced Electrochemical Properties of $LiNi_{0.8}Co_{0.1}Mn_{0.1}O_2$ at Elevated Temperature by Simultaneous Structure and Interface Regulating. *Journal of The Electrochemical Society* **2019,** 166, (8), A1439-A1448.
137. Hu, G.; Shi, Y.; Fan, J.; Cao, Y.; Peng, Z.; Zhang, Y.; Zhu, F.; Sun, Q.; Xue, Z.; Liu, Y.; Du, K., Sb doping and Sb_2O_3 coating collaboration to improve the electrochemical performance of $LiNi_{0.5}Mn_{0.5}O_2$ cathode material for lithium ion batteries. *Electrochimica Acta* **2020,** 364.
138. Jiao, J.; Wu, K.; Dang, R.; Li, N.; Deng, X.; Liu, X.; Hu, Z.; Xiao, X., A collaborative strategy with ionic conductive Na_2SiO_3 coating and Si doping of P2-$Na_{0.67}Fe_{0.5}Mn_{0.5}O_2$ cathode: An effective solution to capacity attenuation. *Electrochimica Acta* **2021,** 384.
139. Sun, Y.; Liu, Z.; Chen, X.; Yang, X.; Xiang, F.; Lu, W., Enhancing the stabilities and electrochemical performances of $LiNi_{0.5}Co_{0.2}Mn_{0.3}O_2$ cathode material by simultaneous $LiAlO_2$ coating and Al doping. *Electrochimica Acta* **2021,** 376.
140. Zhu, C.; Cao, M.; Zhang, H.; Lv, G.; Zhang, J.; Meng, Y.; Shu, C.; Fan, W.; Zuo, M.; Xiang, W.; Guo, X., Synergistic Effect of Microstructure Engineering and Local Crystal Structure Tuning to Improve the Cycling Stability of Ni-Rich Cathodes. *ACS Appl Mater Interfaces* **2021,** 13, (41), 48720-48729.
141. Dang, R.; Li, Q.; Chen, M.; Hu, Z.; Xiao, X., CuO-Coated and Cu^{2+}-doped Co-modified P2-type $Na_{2/3}[Ni_{1/3}Mn_{2/3}]O_2$ for sodium-ion batteries. *Physical Chemistry Chemical Physics* **2019,** 21, (1), 314-321.
142. Hwang, J.-Y.; Yu, T.-Y.; Sun, Y.-K., Simultaneous MgO coating and Mg doping of $Na[Ni_{0.5}Mn_{0.5}]O_2$ cathode: facile and customizable approach to high-voltage sodium-ion batteries. *Journal of Materials Chemistry A* **2018,** 6, (35), 16854-16862.
143. Chen, C.; Han, Z.; Chen, S.; Qi, S.; Lan, X.; Zhang, C.; Chen, L.; Wang, P.; Wei, W., Core-Shell Layered Oxide Cathode for High-Performance Sodium-Ion Batteries. *ACS Appl Mater Interfaces* **2020,** 12, (6), 7144-7152.
144. Hwang, J.-Y.; Myung, S.-T.; Yoon, C. S.; Kim, S.-S.; Aurbach, D.; Sun, Y.-K., Novel Cathode Materials for Na-Ion Batteries Composed of Spoke-Like Nanorods of $Na[Ni_{0.61}Co_{0.12}Mn_{0.27}]O2$Assembled in Spherical Secondary Particles. *Advanced Functional Materials* **2016,** 26, (44), 8083-8093.
145. Hwang, J. Y.; Oh, S. M.; Myung, S. T.; Chung, K. Y.; Belharouak, I.; Sun, Y. K., Radially aligned hierarchical columnar structure as a cathode material for high energy density sodium-ion batteries. *Nat Commun* **2015,** 6, 6865.
146. You, Y.; Kim, S. O.; Manthiram, A., A Honeycomb-Layered Oxide Cathode for Sodium-Ion Batteries with Suppressed P3-O1 Phase Transition. *Advanced Energy Materials* **2017,** 7, (5).
147. Xiao, Y.; Wang, P. F.; Yin, Y. X.; Zhu, Y. F.; Niu, Y. B.; Zhang, X. D.; Zhang, J.; Yu, X.; Guo, X. D.; Zhong, B. H.; Guo, Y. G., Exposing {010} Active Facets by Multiple-Layer Oriented Stacking Nanosheets for High-Performance Capacitive Sodium-Ion Oxide Cathode. *Adv Mater* **2018**, e1803765.
148. Gavin D J Harper *et al*., Roadmap for a sustainable circular economy in lithium-ion and future battery technologies. *Journal of Physics: Energy* **2023,** 5, (2).
149. Dahbi, M.; Yabuuchi, N.; Kubota, K.; Tokiwa, K.; Komaba, S., Negative electrodes for Na-ion batteries. *Phys Chem Chem Phys* **2014,** 16, (29), 15007-28.

150. Chen, X.; Zhang, Y., The main problems and solutions in practical application of anode materials for sodium ion batteries and the latest research progress. *International Journal of Energy Research* **2021,** 45, (7), 9753-9779.
151. Ge, P., Electrochemical intercalation of sodium in graphite. *Solid State Ionics* **1988,** 28-30, 1172-1175.
152. Jache, B.; Adelhelm, P., Use of Graphite as a Highly Reversible Electrode with Superior Cycle Life for Sodium-Ion Batteries by Making Use of Co-Intercalation Phenomena. *Angew. Chem.* **2014,** 126, (38), 10333-10337.
153. Stevens, D. A.; Dahn, J. R., High Capacity Anode Materials for Rechargeable Sodium-Ion Batteries. *Journal of The Electrochemical Society* **2000,** 147, (4).
154. Chen, K. H.; Goel, V.; Namkoong, M. J.; Wied, M.; Müller, S.; Wood, V.; Sakamoto, J.; Thornton, K.; Dasgupta, N. P., Enabling 6C Fast Charging of Li‐Ion Batteries with Graphite/Hard Carbon Hybrid Anodes. *Advanced Energy Materials* **2020,** 11, (5).
155. Li, X.; Sun, J.; Zhao, W.; Lai, Y.; Yu, X.; Liu, Y., Intergrowth of Graphite‐Like Crystals in Hard Carbon for Highly Reversible Na‐Ion Storage. *Advanced Functional Materials* **2021,** 32, (2).
156. Yu, Z. L.; Xin, S.; You, Y.; Yu, L.; Lin, Y.; Xu, D. W.; Qiao, C.; Huang, Z. H.; Yang, N.; Yu, S. H.; Goodenough, J. B., Ion-Catalyzed Synthesis of Microporous Hard Carbon Embedded with Expanded Nanographite for Enhanced Lithium/Sodium Storage. *J Am Chem Soc* **2016,** 138, (45), 14915-14922.
157. Gong, D.; Wei, C.; Liang, Z.; Tang, Y., Recent Advances on Sodium‐Ion Batteries and Sodium Dual‐Ion Batteries: State‐of‐the‐Art Na^+Host Anode Materials. *Small Science* **2021,** 1, (6).
158. Dou, X.; Hasa, I.; Saurel, D.; Vaalma, C.; Wu, L.; Buchholz, D.; Bresser, D.; Komaba, S.; Passerini, S., Hard carbons for sodium-ion batteries: Structure, analysis, sustainability, and electrochemistry. *Mater. Today* **2019,** 23, 87-104.
159. Hasegawa, G.; Kanamori, K.; Kannari, N.; Ozaki, J.-i.; Nakanishi, K.; Abe, T., Hard Carbon Anodes for Na-Ion Batteries: Toward a Practical Use. *ChemElectroChem* **2015,** 2, (12), 1917-1920.
160. Sun, C.; Zhang, X.; An, Y.; Li, C.; Wang, L.; Zhang, X.; Sun, X.; Wang, K.; Zhang, H.; Ma, Y., Low‐Temperature Carbonized Nitrogen‐Doped Hard Carbon Nanofiber Toward High‐Performance Sodium‐Ion Capacitors. *Energy & Environmental Materials* **2023**.
161. Gong, H.; Chen, Y.; Chen, S.; Xu, C.; Yang, Y.; Ye, Y.; Huang, Z.; Ning, R.; Cui, Y.; Bao, Z., Fast-Charging of Hybrid Lithium-Ion/Lithium-Metal Anodes by Nanostructured Hard Carbon Host. *ACS Energy Letters* **2022,** 7, (12), 4417-4426.
162. Lei, H.; Li, J.; Zhang, X.; Ma, L.; Ji, Z.; Wang, Z.; Pan, L.; Tan, S.; Mai, W., A review of hard carbon anode: Rational design and advanced characterization in potassium ion batteries. *InfoMat* **2022,** 4, (2).
163. Dahn, J. R.; Xing, W.; Gao, Y., The "falling cards model" for the structure of microporous carbons. *Carbon* **1997,** 35, (6), 825-830.
164. Gotoh, K.; Ishikawa, T.; Shimadzu, S.; Yabuuchi, N.; Komaba, S.; Takeda, K.; Goto, A.; Deguchi, K.; Ohki, S.; Hashi, K.; Shimizu, T.; Ishida, H., NMR study for electrochemically inserted Na in hard carbon electrode of sodium ion battery. *Journal of Power Sources* **2013,** 225, 137-140.
165. Qiu, S.; Xiao, L.; Sushko, M. L.; Han, K. S.; Shao, Y.; Yan, M.; Liang, X.; Mai, L.; Feng, J.; Cao, Y.; Ai, X.; Yang, H.; Liu, J., Manipulating Adsorption‐Insertion Mechanisms in Nanostructured Carbon Materials for High‐Efficiency Sodium Ion Storage. *Advanced Energy Materials* **2017,** 7, (17).
166. Hou, L.; Liu, T.; Wang, H.; Bai, M.; Tang, X.; Wang, Z.; Zhang, M.; Li, S.; Wang, T.; Zhou, K.; Ma, Y., Boosting the Reversible, High-Rate Na^+ Storage Capability of the Hard Carbon Anode Via the Synergistic Structural Tailoring and Controlled Presodiation. *Small* **2023,** 19, (21), e2207638.
167. Alvin, S.; Cahyadi, H. S.; Hwang, J.; Chang, W.; Kwak, S. K.; Kim, J., Revealing the Intercalation Mechanisms of Lithium, Sodium, and Potassium in Hard Carbon. *Advanced Energy Materials* **2020,** 10, (20).
168. Yu, K.; Wang, X.; Yang, H.; Bai, Y.; Wu, C., Insight to defects regulation on sugarcane waste-derived hard carbon anode for sodium-ion batteries. *Journal of Energy Chemistry* **2021,** 55, 499-508.

169. Ilic, I. K.; Schutjajew, K.; Zhang, W.; Oschatz, M., Changes of porosity of hard carbons during mechanical treatment and the relevance for sodium-ion anodes. *Carbon* **2022,** 186, 55-63.
170. Chen, X.; Liu, C.; Fang, Y.; Ai, X.; Zhong, F.; Yang, H.; Cao, Y., Understanding of the sodium storage mechanism in hard carbon anodes. *Carbon Energy* **2022,** 4, (6), 1133-1150.
171. Kume, T.; Iwai, Y.; Sugiyama, T.; Ohashi, F.; Ban, T.; Sasaki, S.; Nonomura, S., NaSi and Si clathrate prepared on Si substrate. *physica status solidi c* **2013,** 10, (12), 1739-1741.
172. Xu, Y.; Swaans, E.; Basak, S.; Zandbergen, H. W.; Borsa, D. M.; Mulder, F. M., Reversible Na-Ion Uptake in Si Nanoparticles. *Advanced Energy Materials* **2016,** 6, (2).
173. Niu, L.; Guo, S.; Liang, W.; Song, L.; Song, B.; Zhang, Q.; Wu, L., In Situ Electrochemical Derivation of Sodium-Tin Alloy as Sodium-Ion Energy Storage Devices Anode with Overall Electrochemical Characteristics. *Crystals* **2022,** 12, (5).
174. Dahunsi, O. J.; Li, B.; Gao, S.; Lu, K.; Xia, F.; Xu, T.; Cheng, Y., One-Step Synthesis of Na–Sn Alloy with Internal 3D $Na_{15}Sn_4$ Support for Fast and Stable Na Metal Batteries. *ACS Applied Energy Materials* **2021,** 5, (1), 20-26.
175. Allan, P. K.; Griffin, J. M.; Darwiche, A.; Borkiewicz, O. J.; Wiaderek, K. M.; Chapman, K. W.; Morris, A. J.; Chupas, P. J.; Monconduit, L.; Grey, C. P., Tracking Sodium-Antimonide Phase Transformations in Sodium-Ion Anodes: Insights from Operando Pair Distribution Function Analysis and Solid-State NMR Spectroscopy. *J Am Chem Soc* **2016,** 138, (7), 2352-65.
176. Darwiche, A.; Marino, C.; Sougrati, M. T.; Fraisse, B.; Stievano, L.; Monconduit, L., Better cycling performances of bulk Sb in Na-ion batteries compared to Li-ion systems: an unexpected electrochemical mechanism. *J Am Chem Soc* **2012,** 134, (51), 20805-11.
177. Hou, H.; Jing, M.; Yang, Y.; Zhang, Y.; Song, W.; Yang, X.; Chen, J.; Chen, Q.; Ji, X., Antimony nanoparticles anchored on interconnected carbon nanofibers networks as advanced anode material for sodium-ion batteries. *Journal of Power Sources* **2015,** 284, 227-235.
178. Li, K.; Liu, H.; Wang, G., Sb_2O_3 Nanowires as Anode Material for Sodium-Ion Battery. *Arabian Journal for Science and Engineering* **2014,** 39, (9), 6589-6593.
179. Hu, M.; Jiang, Y.; Sun, W.; Wang, H.; Jin, C.; Yan, M., Reversible conversion-alloying of Sb_2O_3 as a high-capacity, high-rate, and durable anode for sodium ion batteries. *ACS Appl Mater Interfaces* **2014,** 6, (21), 19449-55.
180. Wang, Q.; Zhao, C.; Lu, Y.; Li, Y.; Zheng, Y.; Qi, Y.; Rong, X.; Jiang, L.; Qi, X.; Shao, Y.; Pan, D.; Li, B.; Hu, Y. S.; Chen, L., Advanced Nanostructured Anode Materials for Sodium-Ion Batteries. *Small* **2017,** 13, (42).
181. Fukunishi, M.; Yabuuchi, N.; Dahbi, M.; Son, J.-Y.; Cui, Y.; Oji, H.; Komaba, S., Impact of the Cut-Off Voltage on Cyclability and Passive Interphase of Sn-Polyacrylate Composite Electrodes for Sodium-Ion Batteries. *The Journal of Physical Chemistry C* **2016,** 120, (28), 15017-15026.
182. Nam, D.-H.; Hong, K.-S.; Lim, S.-J.; Kim, T.-H.; Kwon, H.-S., Electrochemical Properties of Electrodeposited Sn Anodes for Na-Ion Batteries. *The Journal of Physical Chemistry C* **2014,** 118, (35), 20086-20093.
183. Wang, J. W.; Liu, X. H.; Mao, S. X.; Huang, J. Y., Microstructural evolution of tin nanoparticles during in situ sodium insertion and extraction. *Nano Lett* **2012,** 12, (11), 5897-902.
184. Wu, L.; Lu, H.; Xiao, L.; Ai, X.; Yang, H.; Cao, Y., Electrochemical properties and morphological evolution of pitaya-like Sb@C microspheres as high-performance anode for sodium ion batteries. *Journal of Materials Chemistry A* **2015,** 3, (10), 5708-5713.
185. Lao, M.; Zhang, Y.; Luo, W.; Yan, Q.; Sun, W.; Dou, S. X., Alloy-Based Anode Materials toward Advanced Sodium-Ion Batteries. *Adv Mater* **2017,** 29, (48).
186. Dae Kyeong Kim, S. Y., Ali Zain Banatwala, YuTack Kim *Handbook on Battery Energy Storage System*. **2018**

Chapter 2 Literature review- Strategies to improve the high-voltage stability of layered-oxide cathode materials

This work has been published in ***J.Phys. Mater*. 2021, 4, 032004. (**Tengfei Song, and Emma Kendrick**)**

DOI: 10.1088/2515-7639/abf545

Submitted: 16/11/2020

Accepted: 06/04/2021

Author contribution: T.F. Song: Conceptualisation, writing-original draft.

E.M. Kendrick: Lead supervision, review & editing

2.1 Introduction

Sodium-ion batteries offer a low-cost sustainable alternative to current lithium-ion batteries and can be made on the same manufacturing lines. The sustainability arises from the low cost, reduction in the use of critical elements and strategic materials, and potential long-life.

In recent years, efforts have been devoted to further improving the structural stability and electrochemical properties of layered materials under higher operation voltage with the aim to narrow the gap between the energy density of SIBs and LIBs. Despite such efforts, the capacity and cycling stability of Na_xTMO_2-layered oxide materials still require further improvements.

In this chapter, we summarize the failure and degradation processes associated with the high capacity and higher voltage layered oxide cathode materials. Progress on cutting-edge strategies to prevent these degradation processes is summarised and discussed in detail, and the synergistic requirements to stabilize the structure of the material and the interfaces are highlighted. The importance of surface engineering in future materials design is emphasized.

2.2 Main causes of failure under high-voltage operation

2.2.1 Phase transitions and induced bulk degradation

Though various reasons contribute to the performance degradation under high-voltage operation, the irreversible bulk phase transitions are undoubtedly the most prominent. From the perspective of crystal structure, these multiphase transformations originated from the Na^+ vacancy ordering and MO_2 layers gliding easily lead to structural evolution, and inevitably cause large expansion or shrinkage of the lattice volume as well as sluggish kinetics during the cycling process[1, 2], which are unfavorable to the structural stability and rate performance. From the macroscopic particle point of view, the phase transition induced volume change not only causes the collapse of active layered crystal structure, but the resulting stress and strain induce cracks within a single particle. Those bulk cracks will further lead to poor electronic conduction, TM dissolution, surface corrosion, and electrolyte consumption[3]. In addition, these unwanted side reactions become more prevalent when increasing the state of Na^+ extraction by elevating the charging cut-off voltage. For example, $NaNi_{1/3}Fe_{1/3}Mn_{1/3}O_2$ illustrates high reversibility through an O3-P3-P3-O3 sequence during cycling in the voltage range of 2.0-4.0 V, and the R-3m layered structure remained intact after more than 100 cycles. However, when the cut-off voltage is higher than 4.0 V, a new nonequilibrium $O3'$ monoclinic phase is observed along with a significant contraction in d-spacing and c axis, which leads to severely deteriorated structural stability and cycling performance [4, 5].

Stabilizing, eliminating, suppressing, or delaying this high voltage phase transition and extending the solid solution zone are critical to further improve the structural stability of sodium layered oxide materials at high charge cut-off voltages.

2.2.2 Surface-related chemical degradation

In addition to structural stability challenges, the interface instability also requires further development to enable practical high-voltage SIBs. The interface issues include surface instability in air and interfacial reactions between deep-charged cathode and electrolyte above 4.2 V.

2.2.2.1 Surface instability in air and moisture

Due to the larger spacing between transition metal layers than the lithium analogues, the sodiated transition metal oxides are highly hygroscopic, and they will readily react with water and CO_2 to form NaOH and Na_2CO_3 on the particle surface even with brief exposure to ambient air [6, 7]. These impurities can severely accelerate the structural degradation of cathode material, diminishing the electrochemical performance while cycling because of : (i) the surface becomes more basic, which will lead to difficulty in producing stable inks and uniform casting [8]; (ii) the formed NaOH and Na_2CO_3 are insulative for ionic/electronic conduction, which will lead to an increase in cell polarization and decrease in capacity; (iii) the intercalated water molecules within the layers will trigger side reactions with electrolyte through the following reactions: $NaPF_6 \rightarrow NaF + PF_5$, $PF_5 + H_2O \rightarrow POF_3 + 2HF$ [9-12]. On one side, the as-formed HF tends to react with the surface by-products such as Na_2CO_3 to form further NaF and H_2O. On the other side, HF will aggressively attack the TM ions, inducing the transition metal dissolution and forming TM fluorides on the cathode surface, which will result in irreversible active mass loss [13-15].

2.2.2.2 Interfacial reactions between deep-charged cathode and electrolyte

The interfacial stability between the cathode and electrolyte plays a crucial role on the ultimate electrochemical performance for a cell. Under ideal conditions, the commonly used nonaqueous electrolytes for SIBs ($NaPF_6$ or $NaClO_4$ salt in carbonate-based solvents) are not thought to degrade upon the surface or form a particular cathode electrolyte interface (CEI). However, during cycling, and at high voltages surface films have been observed. Particularly at higher voltages cycling limits. It is thought that at the higher voltages, particularly above $\approx$4.2 V, the electrolyte may become thermodynamically unstable, and oxidize at the surface causing an insulating interface layer, which has negative effects upon the performance properties[16].

There are several possible causes of these higher voltage (>4.2 V vs Na/Na^+) parasitic oxidative reactions at the cathode interface. One widespread mechanism is the chemical oxidation of electrolytes caused by the release of lattice oxygen: Under high state of charge (or high voltage), the valences of transition metal ions increase and become more oxidative, which makes them more likely to get electrons from the lattice oxygen (O^{2-}), eventually leading to the release of gaseous O_2. The released O_2 subsequently reacts with the electrolyte, resulting in the

decomposition of the electrolyte and form of CO_2, CO, O^{-2} and H_2O, etc. The side reactions consume O from the cathode as reactants, thus driving and intensifying the oxygen loss from the cathode lattice[17, 18].

Several subsequent reactions occur including the reduction of the transition metals. This metal dissolution from the lattice causes surface crystal structure reconstruction and the dissolved transition metal ions can also migrate through the electrolyte and deposit on the anode to form a film, increasing the impedance of the cell. Meanwhile, the intragranular nano cracks caused by the TMs leaching in the outer layer will generate more fresh oxide surfaces that can further be involved in the previously mentioned side reactions, this "domino effect" contributes to cascade failure of cells [19-21]. Furthermore, the decay observed from this sequential reduction-dissolution process will exponentially aggravate when operating at higher cut-off voltage or elevated temperatures. Given the general instability of the surface, engineering a robust interface between cathode/electrolyte is essential for building a battery with superior cycling stability. A summary of these degradation processes is shown in figure 2.1.



Figure 2.1 Overview on proposed degradation mechanisms for sodium layered oxide materials under high voltage operations.

In short, the lower standard electrochemical potential of sodium-ion electrode materials determines that they must operate under higher voltages to pursue equivalent energy density to their lithium counterpart; however, complex phase transitions and severe interfacial reactions at high voltages will inevitably reduce its service life significantly. This inherent contradiction makes it extremely difficult to develop sodium-containing layered oxide materials with

simultaneous high energy density and long cycle life, which has become a significant obstacle to the practical application of these layered oxides in SIBs.

2.3 Strategies for high voltage stabilization

2.3.1 Selective cationic doping into the crystal framework

The irreversible migration of transition metal ions during the charge process triggers a structural distortion, leading to phase reforming and transition, resulting in the observed electrochemical performance fading [22]. To suppress phase transformation (structure changes), many researchers have focused on developing effective structural modifications for practical use in SIBs. Doping elective electrochemically active/inactive elements, such as Li[23], Cu[24-26], Mg[27, 28], Ti[29-32], and Sn[33-38], has been proven as an effective strategy to modify a material's bulk structure properties and improve the high-voltage stability of layered oxides. Cationic dopants can be broadly divided into three categories according to the corresponding working mechanisms.

(i) Strengthening the bonding between TM and O

The most widely accepted role of element doping in layered oxides is to stabilize the TM slabs through strengthening the bonds between TM and O and thus suppress the host rearrangement and TMO_2 gliding[1]. Chen *et al.* found that partial substituted Mn^{4+} by Ti^{4+} in $Na[Ni_{0.4}Fe_{0.2}Mn_{0.4-x}Ti_x]O_2$ can not only lift the working potentials but also improve the reversibility[29]. Huang *et al.* systematically investigated the effects of Ti doping on structural modification in O3-type $Na(Fe_{0.25}Ni_{0.25}Mn_{0.5})O_2$ based on experiments and first-principles calculations, and elucidated the mechanism for the first time. They suggested that Ti^{4+} ($3d^0$) without d electrons effectively enhances the bonding between transition metals and oxygen by increasing the oxygen electron density, which in turn makes the host structure more stable and lowers the energy barrier of Na^+ migration, leading to a notable enhancement in cycling performance and rate capability of $Na[Ti_{0.03}(Fe_{0.25}Ni_{0.25}Mn_{0.5})_{0.97}]O_2$ [31]. In addition to stabilizing the host structure, Ti^{4+} substitution has also been found to be beneficial to improving water-stability. Tripathi et al. compared the hydro-stability and surface composition of $Na_{0.9}Cu_{0.22}Fe_{0.30}Mn_{0.48}O_2$ (NCFM) and $Na_{0.9}Cu_{0.22}Fe_{0.30}Mn_{0.43}Ti_{0.05}O_2$ (NCFMT) by X-ray photoelectron spectroscopy, found that the Ti^{4+} substituted oxides tend to form a titanium-rich surface which helps reduce the reactivity of the active material with moisture, leading to improved water-stability[39].

$Sn^{4+}(4d^{10})$, a non-transition metal, has a fully filled 4d electronshell, and therefore it cannot interact with oxygen p orbitals, unlike the redox active TMs. This doping effect strengthens the ionic bonding between the remaining transition metals within the lattice and is reflected by the increase in the observed average voltage, the suppression of the high voltage phase and hence the improved cycle life of these materials[34]. Sathiya et al. synthesized a series of Sn substituted materials $NaNi_{0.5}Mn_{0.5-y}Sn_yO_2$ (y=0-0.5) and found that the Sn substituted material $NaNi_{0.5}Sn_{0.5}O_2$ showed significantly enhanced stability against O3 ⇔ P3 transformation. This transition did not occur till the removal of 0.5 sodium from the structure as compared to 0.2 for the pristine $NaNi_{0.5}Mn_{0.5}O_2$ material, and the P3⇔P′3 completely avoided (Figure 2.2a)[35]. Wang et al. confirmed this conclusion: they synthesized a whole new family of O3-type cathode materials with the general formula $Na_xNi_{x/2}Sn_{1-x/2}O_2$ and found that the phase transition from O3 to P3 was largely delayed by Sn substitution, and the first candidate $Na_{0.7}Ni_{0.35}Sn_{0.65}O_2$ displayed a high average voltage and working potential of 3.7 V (vs. Na^+/Na) [34]. Rong et al. found that Sn-substitution in $Na_{0.67}Ni_{0.33}Mn_{0.67}O_2$ has a triple effect: the formation of O3-stacking, smoothing the charge/discharge voltage profile by inhibiting complex phase transitions, and increasing the average working voltage (3.34 V for $Na_{0.67}Ni_{0.33}Mn_{0.67}O_2$ and 3.60 V for $Na_{0.67}Ni_{0.33}Mn_{0.33}Sn_{0.33}O_2$ in half-cell)[37].

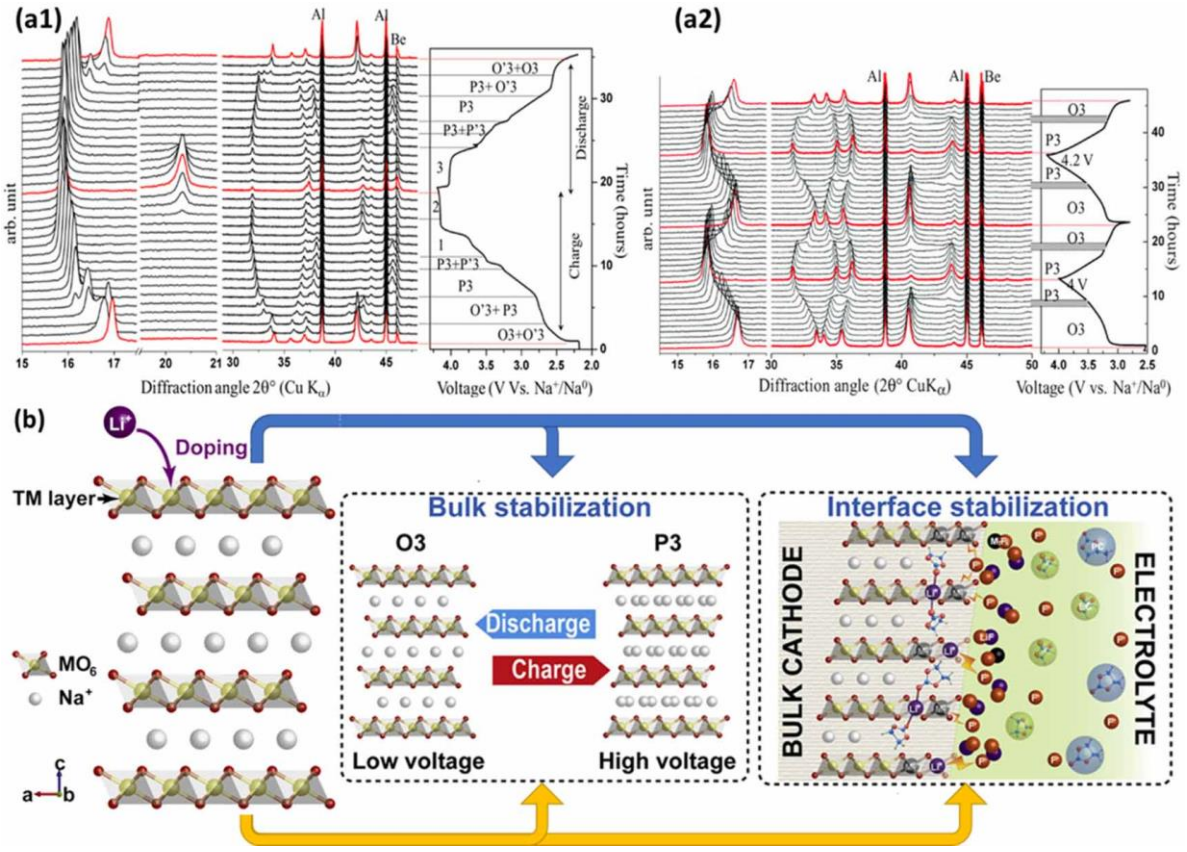


Figure 2.2 (a) In situ XRD patterns of (a1) $NaNi_{0.5}Mn_{0.5}O2$ and (a2) $NaNi_{0.5}Sn_{0.5}O2$ cycled between 4.2 and 2.8 V in the first cycle showing the largely delayed O3⇔P3 phase transition[35]. JohnWiley & Sons. [© 2018 WILEY-VCH Verlag GmbH & Co. KGaA, Weinheim]. (b) Schematic illustration shows the dual-stabilization effect (stabilization of bulk structure and interphase) of Li doping. Reprinted from [15], Copyright (2018), with permission from Elsevier.

Other non-redox active elements with empty d orbitals, have also been found to suppress the high voltage phase transition. Mao found that Zn^{2+} doped O3-type $NaNi_{0.2}Fe_{0.35}Mn_{0.45-x}Zn_xO_2$ enhanced the Na^+ diffusion rate, but also reduced the lattice cell variations during Na^+ extraction/insertion, extending the O3-P3 reversible phase transformation region. In addition, it was suggested that the substitution of Zn for Mn can reduce the content of unfavourable Mn^{3+} in the crystal structure and hence improves the cycling stability[40]. Other substitutions, like Ca^{2+}, Zn^{2+} substitution at the Na site has also been shown effective to suppress the formation of these unstable high voltage phases[41, 42].

(ii) Modulating the interlayer spacing

Another major role of element doping is to modulate the interlayer spacing within the layered oxide crystal structure. It is well known that P2-type oxides process a larger Na layer spacing compared to O3-oxides, which is beneficial for tolerating the lattice strains induced by Na^+ intercalation/deintercalation, thus mitigating the structure distortion and maintaining the original structure. Inspired by this principle, substitution of Mn^{3+} with divalent ions (e.g., Mg^{2+}, Zn^{2+}, Cu^{2+}) has been performed. Liu *et al.* investigated the effects of the substitution of Mn by Mg on the crystal structure, electronic structure, and electrochemical performances of O3-$NaMn_{0.48}Ni_{0.2}Fe_{0.3}Mg_{0.02}O_2$. Their results illustrated that a small quantity of Mg^{2+} incorporated into the structure, enlarges the Na layer spacing, which not only improves the Na^+ diffusion coefficient but also alleviates the lattice strain or the volume change, thus the irreversible phase transitions induced by sodiation/desodiation are suppressed [27]. Similar effects are also exhibited in Zn^{2+} and Cu^{2+} doped oxides. The increase in the d-layer spacing, is likely also due to the enhanced ionic bonding strength between the TM-O as discussed above. Yan and Sui conducted a comprehensive study on the degradation mechanism of layered Na_xTMO_2 oxides upon high voltage cycling by taking P2-type $Na_{2/3}Ni_{1/3}Mn_{2/3}O_2$ as an example[3]. Through systematic characterizations and statistical analysis, they found that the capacity decrease had a close correlation with the intragranular crack density, and thus determined that the phase transition induced grain cracking is the main cause of performance decay compared with surface degradation, which is different from the layered cathodes of LIBs. Yan and Sui also successfully demonstrated that intragranular cracking related degradation can be mitigated by deploying a dopant segregation strategy [43]. Based on electrochemical tests, microstructural characterizations and DFT calculation, they found that the randomly distributed Mg dopants in P2-structured $Na_{0.67}Ni_{0.33-x}Mn_{0.67}Mg_xO_2$ migrated from the TM layer and segregated into the Na layer during high-voltage cycling, which led to the formation of Mg-enriched precipitates. The electrochemical cation migration acts as 3D network pillars and enhances the material's capability to tolerate the stress caused by structural changes, suppressing cracking formation effectively during cycling. As a result, the Mg-doped electrodes showed improved cycling stability when cycled at higher charge cut-off voltage (2.0-4.5 V) with a capacity retention of 82% compared with only 67% retention cycled at 2.0-4.3 V after 100 cycles. This phenomenon can be contributed to the fewer grain cracks generated when cycled at 2.0-4.5 V than when cycled at 2.0-4.3 V. This *'in-situ'* conceptual strategy using electrochemical cation migration, opens a new direction to further engineer the bulk material and enhance high voltage cycling

stability, which could be realized by adjusting cycling condition or formation protocols to control the migration in the first few cycles.

(iii) Mitigating the Jahn-Teller effect

Mn-based layered materials usually suffer from structure degradation caused by Jahan-Teller effect of Mn^{3+}. As mentioned above, the incorporation of M^{2+} cations, such as Mg^{2+}, Zn^{2+} and Cu^{2+} has been shown to effectively suppress the Jahn-Teller effect of Mn^{3+} by promoting the formation of Mn^{4+} oxidation state. This improves and reduces the phase transitions relating to the Na^+/vacancy-ordering and contributes to forming a stable structure with lower levels of sodium concentration and hence a greater reversible capacity[44].

Excess Li-ions can play a significant role in improving the capacity and modifying the surface structure of traditional layered oxides for Li-ion batteries[45] and Li-rich layered TM Na oxides have also been proposed. Kim *et al.* investigated the effects of lithium substitution on sodium layered oxides [46]. A series of layered $Na_xLi_yNi_{0.25}Mn_{0.75}O_\delta$ oxides ($0.7 \leq x \leq 1.2$; $0 < y \leq 0.5$) were synthesized and it was observed that low levels of Li in the TM layer can act in stabilizing the crystal structure and reduce charge-ordering (superstructure) effects, in addition to the negation of Ni movement into the Na layer during cycling. As a result, the Li-substituted $Na_{0.85}Li_{0.17}Ni_{0.21}Mn_{0.64}O_2$ demonstrated a single smooth charge/discharge curve and excellent structural stability with less than 1% crystallographic volume change during cycling. Li-substitution has also been applied successfully to O3-type oxides with similar electrochemical observations. Meng *et al.* explored the replacement effect of Li in O3 type $NaLi_xNi_{1/3-x}Mn_{1/3+x}Co_{1/3-x}O_2$ (x=0.07, 0.13, and 0.2) [47]. The optimized composition, $NaLi_{0.07}Ni_{0.26}Mn_{0.4}Co_{0.26}O_2$ with single-phase, demonstrates excellent capacity retention with above 98% after 50 cycles between 1.5 V and 4.5 V vs Na/Na^+ at 125 mA g^{-1}, as well as superior rate performance when compared to non-doped. Though they attributed the improved performance to the suppressed phase transformation and enhanced electronic conductivity, the exact role of Li in stabilizing the O3 structure is still unclear. You *et al.* conducted a systematic study of the potential influence of Li doping on the high-voltage electrochemistry of O3-type cathodes by taking Li-substituted $Na_{0.85}Li_{0.1}Ni_{0.175}Mn_{0.525}Fe_{0.2}O_2$ (NLNMF) as an example[15]. By using advanced experimental techniques combined with DFT theoretical calculation, they revealed that the incorporation of Li into the TM layer can suppress the unfavorable P3-P'3 phase transition at high voltage (>4.2 V versus Na^+/Na) by mitigating the Jahn-Teller distortion

of Ni^{3+} during Na (de)intercalation process, thus leading to a smooth structural evolution in the bulk material during sodiation and de sodiation (only the O3-P3 phase transition was observed). In addition, this study also showed that the electrolyte-cathode interphase was effectively stabilized by introducing Li^+ ion in the TM layer. The incorporated Li^+ tends to bond with the F^- anion and coordinates with solvent molecules, which may help to prevent the unfavorable loss of active TM ions from the bulk structure, resulting in a greater stability of the CEI at high voltages (Figure 2.2b). Benefiting from the dual-stabilization effect (stabilization of bulk structure and interphase), the Li-substituted NLNMF material shows improved high-voltage durability with 88% capacity retention after 100 cycles at 1 C (1 C= 150 mA g^{-1}) when operated to a cut-off voltage of 4.5 V. Although its mechanism remains controversial, these Li-Na co-doped systems provide a possible feasible approach for further stabilization of the O3-type crystal structures for long-term and high voltage cycling.

Though a large number of doping elements have been reported to be effective in stabilizing the structure and improving the electrochemical performance of layered transition metal oxides, the exact role and improvement mechanism of those incorporated doping elements are still not very clear due to the difference in the size, valence, electrochemical activity, substituted atoms types, and the atoms coordination environments[27]. Although these initial results point towards dopant strategies which stabilize the structures and shift the high voltage phase transitions to lower sodium concentrations in the layered oxide (higher voltages *vs* Na/Na^+). This stabilization is likely achieved through changes in the ionicity of the bond strengths of the transition metal oxide layer. However, systematic research is still needed to further reveal how the introduced dopants regulate the crystal structure, and careful selection should be made according to the characteristics of the substrate and the desired improved properties.

2.3.2 Particle surface coating and modifications

In addition to the contribution from the bulk structure deterioration, the interface reactions between cathode and moisture, cathode and electrolyte, also play vital roles in the manufacturability and determining the final performance of batteries. Surface coating, as an effective surface modification strategy, has been widely used in lithium-containing cathode materials, and various coating substances (i.e., oxides[48], fluorides[49] and phosphates[50, 51]), as well as coating methods (i.e., mechanical mixing[52], sol-gel[53], CVD[54] and ALD[55-57]) have been

well developed and investigated. It is intuitively easy to apply those approaches to the development of highly stable materials for sodium-ion batteries. According to the performance degradation mechanisms mentioned in section 2.2, the roles of surface coatings can be summarized as follows:

(i) Reduction of insulating residues from powder surfaces. As mentioned in section **2.2.2** , most of the current oxide materials are prone to react to form carbonates and hydroxides on the surface once exposure to air, which not only forms an insulating layer upon the particle surface, but it also induces the electrode inks and slurries to gel (PVDF-NMP systems) under certain moisture and temperature conditions. Removing this layer, by forming a protective coating on the surface can prevent the active portion of the material from coming into direct contact with air in the materials storage and cathode preparation process. This in turn will facilitate easier handing of the material and make the whole manufacturing process easier with greater reproducibility. In addition, the removal of the insulating layer from the surface will benefit the cell performance; reducing the internal resistances, promoting higher capacities, higher rates and longer cycle life.

(ii) HF and H_2O scavengers. HF is one of the by-products when $NaPF_6$ decomposes in the presence of H_2O, and it will induce the TM dissolution by attacking the cathode and dissolving its components into the electrolyte. Most of the metal oxides used for surface coating can act as HF scavenger through the following reaction: $TMO + 2HF \rightarrow TMF_2 + H_2O$. Different from the commonly used metal oxides via a self-sacrificing mechanism, recent studies have demonstrated that nano-zeolite can be used as a novel promising scavenger by trapping HF, H_2O and even CO_2 simultaneously into its open framework, which is beneficial for generating a thinner and more stable SEI layer[11, 58].

(iii) Physical protection layer. The surface coating can also act as a barrier layer to reduce the direct contact between electrode and electrolyte, inhibiting electrolyte penetration along the grain boundary, thus suppressing the side reactions at the interface, protecting the surface from oxygen redox which occurs at high voltages and reacts with the electrolyte, as well as preventing TM dissolution.

So far, efforts have been made to investigate the effects of surface coating on the high-voltage stability for sodium layered oxide cathode, via a variety of routes. Based on the ultimate surface

coating morphology, we can simply divide the surface coating into two subgroups (Figure 2.3). a). Mechanical coating methods to produce particulate coated rough surface coating and, b). Chemical coatings methods, where an additional step to the synthesis of the cathode is used, and a more homogeneous surface coating is produced.

2.3.2.1 Mechanical coating methods

Hwang *et al.* have successfully modified an O3-type $Na[Ni_{0.6}Co_{0.2}Mn_{0.2}]O_2$ cathode by coating Al_2O_3 nanoparticles onto the particle surface using a simple dry ball-milling route, which was carefully operated in a dry room to minimize the exposure to moisture. As expected, the coated Al_2O_3 particles effectively suppressed the parasitic reactions by scavenging HF in the electrolyte and simultaneously formed an AlF_3 protection layer on the outermost surface of particles. The reduction in HF also delayed the dissolution of transition metals, which leads to less degradation and cracking of the cathode particles (Figure 2.3a,b,c) [59]. As a result, the proposed Al_2O_3-coated electrode exhibited a higher capacity of 151 mAh g^{-1}, as well as improved rate capability and capacity retention of 75% after 300 cycles in a pouch cell. A similar phenomenon was also confirmed by Liu *et al*, who enhanced the cycling stability of P2-$Na_{2/3}[Ni_{1/3}Mn_{2/3}]O_2$ in the high voltage range (2.0-4.3 V) by applying a thin surface layer of Al_2O_3 [60].

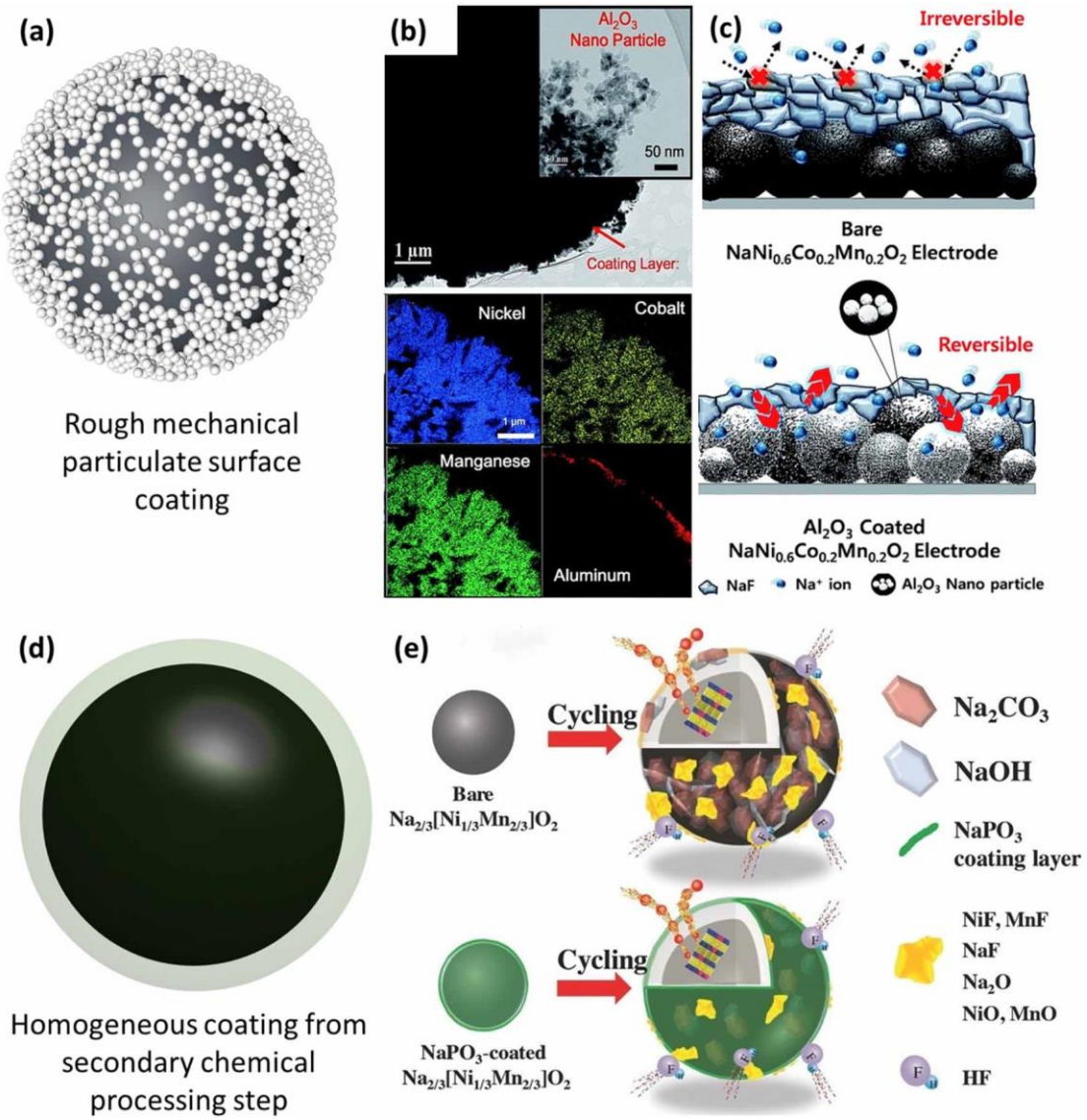


Figure 2.3 (a) Rough particulate surface coating synthesized via mechanical mixing, with example (b) TEM images of Al_2O_3-coated $Na(Ni_{0.6}Co_{0.2}Mn_{0.2})O_2$ and TEM EDX mapping. (c) Schematic diagram showing the effects ofAl_2O_3 coating on the thickness of electrically insulating surface and the Na^+ transport during cycling. Reproduced from [59] with permission of The Royal Society of Chemistry. (d) the schematic of a complete coating, synthesized by chemical processes and an example (e) of a $NaPO_3$ coating layer on $Na_{2/3}(Ni_{1/3}Mn_{2/3})O_2$ formed via reaction with residual NaOH and Na_2CO_3 on the surface, and a schematic illustration ofby-products at the surface ofbare-$Na_{2/3}Ni_{1/3}Mn_{2/3}O_2$ (top) and $NaPO_3$-coated $Na_{2/3}Ni_{1/3}Mn_{2/3}O_2$ (bottom). [104] John Wiley & Sons. [© 2018 WILEY-VCH Verlag GmbH & Co. KGaA, Weinheim].

Oxide coatings obtained through mechanical mixing processes possess the advantages of simplicity and low cost. However, it also demonstrates some obvious shortcomings: a). Metal

oxides are generally insulating to ionic/electronic conduction. This will lead to an increase in cell polarization and reduce rate capability and cycle life. b). Though the metal oxides can capture HF, the scavenger itself will also be constantly consumed and therefore have a finite life-time, whilst water will still be generated, further degrading the battery performance over extended period of cycling. c). The mechanical mixing of the cathode particles with coatings is very rough, the metal oxides tend to discontinuously and incompletely cover the surface, some areas are heavily coated while other areas are only barely coated (Figure 2.3 a,b,c) [61]. To tackle these problems, it is necessary to develop novel coating methods and optimize the coating composition to obtain a uniform and controllable coating layer with high Na^+/e^- conductivities.

2.3.2.2 Chemical coating processes

Xiao *et al.* successfully constructed a homogeneous layer of Na-ion conductor Na_2SiO_3 on the O3-$NaNi_{1/3}Fe_{1/3}Mn_{1/3}O_2$ electrode by an *in-situ* coating approach. Firstly, a SiO_2 uniformly coated $Ni_{1/3}Mn_{1/3}Fe_{1/3}C_2O_4{\cdot}yH_2O$ was obtained by mixing $Ni_{1/3}Mn_{1/3}Fe_{1/3}C_2O_4{\cdot}xH_2O$ precursor and $Si(OC_2H_5)_4$, followed by a solvothermal process based on hydrolysis of $Si(OC_2H_5)_4$ by $Ni_{1/3}Mn_{1/3}Fe_{1/3}C_2O_4{\cdot}xH_2O$ at 180 °C. Then, SiO_2- $Ni_{1/3}Mn_{1/3}Fe_{1/3}C_2O_4{\cdot}yH_2O$ reacted with Na_2CO_3 to form Na_2SiO_3 coated $NaNi_{1/3}Fe_{1/3}Mn_{1/3}O_2$ under high-temperature calcination [62]. This coating method can not only create a uniform and complete coating layer but also forms a well adhered coating layer. The results indicate that the Na_2SiO_3 coating layer can effectively increase Na^+-ion conduction and suppress the particle cracking, whilst minimizing parasitic side reactions. Meanwhile, Na_2SiO_3 coating also effectively facilitates the reversible O3−P3 phase transitions during cycling, by preventing transition metal migration. As a result, the as-coated sample exhibits highly improved cycling stability (increased by 28% after 50 cycles) and good rate capability. In a similar way, they also used 5 wt.% $Ti(OC_4H_9)_4$ to treat $Ni_{1/3}Mn_{2/3}C_2O_4{\cdot}xH_2O$ for $Na_2Ti_3O_7$-modified P2-type $Na_{2/3}Ni_{1/3}Mn_{2/3}O_2$ electrode[63].

Sodiated transition metal oxides are sensitive to moisture, NaOH and Na_2CO_3 will be immediately generated once exposed to air, resulting in Na-deficient surface with low electron and ion conductivity. There is no doubt that it would be beneficial if we could remove these sodium by-products during the coating process, simultaneously dealing with two short comings in the manufacturing process at once. Inspired by this, Myung and Sun *et al.* have attempted to minimize these surface sodium residues content (Na_2O, NaOH, and Na_2CO_3) by reacting with $NH_4H_2PO_4$ via melt-impregnation at 300 ℃ to form a uniform coating layer on the surface of

the parent $Na_{2/3}[Ni_{1/3}Mn_{2/3}]O_2$ particles. During the heating process, $NH_4H_2PO_4$ spontaneously transforms to HPO_3 melt, which impregnates or encapsulates all the particles which undergoes a reaction with the surface residues to form an ionic conducting $NaPO_3$ coating layer (Figure 2.3d,e) [64]. This artificial conformal $NaPO_3$ lowers the surface residue content but also acts as HF/H_2O scavenger to suppress the corrosion of the cathode materials (Figure 2.3e), thus, structural integrity and superior cyclability are achieved. Similarly, $Ca(NO_3)_2$ and H_3PO_4 have been used to generate a uniform and ionically conducting protective layer of β-$NaCaPO_4$ on the surface of $Na_{2/3}[Ni_{1/3}Mn_{2/3}]O_2$ powders after heating at 700 °C in air [65]. Like the $NaPO_3$ layer, the native β-$NaCaPO_4$ surface layer can also scavenge HF/H_2O in the electrolyte to alleviate the surface degradation phenomena. As a result, the capacity retention remarkably improved from 31% for the bare electrode to 74% for the coated electrode after 200 cycles within 2.5-4.3 V at 0.2C. The lowering, or removal of the residual surface compounds reduce the resistances of the materials, improve ionic conductivity, and help to maintaining the integrity of the crystal structure during cycling. The removal of these surface residues is extremely important when developing these SIB oxide cathodes but is often overlooked. Future optimization strategies should include this consideration.

Surface coatings that aim to suppress surface-related chemical degradations might work in suppressing electrolyte decomposition, metal dissolution, and improving conductivity, but do not, in general, suppress the high voltage phase transitions[8]. This is different from the layered cathodes for LIBs, where surface degradation is more dominated by bulk structure changes. The sodium-containing layered oxides possess more complicated phase transformations accompanied by repeated large volume changes during cycling. This suggests that simple coating layers, tens of nanometers in thickness, are unlikely to be robust, or flexible, enough to sufficiently compensate for the volume change and structure collapse of SIBs layered cathodes under adverse operations (high voltage and long-term cycling). Therefore, to optimize the SIBs layered oxides for high-voltage applications, the combination of bulk doping and surface coating to simultaneously stabilize the bulk structure and interface will be more effective. It should also be noted that some of the modification methods that are widely used for LIBs may not be applicable to SIBs due to the highly hygroscopic nature of sodiated transition metal oxides. Some commonly used methods for LIBs involve wet mixing and post-heating treatment which would most likely expose the layered oxides to moisture resulting in the formation of NaOH and Na_2CO_3 on the particle surfaces. Therefore, novel coating routes that minimize

contact with air or liquids could be more appropriate for constructing stable particle interfaces for sodium layered oxides.

2.3.3 Combined composition and coating strategies

Hwang *et al.* have demonstrated a combined structure modification to enhance the electrochemical performance of $Na[Ni_{0.5}Mn_{0.5}]O_2$ (NM55) electrode by MgO surface coating and simultaneously doping Mg via a one-step synthesis process [66]. During the high-temperature calcination process, up to about 5 at% of Mg is uniformly incorporated into the bulk structure due to the thermodynamics (Figure 2.4a), which could effectively improve the structural stability by suppressing the irreversible phase transformation. Meanwhile, the surface-related degradation process may be eliminated by the residual MgO coating layer. As a result, the co-modified NM55 cathode exhibited a significant enhanced cycling stability with 75% capacity retention after 100 cycles in the wide voltage range of 2.0-4.2 V, compared to only 46% for the bare cathode. Later, they have also applied this effective coating-induced doping strategy in O3-$Na[Ni_{0.6}Co_{0.2}Mn_{0.2}]O_2$ cathode to boost the structural stability by concurrent TiO_2 coating and partial Ti doping[30]. Similarly, Xiao *et al.* successfully prepared a CuO-coated and Cu^{2+}-doped co-modified P2-type $Na_{2/3}[Ni_{1/3}Mn_{2/3}]O_2$ via a wet-chemistry approach[67]. The CuO covering layer hinders the corrosion of the electrolyte and prevents particle exfoliation phenomena, while the partial incorporated Cu^{2+} shrinks TMO_2 sheets and shortens TM-O bond, leading to a crystal structure with enhanced stability. The above-mentioned results suggest that the phenomenon of the coating constituents penetrating the bulk structure may be common during the annealing process, thus, a systematic study of the effect of the annealing temperature and time should be taken to elucidate the interplay between the coating and doping levels.

Guo *et al.* proposed an exact opposite strategy, doping-induced surface reconstruction [19]. They found that the doped Ti^{4+} tends to concentrate on the particle surface, forming an atomic-scale interface composed of spinel-like titanium (III) oxides (Figure 2.4b). This Ti (III)-concentrated spinel-like overlayer can not only suppress the atmospheric and electrochemical corrosion but also enhance the structural stability and electronic/ionic conductivity. Consequently, the Ti doping-induced surface-engineered electrode showed astonishing cycling stability with 85% capacity retention after 100 cycles at 0.5 C, compared to 36% for the Ti-free electrode. Though the underlying mechanism of this spontaneous surface segregation still needs further studies,

this doping-induced surface reconstruction strategy provides new insight to tailor and modify the interface, which is completely different from the general coating methods.

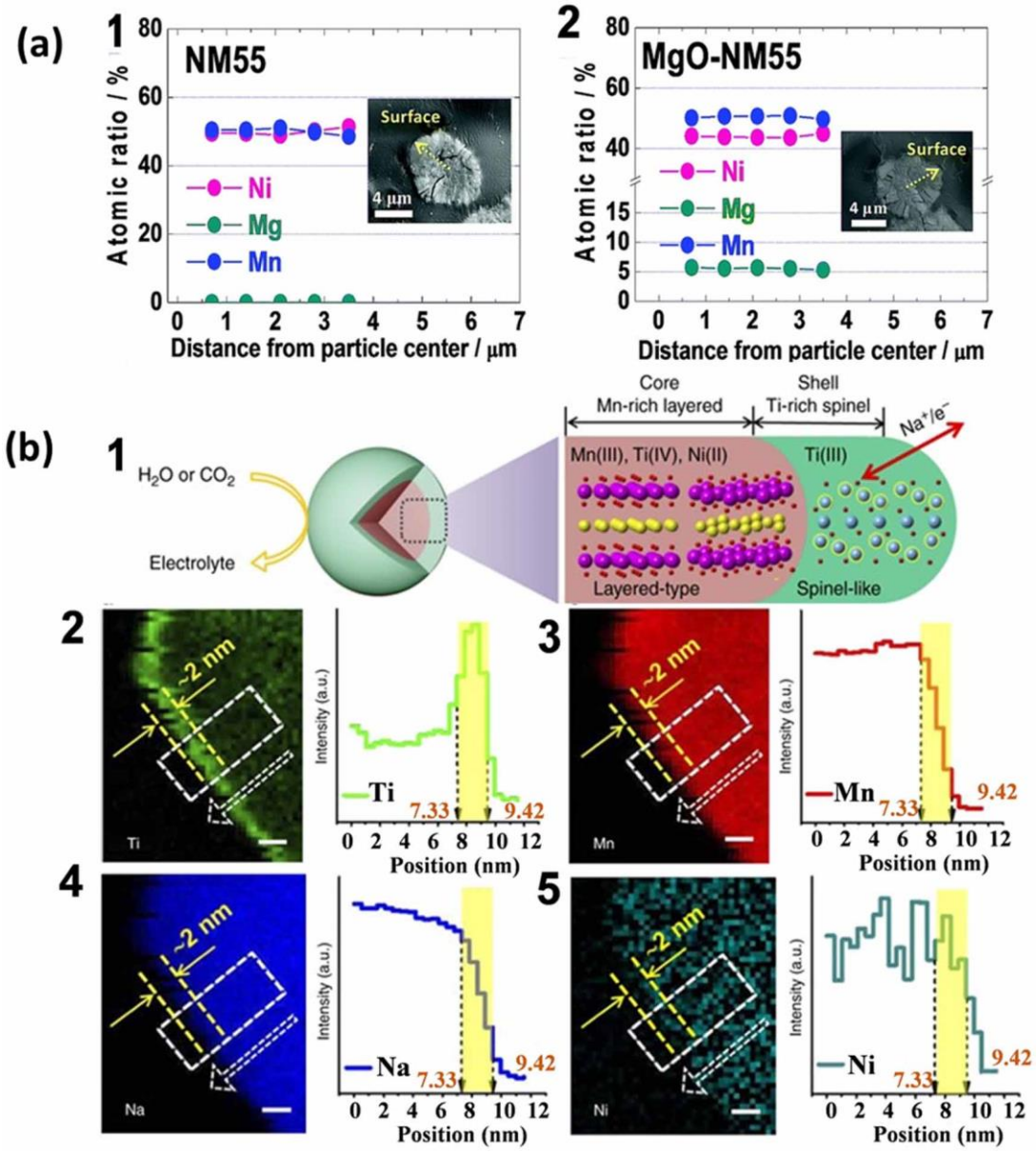


Figure 2.4 (a) Example ofdual effect from a one-step synthesis process for fabricating the MgO coated and Mg doped $Na(Ni_{0.5}Mn_{0.5})O_2$ (MgO–NM55) cathode. EPMA results of (a1) NM55 and (a2) MgO–NM55 cathodes. Reproduced from [66] with permission of The Royal Society of Chemistry.(b1) 3D structural model of the NMTN samples composed of a Ti-rich spinel-like interface (green shell) and Mn-rich layered bulk (brown core). (b2–5) EELS chemical mapping of the NMTN samples and corresponding chemical compositions (white rectangle) for b2 Ti, b3 Na, b4 Mn, and b5 Ni elements showing that the interface 2 nm from the particle edge is enriched by titanium rather than other elements. Reproduced from [19]. CC BY 4.0.

Apart from the use of metal oxide as coating layer, very recently, Tang *et al.* designed a dual-modified P2-type $Na_{0.67}Ni_{0.33}Mn_{0.67}O_2$ (NMO) cathode via bulk Mg substitution (NMMO) and $NaTi_2(PO_4)_3$ (NTP) surface coating through sol-gel method[68]. The bulk Mg substitution reduces the volume contraction and stabilizes the bulk structure through suppressing the P2-O2 phase transition, while the NASICON-type NTP coating layer can both stabilize the interface and facilitate the Na^+ migration due to its stable and open framework. Therefore, the dual-modified NMMO/NTP exhibited a cycling performance with 77.4% capacity retention after 200 cycles at 1 C within 2.5-4.3 V. By contrast, the bare NMO and Mg-doped NMMO electrodes showed more rapid capacity degradation, with only 19.7% and 59.8% capacity retention, respectively.

We believe that the combination of host structure doping and surface coating through in-situ will be supportive for achieving high energy density Na-ion batteries with improved cycling performance.

2.3.4 Particle morphology and material structure design

2.3.4.1 Multi and bi-phasic hybrid materials

As two of the most common layered oxide materials for sodium-ion batteries, O3 and P2 phase oxides have been extensively investigated in the last ten years. In general, O3 type oxides possess the advantage of a higher capacity than P2 type but suffer from unsatisfactory cycling properties owing to the easily contaminated surface and complex phase transitions during the electrochemical process. P2 type oxides are just the opposite, these oxides possess relatively strong resistances to hygroscopic degradation, and can maintain its original structure over a wider voltage range, thus exhibiting improved capacity retention. However, the lower capacity and an initial coulombic efficiency higher than 100%, as observed in a sodium metal anode cell. This efficiency originates from the deficient sodium content and the further electrochemical sodiation of the material upon discharge. This not only narrows its competitiveness in terms of energy density but brings many difficulties in terms of the full cell design. Though efforts have been devoted to modifying the structure and overcome the intrinsic drawbacks of each material, it is still a challenge to obtain an ideal cathode material which possesses all the desired properties, namely high capacity, robust structure, as well as superior rate capability. Therefore, hybrid material structures have been designed with biphasic O3 and P2 phases to combine the

merits and offset the drawbacks of the two pure phases, and a series of composite cathodes with biphasic O3/P2 phases have been proposed.

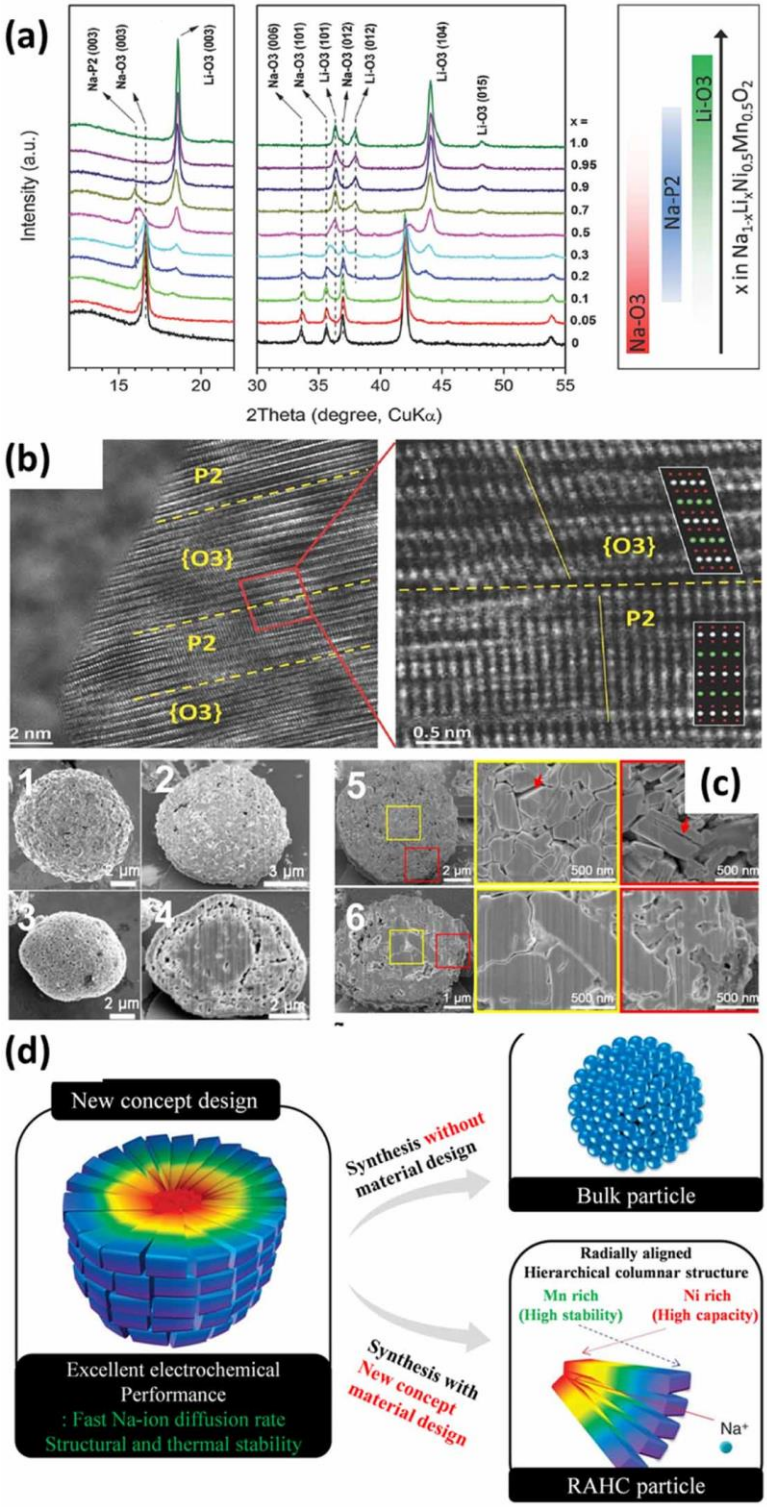


Figure 2.5 (a) X-ray diffraction patterns of $Na_{1-x}Li_xNi_{0.5}Mn_{0.5}O_{2+d}$ with different Li content, x ($0 \leq x \leq 1$) showing phase evolution as a function of Li content. (b) High-resolution TEM images directly

showing the intergrowth stacking of the P2 and O3 lattices of $Na_{0.7}Li_{0.3}Ni_{0.5}Mn_{0.5}O_{2+d.}$ [69] John Wiley & Sons. [© 2014 WILEY-VCH Verlag GmbH & Co. KGaA, Weinheim]. (c1, c2) Representative plan-view and cross-sectional SEM images of the pristine O3/O'3 material. (c3, c4) Representative plan-view and cross-sectional SEM images of the pristine O3/O'3–P2 material. Comparison of cross-sectional SEM image of the (c5) pristine O3/O'3 and the (c6) O3/O'3–P2 electrode after 50 cycles. Reprinted with permission from [70]. Copyright (2020) American Chemical Society. (d) Scheme illustration of the composition and structure for a typical RAHC particle. Reprinted by permission from Springer Nature Customer Service Centre GmbH: [Nature] [Nature Communications] [71] (2015).

Johnson *et al.* first reported layered O3/P2 intergrowth cathode in the study of the effects of Li substitution for Na in $Na_{1-x}Li_xNi_{0.5}Mn_{0.5}O_2$ [69]. They found that with Li substitution, the P2 phase fraction increases at the expense of O3 until x = 0.5 (Figure 2.5a, 6b), and the capacity, as well as rate capability significantly improved simultaneously. However, due to the dominant quantity of the O3 phase in this hybrid material, the O3-P3 phase transition is still inevitable. This exhibits a disadvantage, resulting in a significant decrease in capacity within 20 cycles. Based on this, Zhou *et al.* proposed an opposite design strategy, namely introducing minor O3 phases into the P2 host material to increase the capacity while ensuring good cycling performance and rate capability [72]. The synthesized P2-majority composite material $Na_{0.66}Li_{0.18}Mn_{0.71}Ni_{0.21}Co_{0.08}O_2$ presented an improved capacity of 200 mAh g^{-1} (compared with 125 mAh g^{-1} of corresponding single P2), rate capability, cycling stability in the wide voltage range of 1.5-4.5 V (75% capacity retention over 150 cycles) and higher average voltage of 3.2 V vs Na/Na^+. This average voltage and capacity give a gravimetric energy density of 640 Wh kg^{-1} which rivals that of $LiFePO_4$ (about 530 Wh kg^{-1}).

In addition to the Li substitution for Na mentioned above, Li substitution for TMs has also been proven a feasible strategy for synthesis of bi-phasic materials. Liu *et al.* have successfully obtained P2/O3 biphasic $Na_{0.67}Mn_{0.55}Ni_{0.25}Ti_{0.2-x}Li_xO_2$ by Li substitution for Ti[73]. XRD refinement showed that the O3-phase content increases from 0% to 14.87% for x = 0 - 0.2. The Li mainly occupies the TM sites, maintaining the P2 structure, while a low level of Li resides in the Na sites to adjust the Na/TM ratio required for the O3-phase. The generation of the O3 phase improves the observed Na ion diffusion kinetics, this improvement may originate from the greater number of defects with the lower valence of Li^+ compared to Ti^{4+}. Similarly, the work of Huang *et al.* showed that Mg can also be used to substitute TM in layered

$Na_{0.67}(Fe_{0.5}Mn_{0.5})_{1-x}Mg_xO_2$ to obtain a P2/O3 bi-phasic cathode $Na_{0.67}Fe_{0.425}Mn_{0.425}Mg_{0.15}O_2$, which can deliver 155 mAh g^{-1} and good cycling stability within 2.0-4.3 V[74].

Chen *et al.* synthesized a series of O3/P2 hybrid cathodes with various O3/P2 ratio by adjusting the sodium content in $Na_xNi_{0.2}Fe_{x-0.4}Mn_{1.2-x}O_2$[75]. Structural refinements showed that the sodium content x=0.8 is a critical value, above which the pure O3 phase formed, while below 0.8 a O3/P2 hybrid structure is obtained. The optimized formula $Na_{0.78}Ni_{0.2}Fe_{0.38}Mn_{0.42}O_2$ displays the best comprehensive electrochemical performance in terms of capacity, rate capability, and cycling stability. Notably, superior cycling performance was obtained with 90% capacity retention after 1500 cycles within 2.5-4.0 V. This suggests that the high voltage phase transition was not observed within the voltage limits utilized in this study. Further doping strategies could improve the observed specific capacities with increased cycling voltage windows, increasing the observed average voltage whilst maintaining the cycle life.

Apart from P2/O3 hybrid structure, other intergrowth systems, such as P2/P3[76-78], P2/tunnel[44, 79], and some multiphasic intergrowth materials (O3/P2/P3 or P2/O3/O1)[80, 81] have also been proposed and studied.

Multi-phasic materials combine the advantages of different phases and provide a new avenue for exploring novel cathodes with superior comprehensive performance. However, the exact interplay mechanism of different phases has not yet been fully discussed and understood, and it is still a big challenge to synthesize a multiphase cathode material with the correct desirable phase composition due to the complex and uncertain synthesis parameters[81, 82]. In addition, whilst these materials have some advantages, bi and multi-phase materials may also have some negative effects, such as extremely complex electrochemical redox reactions, and consequently complex charge and discharge voltage curves. This may pose greater challenges for state of charge (SOC) management and prediction in practical applications. Therefore, it is necessary to optimize the ratio between O3 and P2 phases within a specific system to achieve a balance between electrochemical properties and the difficulty of translation into practical applications.

2.3.4.2 Core-shell particles

As mentioned above, designing composite phase bulk materials integrate the advantages of separate phases, and demonstrate a positive cooperative effect on the overall performance through suppressing irreversible bulk phase transitions or providing additional capacity. This

approach still leaves the surface-associated chemical degradation un-solved with open facets and surfaces exposed to the electrolyte, which may enable further parasitic reactions to occur.

Considering this, a novel core-shell structure was proposed by Chen *et al.* with Ni-rich O3/O′3 phases $Na_{0.8}[Ni_{0.5}Co_{0.2}Mn_{0.3}]O_2$ as the core and a Mn-rich P2 phase $Na_{0.8}[Ni_{0.33}Mn_{0.67}]O_2$ as the shell. This was synthesized by a two-step co-precipitation method [70]. Complementary microscopy analysis indicated that both the microscale core-shell and nanoscale internal crystal structure interfaces are well formed. The thick and continuous P2 shell appeared robust enough to constrain the structural degradation and crack propagation of the O3-type core, but also provided a stable interface by blocking the chemical attack from the electrolyte (Figure 2.5c). Moreover, the incorporation of a redox active and stable phase, in this case, P2 oxide, means that the shell can participate in the electrochemistry process and facilitate the Na ions diffusion, in addition to the main core. Thus, improved cycling performance, higher reversible capacity, and improved rate capability compared to the bare O3/O′3 cathode was observed.

This core-shell architecture method uses cathode materials with electrochemically active and stable structures as coating substances without sacrificing the capacity. Hence, core-shell structure has been widely used and researched in developing superior cathode materials for LIBs[83-86], and even applied in other types of positive electrode materials for SIBs, such as polyanionic compounds[87, 88], and Prussian blue analogues[89-92]. There is significant scope for further exploring this method for new higher energy density and stable sodium layered oxides for SIBs.

2.3.4.3 Concentration gradient particles

Though the core-shell configuration integrates the advantages of surface coating and hybrid bulk structures, the structure mismatch issue between the core and the shell should be carefully considered when designing this heterostructure. For example, when charged up to 4.0 V, the O3 type core materials transfer to P3 phase with large expansion in d-spacing, while the P2 type shell materials can maintain its original structure before being charged to 4.2 V[70]. This large difference in volume change between the two types of materials during Na insertion/extraction can lead to large voids at the core/shell interface upon cycling, which may result in poor connections between the core and shell, which will inhibit the transfer of Na^+ and electrons, and lead to a sudden drop in capacity from the increased resistance and poor transport properties.

To tackle this issue, a full concentration gradient (FCG) strategy was proposed by Sun *et al.* for high-energy LIB cathode materials. They created a special structure where the concentration of elements providing high capacity (usually Ni or Co) decreases linearly, whereas the concentration of elements improving the structure stability (usually Mn or Al) increases linearly from the center to the outer layer of each particle, forming a special "core-shell" structure with Ni-rich core and Mn-rich shell[93]. Unlike the core-shell structure, this FCG structure has no obvious interface, owing to the continuous and smooth transition of components from the bulk to the surface. Consequently, the structure mismatch caused by the sharp differentiation of components in the core and shell can be effectively alleviated.

This strategy was further applied to sodium-containing cathode materials. A full concentration gradient for sodium O3-type layered oxide was reported whose chemical composition varied from the inner end ($Na[Ni_{0.75}Co_{0.02}Mn_{0.23}]O_2$) to the outer end ($Na[Ni_{0.58}Co_{0.06}Mn_{0.36}]O_2$, giving an average chemical composition of $Na[Ni_{0.6}Co_{0.05}Mn_{0.35}]O_2$ (Figure 2.5d) [71]. This material presented a so-called radially aligned hierarchical columnar structure (RAHC), which is different from the traditional spherical stacking structure. The hierarchical columnar structure provides extended fast channels for Na^+ ion diffusion and was also found to a greater level of Ni^{3+} rather than Ni^{2+}, which has a lower energy level of Ni^{3+}/Ni^{4+} than Ni^{2+}/Ni^{3+} redox reaction. This was reported the reasoning behind the improved discharge capacity (157 mAh g^{-1}) for the RAHC $Na[Ni_{0.6}Co_{0.05}Mn_{0.35}]O_2$ at 15 mA g^{-1}, compared to the standard homogeneous bulk material; $Na[Ni_{0.6}Co_{0.05}Mn_{0.35}]O_2$ (145 mAh g^{-1}) , despite having identical chemical compositions. In addition, these rod-shaped primary particles showed smaller surface area and pore volume values, this minimizes the side reactions with the electrolyte, and improved cycling stability. 300 cycles were achieved in full cell with hard carbon as anode (RAHC: 80.0%, bulk: 49.2%). Moreover, the RAHC electrode, when charged to 4.1 V exhibited lower heat generation of 172 J g^{-1} at a higher temperature (293.5°C) compared to the conventional material (321.6 J g^{-1} at 266.5°C) when heated with electrolyte. This indicates that the thermal runaway temperature onset may be increased, and that the surface is stabilized to reaction with the electrolyte. This may be due to the reduction in catalytic sites from increased manganese content at the surface or that the RAHC structure reduces the oxygen evolution from the host structure by increasing the observed voltage at which the irreversible phase transformation occurs. By taking advantages of the concentration gradients of the transition metals and radially

aligned columnar structure, high capacity and cycling performance as well as thermal stability were simultaneously achieved.

This chemistry and particle structure offers routes for stable high energy density cathode materials for SIBs without sacrificing the cycling stability. However, the synthesis of FCG materials requires a multistep co-precipitation process, which usually requires additional tanks to hold and precisely regulate the feeding rate of transition metals, increasing the time and capital cost.

2.3.5 Morphology and particle engineering

As mentioned **in section 2.2.1,** the excessive deintercalation of sodium ions at high voltages will involve detrimental multi-phase transitions, accompanied by large crystal unit cell volumes changes. The repeated expansion and contraction of the crystal lattice causes high strain in phase boundaries and within particles due to the difference in these lattice parameters, which can further lead to the formation of intergranular cracks between primary particles within the secondary agglomerated particles. This expansion mechanism destroys the contact between primary particles, reducing the number of electronic and ionic transport paths within the cathode particle. The consequence is high observed resistances, which subsequently leads to degradation in the cycling performance, poor rate, and occasionally lower observed capacities if the particles are completely isolated.

There are several conceptual strategies to tackle this expansion and cracking problem at a particle level rather, in addition to those discussed above, including grain boundary engineering and single crystal particles.

2.3.5.1 Grain boundary engineering

Grain boundary engineering is a classic and powerful approach to tailor grain boundary structure and chemistry for the optimization of material properties in material science [94-97]. However, it has not attracted enough attention in the field of batteries, e.g., lithium-ion or sodium-ion batteries. In 2018, Yan *et al.* used this strategy to develop Ni-rich layered cathodes LIBs, and systematically studied its effects on structure and electrochemical properties[98]. They infused the grain boundaries of secondary particles with a solid electrolyte (Li_3PO_4) through surface coating and subsequent annealing treatment at 600°C (Figure 2.6a). Detailed structural

and chemical analysis revealed that the grain-boundary modification played a vital role in enhancing the structural stability and electrochemical properties. The grain boundaries provided additional transport paths for lithium-ion conduction but also act as a blocking agent for preventing the penetration of liquid electrolyte into the boundaries, thus successfully eliminating the interfacial reactions, and suppressing the cracking of secondary particles. Although grain boundary engineering has demonstrated its effectiveness in alleviating the degradation associated with intergranular cracks in layered lithium transition cathodes. However, it is yet to be applied to sodium-ion cathodes and is a promising area for future SIB cathode particle morphology and compositional optimization.

2.3.5.2 Single crystal particles

Single crystalline particles formed by adjusting sintering temperature and alkali/transition metal molarity offers another strategy for mitigating the issues cause because of cracks forming between primary particles.

Single crystal lithium-based cathodes, like NMC532, NMC622, NCA, were shown to demonstrate superior stability at high voltages compared to conventional polycrystalline particles[99]. It is expected that single crystal sodium-based layered oxides could also provide structural stability and improved electrochemical properties compared to typical polycrystalline materials. In 2013, Wang *et al.* successfully synthesized single crystalline rhombus-shaped $Na_{0.7}MnO_2$ nanoplates by a hydrothermal method (Figure 2.6b). Electrochemical tests showed that the single crystalline $Na_{0.7}MnO_2$ exhibited a near theoretical capacity of 164 mAh g^{-1}, a good high-rate performance, and a durable cyclability [100]. S.Tepavcevic *et al.* reported a highly ordered single crystal Na_2IrO_3 electrode that may boost the energy density of SIBs[101]. Compared to its polycrystalline counterpart, single crystal Na_2IrO_3 electrode presented an improved cycling stability in the voltage window 1.5-4.2 V (Figure 2.6c). Though the single crystal Na_2IrO_3 still experienced strong capacity fade with cycling because of the formation of a new phase, this single crystal strategy can play a vital role in understanding and developing novel new cathodes with robust structure.

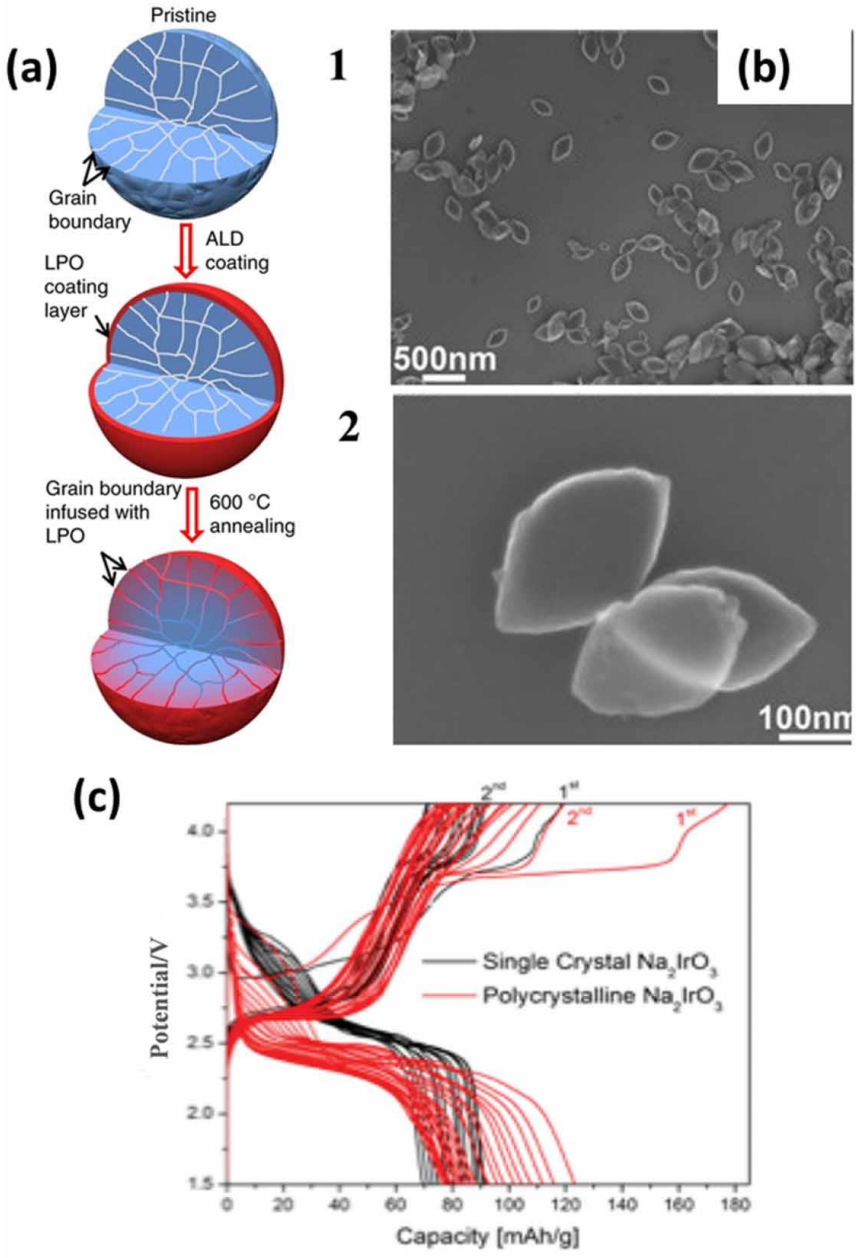


Figure 2.6 (a) Schematic illustration shows the evolution of the Li_3PO_4 coating layer on the secondary particle following coating and annealing. Reprinted by permission from Springer Nature Customer Service Centre GmbH: [Nature] [Nature Energy] [98] (2018). (b1) Low- and (b2) high-magnification FESEM images of $Na_{0.7}MnO_2$ nanoplates. [100] John Wiley & Sons. [© 2013 WILEY-VCH Verlag GmbH & Co. KGaA, Weinheim]. (c) Capacity–voltage plots of the very first 20 cycles obtained from a single-crystal and polycrystalline Na_2IrO_3 electrodes in the voltage window 1.5–4.2 V. [101] John Wiley & Sons. [© 2020 WILEY-VCH Verlag GmbH & Co. KGaA, Weinheim].

2.4 Conclusion and critical opinions

In summary, SIBs offer a wealth of possibilities for the development of inexpensive and sustainable energy storage devices. However, many challenges are inevitably encountered in the pursuit of higher energy density to make it a true 'drop-in' technology for LIBs. In this review, the main aspects of degradation at high-voltage sodium layered oxide type materials are summarized:

(a) *Reactive surfaces*: the oxides are prone to react with water and CO_2 to form NaOH and Na_2CO_3 on the particle surface, which will induce possible ink gelation during the mixing and coating procedures, increase the cell polarization, as well as cause water formation from reacting with the electrolyte in a cell.

(b) *Electrolyte oxidation and oxygen loss:* high voltage operation often involves partial oxygen redox, which will result in the decomposition of electrolyte via oxidation reaction.

(c) *Surface reconstruction:* with the loss of oxygen, transition metals are reduced, and ultimately resulting in metals dissolution into electrolyte (particularly Mn^{3+}) and surface reconstruction. These dissolved transition metal ions then deposit on the anode to form a resistive interface.

(d) *Phase transitions and induced particle cracking:* the large volume change during complex phase transformations along with the enhancement of the degradation surface effects can induce cracking and pulverizing of the particles. The cracks within the particles will further lead to poor electronic conduction, TM dissolution, surface corrosion, and electrolyte consumption.

To prevent the above degradation mechanisms, various strategies including bulk-doping, surface coating, microstructure tailoring, and particle morphology design, have been investigated to date (Figure 2.7). However, it should be noted that the bulk structure and surface degradations do not occur independently but work synergistically leading to the cathode failure at high voltages. Thus, a single approach is unlikely to eliminate all the degradation issues. We believe that to develop sodium layered oxide materials with simultaneous high energy density and long cycle life a multi-approach is required. In particular, the morphological control of the particles to produce materials with few grain boundaries or single crystals is of great importance

to minimize the surface side reactions and reduce cracking along the grain boundaries thus limiting any surface-related degradations. Meanwhile, constructing a stable interface to generate residual-free particle surfaces will be beneficial for improving the manufacturability, and the stability in the cell. In addition, the voltage or average voltage needs to be increased through elective element substitution to stabilize the 'high voltage region' (associated with the oxygen redox and loss), thus minimizing the irreversible phase transitions at higher voltages, and maximizing the solid solution zone. Furthermore, HF and H_2O scavengers are required to limit the formation of fluorides on the surface of the cathodes. Therefore, constructing a synergetic structure through particle morphology design, bulk doping and surface coating is proposed to simultaneously reduce the irreversible phase transformation and surface degradation.

In addition to enhancing the stability of cathode materials itself, more attention should be focused on interfacial engineering by developing new electrolytes with wider electrochemical stability window and optimizing the formation process to form a dense, stable, and high ionic conductivity CEI film on the cathode/electrolyte surface.

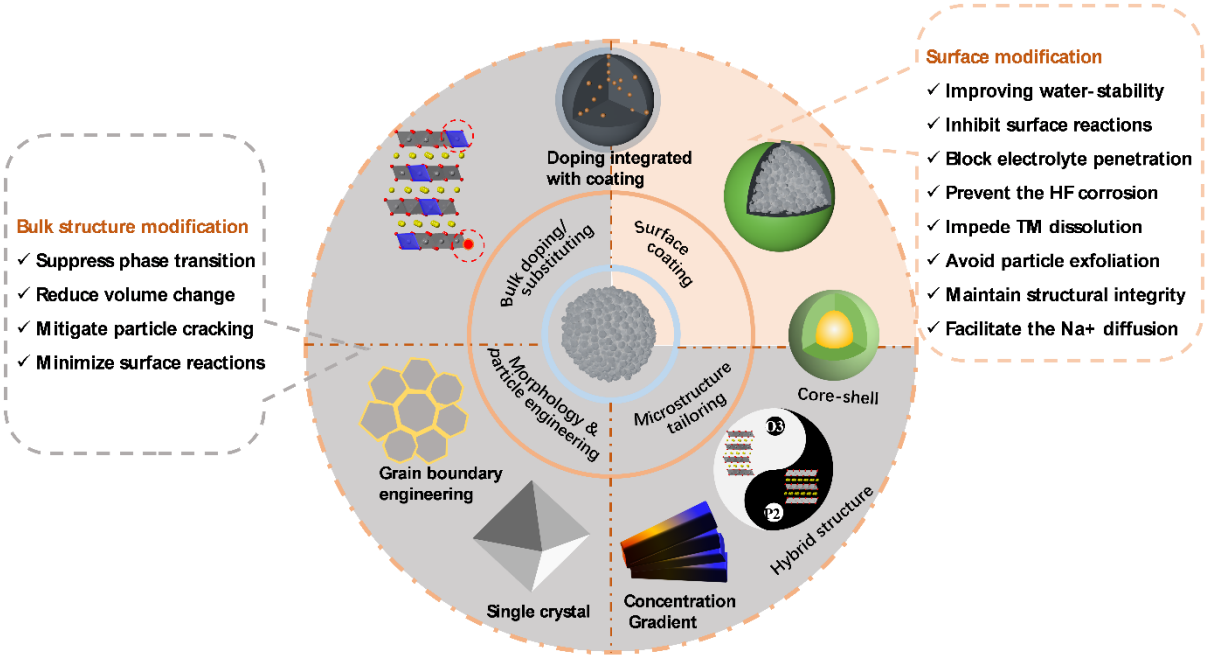


Figure 2.7 Overview on corresponding modifying strategies for sodium layered oxide materials under high voltage operation.

2.5 References

1. Xiao, Y.; Abbasi, N. M.; Zhu, Y. F.; Li, S.; Tan, S. J.; Ling, W.; Peng, L.; Yang, T.; Wang, L.; Guo, X. D.; Yin, Y. X.; Zhang, H.; Guo, Y. G., Layered Oxide Cathodes Promoted by Structure Modulation Technology for Sodium‐Ion Batteries. *Advanced Functional Materials* **2020**, (30), 2001334.
2. Sun, Y.; Guo, S.; Zhou, H., Adverse effects of interlayer-gliding in layered transition-metal oxides on electrochemical sodium-ion storage. *Energy & Environmental Science* **2019,** 12, (3), 825-840.
3. Wang, K.; Yan, P.; Sui, M., Phase transition induced cracking plaguing layered cathode for sodium-ion battery. *Nano Energy* **2018,** 54, 148-155.
4. Xie, Y.; Wang, H.; Xu, G.; Wang, J.; Sheng, H.; Chen, Z.; Ren, Y.; Sun, C.-J.; Wen, J.; Wang, J.; Miller, D. J.; Lu, J.; Amine, K.; Ma, Z.-F., In Operando XRD and TXM Study on the Metastable Structure Change of $NaNi_{1/3}Fe_{1/3}Mn_{1/3}O_2$ under Electrochemical Sodium-Ion Intercalation. *Advanced Energy Materials* **2016,** 6, (24).
5. Jeong, M.; Lee, H.; Yoon, J.; Yoon, W.-S., O3-type $NaNi_{1/3}Fe_{1/3}Mn_{1/3}O_2$ layered cathode for Na-ion batteries: Structural evolution and redox mechanism upon Na (de) intercalation. *Journal of Power Sources* **2019,** 439.
6. Buchholz, D.; Chagas, L. G.; Vaalma, C.; Wu, L.; Passerini, S., Water sensitivity of layered P2/P3-$Na_xNi_{0.22}Co_{0.11}Mn_{0.66}O_2$ cathode material. *J. Mater. Chem. A* **2014,** 2, (33), 13415-13421.
7. Duffort, V.; Talaie, E.; Black, R.; Nazar, L. F., Uptake of CO2 in Layered P2-Na0.67Mn0.5Fe0.5O2: Insertion of Carbonate Anions. *Chemistry of Materials* **2015,** 27, (7), 2515-2524.
8. Xiao, B.; Sun, X., Surface and Subsurface Reactions of Lithium Transition Metal Oxide Cathode Materials: An Overview of the Fundamental Origins and Remedying Approaches. *Advanced Energy Materials* **2018,** 8, (29).
9. Han, M. H.; Sharma, N.; Gonzalo, E.; Pramudita, J. C.; Brand, H. E. A.; López del Amo, J. M.; Rojo, T., Moisture exposed layered oxide electrodes as Na-ion battery cathodes. *Journal of Materials Chemistry A* **2016,** 4, (48), 18963-18975.
10. Zhang, Y.; Zhang, R.; Huang, Y., Air-Stable Na_xTMO_2 Cathodes for Sodium Storage. *Front Chem* **2019,** 7, 335.
11. Chen, L.; Kishore, B.; Walker, M.; Dancer, C.; Kendrick, E., Nanozeolite ZSM-5 electrolyte additive for long life sodium-ion batteries. *Chemical Communications* **2020**.
12. Alvarado, J.; Ma, C.; Wang, S.; Nguyen, K.; Kodur, M.; Meng, Y. S., Improvement of the Cathode Electrolyte Interphase on P2-$Na_{2/3}Ni_{1/3}Mn_{2/3}O_2$ by Atomic Layer Deposition. *ACS Appl Mater Interfaces* **2017,** 9, (31), 26518-26530.
13. Wohlfahrt-Mehrens, M.; Vogler, C.; Garche, J., Aging mechanisms of lithium cathode materials. *Journal of Power Sources* **2004,** 127, (1-2), 58-64.
14. Zheng, H.; Sun, Q.; Liu, G.; Song, X.; Battaglia, V. S., Correlation between dissolution behavior and electrochemical cycling performance for $LiNi_{1/3}Co_{1/3}Mn_{1/3}O_2$-based cells. *Journal of Power Sources* **2012,** 207, 134-140.
15. You, Y.; Xin, S.; Asl, H. Y.; Li, W.; Wang, P.-F.; Guo, Y.-G.; Manthiram, A., Insights into the Improved High-Voltage Performance of Li-Incorporated Layered Oxide Cathodes for Sodium-Ion Batteries. *Chem* **2018,** 4, (9), 2124-2139.
16. You, Y.; Manthiram, A., Progress in High-Voltage Cathode Materials for Rechargeable Sodium-Ion Batteries. *Advanced Energy Materials* **2018,** 8, (2).
17. Jung, R.; Metzger, M.; Maglia, F.; Stinner, C.; Gasteiger, H. A., Chemical versus Electrochemical Electrolyte Oxidation on NMC111, NMC622, NMC811, LNMO, and Conductive Carbon. *J Phys Chem Lett* **2017,** 8, (19), 4820-4825.
18. Zhang, H.; Liu, H.; Piper, L. F. J.; Whittingham, M. S.; Zhou, G., Oxygen Loss in Layered Oxide Cathodes for Li-Ion Batteries: Mechanisms, Effects, and Mitigation. *Chem Rev* **2022,** 122, (6), 5641-5681.

19. Guo, S.; Li, Q.; Liu, P.; Chen, M.; Zhou, H., Environmentally stable interface of layered oxide cathodes for sodium-ion batteries. *Nature Communications* **2017,** 8, (1).
20. Mu, L.; Feng, X.; Kou, R.; Zhang, Y.; Guo, H.; Tian, C.; Sun, C.-J.; Du, X.-W.; Nordlund, D.; Xin, H. L.; Lin, F., Deciphering the Cathode-Electrolyte Interfacial Chemistry in Sodium Layered Cathode Materials. *Advanced Energy Materials* **2018,** 8, (34).
21. Song, X.; Meng, T.; Deng, Y.; Gao, A.; Nan, J.; Shu, D.; Yi, F., The effects of the functional electrolyte additive on the cathode material $Na_{0.76}Ni_{0.3}Fe_{0.4}Mn_{0.3}O_2$ for sodium-ion batteries. *Electrochimica Acta* **2018,** 281, 370-377.
22. Wu, X.; Xu, G. L.; Zhong, G.; Gong, Z.; McDonald, M. J.; Zheng, S.; Fu, R.; Chen, Z.; Amine, K.; Yang, Y., Insights into the Effects of Zinc Doping on Structural Phase Transition of P2-Type Sodium Nickel Manganese Oxide Cathodes for High-Energy Sodium Ion Batteries. *ACS Appl Mater Interfaces* **2016,** 8, (34), 22227-37.
23. Chen, T.; Guo, J.; Zhuo, Y.; Hu, H.; Liu, W.; Liu, F.; Liu, P.; Yan, J.; Liu, K., An inactive metal supported oxide cathode material with high rate capability for sodium ion batteries. *Energy Storage Materials* **2019,** 20, 263-268.
24. Deng, J.; Luo, W.-B.; Lu, X.; Yao, Q.; Wang, Z.; Liu, H.-K.; Zhou, H.; Dou, S.-X., High Energy Density Sodium-Ion Battery with Industrially Feasible and Air-Stable O3-Type Layered Oxide Cathode. *Advanced Energy Materials* **2018,** 8, (5).
25. Rahman, M. M.; Xu, Y.; Cheng, H.; Shi, Q.; Kou, R.; Mu, L.; Liu, Q.; Xia, S.; Xiao, X.; Sun, C.-J.; Sokaras, D.; Nordlund, D.; Zheng, J.-C.; Liu, Y.; Lin, F., Empowering multicomponent cathode materials for sodium ion batteries by exploring three-dimensional compositional heterogeneities. *Energy & Environmental Science* **2018,** 11, (9), 2496-2508.
26. Wang, Q.; Mariyappan, S.; Vergnet, J.; Abakumov, A. M.; Rousse, G.; Rabuel, F.; Chakir, M.; Tarascon, J. M., Reaching the Energy Density Limit of Layered O3- $NaNi_{0.5}Mn_{0.5}O_2$ Electrodes via Dual Cu and Ti Substitution. *Advanced Energy Materials* **2019,** 9, (36).
27. Zhang, C.; Gao, R.; Zheng, L.; Hao, Y.; Liu, X., New Insights into the Roles of Mg in Improving the Rate Capability and Cycling Stability of O3-$NaMn_{0.48}Ni_{0.2}Fe_{0.3}Mg_{0.02}O_2$ for Sodium-Ion Batteries. *ACS Appl Mater Interfaces* **2018,** 10, (13), 10819-10827.
28. Yao, H.-R.; Wang, P.-F.; Wang, Y.; Yu, X.; Yin, Y.-X.; Guo, Y.-G., Excellent Comprehensive Performance of Na-Based Layered Oxide Benefiting from the Synergetic Contributions of Multimetal Ions. *Advanced Energy Materials* **2017,** 7, (15).
29. Sun, X.; Jin, Y.; Zhang, C.-Y.; Wen, J.-W.; Shao, Y.; Zang, Y.; Chen, C.-H., $Na[Ni_{0.4}Fe_{0.2}Mn_{0.4-x}Ti_x]O_2$: a cathode of high capacity and superior cyclability for Na-ion batteries. *J. Mater. Chem. A* **2014,** 2, (41), 17268-17271.
30. Yu, T.-Y.; Hwang, J.-Y.; Bae, I. T.; Jung, H.-G.; Sun, Y.-K., High-performance Ti-doped O3-type $Na[Ti_x(Ni_{0.6}Co_{0.2}Mn_{0.2})_{1-x}]O_2$ cathodes for practical sodium-ion batteries. *Journal of Power Sources* **2019,** 422, 1-8.
31. Hwang, T.; Lee, J. H.; Choi, S. H.; Oh, R. G.; Kim, D.; Cho, M.; Cho, W.; Park, M. S., Critical Role of Titanium in O3-Type Layered Cathode Materials for Sodium-Ion Batteries. *ACS Appl Mater Interfaces* **2019,** 11, (34), 30894-30901.
32. Leng, M.; Bi, J.; Wang, W.; Xing, Z.; Yan, W.; Gao, X.; Wang, J.; Liu, R., Superior electrochemical performance of O3-type $NaN_{i0.5-x}Mn_{0.3}Ti_{0.2}Zr_xO_2$ cathode material for sodium-ion batteries from Ti and Zr substitution of the transition metals. *Journal of Alloys and Compounds* **2020,** 816.
33. Zhao, Y.; Xia, M.; Hu, X.; Zhao, Z.; Wang, Y.; Lv, Z., Effects of Sn doping on the structural and electrochemical properties of $Li_{1.2}Ni_{0.2}Mn_{0.8}O_2$ Li-rich cathode materials. *Electrochimica Acta* **2015,** 174, 1167-1174.
34. Wang, P. F.; Xin, H.; Zuo, T. T.; Li, Q.; Yang, X.; Yin, Y. X.; Gao, X.; Yu, X.; Guo, Y. G., An Abnormal 3.7 Volt O3-Type Sodium-Ion Battery Cathode. *Angew Chem Int Ed Engl* **2018,** 57, (27), 8178-8183.

35. Sathiya, M.; Jacquet, Q.; Doublet, M.-L.; Karakulina, O. M.; Hadermann, J.; Tarascon, J.-M., A Chemical Approach to Raise Cell Voltage and Suppress Phase Transition in O3 Sodium Layered Oxide Electrodes. *Advanced Energy Materials* **2018,** 8, (11).
36. Rong, X.; Qi, X.; Lu, Y.; Wang, Y.; Li, Y.; Jiang, L.; Yang, K.; Gao, F.; Huang, X.; Chen, L.; Hu, Y.-S., A new Tin-based O3-$Na_{0.9}[Ni_{0.45-x/2}Mn_xSn_{0.55-x/2}]O_2$ as sodium-ion battery cathode. *Journal of Energy Chemistry* **2019,** 31, 132-137.
37. Rong, X.; Gao, F.; Ding, F.; Lu, Y.; Yang, K.; Li, H.; Huang, X.; Chen, L.; Hu, Y.-S., Triple effects of Sn-substitution on $Na_{0.67}Ni_{0.33}Mn_{0.67}O_2$. *Journal of Materials Science & Technology* **2019,** 35, (7), 1250-1254.
38. Li, J.; Risthaus, T.; Wang, J.; Zhou, D.; He, X.; Ehteshami, N.; Murzin, V.; Friesen, A.; Liu, H.; Hou, X.; Diehl, M.; Paillard, E.; Winter, M.; Li, J., The effect of Sn substitution on the structure and oxygen activity of $Na_{0.67}Ni_{0.33}Mn_{0.67}O_2$ cathode materials for sodium ion batteries. *Journal of Power Sources* **2020,** 449.
39. Tripathi, A.; Rudola, A.; Gajjela, S. R.; Xi, S.; Balaya, P., Developing an O3 type layered oxide cathode and its application in 18650 commercial type Na-ion batteries. *Journal of Materials Chemistry A* **2019,** 7, (45), 25944-25960.
40. Mao, Q.; Zhang, C.; Yang, W.; Yang, J.; Sun, L.; Hao, Y.; Liu, X., Mitigating the voltage fading and lattice cell variations of O3-$NaNi_{0.2}Fe_{0.35}Mn_{0.45}O_2$ for high performance Na-ion battery cathode by Zn doping. *Journal of Alloys and Compounds* **2019,** 794, 509-517.
41. Sun, L.; Xie, Y.; Liao, X. Z.; Wang, H.; Tan, G.; Chen, Z.; Ren, Y.; Gim, J.; Tang, W.; He, Y. S.; Amine, K.; Ma, Z. F., Insight into Ca-Substitution Effects on O3-Type $NaNi_{1/3}$ $Fe_{1/3}$ $Mn_{1/3}$ O_2 Cathode Materials for Sodium-Ion Batteries Application. *Small* **2018,** 14, (21), e1704523.
42. Zhang, K.; Kim, D.; Hu, Z.; Park, M.; Noh, G.; Yang, Y.; Zhang, J.; Lau, V. W.; Chou, S. L.; Cho, M.; Choi, S. Y.; Kang, Y. M., Manganese based layered oxides with modulated electronic and thermodynamic properties for sodium ion batteries. *Nat Commun* **2019,** 10, (1), 5203.
43. Wang, K.; Wan, H.; Yan, P.; Chen, X.; Fu, J.; Liu, Z.; Deng, H.; Gao, F.; Sui, M., Dopant Segregation Boosting High-Voltage Cyclability of Layered Cathode for Sodium Ion Batteries. *Adv Mater* **2019,** 31, (46), e1904816.
44. Chen, T. R.; Sheng, T.; Wu, Z. G.; Li, J. T.; Wang, E. H.; Wu, C. J.; Li, H. T.; Guo, X. D.; Zhong, B. H.; Huang, L.; Sun, S. G., Cu^{2+} Dual-Doped Layer-Tunnel Hybrid $Na_{0.6}Mn_{1-x}Cu_xO_2$ as a Cathode of Sodium-Ion Battery with Enhanced Structure Stability, Electrochemical Property, and Air Stability. *ACS Appl Mater Interfaces* **2018,** 10, (12), 10147-10156.
45. Xu, B.; Fell, C. R.; Chi, M.; Meng, Y. S., Identifying surface structural changes in layered Li-excess nickel manganese oxides in high voltage lithium ion batteries: A joint experimental and theoretical study. *Energy & Environmental Science* **2011,** 4, (6).
46. Kim, D.; Kang, S.-H.; Slater, M.; Rood, S.; Vaughey, J. T.; Karan, N.; Balasubramanian, M.; Johnson, C. S., Enabling Sodium Batteries Using Lithium-Substituted Sodium Layered Transition Metal Oxide Cathodes. *Advanced Energy Materials* **2011,** 1, (3), 333-336.
47. Xu, J.; Liu, H.; Meng, Y. S., Exploring Li substituted O3-structured layered oxides $NaLi_xNi_{1/3-x}Mn_{1/3+x}Co_{1/3-x}O_2$ (x = 0.07, 0.13, and 0.2) as promising cathode materials for rechargeable Na batteries. *Electrochemistry Communications* **2015,** 60, 13-16.
48. Chen, Z.; Dahn, J. R., Studies of $LiCoO_2$ Coated with Metal Oxides. *Electrochemical and Solid-State Letters* **2003,** 6, (11).
49. Zhou, Y.; Lee, Y.; Sun, H.; Wallas, J. M.; George, S. M.; Xie, M., Coating Solution for High-Voltage Cathode: AlF_3 Atomic Layer Deposition for Freestanding $LiCoO_2$ Electrodes with High Energy Density and Excellent Flexibility. *ACS Appl Mater Interfaces* **2017,** 9, (11), 9614-9619.
50. Zhang, H.; Song, T., Synthesis and performance of fluorine substituted $Li_{1.05}(Ni_{0.5}Mn_{0.5})_{0.95}O_{2-x}F_x$ cathode materials modified by surface coating with $FePO_4$. *Electrochimica Acta* **2013,** 114, 116-124.

51. Bian, X.; Fu, Q.; Bie, X.; Yang, P.; Qiu, H.; Pang, Q.; Chen, G.; Du, F.; Wei, Y., Improved Electrochemical Performance and Thermal Stability of Li-excess $Li_{1.18}Co_{0.15}Ni_{0.15}Mn_{0.52}O_2$ Cathode Material by Li_3PO_4 Surface Coating. *Electrochimica Acta* **2015,** 174, 875-884.
52. Li, C.; Zhang, H. P.; Fu, L. J.; Liu, H.; Wu, Y. P.; Rahm, E.; Holze, R.; Wu, H. Q., Cathode materials modified by surface coating for lithium ion batteries. *Electrochimica Acta* **2006,** 51, (19), 3872-3883.
53. Lee, Y.; Mun, J.; Kim, D.-W.; Lee, J. K.; Choi, W., Surface modification of $LiNi_{0.5}Mn_{1.5}O_4$ cathodes with $ZnAl_2O_4$ by a sol–gel method for lithium ion batteries. *Electrochimica Acta* **2014,** 115, 326-331.
54. Lu, J.; Peng, Q.; Wang, W.; Nan, C.; Li, L.; Li, Y., Nanoscale coating of $LiMO_2$ (M = Ni, Co, Mn) nanobelts with Li^+-conductive Li_2TiO_3: toward better rate capabilities for Li-ion batteries. *J Am Chem Soc* **2013,** 135, (5), 1649-52.
55. Cheng, H.-M.; Wang, F.-M.; Chu, J. P.; Santhanam, R.; Rick, J.; Lo, S.-C., Enhanced Cycleabity in Lithium Ion Batteries: Resulting from Atomic Layer Depostion of Al_2O_3 or TiO_2 on $LiCoO_2$ Electrodes. *The Journal of Physical Chemistry C* **2012,** 116, (14), 7629-7637.
56. Zhao, J.; Wang, Y., Ultrathin Surface Coatings for Improved Electrochemical Performance of Lithium Ion Battery Electrodes at Elevated Temperature. *The Journal of Physical Chemistry C* **2012,** 116, (22), 11867-11876.
57. Xie, J.; Sendek, A. D.; Cubuk, E. D.; Zhang, X.; Lu, Z.; Gong, Y.; Wu, T.; Shi, F.; Liu, W.; Reed, E. J.; Cui, Y., Atomic Layer Deposition of Stable LiAlF4 Lithium Ion Conductive Interfacial Layer for Stable Cathode Cycling. *ACS Nano* **2017,** 11, (7), 7019-7027.
58. Ledwoch, D.; Robinson, J. B.; Gastol, D.; Smith, K.; Shearing, P. R.; Brett, D. J. L.; Kendrick, E., Hard Carbon Composite Electrodes for Sodium‐Ion Batteries with Nano‐Zeolite and Carbon Black Additives. *Batteries & Supercaps* **2020**.
59. Hwang, J.-Y.; Myung, S.-T.; Choi, J. U.; Yoon, C. S.; Yashiro, H.; Sun, Y.-K., Resolving the degradation pathways of the O3-type layered oxide cathode surface through the nano-scale aluminum oxide coating for high-energy density sodium-ion batteries. *Journal of Materials Chemistry A* **2017,** 5, (45), 23671-23680.
60. Liu, Y.; Fang, X.; Zhang, A.; Shen, C.; Liu, Q.; Enaya, H. A.; Zhou, C., Layered P2-$Na_{2/3}[Ni_{1/3}Mn_{2/3}]O_2$ as high-voltage cathode for sodium-ion batteries: The capacity decay mechanism and Al_2O_3 surface modification. *Nano Energy* **2016,** 27, 27-34.
61. Chen, Z.; Qin, Y.; Amine, K.; Sun, Y. K., Role of surface coating on cathode materials for lithium-ion batteries. *Journal of Materials Chemistry* **2010,** 20, (36).
62. Li, N.; Ren, J.; Dang, R.; Wu, K.; Lee, Y. L.; Hu, Z.; Xiao, X., Suppressing phase transition and improving electrochemical performances of O3-$NaNi_{1/3}Mn_{1/3}Fe_{1/3}O_2$ through ionic conductive Na_2SiO_3 coating. *Journal of Power Sources* **2019,** 429, 38-45.
63. Dang, R.; Chen, M.; Li, Q.; Wu, K.; Lee, Y. L.; Hu, Z.; Xiao, X., Na^+-Conductive $Na_2Ti_3O_7$-Modified P2-type $Na_{2/3}Ni_{1/3}Mn_{2/3}O_2$ via a Smart in Situ Coating Approach: Suppressing Na^+/Vacancy Ordering and P2-O2 Phase Transition. *ACS Appl Mater Interfaces* **2019,** 11, (1), 856-864.
64. Jo, J. H.; Choi, J. U.; Konarov, A.; Yashiro, H.; Yuan, S.; Shi, L.; Sun, Y.-K.; Myung, S.-T., Sodium-Ion Batteries: Building Effective Layered Cathode Materials with Long-Term Cycling by Modifying the Surface via Sodium Phosphate. *Advanced Functional Materials* **2018,** 28, (14).
65. Jo, C.-H.; Jo, J.-H.; Yashiro, H.; Kim, S.-J.; Sun, Y.-K.; Myung, S.-T., Bioinspired Surface Layer for the Cathode Material of High-Energy-Density Sodium-Ion Batteries. *Advanced Energy Materials* **2018,** 8, (13).
66. Hwang, J.-Y.; Yu, T.-Y.; Sun, Y.-K., Simultaneous MgO coating and Mg doping of $Na[Ni_{0.5}Mn_{0.5}]O_2$ cathode: facile and customizable approach to high-voltage sodium-ion batteries. *Journal of Materials Chemistry A* **2018,** 6, (35), 16854-16862.
67. Dang, R.; Li, Q.; Chen, M.; Hu, Z.; Xiao, X., CuO-Coated and Cu^{2+}-doped Co-modified P2-type $Na_{2/3}[Ni_{1/3}Mn_{2/3}]O_2$ for sodium-ion batteries. *Physical Chemistry Chemical Physics* **2019,** 21, (1), 314-321.

68. Tang, K.; Huang, Y.; Xie, X.; Cao, S.; Liu, L.; Liu, M.; Huang, Y.; Chang, B.; Luo, Z.; Wang, X., The effects of dual modification on structure and performance of P2-type layered oxide cathode for sodium-ion batteries. *Chemical Engineering Journal* **2020,** 384.
69. Lee, E.; Lu, J.; Ren, Y.; Luo, X.; Zhang, X.; Wen, J.; Miller, D.; DeWahl, A.; Hackney, S.; Key, B.; Kim, D.; Slater, M. D.; Johnson, C. S., Layered P2/O3 Intergrowth Cathode: Toward High Power Na-Ion Batteries. *Advanced Energy Materials* **2014,** 4, (17).
70. Chen, C.; Han, Z.; Chen, S.; Qi, S.; Lan, X.; Zhang, C.; Chen, L.; Wang, P.; Wei, W., Core-Shell Layered Oxide Cathode for High-Performance Sodium-Ion Batteries. *ACS Appl Mater Interfaces* **2020,** 12, (6), 7144-7152.
71. Hwang, J. Y.; Oh, S. M.; Myung, S. T.; Chung, K. Y.; Belharouak, I.; Sun, Y. K., Radially aligned hierarchical columnar structure as a cathode material for high energy density sodium-ion batteries. *Nat Commun* **2015,** 6, 6865.
72. Guo, S.; Liu, P.; Yu, H.; Zhu, Y.; Chen, M.; Ishida, M.; Zhou, H., A layered P2- and O3-type composite as a high-energy cathode for rechargeable sodium-ion batteries. *Angew Chem Int Ed Engl* **2015,** 54, (20), 5894-9.
73. Li, Z.-Y.; Zhang, J.; Gao, R.; Zhang, H.; Zheng, L.; Hu, Z.; Liu, X., Li-Substituted Co-Free Layered P2/O3 Biphasic Na0.67Mn0.55Ni0.25Ti0.2–xLixO2 as High-Rate-Capability Cathode Materials for Sodium Ion Batteries. *The Journal of Physical Chemistry C* **2016,** 120, (17), 9007-9016.
74. Zhou, D.; Huang, W.; Lv, X.; Zhao, F., A novel P2/O3 biphase $Na_{0.67}Fe_{0.425}Mn_{0.425}Mg_{0.15}O_2$ as cathode for high-performance sodium-ion batteries. *Journal of Power Sources* **2019,** 421, 147-155.
75. Qi, X.; Liu, L.; Song, N.; Gao, F.; Yang, K.; Lu, Y.; Yang, H.; Hu, Y. S.; Cheng, Z. H.; Chen, L., Design and Comparative Study of O3/P2 Hybrid Structures for Room Temperature Sodium-Ion Batteries. *ACS Appl Mater Interfaces* **2017,** 9, (46), 40215-40223.
76. Zhou, Y.-N.; Wang, P.-F.; Niu, Y.-B.; Li, Q.; Yu, X.; Yin, Y.-X.; Xu, S.; Guo, Y.-G., A P2/P3 composite layered cathode for high-performance Na-ion full batteries. *Nano Energy* **2019,** 55, 143-150.
77. Yan, Z.; Tang, L.; Huang, Y.; Hua, W.; Wang, Y.; Liu, R.; Gu, Q.; Indris, S.; Chou, S. L.; Huang, Y.; Wu, M.; Dou, S. X., A Hydrostable Cathode Material Based on the Layered P2@P3 Composite that Shows Redox Behavior for Copper in High-Rate and Long-Cycling Sodium-Ion Batteries. *Angew Chem Int Ed Engl* **2019,** 58, (5), 1412-1416.
78. Chen, X.; Zhou, X.; Hu, M.; Liang, J.; Wu, D.; Wei, J.; Zhou, Z., Stable layered P3/P2 $Na_{0.66}Co_{0.5}Mn_{0.5}O_2$ cathode materials for sodium-ion batteries. *Journal of Materials Chemistry A* **2015,** 3, (41), 20708-20714.
79. Shi, W.-J.; Yan, Y.-W.; Chi, C.; Ma, X.-T.; Zhang, D.; Xu, S.-D.; Chen, L.; Wang, X.-M.; Liu, S.-B., Fluorine anion doped $Na_{0.44}MnO_2$ with layer-tunnel hybrid structure as advanced cathode for sodium ion batteries. *Journal of Power Sources* **2019,** 427, 129-137.
80. Keller, M.; Buchholz, D.; Passerini, S., Layered Na-Ion Cathodes with Outstanding Performance Resulting from the Synergetic Effect of Mixed P- and O-Type Phases. *Adv Energy Mater* **2016,** 6, (3), 1501555.
81. Xu, G.-L.; Amine, R.; Xu, Y.-F.; Liu, J.; Gim, J.; Ma, T.; Ren, Y.; Sun, C.-J.; Liu, Y.; Zhang, X.; Heald, S. M.; Solhy, A.; Saadoune, I.; Mattis, W. L.; Sun, S.-G.; Chen, Z.; Amine, K., Insights into the structural effects of layered cathode materials for high voltage sodium-ion batteries. *Energy & Environmental Science* **2017,** 10, (7), 1677-1693.
82. Chagas, L. G.; Buchholz, D.; Vaalma, C.; Wu, L.; Passerini, S., P-type $NaxNi_{0.22}Co_{0.11}Mn_{0.66}O_2$materials: linking synthesis with structure and electrochemical performance. *J. Mater. Chem. A* **2014,** 2, (47), 20263-20270.
83. Ju, J.-H.; Ryu, K.-S., Synthesis and electrochemical performance of $Li(Ni_{0.8}Co_{0.15}Al_{0.05})_{0.8}(Ni_{0.5}Mn_{0.5})_{0.2}O_2$ with core–shell structure as cathode material for Li-ion batteries. *Journal of Alloys and Compounds* **2011,** 509, (30), 7985-7992.

84. Jun, D.-W.; Yoon, C. S.; Kim, U.-H.; Sun, Y.-K., High-Energy Density Core–Shell Structured $Li[Ni_{0.95}Co_{0.025}Mn_{0.025}]O_2$ Cathode for Lithium-Ion Batteries. *Chemistry of Materials* **2017,** 29, (12), 5048-5052.
85. Liang, L.; Jiang, J.; Jiang, F.; Hu, G.; Cao, Y.; Peng, Z.; Du, K., An ordered olivine-type $LiCoPO_4$ layer grown on $LiNi_{0.6}Mn_{0.2}Co_{0.2}O_2$ cathode materials applied to lithium-ion batteries. *Journal of Alloys and Compounds* **2017,** 695, 1993-1997.
86. Su, L.; Jing, Y.; Zhou, Z., Li ion battery materials with core-shell nanostructures. *Nanoscale* **2011,** 3, (10), 3967-83.
87. Duan, W.; Zhu, Z.; Li, H.; Hu, Z.; Zhang, K.; Cheng, F.; Chen, J., $Na_3V_2(PO_4)_3$@C core–shell nanocomposites for rechargeable sodium-ion batteries. *J. Mater. Chem. A* **2014,** 2, (23), 8668-8675.
88. Yan, H.; Fu, Y.; Wu, X.; Xue, X.; Li, C.; Zhang, L., Core-shell structured $NaTi_{2(}PO_4)_3$@polyaniline as an efficient electrode material for electrochemical energy storage. *Solid State Ionics* **2019,** 336, 95-101.
89. Huang, Y.; Xie, M.; Wang, Z.; Jiang, Y.; Yao, Y.; Li, S.; Li, Z.; Li, L.; Wu, F.; Chen, R., A Chemical Precipitation Method Preparing Hollow-Core-Shell Heterostructures Based on the Prussian Blue Analogs as Cathode for Sodium-Ion Batteries. *Small* **2018,** 14, (28), e1801246.
90. Okubo, M.; Li, C. H.; Talham, D. R., High rate sodium ion insertion into core-shell nanoparticles of Prussian blue analogues. *Chem Commun (Camb)* **2014,** 50, (11), 1353-5.
91. Wan, M.; Tang, Y.; Wang, L.; Xiang, X.; Li, X.; Chen, K.; Xue, L.; Zhang, W.; Huang, Y., Core-shell hexacyanoferrate for superior Na-ion batteries. *Journal of Power Sources* **2016,** 329, 290-296.
92. Zhang, Q.; Fu, L.; Luan, J.; Huang, X.; Tang, Y.; Xie, H.; Wang, H., Surface engineering induced core-shell Prussian blue@polyaniline nanocubes as a high-rate and long-life sodium-ion battery cathode. *Journal of Power Sources* **2018,** 395, 305-313.
93. Sun, Y.-K.; Chen, Z.; Noh, H.-J.; Lee, D.-J.; Jung, H.-G.; Ren, Y.; Wang, S.; Yoon, C. S.; Myung, S.-T.; Amine, K., Nanostructured high-energy cathode materials for advanced lithium batteries. *Nature Materials* **2012,** 11, (11), 942-947.
94. M.P.Harmer, J. C. C. M. W. H. M. C. J. M. R., Role of segregating dopants on the improved creep resistance of aluminum oxide. *Acta Materialia* **1999,** 47, (15), 4197-4207.
95. Fromhold, T. M.; Patane, A.; Bujkiewicz, S.; Wilkinson, P. B.; Fowler, D.; Sherwood, D.; Stapleton, S. P.; Krokhin, A. A.; Eaves, L.; Henini, M.; Sankeshwar, N. S.; Sheard, F. W., Chaotic electron diffusion through stochastic webs enhances current flow in superlattices. *Nature* **2004,** 428, (6984), 726-30.
96. J. P. Buban, K. Matsunaga, J. Chen, N. Shibata, W. Y. Ching, T. Yamamoto., Grain Boundary Strengthening in Alumina by Rare Earth Impurities. *Science* **2006,** 311, 212-215.
97. Luo J, Cheng H, Asl K M, Kiely C J and Harmer M P., The Role of a Bilayer Interfacial Phase on Liquid Metal Embrittlement. *Science* **2011,** 333, 1730-1733.
98. Yan, P.; Zheng, J.; Liu, J.; Wang, B.; Cheng, X.; Zhang, Y.; Sun, X.; Wang, C.; Zhang, J.-G., Tailoring grain boundary structures and chemistry of Ni-rich layered cathodes for enhanced cycle stability of lithium-ion batteries. *Nature Energy* **2018,** 3, (7), 600-605.
99. Li, H.; Li, J.; Ma, X.; Dahn, J. R., Synthesis of Single Crystal $LiNi_{0.6}Mn_{0.2}Co_{0.2}O_2$ with Enhanced Electrochemical Performance for Lithium Ion Batteries. *Journal of The Electrochemical Society* **2018,** 165, (5), A1038-A1045.
100. Su, D.; Wang, C.; Ahn, H. J.; Wang, G., Single crystalline $Na_{0.7}MnO_2$ nanoplates as cathode materials for sodium-ion batteries with enhanced performance. *Chemistry* **2013,** 19, (33), 10884-9.
101. Tepavcevic, S.; Zheng, H.; Hinks, D. G.; Key, B.; Ward, L.; Lu, Z.; Stoumpos, C.; Ren, Y.; Freeland, J. W.; Wolverton, C.; Phillips, P.; Klie, R.; Mitchell, J. F.; Markovic, N. M., Fundamental Insights from a Single‐Crystal Sodium Iridate Battery. *Advanced Energy Materials* **2020,** 10, (10).

Chapter 3 Experimental and characterisation techniques

This chapter focuses on the techniques used in synthesizing and characterizing the synthesized materials.

3.1 Experimental techniques

3.1.1 Co-precipitation synthesis

Materials developed in this work were synthesized by the co-precipitation method. This is one method widely used in industry for the synthesis of ternary or multi-component layered cathode materials for both lithium and sodium-ion batteries. This method possesses the advantages of good mixing of multi-ionic components, ease of scalability and reproducibility, as well as controllable particle size and morphology[1-5].

The synthesis process is based on the chemical reaction of a mixed metal salt solution with a precipitating agent and chelating agent, which involves the formation, growth, and maturation of crystals as well as agglomeration and fragmentation of particles in the reactor. In a typical synthesis, the mixed metal salts (Ni^{2+}, Co^{2+}, Mn^{2+}, Fe^{2+}, Cu^{2+}…) are stoichiometrically weighed and dissolved in deionized water to form solution A. Solution B is prepared by dissolving an alkali compound, typically NaOH or Na_2CO_3 as a precipitant. The precipitation equilibrium constant ($K_{sp,\ M(OH)n}$) of metals are different, for example, $K_{sp,\ Ni(OH)_2}= 2.0*10^{-15}$, $Co(OH)_2= 1.58*10^{-15}$, $Mn(OH)_2= 2.06*10^{-13}$, resulting in the precipitation of descrete single phases in order if directly precipitated with NaOH, instead of the desired ternary phase[6]. To minimize the formation of impurities from undesirable reactions, chelating agent, e.g. NH_4OH (solution C) is used. These three solutions are then pumped into a reactor at the same time under continuous stirring to ensure homogeneity. The formation of hydroxide precursors involves nucleation of single crystal, crystal growth, and particle agglomeration. One of the well-known reaction paths for the formation of hydroxide precursors is the two-step complexation-precipitation process[7-9], as expressed as:

$$TM^{2+}_{aq}+nNH_3{\cdot}H_2O_{aq}\rightarrow[TM(NH_3)_n]^{2+}_{aq}+nH_2O \qquad (3\text{-}1)$$

$$[TM(NH_3)_n]^{2+}_{aq}+2OH^-_{aq}+nH_2O\rightarrow TM(OH)_{2(S)}+nNH_3{\cdot}H_2O_{aq} \qquad (3\text{-}2)$$

where TM stands for mixed transition metals. Firstly, metal ions will chelate with NH_4^+ to form complex $[TM(NH_3)_n]^{2+}$, which will reduce the concentration of free TM^{2+} in the mixed solution and further decrease the nucleation rate of $TM(OH)_2$. Secondly, metal ions in the formed complex will be slowly released into the mixed solution and react with OH^- to form a $TM(OH)_2$ sediment. This slow cheating, release, and then precipitation process is beneficial for preparing particles with pure phase and uniform size distribution.

Another proposed mechanism in the presence of ammonia involves a dissolution-recrystallization process as shown in the equilibrium below[10, 11]:

$$TM(OH)_{2(S)} + nNH_3 \cdot H_2O_{aq} \rightleftharpoons [TM(NH_3)_n]^{2+}_{aq} + 2OH^- \quad (3\text{-}3)$$

In this mechanism, the formation and growth of hydroxides are based on the dynamic equilibrium between the solid metal hydroxide and aqueous metal ammonia complex.

Regardless of which mechanism it is based on, the synthesis conditions, such as pH, temperature, stirring speed, as well as feeding rate should be well controlled during the whole process to obtain the particles with desired physical properties[9, 11-13]. Also, N_2 gas is usually required in the presence of Mn^{2+} to prevent the oxidation of Mn^{2+} ($Mn(OH)_2$) to Mn^{3+} (MnOOH) or Mn^{4+} (MnO_2)[14].

After vigorous stirring for 24 h, the precipitate hydroxide precursor $[Ni_{1/3}Fe_{1/3}Mn_{1/3}](OH)_2$ was filtered and rinsed thoroughly with deionized water to remove the residual acidic and base ions (Me^{2+}, SO_4^{2-}, Na^+, OH^- and NH_4^+) until the pH value of filtrate close to 7, followed by vacuum drying at 120 °C overnight.

The obtained precursor was mixed with a stoichiometric ratio Na_2CO_3 (99.9%, Sigma-Aldrich Co.) powder (TM/Na=1:1.05) and ball milled at 250 rpm for 30 min. Here, 5% excess Na was used to compensate for the losses in Na through evaporation during calcination. The calcination procedure is as follows: the mixture was heated to 550 °C from room temperature at a heating rate of 5 °C min^{-1} and held for 2 h, followed by increasing the temperature to 900 °C with a ramp rate of 2 °C min^{-1} and held for 9 h in air, and then slowly cooled (1 °C min^{-1}) to 150 °C[15], as illustrated in Figure 3.1. The annealed materials were transferred to glovebox filled with argon to keep the sample moisture-free. Samples were sieved with a 100-mesh sieve before use.

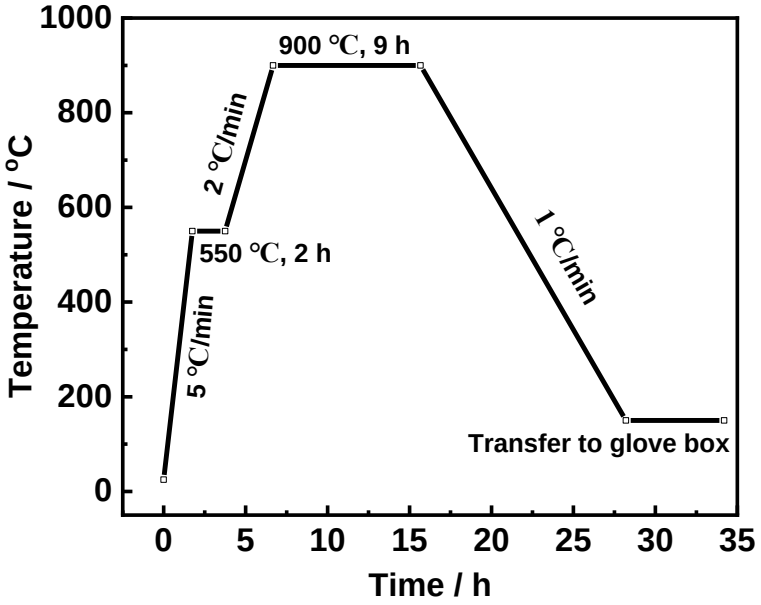


Figure 3.1 Diagrams of the sample calcination procedure.

3.1.2 Electrode preparation

Cathode: The cathodes were prepared by mixing the synthesized active material from last step (3.1.1) with carbon black (C65, TimCal), multiwalled carbon nanotubes (MWCNT), oxalic acid additive, and polyvinylidene fluoride (PVDF 5130, Solvay) binder in a mass ratio of 87.0: 5.8: 0.2: 1.0: 6.0 in Nmethyl-2-pyrrolidine (NMP) solvent. PVDF was pre-dispersed in NMP to form a solution with 8% solid content. Here, 1% oxalic acid was added based on previous studies to prevent slurry gelation[16]. Mixing was processed in a Thinky ARE-250 planetary mixer with the following protocol:

- 1. Oxalic acid + NMP, 1300rpm/5min
- 2. Add active material + C65, 1300rpm/5min
- 3. Add PVDF solution + CNTs, 1300rpm/5min
- 4. Add more NMP to adjust the slurry solid content, 1300rpm/5min

The well mixed slurry was then applied to the aluminium foil (16 μm thickness) with a Doctor blade (K Paint Applicator, RK Printcoat Instruments, U.K.) at a thickness around 150 um, followed by drying at 120 °C for 24 h in vacuum oven. The dried electrodes were then calendared to the desired thickness, with a porosity of about 35% using a rolling press (MSK-

HRP-01, MTI Corporation, USA). Calendared cathodes were punched into small disks with a diameter of 14.8 mm for coin-cell and 12.0 mm for Swagelok cell, respectively.

Na Anode:

For half coin-cell, Na metal was used as the counter electrode. A sodium metal disk was cut from sodium cubes (Aldrich, 99%) in glove box[15], and then it was rolled to ≈100 um thickness and punched into 15.0 mm discs for coin-cell and 12.0 mm for Swagelok cell, respectively.

Hard Carbon Anode:

For full cell testing, a Hard Carbon (HC) anode is required to accommodate the Na^+ extracted from cathode. A commercially available HC (Kuranode, Kuraray) was used in this work. The anode was prepared by mixing HC material, CMC (Bondwell™), and conductive additive (C45, Timcal) in a mass ratio of 90: 5: 5. CMC was pre-dispersed in deionized water to form a solution with 1.5% solid content. Mixing was processed in a similar manner to the cathode with the following protocol:

- 1. CMC solution + C45, 1500rpm/5min
- 2. Add HC + water, 1500rpm/5min
- 3. Add SBR, 500rpm/5min
- 4. Add more water to adjust the slurry solid content, 500rpm/5min

The coating, and drying process was conducted in a similar manner to the cathode part. As aluminium does not alloy with sodium[17], aluminium foil was also used for the HC anode. The dried anode was pressed to reach a porosity about 25%. 15.0 mm and 12.0 mm discs for coin-cell and Swagelok cell are punched, respectively.

3.1.3 Coin Cell assembly

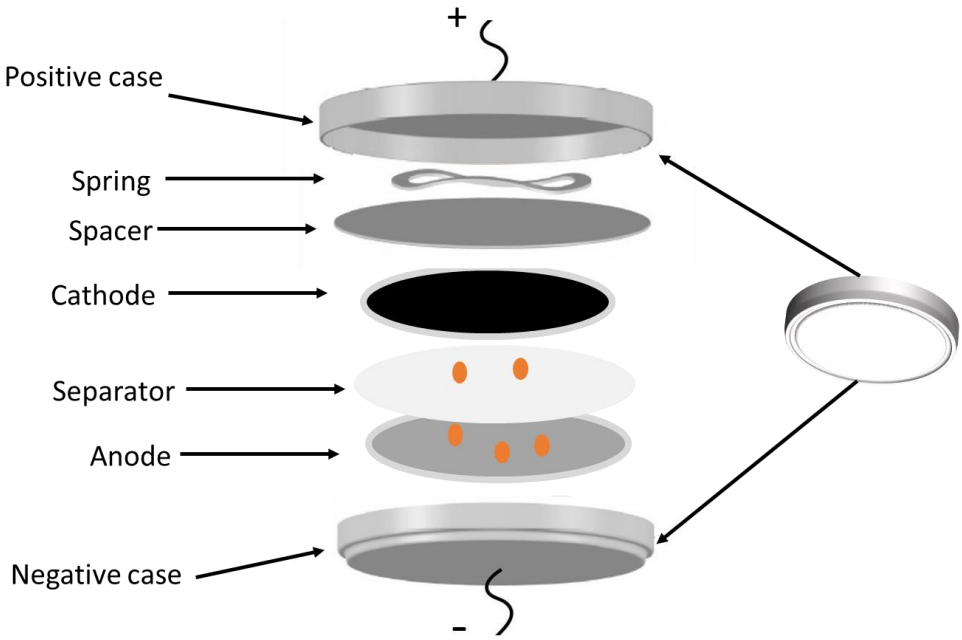


Figure 3.2 Structure diagrams of two-electrode coin cell.

In this work, the electrochemical properties of the synthesized materials, including capacity, cycling stability and kinetics behavior of Na^+ were examined using CR2032 two-electrode coin cell, which was also called 'Half-cell'. This type cell was composed of a positive cell case, a cathode electrode, a 25 μm thick porous polypropylene film (Celgard 2325), a Na metal anode, and a negative cell case from bottom to top, as shown in Figure 3.2. 70 uL 1 M $NaPF_6$ in EC: DEC: FEC (12.6: 47.1: 35: 5.3 wt%) was used as electrolyte. Cells were assembled in an argon-filled glovebox.

3.1.4 Swagelok Cell assembly

Two-electrode type cell has the advantage of easy assembling but has the limitation of not being able to monitor the potential of individual electrodes. In a three-electrode cell, a Na metal reference electrode (RE) is positioned at the edge of the cell, connected to both the working and counter electrode (Figure 3.3), which allows a specific electrode to be studied.

In this work, three-electrode Swagelok cell was used in Chapter 6 to optimize the N/P ratio (area capacity ratio between anode and cathode) of full-cell. By studying the potential behavior

of cathode and anode under different N/P ratios, the effects of cathode and anode on the cycling performance can be detected. Thus, safe and high performance full cell design can be obtained.

Three-electrode Swagelok cell was also used for impedance spectroscopy (EIS) measurements in Chapter 4-6. In conventional two-electrode half-cell, sodium metal acts as both counter electrode (CE) and reference electrode (RE) simultaneously, thus, the recorded impedance will be affected by the anode film resistance[18]. Three-electrode configuration can eliminate the signal of anode part and enable a more reliable EIS analysis.

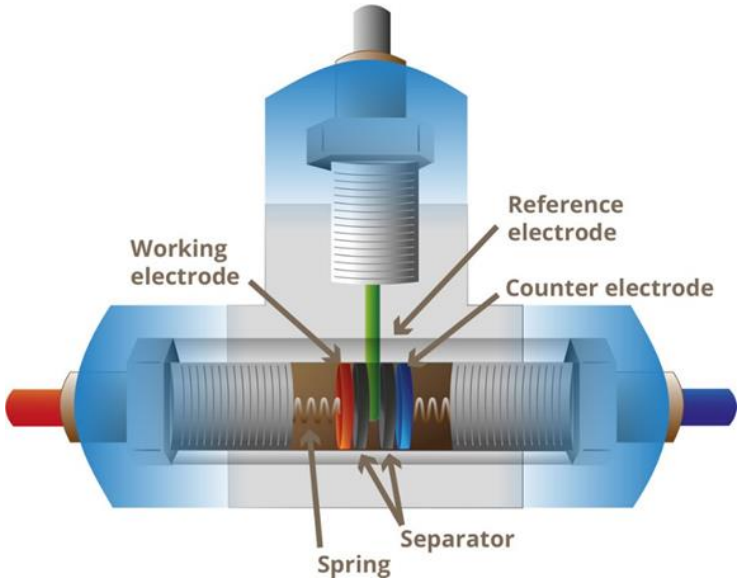


Figure 3.3 Structure diagrams of three-electrode Swagelok cell.

3.2 Characterisation techniques

3.2.1 Physical characterisation

3.2.1.1 Powder X-ray diffraction (XRD)

The structural characteristics of the as-prepared powder materials were examined by X-ray diffraction (XRD, Proto, Cu Kα, radiation, λ= 1.5406A˚). The diffracted data were collected from 10° to 100° in 2θ with a step size of 0.0149°.

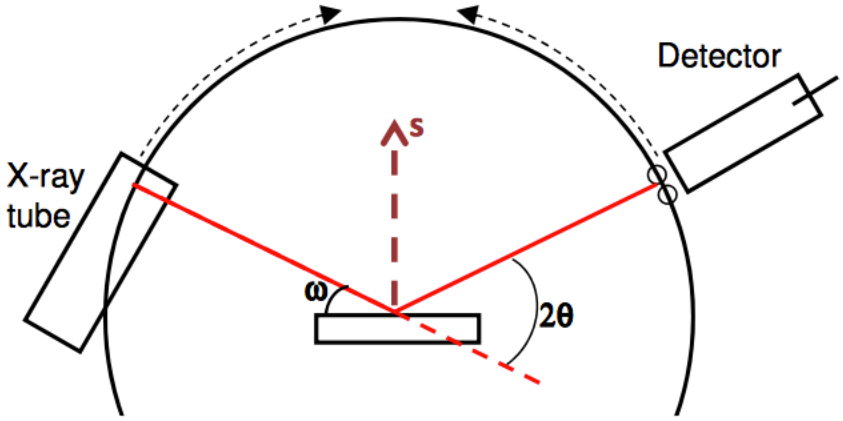


Figure 3.4 Diagram of an X-ray diffractometer

X-ray diffraction is an analytical method that analyzes the internal structure of a crystal by means of the diffraction phenomenon produced by X-rays in the crystal. It can determine the type of atoms in the crystal, the dimensions, and the crystal classes of the unit cells[19-21].

X-rays are essentially electromagnetic waves with a wavelength of 0.01-100Å, which is of the same order of magnitude as the interlayer spacing in crystals. In 1912, Lauer et al. found that when a beam of monochromatic X-rays is incident on a crystal, it will be scattered by atoms in the crystal. Since the atoms are arranged periodically in the crystal, a fixed phase relationship between these scattered waves will cause the waves to strengthen each other in some scattering directions and cancel each other in some directions, resulting in diffraction phenomena. This experiment became a milestone in X-ray diffraction[22].

The arrangement of atoms inside each crystal is unique, so the corresponding diffraction pattern is unique, which is similar to a human fingerprint, so phase analysis can be performed. Among them, the distribution of diffraction lines in the diffraction pattern is determined by the size, shape, and orientation of the unit cell. The intensity of the diffraction lines is determined by the types of atoms and their positions in the unit cell.

A typical X-ray diffractometer includes an X-ray tube (source of radiation), a detector placed on the opposite side of the X-ray tube, and a sample stage, see Figure 3.4. When testing, the X-ray source emits X-ray beams, which are directed at the sample at a specific angle of incidence (θ). The angle is usually controlled by rotating the sample stage or the detector relative to the X-ray source. The X-rays interact with the atoms in the crystal lattice and are subsequently re-emitted. The intensity and angle of the scattered X-rays are then recorded by the detector. The

data recorded are then processed to create an X-ray diffraction pattern of 2θ against observed intensity.

Rietveld refinement was used to calculate the lattice parameters, atom occupancy, phase purity, and particle size (to name but a few). The refinement process is based on a least squares approach, which fits the calculated peak profile to the experimental data[23, 24]. However, the accuracy of the outcome of refinements heavily depends on the quality of initial approximations. Therefore, a reasonable initial structure model is required, including the background, peak positions, peak intensities, atom types, unit cell parameters, and coordinates of atoms in the crystal structure.

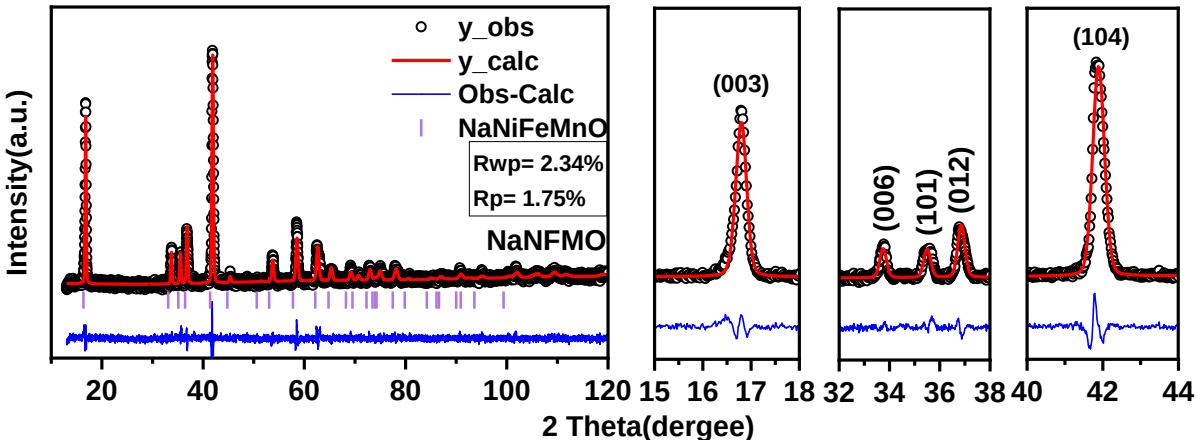


Figure 3.5 A example refinement profile with observed, calculated and difference profile of an O3 type layered material, R_{wp} = 2.34%.

In this work, refinements were conducted using the refinement program GSAS based on the initial structural model of O3 $NaMO_2$ (ICSD_CollCode184734)[15].

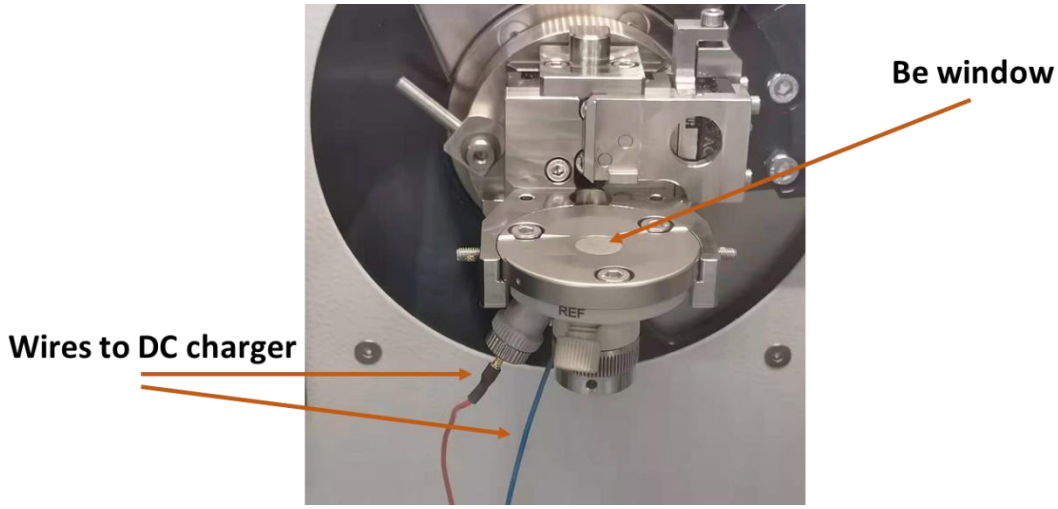


Figure 3.6 Real photos of In situ X-ray diffraction coin cell.

To gain insight into the structural evolution mechanism of the sample upon Na^+ extraction/insertion, operando XRD was also carried out in an El-cell in situ cell in this study. Figure 3.6 shows the schematic review and real photos of the in-situ cell, which is equipped with a beryllium (Be) window (Ø 10 mm, 0.2 mm thickness). Beryllium is transparent to x-rays, and it is therefore the structural evolution of the sample during charging and discharging can be observed in situ by coupling the XRD instrument with an electrochemical workstation. In this work, operando XRD was used in Chapter 4 to record the XRD patterns of samples before and after Sn modification at various charge and discharge. By comparing the evolution of the main characteristic peaks, the enhanced cycling performance after Sn modification can be explained by the improved structural stability with via the mitigation of irreversible phase transition.

3.2.1.2 Scanning electron microscopy (SEM)

Scanning electron microscopy is to generate various signals, such as secondary electrons, backscattered electrons, absorbed electrons, X-rays, etc., through the interaction between the high-energy electron beam focused on the sample surface, which are converted into images to observe the surface morphology of the material.

In generally, material morphology is strongly related to its electrochemical properties. The observation of the material morphology can be used to determine the influence of the synthesis parameters on the particle morphology, size and homogeneity, and can also be used to initially judge or explain the electrochemical properties.

In this work, a Zeiss EVO15 field emission electron microscope coupled with energy-dispersive spectroscopy (EDS) was used to characterize the surface morphology and elemental distribution of the synthesized samples. SEM samples were prepared by sticking the powders or electrodes on a carbon sticker. To improve the image quality obtained Au coating is performed before testing.

3.2.1.3 Transmission electron microscopy (TEM)

Transmission electron microscopy (TEM) is an imaging technique that utilizes a high-energy electron beam to obtain detailed information about the structure, morphology, and composition of materials at the nanoscale. It provides high-resolution images and allows for the analysis of various properties, such as crystallographic structure, defects, and elemental distribution.

In this work, TEM testing was conducted with the help of Henry Royce Institute, using a JEOL JEM-F200 electron microscope operated at 200 kV. The objectives of TEM testing were:

(1) Detecting the atomic structure and the inter-slab distance (d003) of crystal structure before and after Sn modification, thereby measuring the effects of Sn substitution on the crystal structure.

(2) Checking whether there is a coating layer formed at the surface of the particle as well as the thickness of the coating.

(3) Combined with energy-dispersive X-ray spectroscopy (EDS) to detect the distribution of elements within a single primary particle, thus helps in identifying the compositional variations.

3.2.1.4 Transmission electron inductively coupled plasma atomic emission spectrometry (ICP-AES)

ICP-AES (Agilent Technologies) was used in this work to examine the precise chemical compositions of the prepared cathode materials.

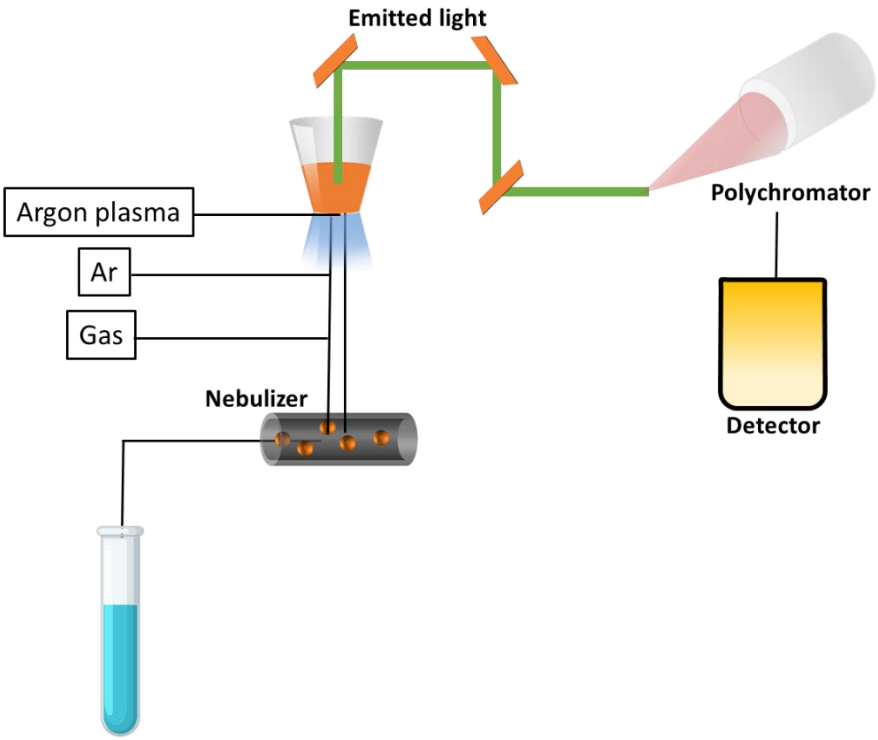


Figure 3.7 Simple Diagram of ICP-AES.

ICP-AES is a spectral analysis technique to measure the chemical composition of a sample according to the optical spectrum emitted by atoms. Different substances are made up of different atoms surrounded by electrons around the nucleus. Each electron is in a particular orbital and has a different energy. Under normal conditions, the atom is in a steady state, which has the lowest energy, and this state is known as the ground state. When an atom is vaporized by external energy, the outer electrons of the atom are excited to a higher energy state, called the excited state. Due to the instability of the atom in the excited state, the electrons leap from the higher energy level to a lower energy level and emit specific wavelengths. After spectroscopy by grating, the elements can be analyzed qualitatively based on the obtained specific wavelengths. The intensity of a specific wavelength is proportional to the concentration of the element to be measured, whereby a quantitative analysis can be performed. In ICP-AES, the source of external energy is the heat from an argon plasma that operates around 10,000 K.

Prior to testing, the ICP-AES needs to be calibrated, which involves measuring a series of different concentrations of standard solutions containing each known element in the sample to investigated. From these data, a calibration curve can be created. The calibration curve gives the relationship between the intensity of the emitted light at a specific wavelength and the

concentration of the element in the solution. Calibration standards were prepared by diluting a stock multi-elemental standard solution (1000 mg dm^{-3}) in 0.2 % nitric acid.

For the synthesized samples, 0.1 g of each sample was dissolved in 30 mL of aqua regia solution and made up to 1000 mL using distilled water in volumetric flask[15]. Dispense 50 mL from the above solution into a 1000 mL volumetric flask so that the final solubility of the sample to be measured is 5 ppm. Three repeats were performed with the instrument on each sample.

3.2.1.5 Raman spectroscopy (Raman)

Raman spectroscopy can provide insights into the crystal structure of battery materials. In this work, Raman spectra were recorded on a Renishaw InVia Raman spectrometer with a laser wavelength of 488 nm[15]. Three intense bonds originated from the TM−O vibrations and the Na vibrations of the layered hexagonal $R\bar{3}m$ symmetry were recorded for samples before and after Sn modification. By monitoring the changes in peak position and intensity, the local structure evolution induced by Sn modification can be confirmed.

3.2.1.6 X-ray photoelectron spectroscopy (XPS)

XPS measurements were carried out to detect the surface composition and valence of TM ions on the particle surface, which is beneficial for locating the Sn within these materials and understanding its role in enhancing the materials properties.

The x-ray photoelectron (XPS) data collection and analysis were performed by the Instituto de Química Física ″Rocasolano″, CSIC (Spain). All data were recorded under a vacuum of better than $1 \cdot 10^{-9}$ mbar with a PHOIBOS 150 electron analyzer (SPECS) using Al Kα radiation (1486.6 eV) and a constant pass energy of 100 and 20 eV for the wide and narrow scans, respectively[15]. The binding energy scale was referenced to the main C 1s contribution of the adventitious carbon layer, which was set at 284.6 eV. All of the spectra were computer-fitted using pseudo-Voight profiles (30% Lorentzian-70% Gaussian) and a Shirley background. The binding energies are accurate within ±0.2 eV [15]. ***(Note: The methodology described in this paragraph has been lifted from my published paper*** **https://pubs.acs.org/doi/10.1021/acs.chemmater.2c00522*.)***

3.2.2 Electrochemical characterisation

Galvanostatic charge/discharge, and galvanostatic intermittent titration technique (GITT) measurement were performed on a Bio-Logic BCS 805 series battery test system (Seyssinet-Pariset, 39170 France).

The EIS and three-electrode swagelok cells were conducting using a Bio-Logic VMP3 system.

3.2.2.1 Galvanostatic charge/discharge

The galvanostatic charge/discharge test is a technique of repeatedly charging and discharging a battery at a constant current density over a fixed voltage window. By recording the process current and voltage, information such as charge/discharge energy, specific capacity, coulomb efficiency and median voltage can be obtained.

In this study, galvanostatic charge/discharge were performed on a BCS battery test system at room temperature. The initial capacity and formation were obtained by applying the following protocol: at C/10 CC-CV (C/50 current cut off limit) charge and C/10 discharge, followed by cycling at C/2 CC-CV (C/20 current cut off limit) charge and C/2 discharge. The rate capability of cathode materials were evaluated by fixing the charge current at C/2 CC-CV (C/20 current cut off limit) and varying the discharge current from C/2 to 3C.

C-rate refers to the rate at which a battery is charged or discharged relative to its capacity, it can be defined as following:

$$C_{\text{rate}} = \frac{\text{A}_{cur}}{\text{m}_{AM}\, Q_T} \qquad (3\text{-}4)$$

Where A_{cur} is the charging or discharging current (in Amperes), m_{AM} means the mass of active material of the electrode (g), Q_c stands for the theoretical specific capacity of active material (mAh g^{-1}). 1C is refer to the current density that can fully discharge the battery in one-hour. For example, a 1000 mAh battery supplying 1C of current would be supplying 1000 mA. 0.1C for the same battery would be 100 mA, 2C for the same battery would be 2000 mA.

In this study, the theoretical specific capacity (Q_c) of the synthesized cathode material is 150 mAh g^{-1}.

3.2.2.2 Electrochemical impedance spectroscopy (EIS)

Electrochemical impedance spectroscopy (EIS) is a non-destructive method for investigating the kinetic behaviour of electrodes and electrochemical processes occurring at the electrode/electrolyte interfaces. Potentiostatic EIS involves applying a sinusoidal voltage signal of small amplitude to the electrochemical system and measuring the sinusoidal current response generated by the studied system when the system reaches the AC (alternating current) steady state. The shift in the applied and measured signal (phase angle) is related to the time constant of the process at that specific frequency. Diffusive processes have a phase angle of 45 degrees, since they follow Ficks Law of Diffusion, and capacitive processes have a phase angle of 90 degrees. The frequency at which the processes occur relates to the speed, for example, electron transfer is fast and therefore observed at higher frequencies compared to ionic diffusion which is observed at lower frequencies. Using Ohm law (V=IR) the resistivity can be calculated at these different frequencies. The sinusoidal signal can be expressed by an imaginary number and is so converted into a real and imaginary impedance. The change of frequency and impedance of the measured output gives information about the cell and electrode transport properties, such as ohmic or series resistance, diffusivity, and charge transfer properties[25-27].

The impedance is composed of resistance and capacitance, where resistance is the real part (Z') of the impedance and reactance (Z'') or capacitance (-Z'') is the imaginary part of the impedance. The generated data is usually plotted as -Z'' against Z' on a linear scale as a Z^* complex plane plot, also known as Nyquist plot[27]. In this plot, every data point represents the imaginary impedance (*Y*-axis) plotted against the real impedance (*X*-axis) at varying frequencies. The plot arranges higher frequencies to the left and lower frequencies to the right. In a typical Nyquist plot, the impedance spectrum for a cell consists of four parts: a high frequency impedance value where the imaginary impedance is zero, two semicircles at middle frequencies, and a sloping straight line at low frequency region as shown in Figure 3.8a, a typical Nyquist plot (-Z'' vs. Z') of sodium-ion cells.

The impedances or internal resistances corresponding to the electrochemical processes of a battery can correspond to the parts of the impedance spectrum[28, 29].

(1) Ohmic resistance (Rs): This resistance is related to the transportation of sodium ions and electrons through the electrolyte, separator, wire, active material particles, etc. It comprises the cumulative contribution of all the battery components exhibiting simple

resistor-like behaviour. This resistance is affected by electrolyte composition, electrode thickness, electrode porosity, temperature, etc. It is typically represented as a small interrupt at the origin on the *X*-axis.

(2) Solid Electrolyte Interphase (SEI) resistance (Rsf): This resistance arises from the resistance of Na ions migration through the SEI film, and usually refers to the first semicircle at middle frequencies. This can be affected by the SEI film composition and thickness.

(3) Charge transfer resistance (Rct): Rct is represented by the second semicircle in the Nyquist plot and is associated with the charge-transfer reaction resistance taking place at the electrode-SEI interface. It encompasses processes such as the de-solvation of Na-ion and the transfer of an electron from the electrode to Na-ion at the electrode-SEI interface. Rct reflects the difficulty of transferring charge between electrode and electrolyte. Typically, it steadily increases during cycling due to the active material surface structural change with cycling.

(4) Diffusion resistance (Ws): Diffusion resistance is represented by the sloping line at low frequencies and arises due to the solid-state diffusion process of Na^+ within the cathode bulk crystal. This process is related to the electronic properties of the electrode and is usually used to extract the Na-ion diffusion coefficient.

It's worth mentioning that the Nyquist plot is strongly potential-dependent and significantly influenced by the temperature and State of Health (SOH) of the cell. Changes in impedance are reflected through alterations in the diameter and curvature of the semicircle. In certain cases, some of them would overlap with each other, making it challenging to interpret the obtained EIS data directly.

Equivalent Circuit Model (ECM) was widely used to fit and help interpret the EIS data. The basic idea of using ECM to interpret EIS data is to understand a battery system as an electrical circuit system. This equivalent circuit is composed of basic electric elements such as resistance, inductance, capacitance, etc., arranged in different configurations such as series or parallel as shown in Figure 3.8b. Each element in the circuit corresponds to a specific electrical behaviour of the battery. By constructing an ECM and fitting the model to experimental data, researchers can obtain numerical values for the circuit elements, enabling a quantitative analysis of the electrode reaction processes in the battery system.

Resistor (*R*), capacitor (*C*), and Warburg (*W*) are three basic electric elements (Figure 3.8c) that can be used to simulate the electric behaviours in a battery system. Among these, the *R*-element represents the electronic Ohmic resistance of the cell; the *C*-element is employed to simulate the capacitance behaviour occurring at the electrode and electrolyte interface due to the charge separation across the reaction interface, forming a double-layer capacitance; *W*-element is used to simulate the diffusion impedance originating from the ions diffusion process within the electrode. An *RC*-element is formed by the parallel connection of a resistor and a capacitor. This element can be used to simulate the ideal interfacial electrochemical process, which is reflected as a perfect semicircle in the EIS data. However, in most cases, the semicircle in the mid-frequency region tends to flatten, appearing as a curved segment (as shown in Figure 3.8a), a phenomenon referred to as "dispersion phenomenon." This is generally considered to be associated with the unevenness of the electrode surface and poor conductivity of the electrolyte. It reflects the deviation of the electrode double-layer capacitance from the ideal capacitance. In other words, simplifying the double layer at the electrode interface as a purely capacitive element is not accurate enough. Therefore, the Constant Phase Element (*CPE*) has been developed to calibrate the deviations of the pure capacitor. Correspondingly, a combination of an ohmic resistor and *CPE* is connected in parallel to form an impedance element called a *ZARC* (Zigzagged Arc) to simulate the actual interfacial electrochemical processes in a battery system as shown in Figure 3.8c. Based on these fundamental electric elements (*R, C, CPE, ZARC, W*), different ECMs can be obtained through arrangements and combinations to simulate the practical electrochemical processes inside a battery system[27, 30].

The insert in Figure 3.8a shows a typical equivalent circuit used in the following chapters, in which the ohmic resistance (Re) is represented by a resistor, two *ZARC* elements are used to simulate the surface layer resistance (Rsf) and charge transfer resistance (Rct), Warburg element represents the solid diffusion process (Ws). It should be noted that the ECM is an a priori method, and there is no one-to-one correspondence between EIS data and ECM. In other words, the same EIS spectrum can have multiple appropriate ECMs. The construction of an ECM needs to be combined with previous experience and adjusted according to the fitting results.

In this study, EIS was applied in chapter 4 to demonstrate the benefits of Sn-dual modification on the interface stability with cycling. All the tests were conducted in a three-electrode Swagelok cell to avoid the contribution of Na anode passivation in a commonly used two-electrode coin-cell. The equivalent circuits were fitted by Z View 2.0 software.

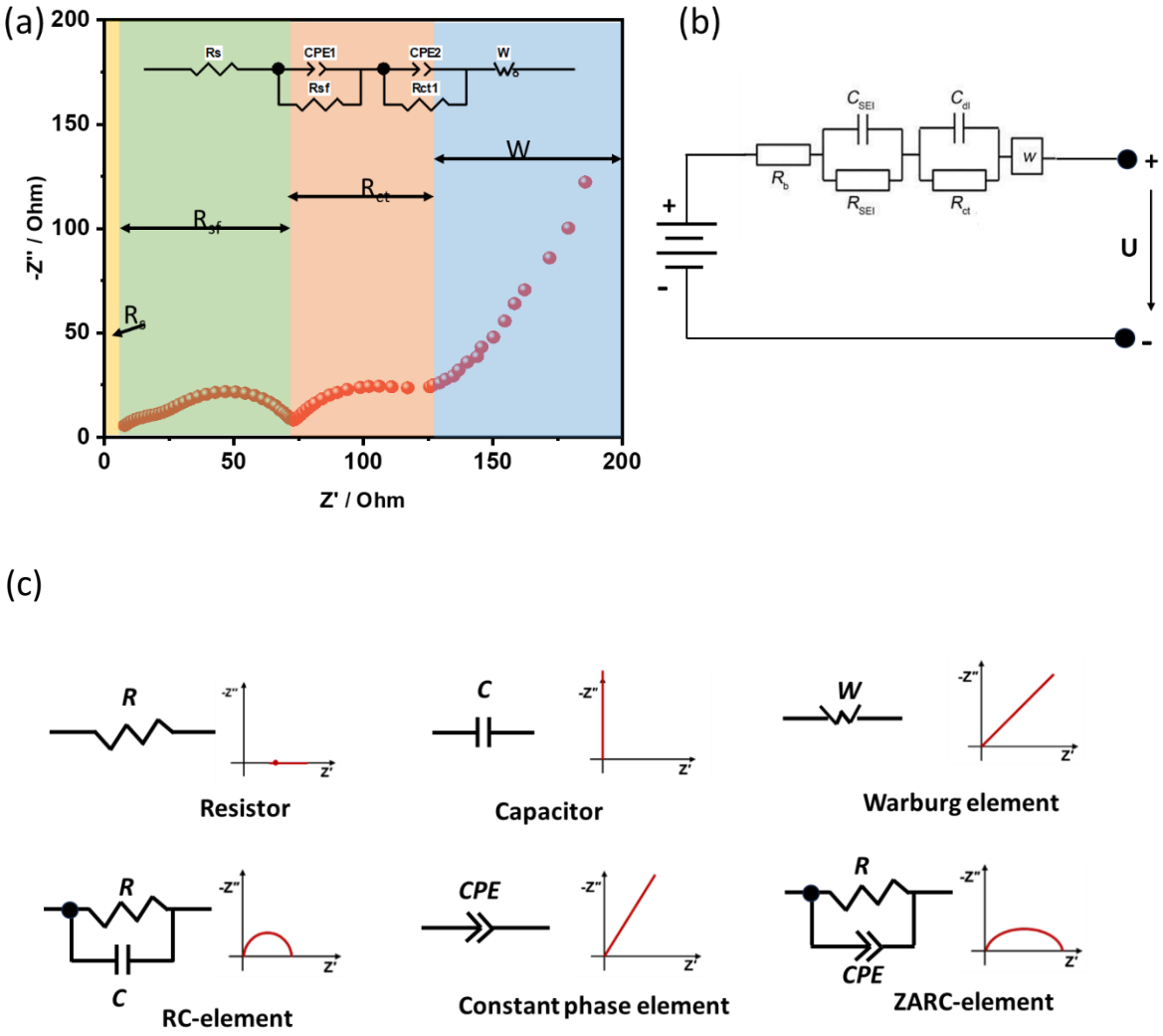


Figure 3.8 (a) A typical impedance spectrum of sodium-ion cells, inserted is the equivalent circuit model. (b) A diagram shows that a battery system can be understood as a circuit system. (c) The symbols and corresponding figures in the EIS complex plane of the basic electrical elements used for equivalent circuits.

3.2.2.3 Differential Capacity (dQ/dV)

Differential capacity analysis is one common technique for probing the degradation mechanisms of a battery. The physical definition of dQ/dV is the capacity of a material

contained in a unit voltage range, which was calculated based on the derivation of the capacity (Q) with respect to the voltage (V), defined as:

$$\frac{dQ}{dV} = \frac{\Delta Q}{\Delta V} = \frac{Q_{t+1} - Q_{t-1}}{V_{t+1} - V_{t-1}} \qquad (3\text{-}5)$$

$$\Delta V = x_2 - x_1, \quad \Delta Q = y_2 - y_1$$

Where the capacity (Q) and voltage (V) were collected during the charge and discharge cycles by precision test equipment.

Figure 3.9a shows the typical Voltage vs. Q charge/discharge curves for an O3-type layered oxide $NaNFMO_2$ under different cycling numbers. In the curves, slope regions are related to single-phase (solid solution) where voltage varies continually, plateaus on the curves indicate the two-phase coexistence (phase transformation) region, where voltage stays constant[31]. It is a challenge to read the cause of battery failure from the Voltage vs. Q curves directly. The advantage of dQ/dV analysis is that plateaus in the Voltage vs. Q charge/discharge curves can be reflected as peaks in the dQ/dV curves. Figure 3.9b gives the calcuated dQ/dV vs. voltage plots, where the first peak around 3.0 V (vs Na^+/Na) is related to the phase transition from O3 to P3, peak around 3.8 V(vs Na^+/Na) (marked as an arrow) can be attributed to the phase transition from P3 to monoclinic P'3[15]. By comparing the changes of those identifiable peaks with cycles (like shape, intensity and position), underlying degradation cause could be obtained.

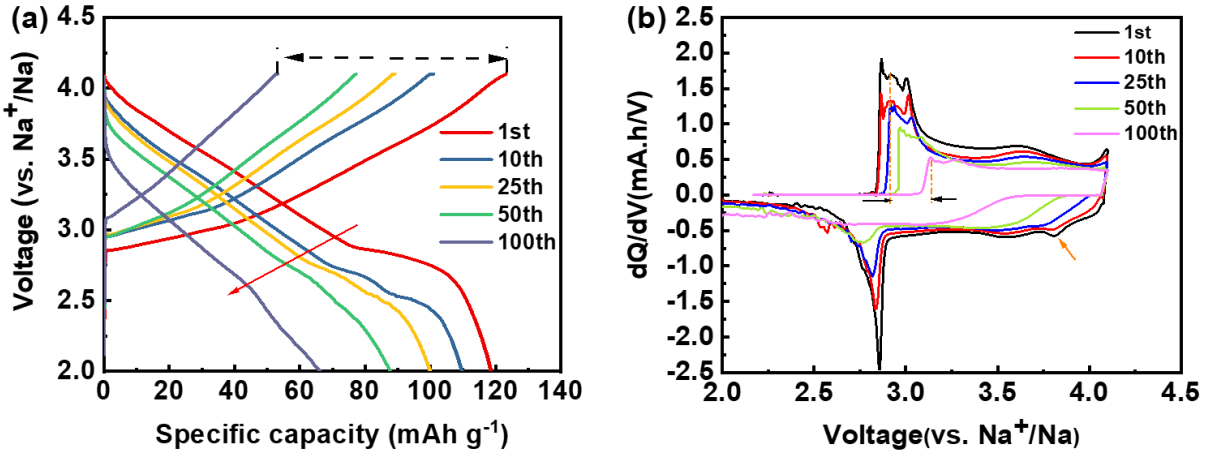


Figure 3.9 (a) Example of Voltage vs. Q charge/discharge curves of different cycles for an O3-type layered oxide. (b) dQ/dV curves derived from (a) showing the varies of peaks with cycling.

In this work, dQ/dV analysis was used to understand the mechanism of improved cycling stability of the cathode materials after Sn modification as well as the degradation origin of full cells with different N/P ratio.

3.2.2.4 Galvanostatic intermittent titration technique (GITT)

The Galvanostatic intermittent titration technique has been widely used in battery research to determine the Li^+ or Na^+ diffusion coefficients. The GITT test consists of two parts: the first step is a short period of low-current pulses (normally 10/C or 20/C) to ensure that the ion diffusion process occurs only in the surface layer of the material. The total change of the cell voltage during the current plus step is recorded as ΔEt, as shown in Figure 3.10. The second step is a steady state which is a long period of resting process (hours) after the current plus to ensure full diffusion of ions inside the active material to reach an equilibrium state (when $dE/dt \approx 0$). The changes of the steady-state voltage are recorded as ΔE_S. This sequence of current plus followed by a resting process is repeated until the battery is fully charged or discharged. During this process, steady state voltage E(V) is recorded after sequence.

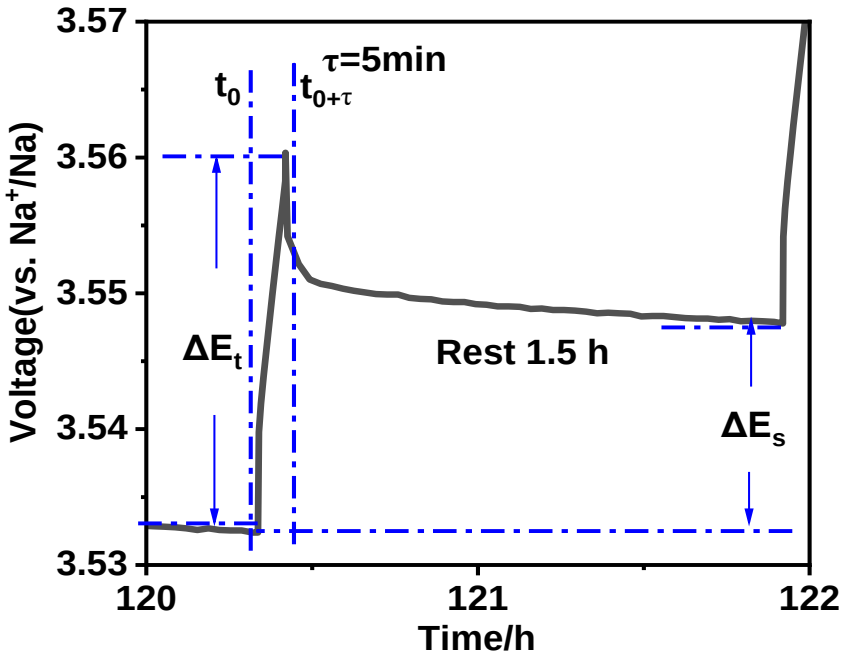


Figure 3.10 The schematic diagram of a single sequence for GITT.

The recorded data can be used to extract the apparent diffusion capability of Na^+ (D_{Na}) at the different stoichiometries based on a simplified equation (Eq. 3-6) introduced by Weppner and Huggins[32].

$$D_{Na} = \frac{4}{\pi\tau}\left(\frac{m_{AM}V_M}{M_{AM}S}\right)^2\left(\frac{\Delta E_s}{\Delta E_t}\right), \text{ with } \tau \ll \frac{L^2}{D} \quad (3\text{-}6)$$

where D is the apparent diffusion coefficient ($cm^2\ s^{-1}$), τ is the applied current time interval, m_{AM} means the mass of active material of the electrode, M_{AM} stands for the molar weight of active material ($g\ mol^{-1}$), V_M represents the molar volume of active materials ($cm^3\ mol^{-1}$), which was obtained by dividing the molar weight ($g\ mol^{-1}$) of active material by its true density. L is the thickness of the electrode. S is the effective surface area of the porous electrode, which was calculated from the total number of particles and the average particle size in the electrode based on Eq. 3-7[33].

$$S = n \cdot S_{particle} = \frac{\varepsilon_{AM}V_{electrode}}{V_{particle}} S_{particle} \quad (3\text{-}7)$$

ε_{AM} represents the active material volume fraction of the whole electrode, $V_{electrode}$ is the electrode's total volume, $V_{particle}$ means the volume of a single particle, $S_{particle}$ stands for the particle surface area, which can be measured using SEM or particle size analyzer.

In this work, GITT was applied to evaluate the influence of Sn modification on the kinetic behavior of Na^+ in $NaNi_{1/3}Fe_{1/3}Mn_{1/3}O_2$ electrode. Transients were C/10 CC for 5min and then rested for 1.5 hours.

3.3 References

1. Huang, Y.; Wang, Z.-x.; Li, X.-h.; Guo, H.-j.; Wang, J.-x., Synthesis of $Ni_{0.8}Co_{0.1}Mn_{0.1}(OH)_2$ precursor and electrochemical performance of $LiNi_{0.8}Co_{0.1}Mn_{0.1}O_2$ cathode material for lithium batteries. *Transactions of Nonferrous Metals Society of China* **2015,** 25, (7), 2253-2259.
2. Robinson, J. P.; Koenig, G. M., Tuning solution chemistry for morphology control of lithium-ion battery precursor particles. *Powder Technol.* **2015,** 284, 225-230.
3. Liu, D.; Han, J.; Goodenough, J. B., Structure, morphology, and cathode performance of $Li_{-x}[Ni_{0.5}Mn_{1.5}]O_4$ prepared by coprecipitation with oxalic acid. *Journal of Power Sources* **2010,** 195, (9), 2918-2923.
4. Luo, W.; Li, X.; Dahn, J. R., Synthesis, Characterization, and Thermal Stability of $Li[Ni_{1/3}Mn_{1/3}Co_{1/3-z}(MnMg)_{z/2}]O_2$. *Chemistry of Materials* **2010,** 22, (17), 5065-5073.
5. Dong, H.; Koenig, G. M., A review on synthesis and engineering of crystal precursors produced via coprecipitation for multicomponent lithium-ion battery cathode materials. *CrystEngComm* **2020,** 22, (9), 1514-1530.
6. Xu, C.; Guan, S.; Li, L.; Sun, C.; An, B.; Geng, X., Electrochemical Properties of $LiNi_{0.6}Co_{0.2}Mn_{0.2}O_2$ Cathode Materials Prepared with Different Ammonia Content. *Coatings* **2021,** 11, (8).
7. Yang, Y.; Xu, S.; Xie, M.; He, Y.; Huang, G.; Yang, Y., Growth mechanisms for spherical mixed hydroxide agglomerates prepared by co-precipitation method: A case of $Ni_{1/3}Co_{1/3}Mn_{1/3}(OH)_2$. *Journal of Alloys and Compounds* **2015,** 619, 846-853.
8. Cho, J., $LiNi_{0.74}Co_{0.26-x}Mg_xO_2$ Cathode Material for a Li-Ion Cell. *Chemistry of Materials* **2000,** 12, (10), 3089-3094.
9. Lee, M. H.; Kang, Y. J.; Myung, S. T.; Sun, Y. K., Synthetic optimization of $Li[Ni_{1/3}Co_{1/3}Mn_{1/3}]O_2$ via co-precipitation. *Electrochimica Acta* **2004,** 50, (4), 939-948.
10. van Bommel, A.; Dahn, J. R., Analysis of the Growth Mechanism of Coprecipitated Spherical and Dense Nickel, Manganese, and Cobalt-Containing Hydroxides in the Presence of Aqueous Ammonia. *Chemistry of Materials* **2009,** 21, (8), 1500-1503.
11. Wang, D.; Belharouak, I.; Ortega, L. H.; Zhang, X.; Xu, R.; Zhou, D.; Zhou, G.; Amine, K., Synthesis of high capacity cathodes for lithium-ion batteries by morphology-tailored hydroxide co-precipitation. *Journal of Power Sources* **2015,** 274, 451-457.
12. Liang, L.; Du, K.; Peng, Z.; Cao, Y.; Duan, J.; Jiang, J.; Hu, G., Co–precipitation synthesis of $Ni_{0.6}Co_{0.2}Mn_{0.2}(OH)_2$ precursor and characterization of $LiNi_{0.6}Co_{0.2}Mn_{0.2}O_2$ cathode material for secondary lithium batteries. *Electrochimica Acta* **2014,** 130, 82-89.
13. Noh, M.; Cho, J., Optimized Synthetic Conditions of $LiNi_{0.5}Co_{0.2}Mn_{0.3}O_2$ Cathode Materials for High Rate Lithium Batteries via Co-Precipitation Method. *Journal of The Electrochemical Society* **2012,** 160, (1), A105-A111.
14. Cho, T. H.; Park, S. M.; Yoshio, M.; Hirai, T.; Hideshima, Y., Effect of synthesis condition on the structural and electrochemical properties of $Li[Ni_{1/3}Mn_{1/3}Co_{1/3}]O_2$ prepared by carbonate co-precipitation method. *Journal of Power Sources* **2005,** 142, (1-2), 306-312.
15. Song, T.; Chen, L.; Gastol, D.; Dong, B.; Marco, J. F.; Berry, F.; Slater, P.; Reed, D.; Kendrick, E., High-Voltage Stabilization of O3-Type Layered Oxide for Sodium-Ion Batteries by Simultaneous Tin Dual Modification. *Chemistry of Materials* **2022**.
16. Zhang, S. S.; Ma, L., Oxalic Acid as a Cathode Additive Increasing Rate Capability of Ni-Rich Layered Cathode Materials. *Journal of The Electrochemical Society* **2021,** 168, (8).
17. Vaalma, C.; Buchholz, D.; Weil, M.; Passerini, S., A cost and resource analysis of sodium-ion batteries. *Nature Reviews Materials* **2018,** 3, (4).
18. Zhang, B.; Wang, L.; Zhang, Y.; Wang, X.; Qiao, Y.; Sun, S. G., Reliable impedance analysis of Li-ion battery half-cell by standardization on electrochemical impedance spectroscopy (EIS). *J. Chem. Phys.* **2023,** 158, (5), 054202.

19. Clegg, W.; Blake, A. J.; Cole, J. M.; Evans, J. S. O.; Main, P.; Parsons, S.; Watkin, D. J., *Crystal Structure Analysis*. 2009.
20. Dorset, D. L., X-ray Diffraction: A Practical Approach. *Microsc. Microanal.* **1998,** 4, (5), 513-5.
21. Waseda, Y.; Matsubara, E.; Shinoda, K., *X-Ray Diffraction Crystallography*. 2011.
22. Higgins, M. K.; Lea, S. M., On the state of crystallography at the dawn of the electron microscopy revolution. *Curr Opin Struct Biol* **2017,** 46, 95-101.
23. Rietveld, H. M., A profile refinement method for nuclear and magnetic structures. *J. Appl. Crystallogr.* **1969,** 2, (2), 65-71.
24. Rietveld, H. M., Line profiles of neutron powder-diffraction peaks for structure refinement. *Acta Crystallographica* **1967,** 22, (1), 151-152.
25. Middlemiss, L. A.; Rennie, A. J. R.; Sayers, R.; West, A. R., Characterisation of batteries by electrochemical impedance spectroscopy. *Energy Reports* **2020,** 6, 232-241.
26. Tröltzsch, U.; Kanoun, O.; Tränkler, H.-R., Characterizing aging effects of lithium ion batteries by impedance spectroscopy. *Electrochimica Acta* **2006,** 51, (8-9), 1664-1672.
27. Lazanas, A. C.; Prodromidis, M. I., Electrochemical Impedance Spectroscopy-A Tutorial. *ACS Meas Sci Au* **2023,** 3, (3), 162-193.
28. Qiu, X. Y.; Zhuang, Q. C.; Zhang, Q. Q.; Cao, R.; Ying, P. Z.; Qiang, Y. H.; Sun, S. G., Electrochemical and electronic properties of $LiCoO_2$ cathode investigated by galvanostatic cycling and EIS. *Phys Chem Chem Phys* **2012,** 14, (8), 2617-30.
29. Tatara, R.; Karayaylali, P.; Yu, Y.; Zhang, Y.; Giordano, L.; Maglia, F.; Jung, R.; Schmidt, J. P.; Lund, I.; Shao-Horn, Y., The Effect of Electrode-Electrolyte Interface on the Electrochemical Impedance Spectra for Positive Electrode in Li-Ion Battery. *Journal of The Electrochemical Society* **2018,** 166, (3), A5090-A5098.
30. Hu, W.; Peng, Y.; Wei, Y.; Yang, Y., Application of Electrochemical Impedance Spectroscopy to Degradation and Aging Research of Lithium-Ion Batteries. *The Journal of Physical Chemistry C* **2023,** 127, (9), 4465-4495.
31. Liu, C.; Neale, Z. G.; Cao, G., Understanding electrochemical potentials of cathode materials in rechargeable batteries. *Mater. Today* **2016,** 19, (2), 109-123.
32. Weppner, W.; Huggins, R. A., Electrochemical investigation of the chemical diffusion, partial ionic conductivities, and other kinetic parameters in Li_3Sb and Li_3Bi. *J. Solid State Chem.* **1977,** 22, (3), 297-308.
33. O'Regan, K.; Brosa Planella, F.; Widanage, W. D.; Kendrick, E., Thermal-electrochemical parameters of a high energy lithium-ion cylindrical battery. *Electrochimica Acta* **2022,** 425.

Chapter 4 High-voltage stabilization of O3-type layered oxide for sodium-ion batteries by simultaneous Tin dual modification

This work has been published in **Chem. Mater. 2022, 34, 9, 4153–4165 (**Tengfei Song, Lin Chen, Dominika Gastol, Bo Dong, José F. Marco, Frank Berry, Peter Slater, Daniel Ree, and Emma Kendrick**)**

DOI: 10.1021/acs.chemmater.2c00522

Submitted: 17/02/2022

Accepted: 15/04/2022

Author contribution: T.F. and E.K. conceived and designed the research. T.F. and L.C. performed the experiments and electrochemical testing. D.G. helped with the SEM/EDS and FIB-SEM data acquisition. B.D. and P.R.S. conducted the XRD testing. J.F.M. and F.B. performed the XPS and Mössbauer spectroscopy. D.R. helped with the Operando XRD and Raman data acquisition. T.F. drafted the manuscript. All the authors commented on and revised the manuscript.

4.1 Introduction

Among various reported Na_xTMO_2 materials, cobalt-free O3-type layered $NaNi_{1/3}Fe_{1/3}Mn_{1/3}O_2$ is one of the most promising cathode materials for SIBs, since first reported by the Johnson group.[1] This material illustrates high reversibility, and undergoes an O3-P3-O3 phase change during desodiation /sodiation process in the voltage range of 2.0-4.0 V (*vs* Na/Na^+); this R-3m layered structure remains intact after more than 100 cycles.[1, 2] However, when the cut-off voltage is raised to higher than 4.0 V in order to pursue higher energy density, an irreversible phase change to O3' and P3' monoclinic phase occurs.[3] This irreversible structural evolution mainly originates from the migration of TM ions, and has been proven to be detrimental for stable cycling under higher charging potentials.[4, 5]

As with many of these O3 type layered oxides, interfacial reactions between the cathode and electrolyte also accelerate the degradation of cathode material, causing capacity fade upon cycling.[6-8] Surface degradation becomes more serious when operated at higher potentials.[9] Given these aspects, methods to simultaneously suppress the phase transformation and also stabilize the particle surfaces at a higher cut-off voltage (＞4.0 V) need to be investigated before it can be used in practice.[10]

Electrochemically inactive element substitution, such as Li[11], Mg[12, 13], Ti[14-17], and Sn[18-23], have proven an effective strategy to modify the material's bulk structure properties and improve the high-voltage structural stability of layered oxides. Among these elements, Sn is particularly promising because the binding energy of Sn-O (548 kJ mol^{-1}) is much stronger than that of Ni-O (391.6 kJ mol^{-1}), Fe-O (409 kJ mol^{-1}), and Mn-O (402 kJ mol^{-1}). The stronger binding force between Sn^{4+} and O^{2-} will shrink the thickness of TM slabs. Thus, the average TM-O bond length becomes shorter, which helps suppress the TMO_2 layer gliding and associated phase transition. Recent reports have shown that Sn substitution can smooth the charge/discharge voltage profile, by suppressing the phase transitions and increasing the average working voltage.[20, 24-26] Another benefit of Sn doping is that doping with high valence atoms can generate some sodium vacancies due to charge balance. The presence of sodium vacancies means that the charge in the layer is reduced, resulting in a longer bond between Na-O. This will reduce the Na^+ migration resistance and enhance the Na^+ diffusion kinetics[27, 28]. The suppressed transition metal layer gliding, together with the enhanced Na^+ diffusion kinetics, will help

suppress the phase transition and, thus, improve the cycling stability. This has been verified in the following study.

In this work, the incorporation of Sn into a $NaNi_{1/3}Fe_{1/3}Mn_{1/3}O_2$ cathode has been studied to simultaneously stabilize the crystal structure as well as the particle surface at high cell voltages. Through an extensive study of the structural changes by in-depth in-situ and ex-situ XRD characterization during Na^+ intercalation/de-intercalation, Sn is proven to be effective in stabilizing the layered structure by suppressing the irreversible phase transformation under high voltage region (~4.1 V *vs* Na/Na^+). In addition, the simultaneously formed nano-coating layer with the sodium residues on the surface of the particles can improve the interfacial stability during cycling. As a result, the structural stability and electrochemical performance of $NaNi_{1/3}Fe_{1/3}Mn_{1/3}O_2$ are significantly improved within the voltage range of 2.0-4.1 V *vs* Na/Na^+. The modified cathode demonstrated excellent cycling stability as well as rate capability. The work illustrates that a combination of bulk doping and surface modification should be considered for the optimization of cathode performance and highlights that this combined beneficial effect can be achieved in a single scalable step.

4.2 Experimental section

4.2.1 Materials synthesis

The synthesis method for $[Ni_{1/3}Fe_{1/3}Mn_{1/3}](OH)_2$ precursor and $Na[Ni_{1/3}Fe_{1/3}Mn_{1/3}]O_2$ have been described detaily in **Chapter 3.1.1**. In brief, spherical $[Ni_{1/3}Fe_{1/3}Mn_{1/3}]$ $(OH)_2$ precursors were synthesized by a hydroxide coprecipitation method. First, stoichiometric amounts of $NiSO_4 \cdot 6H_2O$ (Alfa Aesar 98%), $FeSO_4 \cdot 7H_2O$ (Honeywell 99.9%), and $MnSO_4 \cdot H_2O$ (VWR 99.5%) were uniformly mixed and dissolved into deionized water with a concentration of 2 M. This mixed metal solution was pumped into a continuously stirred tank reactor. At the same time, a 4 M NaOH (Alfa Aesar 98%) solution as a precipitant and 4 M NH_4OH solution (28−30%, Sigma-Aldrich) as a chelating agent were also separately fed into the reactor in ambient air. The pump rates were set to achieve a 1:1 mole ratio of NH_4OH to transition metals. Stirring was done at 1000 rpm with a four-finned baffle. The temperature was 50 °C, and the pH was carefully controlled at 11.0 ± 0.1 by adjusting the NaOH pumping rate. After vigorous

stirring for 12 h, the spherical $[Ni_{1/3}Fe_{1/3}Mn_{1/3}](OH)_2$ precursor was filtered and rinsed thoroughly with deionized water, dried in a vacuum oven at 100 °C overnight, and then sieved.

For the Sn-modified $Na[Ni_{1/3}Fe_{1/3}Mn_{1/3}]O_2$, to ensure low-cost, fluorine and chlorine-free layered oxides, a tin oxide precursor was chosen rather than a soluble tin compound. This was added at the milling stage so that the same hydroxide precursor could be utilized for all synthesis batches. In detail, the obtained precursor $[Ni_{1/3}Fe_{1/3}Mn_{1/3}](OH)_2$ was milled with SnO_2 nanoparticles (99.9%, Strem Chemicals) (1.0, 3.0, 5.0, 8.0, and 10.0 mol %) and then ball milled (Retsch, PM100CM) at 250 rpm for 4 h. Then, the SnO_2-covered precursors were thoroughly mixed with the required Na_2CO_3 (99.9%, Sigma-Aldrich Co.) at 250 rpm for 30 min. An excess of 5 mol % Na_2CO_3 was used to compensate for any volatilization of Na during calcination. The mixture was calcined to 550 °C for 6 h with a ramp rate of 5 °C min^{-1}, followed by 900 °C for 9 h with a ramp rate of 2 °C min^{-1} in air, then slowly cooled (1 °C min^{-1}) to 150 °C. Finally, the layered Sn-modified materials (Figure 4.1) were removed from the furnace and transferred into an argon-filled glovebox. For Sn-free pristine $Na[Ni_{1/3}Fe_{1/3}Mn_{1/3}]O_2$ material, the same synthetic process without the addition of SnO_2 was conducted. The obtained samples with different contents of Sn are named as NaNFMO, Sn1%-NaNFMO, Sn3%-NaNFMO, Sn5%-NaNFMO, Sn8%-NaNFMO, and Sn10%-NaNFMO, respectively.

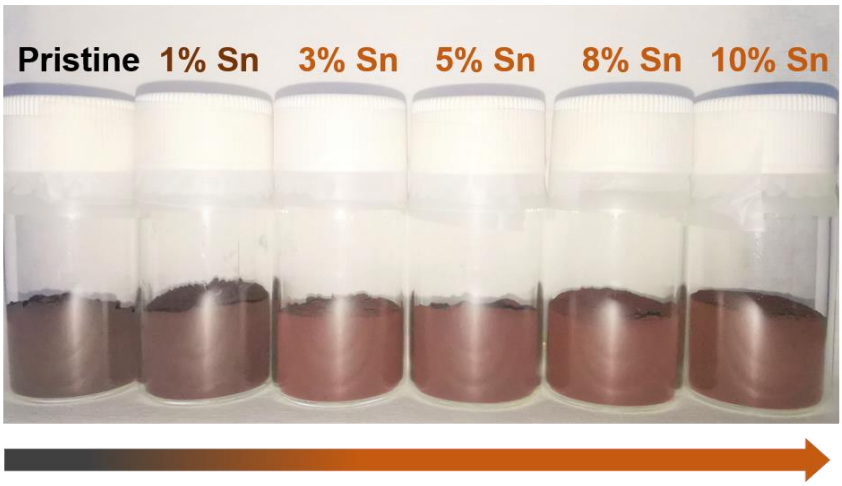


Figure 4.1 The colour of the different Sn stoichiometry doped layered oxides.

4.2.2 Analytical techniques

In this chapter, XRD, *situ* XRD, SEM-EDS, TEM, ICP-OES, Raman, and ^{57}Fe Mössbauer spectroscopy were used for the characterization of the synthesized materials. Coin-cell, Galvanostatic charge/discharge, dQdV, EIS, and GITT were performed to characterize the electrochemical performance. Details about the testing, cell making, and data fitting method can be found on **Chapter 3**.

4.3 Results and discussion

4.3.1 Materials characterization

The detailed chemical compositions of the prepared samples were measured by ICP-AES, as shown in Table 4-1. The experimental Ni/Fe/Mn/Sn molar ratios are in good agreement with the expected stoichiometry within the error of the determination. As expected, ~5% Na is lost during firing, as shown in the final elemental ratio.

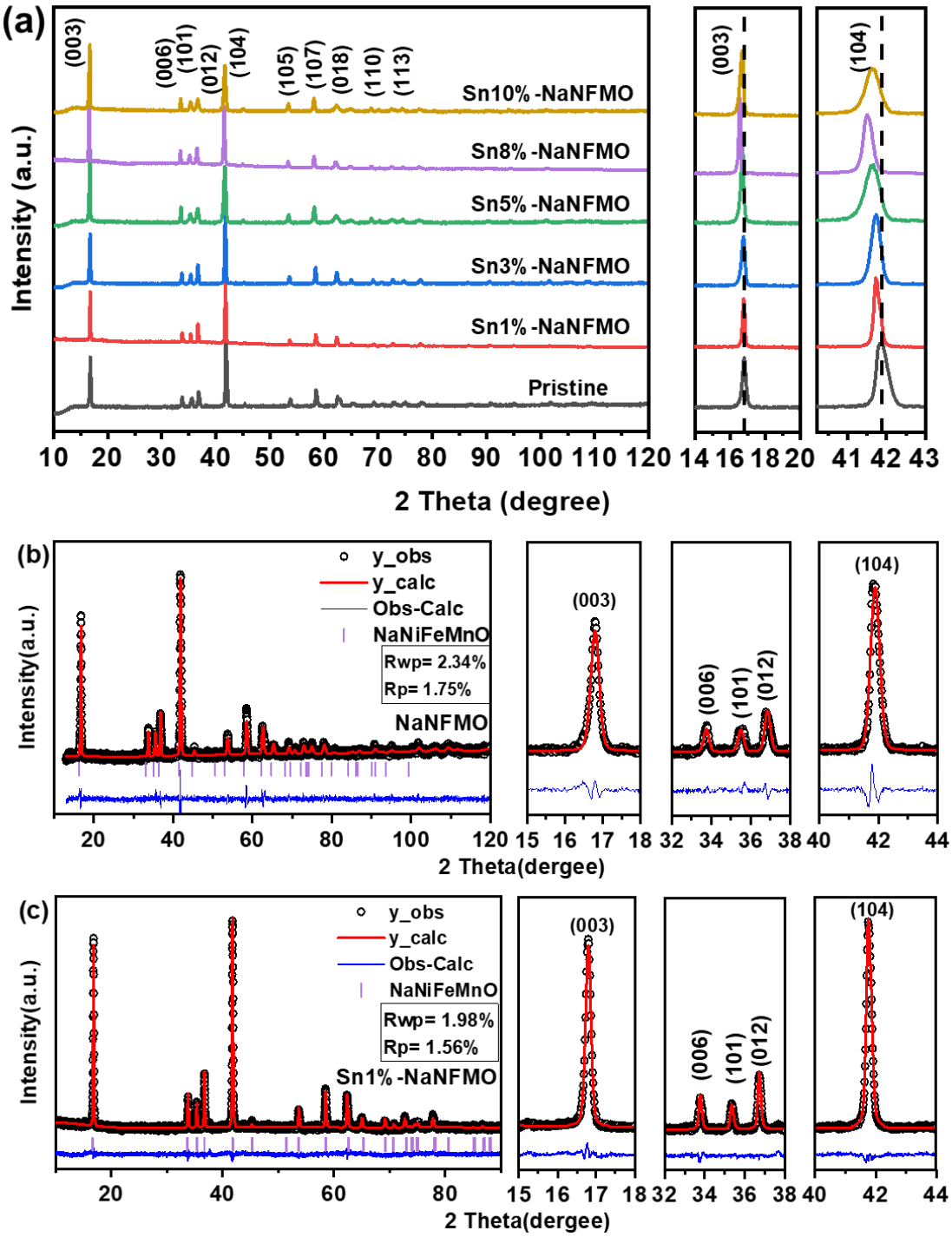
Table 4-1 The chemical compositions of the as-prepared samples measured by inductively coupled plasma mass spectroscopy (ICP-AES).

Compound	Input composition					Final composition				
	Na	Ni	Fe	Mn	Sn	Na	Ni	Fe	Mn	Sn
NaNFMO	1.050	0.333	0.333	0.333	0.000	0.998	0.337	0.339	0.324	0.000
Sn1%-NaNFMO	1.040	0.330	0.330	0.330	0.001	0.996	0.334	0.337	0.323	0.006
Sn3%-NaNFMO	1.019	0.323	0.323	0.323	0.029	0.977	0.324	0.328	0.322	0.026
Sn5%-NaNFMO	1.000	0.317	0.317	0.317	0.048	0.929	0.319	0.318	0.311	0.053
Sn8%-NaNFMO	0.972	0.308	0.308	0.308	0.074	0.919	0.312	0.313	0.303	0.072
Sn10%-NaNFMO	0.955	0.303	0.303	0.303	0.091	1.061	0.309	0.304	0.303	0.084

Note: Errors are within 5% of the values presented.

The crystal structures of the prepared samples have been characterized by XRD and the results are presented in Figure 4.2a. A single-phase material is produced in all cases that can be indexed to a hexagonal O3-type α-$NaFeO_2$ structure (R-3 m space group). No impurity peaks of SnO_2 are observed in the XRD patterns for the Sn modified samples. From the magnification of the (003) and (104) reflections, we can see that both peaks shift toward a lower Bragg angle with increasing Sn content, and Sn8%-NaNFMO presents the largest shift, indicating the largest expansion of the interplanar spacing.

Lattice parameters were calculated using the powder profile refinement program GSAS based on the initial structural model of O3 $NaMO_2$ (Figure 4.2b-g), and the refined crystallographic parameters are summarized in Figure 4.3a and Table 4-2. As shown in Figure 4.3a**,** the lattice parameter *a* gradually increases with increasing Sn content, confirming that Sn^{4+} has entered into the crystal structure successfully. The lattice parameter *c* is first observed to decrease when the doping amount is 1%, due to the stronger binding energy of Sn−O than that of Ni−O, Fe−O, and Mn−O (as described in the Introduction section), which will strengthen the bonding between TM and O and thus shrinking the d-spacing. However, further increasing Sn-doping levels above 1% results in lattice parameter *c* increase, which could be attributed to the larger radius of Sn^{4+} (0.69Å) compared to Mn^{4+} (0.53 Å) and Fe^{3+} (0.645 Å).[16]


(a)
(003)
(006)
(101)
(012)
(104)
(105)
(107)
(018)
(110)
(113)
Sn10% -NaNFMO
Sn8% -NaNFMO
Sn5% -NaNFMO
Sn3% -NaNFMO
Sn1% -NaNFMO
Pristine
Intensity (a.u.)
2 Theta (degree)
(b)
y_obs
y_calc
Obs-Calc
NaNiFeMnO
Rwp= 2.34%
Rp= 1.75%
NaNFMO
Intensity(a.u.)
2 Theta(dergee)
(c)
y_obs
y_calc
Obs-Calc
NaNiFeMnO
Rwp= 1.98%
Rp= 1.56%
Sn1% -NaNFMO
Intensity(a.u.)
2 Theta(dergee)

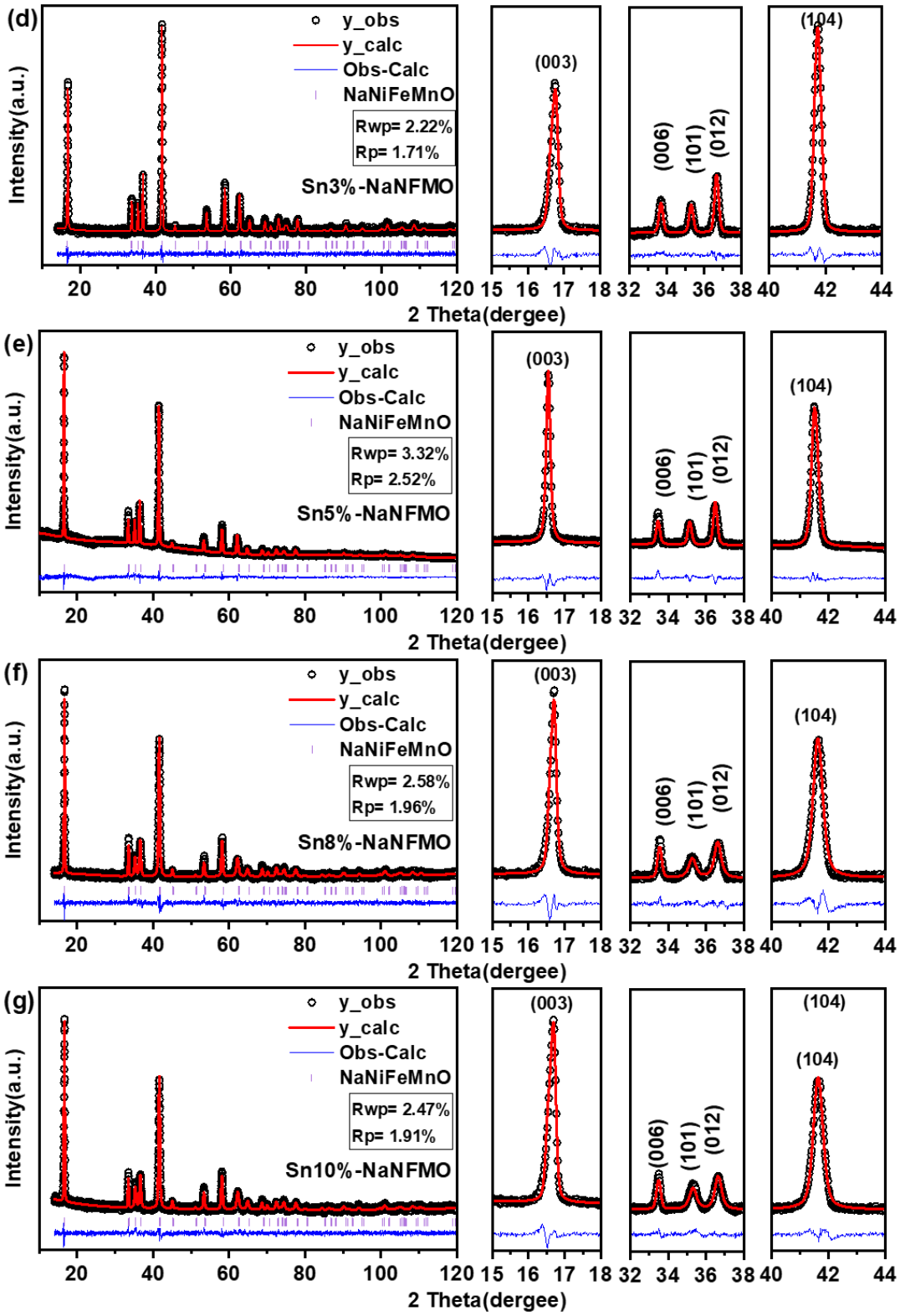


Figure 4.2 Structural characterization of the as-synthesized materials. (a) XRD patterns of all samples; Detailed Rietveld refinements of XRD patterns.

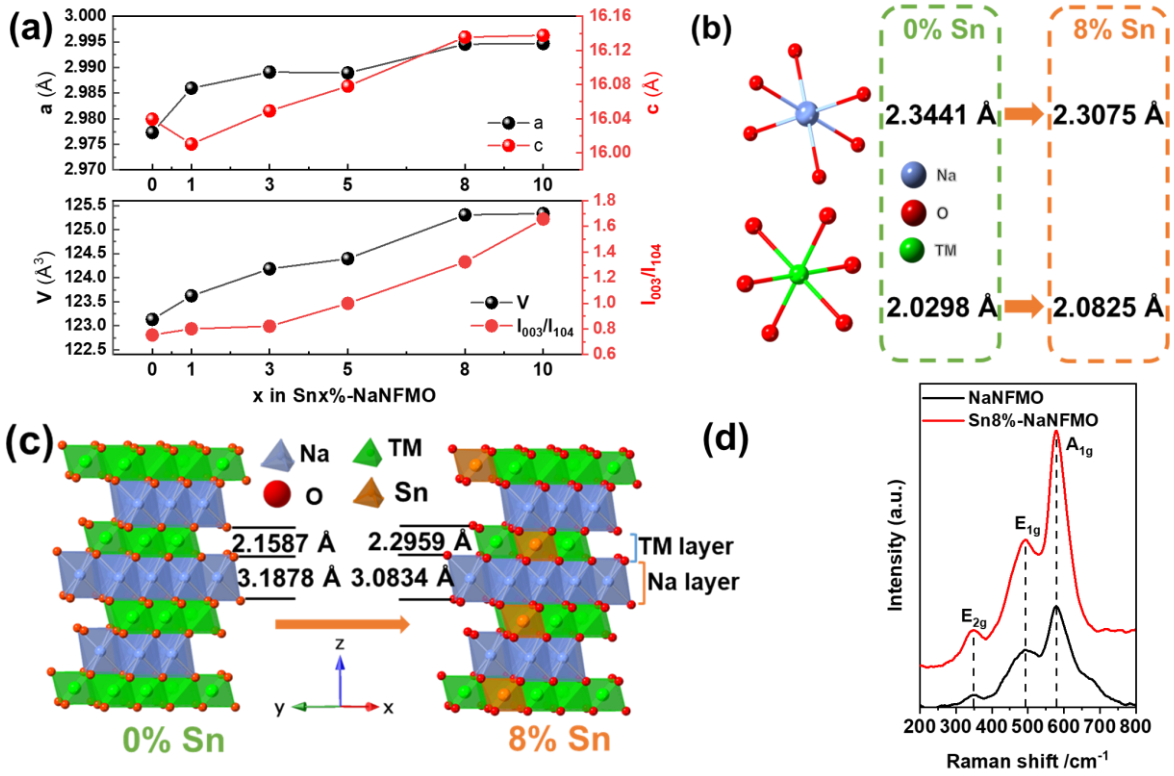


Figure 4.3 (a) Variation of lattice parameters and the I003/I104 value as a function of SnO_2 content; (b, c) Na–O–TM structure evolution before and after 8% Sn modification. (d) Raman spectra of NaNFMO and Sn8%-NaNFMO.

Modulating of O3 NaNFMO via Sn substitution also leads to the expansion of TMO_2 slab (from 2.1587(19) Å to 2.2959(18) Å) and contraction of Na layer spacing (from 3.1878(27) Å to 3.0834(16) Å), associated with the increase in average TM-O bond length, and enhancement of the binding energy between Na and O as illustrated in Figure 4.3b, c and Table 4-2. The change of localized electronic structure upon desodiation /sodiation is considered as the origin of Na^+/vacancy ordering and the resulting phase transitions.[29-32] The enlarged transition metal layers may be beneficial for intensifying the degree of electronic delocalization and thus suppress monoclinic phase transition in high voltage regions and improve electrochemical properties.[29] This effect is confirmed through *in-situ* XRD studies and GITT measurements discussed later.

Additionally, the intensity ratio of I_{003}/I_{104} is a sensitive parameter for indicating the degree of cation mixing. With increasing TM-O bond ionicity, it is more difficult for TM ions to migrate into alternate layers, thus the value of I_{003}/I_{104} dramatically increases from 0.753 for 0% Sn to 1.657 for 10% Sn (Figure 4.3a), indicating that the degree of cation mixing decreases with

increasing Sn content. However, it is worth noting that when the doping amount reaches 10%, the XRD peaks become broadened and reverse back to a higher angle, as evidenced by the d-104 peak. The broadening of the peaks indicates the possibility of having multiple phases with close lattice parameters, which may be due to the sudden increase of Na vacancy (Table 4-3), leading to internal stress and lattice distortion.

The local structure evolution induced by Sn modification was further analyzed by Raman spectroscopy. As shown in Figure 4.3d, both samples show three obvious bonds near 580, 490, and 340 cm^{-1}, which originated from the A_{1g} and E_{1g} modes of TM-O vibrations and the E_{2g} mode of Na vibrations of the layered hexagonal R-3m symmetry, respectively.[33-35] No peak related to Sn-O was found.[36] The intensity of the three bonds all increased after Sn substitution, which indicates the fraction that contributed to the vibrations is increased, and the distortions of the crystal structure decreased. This result also indicates that the Sn^{4+} ions had been successfully incorporated into the lattice.

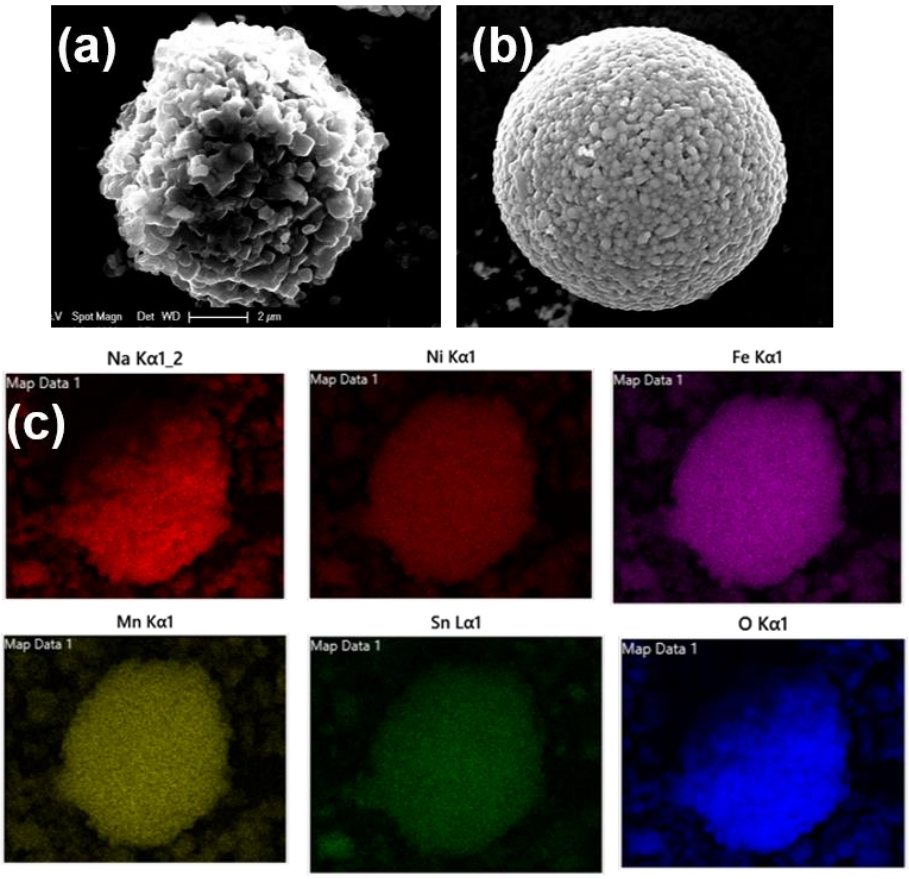


Figure 4.4 SEM images of (a) NaNFMO and (b) Sn8%-NaNFMO. (c) Corresponding EDS elemental mapping for Sn8%-NaNFMO.

The morphology and elemental distribution of Sn-modified samples were analysed by SEM and HRTEM techniques. NaNFMO and Sn8%-NaNFMO are elected as the representative samples. As shown in Figure 4.4a, b, both samples have good spherical secondary particles with an average diameter of ~6 μm, and both spherical secondary particles are comprised of a great number of small primary particles with a diameter in a range of 100-500 nm. However, we can also observe that primary particles of the Sn-modified sample are significantly smaller than those without Sn, and the particles are more densely packed. In addition, the surface of NaNFMO sphere has many voids, while Sn-NaNFMO sphere is much smoother. This difference in morphology suggests that Sn modification may alter the surface properties, particle growth kinetics, and ultimately the final morphology of NaNFMO. The decreased size and enhanced integration could be better for shortening Na^+ diffusion distance and improving the mechanical strength. The EDS mapping of Sn8%-NaNFMO in Figure 4.4c shows that the Sn element is uniformly distributed on the surface of the secondary particle.

To further evaluate the distribution of Sn, cross-section SEM and EDS line scan were used to detect any variation in the elemental distribution within the secondary particle. The Ni, Fe, and Mn elements are relatively uniformly distributed within the particle, while Sn is observed in higher concentrations on the surface of the secondary particles compared to the core, as shown in Figure 4.5a, b. It is expected that the surface-enriched Sn is beneficial for improving-interfacial stability due to the stronger ionic bonding with oxygen.

Figure 4.5c, d show the HRTEM images and corresponding fast Fourier transform (FFT) of NaNFMO and Sn8%-NaNFMO samples, respectively. NaNFMO sample demonstrates well preserved layered lattice fringes in the selected regions with a crystal plane spacing of ~5.34 Å, which can be assigned to a hexagonal phase with the $R\bar{3}m$ space group according to the FFT patterns. By contrast, Sn8%-NaNFMO consists of three structures-from the outermost amorphous structure (≈3 nm) to the upper layer (tens to hundred nm) with rock-salt structure, then to the inner layered structure. The complicated surface structure likely originates from the surface-enriched Sn, which forms a disordered arrangement of sodium and transition metal on the cation lattice.

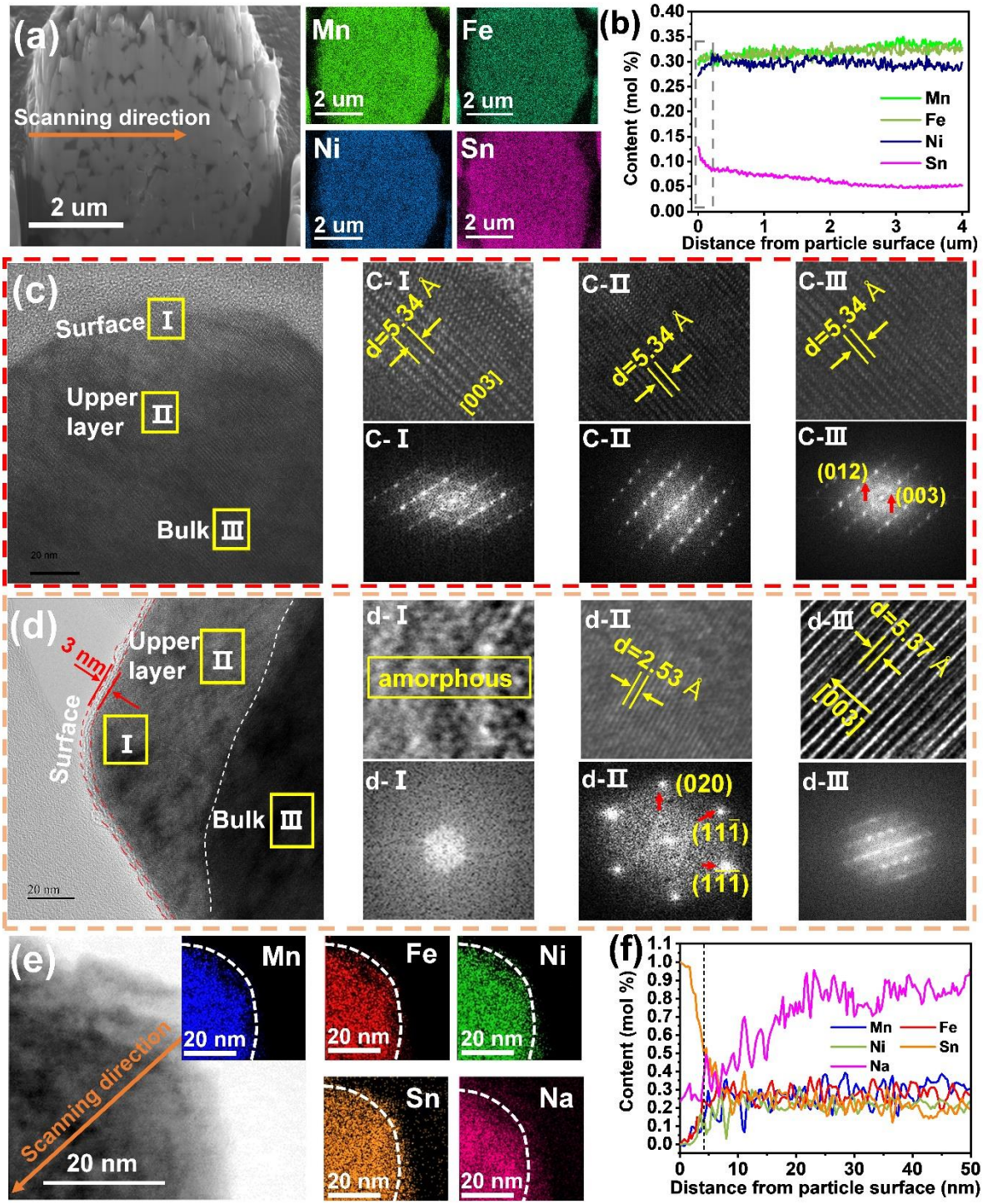
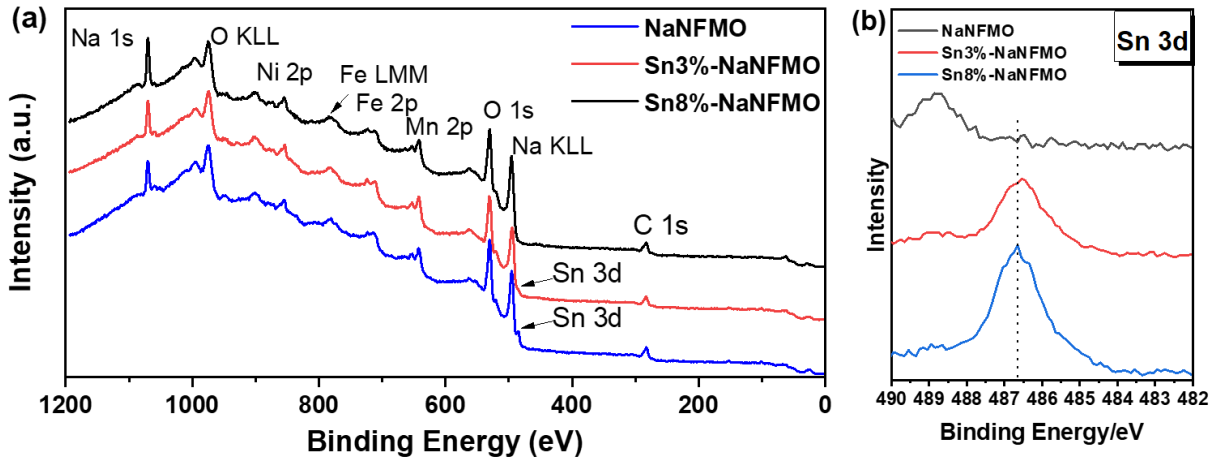


Figure 4.5 (a) Cross-sectional SEM image and EDS element mappings of the as-prepared Sn8%-NaNFMO acquired by FIB, and (b) corresponding counts content distribution of elements along the arrow; HRTEM and the corresponding FFT of (c) NaNFMO and (d) Sn8%-NaNFMO; and (e, f) STEM/EDS mapping and corresponding count content of element distribution in a single primary particle of the Sn8%-NaNFMO.

The surface composition of the particles is complex. Figure 4.5e, f show the elemental mapping and the changes in elemental distribution from the surface of a single primary particle of the as-prepared Sn8%-NaNFMO. To show the distribution of the surface elements more clearly, a curve (white dotted line) is drawn with the range of the Mn element as a benchmark. Sn and Na elements are clearly observed on the outside layer with a thickness of several nanometers, giving direct evidence that the surface coating layer comprises both sodium and tin. XPS results in Figures 4.6 (discussed in detail below) show tin and sodium upon the surface also in these samples. Significant carbonate content is also observed upon the surface in all samples but more so in the nondoped sample. This is attributed to the sensitivity of sodium layered oxides to air[37], as described in Chapter 2.2.2. STEM indicates that the surface of the particles is amorphous in nature. Therefore, from the combination of these characterization techniques, we believe that the amorphous surface to be comprised of a mixture of tin- and sodium-containing carbonates and oxides.

Rietveld refinements were initially performed using the stoichiometric ratio of the elements as designed, with good fitting obtained (Table 4-2). To investigate the tin content in bulk structure, the occupancy of the B site was allowed to refine, the total occupancy of the B site was fixed at 1, the ratio of the Ni, Mn and Fe was fixed at 1:1:1, and the sodium vacancy linked to the Sn content. The resulting crystal structure parameters are shown in Table 4-3. In most cases the Sn content refined to slightly lower than the starting precursor ratio, supporting the observation of Na_2SnO_3 forming on the surface of the particles.



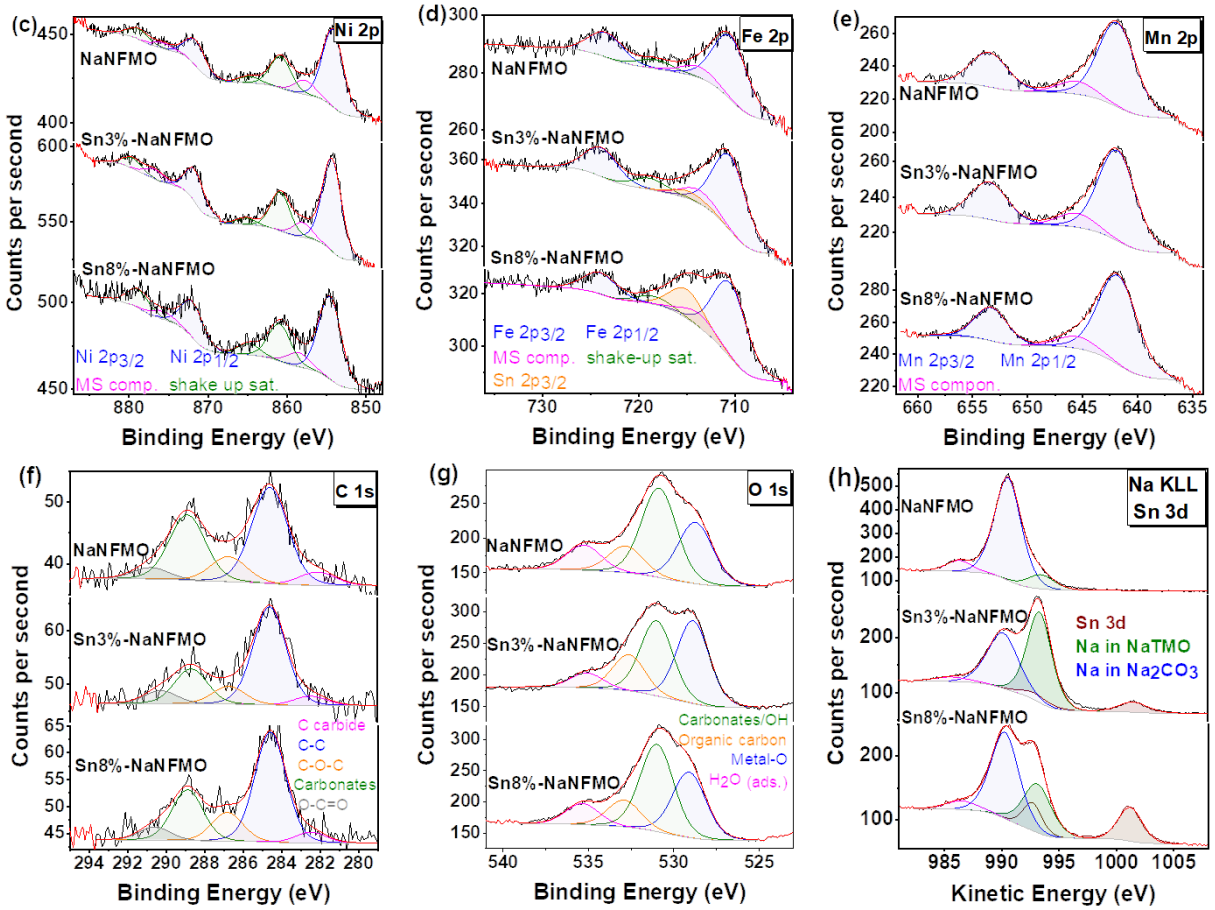


Figure 4.6 XPS spectra from the surface of NaNFMO particles with 0%, 3% and 8% Sn additions (a) Survey XPS spectra, (b) Sn 3d5/2 spectra, (c) Ni 2p, (d) Fe 2p, (e) Mn 2p, (f) C 1s, (g) O 1s , and (h) Na KLL and Sn 3d XPS spectra.

XPS spectra were conducted to investigate the influence of Sn modification on the component and chemical valence. According to the survey spectrum (Figure 4.6a), all the samples show similar peaks, except for the extra peak of Sn located at 486.5 eV in Sn3% and Sn8% modified samples (Figure 4.6b), which corresponds to the existence of Sn^{4+} (486.7 eV in the standard SnO_2 and Na_2SnO_3).[38] The high-resolution XPS spectra of all elements are shown in Figure 4.6c-h. The Ni 2p spectrum (Figure 4.6c) is dominated in the three cases by an intense spin-orbit doublet characterized by binding energies (BE) of the Ni $2p_{3/2}$ and Ni $2p_{1/2}$ core levels of 854.2 eV and 871.5 eV, respectively. The spectra also show intense shake-up satellites at 860.8 eV, 864.7 eV, and 878.9 eV. Since the main photoemission lines are slightly asymmetric in their high binding energy side as a result of unresolved multiplet splitting, two additional components (labelled MS comp. in the Figure) at 857.8 eV and 875.6 eV were added to the fit to account for this asymmetry. All of these binding energy values are compatible with the

presence of Ni^{2+}.[39, 40] The Fe 2p spectra (Figure 4.6d) also show a spin-orbit doublet with BE (Fe $2p_{3/2}$) =710.4 eV and BE (Fe $2p_{1/2}$) =723.9 eV and a small shake-up satellite at 718.3 eV. Similarly to the Ni case, we have simulated the asymmetry in the high binding energy of the main component of the doublet induced by unresolved multiplet splitting by adding a peak at 713.8 eV. All these BE values and spectral features are characteristic of high spin Fe^{3+}.[41, 42] In the case of samples Sn3%-NaNFMO and Sn8%-NaNFMO, there appears an additional peak at 715.0 eV, which corresponds to the Sn $2p_{3/2}$ core level of the tin these samples have been doped with. Finally, the Mn 2p spectra (Figure 4.6e) show a broad spin-orbit doublet, BE (Mn $2p_{3/2}$) = 641.8 eV and BE (Mn $2p_{1/2}$) =653.4 eV, which is characteristic of the presence of Mn^{4+}.[39, 41] A remarkable feature of all these spectra is that no obvious difference was observed with Sn modification, which means TM oxidation states on the surface are essentially identical, indicating likely charge compensation through low level sodium vacancies on the A site with Sn doping rather than a change in oxidation state of the transition metals on the B site.

The recorded C 1s and O 1s spectra are shown in Figure 4.6f, g. The C 1s spectra can be fitted to five different carbon contributions located at 282.1 eV, 284.6 eV, 286.2 eV, 288.9 eV, and 290.8 eV, which can be associated to carbides, C-C bonds, C-O-C bonds, carbonates, and O-C=O groups, respectively.[38, 43, 44] The O 1s spectra were fitted to four different components located at 528.7 eV, 530.8 eV, 532.8 eV, and 535.3 eV corresponding to metal-oxygen bonds, carbonates/OH groups, organic carbon, and adsorbed water, respectively.[45-47] In particular, it is very remarkable that the intensity of the carbonate contribution decreases; it amounts to 46% in the pristine NaNFMO, and down to 20% and 24% in Sn3%-NaNFMO and Sn8%-NaNFMO, respectively. The decrease in the carbonate contribution is also reflected in the O 1s spectra and Na KLL spectra (Figure 4.6h). The modified surface may explain the lower concentration of sodium carbonates on the surface.

Mössbauer spectroscopy was used to further verify Fe^{3+}. The Mössbauer spectra recorded from these samples consisted of a paramagnetic quadrupole doublet (Figure 4.7a). The spectra were best fitted to a distribution of quadrupole split absorptions (Figure 4.7b) with values of chemical isomer shift (0.34 mm/s). The distributions show relative maxima at around 0.54 mm/s and 0.90 mm/s with an average value of 0.65 mm/s, which are characteristic of Fe^{3+} in octahedral oxygen coordination.[48, 49] This is consistent with the XPS data. The fitting to a distribution model as opposed to discrete one or two doublets indicates that whilst the Fe^{3+} ions adopt essentially

identical octahedral sites, the electronic environments of the Fe^{3+} ions experience perturbation from the nearest neighbor or next nearest neighbor ions. The data indicate that the introduction of increasing concentrations of Sn^{4+} enhances the heterogeneity of these minutely different electronic environments presumably as a result of the higher charge on Sn^{4+}.

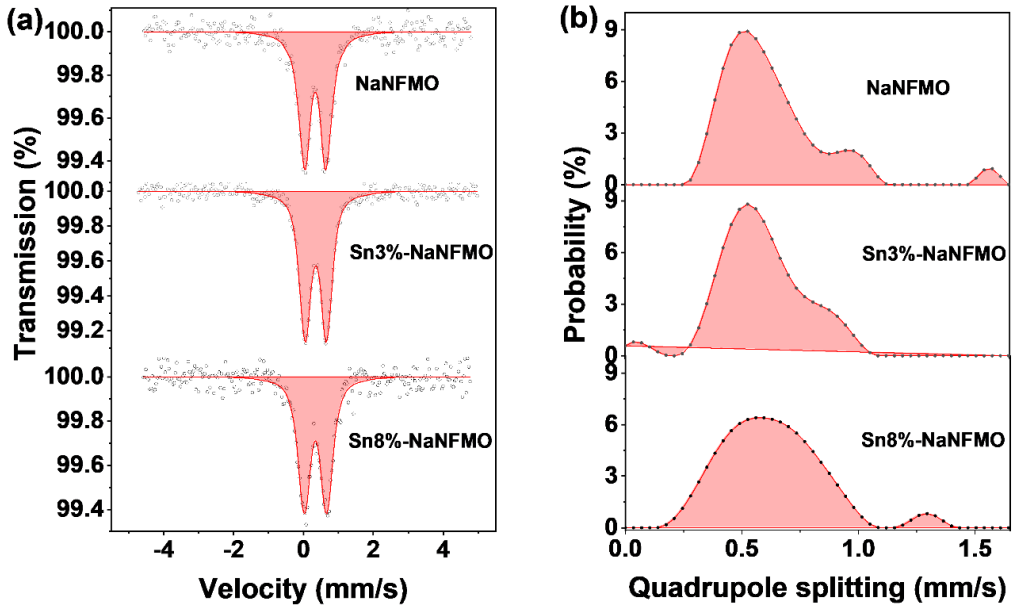


Figure 4.7 (a) Room temperature ^{57}Fe Mössbauer spectra recorded from pristine NaNFMO, Sn3%-NaNFMO, and Sn8%-NaNFMO. (b) Quadrupole splitting distributions obtained from the fit of the spectra presented on (a).

This detailed compositional analysis indicates that simultaneous bulk and surface modifications occur in these samples. Sn^{4+} substitutes onto the B site lattice, with no change to the oxidation states of the other transition metals, forming sodium ion vacancies upon the A site. The remaining sodium and tin form a Sn/Na/O rock salt coating upon the particle surface.

4.3.2 Electrochemical performance

The electrochemical properties of the synthesized cathodes were evaluated in the voltage range of 2.0-4.1 V *vs* Na/Na^+. Figure 4.8a shows the initial galvanostatic charge/discharge curves of the prepared cells with a current density of 15 mA g^{-1} (0.1C). The initial discharge capacity decreases as the Sn content increases, giving 135.1, 132.5, 129.5, 128.6, 126.9, and 120.3 mAh g^{-1} for NaNFMO, Sn1%-NaNFMO, Sn3%-NaNFMO, Sn5%-NaNFMO, Sn8%-NaNFMO, and Sn10%-NaNFMO, respectively, partially due to the higher molecular weight of Sn compared

to Ni, Fe, and Mn, and A site sodium vacancies produced by charge balance of Sn^{4+} on the B site. The Sn modified electrodes exhibit higher charge/discharge voltage over the potential range than the pristine one, and show a smoother voltage profile, indicating greater solid solution phases, rather than phase changes occurring as the sodium intercalates and deintercalates (except the one with 10% Sn).

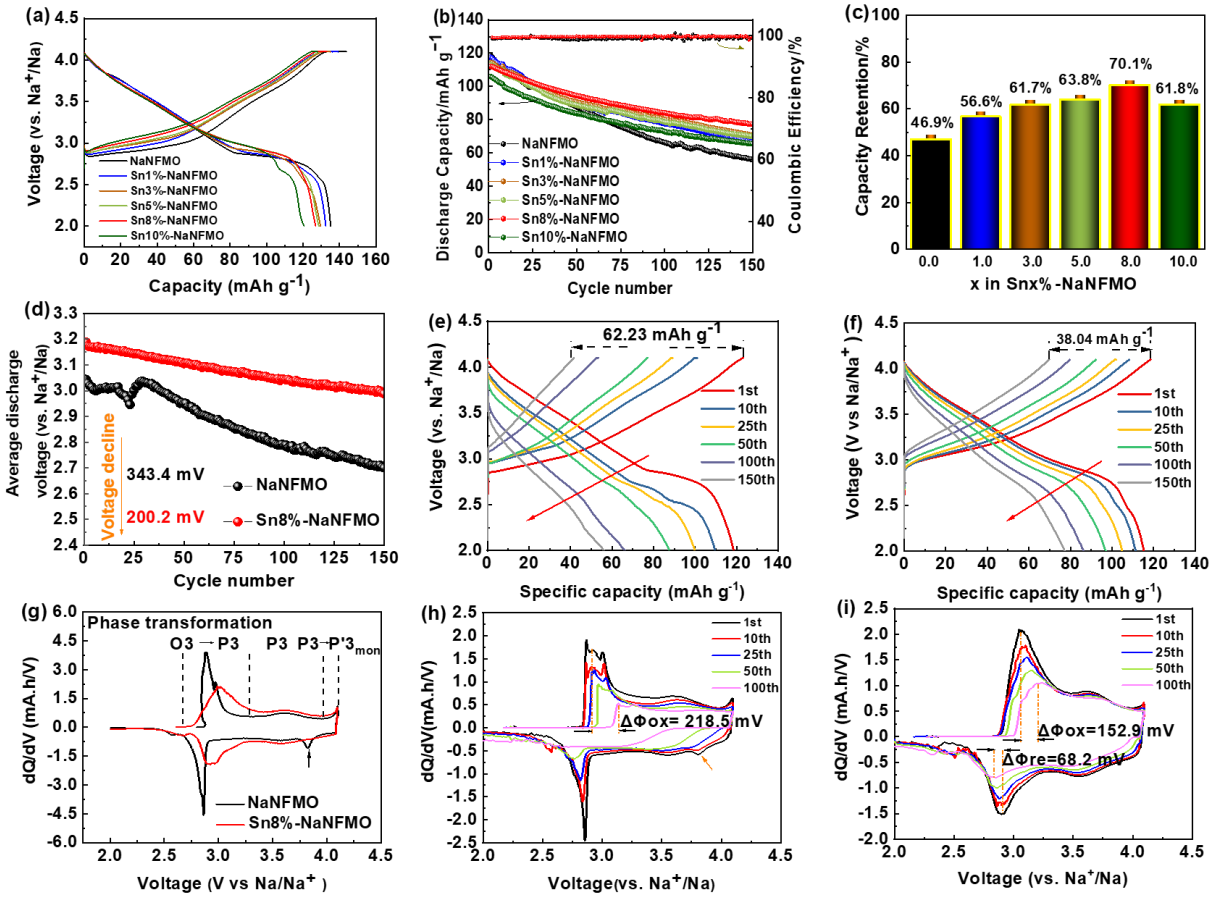


Figure 4.8 Electrochemical performance of the as-synthesized materials. (a) Initial charge-discharge curves at room temperature; (b-c) The cycling performance and capacity retention of all the electrodes after 150 cycles at 75 mA/g (0.5C); (d) The average discharge voltage of NaNFMO and and Sn8%-NaNFMO at 0.5C; Charge/discharge curves of different cycles for (e) NaNFMO and (f) Sn8%-NaNFMO (g) Comparison of initial differential capacity (dQ/dV) curves of NaNFMO and Sn8%-NaNFMO at 0.1C; dQ/dV curves of (h) NaNFMO and (i) Sn8%-NaNFMO cathodes under various cycles at 0.5C;

To understand the effects of Sn modification on the long-term cycling performance, after three cycles at 15 mA g^{-1}, all the cells were cycled between 2.0 and 4.1V *vs* Na/Na^+ at a current density of 75 mA g^{-1} (0.5C) for 150 cycles. As shown in Figure 4.8b, c, although the pristine NaNFMO cathode showed the highest primary capacity (118.9 mAh g^{-1}), it shows a rapid

decrease with cycling, leading to a capacity retention of only 46.9% after 150 cycles. In contrast, Sn modified samples show gradually improved capacity retentions, and Sn8%-NaNFMO displays the best cycling performance with a capacity retention of 70.1% for the same cycling period, which was much higher compared to NaNFMO. In addition, Sn8%-NaNFMO electrode offered the highest and most stable coulombic efficiency among all during the whole cycling period. These results indicate that appropriate SnO_2 modification can greatly improve the electrochemical performance of O3 layered oxides. Sn-free NaNFMO and Sn8%-NaNFMO are further compared in detail.

Figure 4.8d compares the variation of average discharge voltage with cycling between NaNFMO and Sn8%-NaNFMO. The average discharge voltage notably rises from 3.04 V to 3.19 V *vs* Na^+/Na with 8%Sn modification. As previous reports, the rising of the average voltage is caused by the increase of ionicity of the B-O bond in the O3-type ABO_2, after Sn-substitution through reduced d orbital overlap between transition metals and oxygen within the MO_2 slabs.[19, 20, 22] The average voltage upon discharge of NaNFMO dropped significantly from 3.04 to 2.70 V *vs* Na/Na^+ with a retention rate of 88.7% after 150 cycles at 0.5C. Encouragingly, Sn8%-NaNFMO exhibits excellent voltage retention of 93.7%. The average voltage only dropped by 200.2 mV from 3.19 to 2.99 V (*vs* Na^+/Na), compared to 343.4 mV of NaNFMO. This indicates significantly lower polarisation increase upon cycling. The capacity *vs* voltage profiles of NaNFMO and Sn8%-NaNFMO at various cycles are shown in Figure 4.8e, f.

To further verify the improved structural stability of the modified electrode, the dQ/dV studies were performed. Figure 4.8g shows the differential capacity curves of NaNFMO and Sn8%-NaNFMO cathodes at the first cycle. The sharper peaks observed in NaNFMO (black line) represented the phase changes within the structure[50], which is different from the depressed and broader peaks in Sn8%-NaNFMO (blue line), indicating a greater solid solution limit between phase changes. The first peak around 3.0 V (*vs* Na^+/Na) can be attributed to the phase transition from O3 to P3. The redox potential of Sn8%-NaNFMO cathode increases from 2.9 V to 3.0 V (*vs* Na^+/Na), which means that the phase transition from O3 to P3 moved to higher voltages. Furthermore, the depressed and broader peaks imply that Sn8%-NaNFMO undertook a temperate transformation between phases, and the O3 phase remained stable for the majority of the Na-ion deintercalation process. Upon charging above 4.0 V (*vs* Na^+/Na), a new oxidation peak and a corresponding reduction peak around 3.8 V (*vs* Na^+/Na) (marked as an arrow) are

observed for the NaNFMO cathode. It is associated with the conversion of the P3 phase into a new phase, monoclinic P'3 as reported[3, 5], which consists of a distorted lattice in comparison to an ideal hexagonal cell. In contrast, there is no corresponding reduction peak during 3.85-3.75 V (*vs* Na^+/Na) of Sn8%-NaNFMO when discharged to 2.0 V (*vs* Na^+/Na). The higher charging voltage triggers the irreversible P3→P'3 phase transformation, but the Sn modified Sn8%-NaNFMO increases this irreversible phase transition to 4.1 V compared to 4.0 V (*vs* Na^+/Na) for Sn-free NaNFMO sample. Upon cycling, the polarization and irreversibility of NaNFMO electrode are effectively reduced by Sn modification (Figure 4.8h, i). The redox peaks for Sn8%-NaNFMO remain even after 100 cycles while all the oxidation and reduction peaks essentially disappear for NaNFMO. It is noteworthy that the high voltage O3-P'3 oxidation peak, completely disappeared after only 10 cycles, illustrating the irreversibility of the P3-P'3 phase transition.

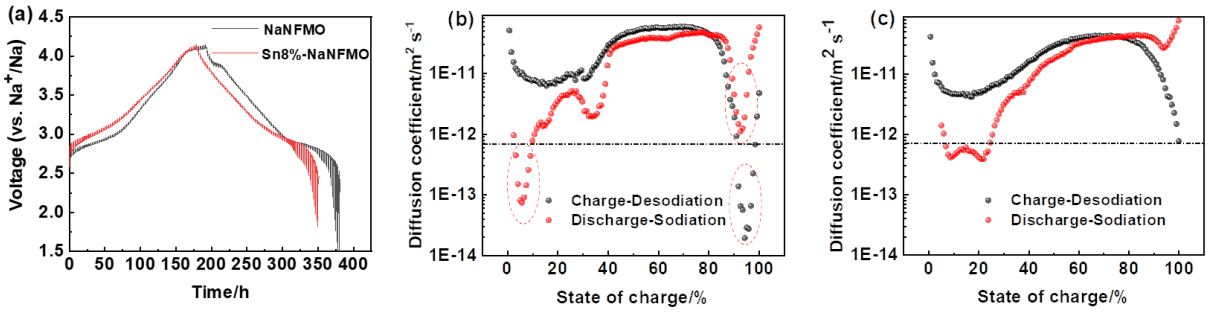


Figure 4.9 (a) GITT curves of NaNFMO and Sn-NaNFMO cathode material in the first cycle within 2.0-4.1V; Na diffusivity versus state of charge and discharge calculated by GITT of (b) NaNFMO and (c) Sn8%-NaNFMO.

To examine the influence of Sn modification on the kinetics behaviour of Na^+, GITT (galvanostatic intermittent titration technique) was carried out to determine the apparent diffusion capability of Na^+ (D_{Na}) in the initial charge/discharge process based on Equation (4-1) introduced by Weppner and Huggins[51]:

$$D = \frac{4}{\pi\tau}\left(\frac{m_{AM}V_M}{M_{AM}S}\right)^2\left(\frac{\Delta E_s}{\Delta E_t}\right), \text{ with } \tau \ll \frac{L^2}{D} \qquad (4\text{-}1)$$

where D is the apparent diffusion coefficient (cm^2 s^{-1}), τ means the applied current time interval, m_{AM}, V_M, M_{AM} and L represent the mass of active material, molecular volume, molar weight and thickness of the electrode, respectively. S refers to the electrode effective surface area, which was calculated from the electrode properties and the average particle size. ΔE_s and

ΔE_t are changes of the steady-state voltage (ΔE_s) and total change of the cell voltage (ΔE_t) during per GITT step. More details are listed in Table 4-4.

The D_{Na} calculated from GITT curves (Figure 4.9a) as a function of state of charge during both sodiation and desodiation processes are shown in Figure 4.9b and Figure 4.9c. In general, both samples show a similar profile, with a peak around 70% SoC, and two troughs at the end of charge and discharge, respectively. Both electrodes display almost the same D_{Na} value most of the time (10%-90% SoC) in the charging and discharging process. However, the Sn modified sample exhibits an increased D_{Na} value at the end of charge and discharge. Specifically, the diffusion coefficient of Na^+ in the Sn8%-NaNFMO electrode is ~2.07×10^{-11} to 4.41×10^{-11} cm^2s^{-1} within the voltage window of 2.5-4.0 V and ~1.88×10^{-11} to 7.75×10^{-13} cm^2s^{-1} within the voltage window of 4.0-4.1 V. By contrast, the D_{Na} value for the NaNFMO electrode is ~ 6.28×10^{-12} to 5.99×10^{-11} cm^2s^{-1} within the voltage window of 2.5-4.0 V (*vs* Na^+/Na) and ~ 1.59×10^{-11} to 1.93×10^{-14} cm^2s^{-1} within the voltage window of 4.0-4.1 V (*vs* Na^+/Na). The D_{Na} value for NaNFMO at the end of charge is only one-tenth of those for Sn8%-NaNFMO, which further indicates that the phase transition in the high voltage region results in sluggish kinetics for Na-ion, and Sn doping suppresses the unfavourable structure change.

The interfacial impedance information and the internal Na^+ diffusion coefficient of the two samples after 100 cycles were analyzed by EIS according to the method reported previously.[52] Figure 4.10a, b display the Nyquist plots of the two samples under fully charged state with different cycles at 0.5C, and the equivalent circuits fitted by Z View 2.0 software are inserted. The small interrupt at the beginning corresponds to the solution resistance Re. The two semicircles in the high and middle frequency can be attributed to the electrified interface resistance (Rsf) and the charge transfer resistance (Rct) between the electrolyte and electrode, respectively. The approximate straight line in the low frequency reflects the Na^+ diffusion impedance within the cathode bulk crystal (Ws).[53] The fitted parameters are shown in Figure 4.10c. The Sn modified sample displays a much lower increase in Rct impedance than the pristine sample after 100 cycles, which indicates that the interface side reaction is significantly suppressed due to the enhanced crystal structure as well as the modified surface. The calculated D_{Na} is 1.59×10^{-12} cm^2 s^{-1} for Sn8%-NaNFMO after 100 cycles, which is much higher than 2.17×10^{-13} cm^2 s^{-1} for NaNFMO. The smaller impedance and higher D_{Na} signify the structure of Sn8%-NaNFMO remains well-ordered after extended cycling. Combining the results of

GITT and EIS, we can conclude that the Sn modification has a positive effect both on the kinetics behaviour of Na^+ and the structural stability of the material after cycling.

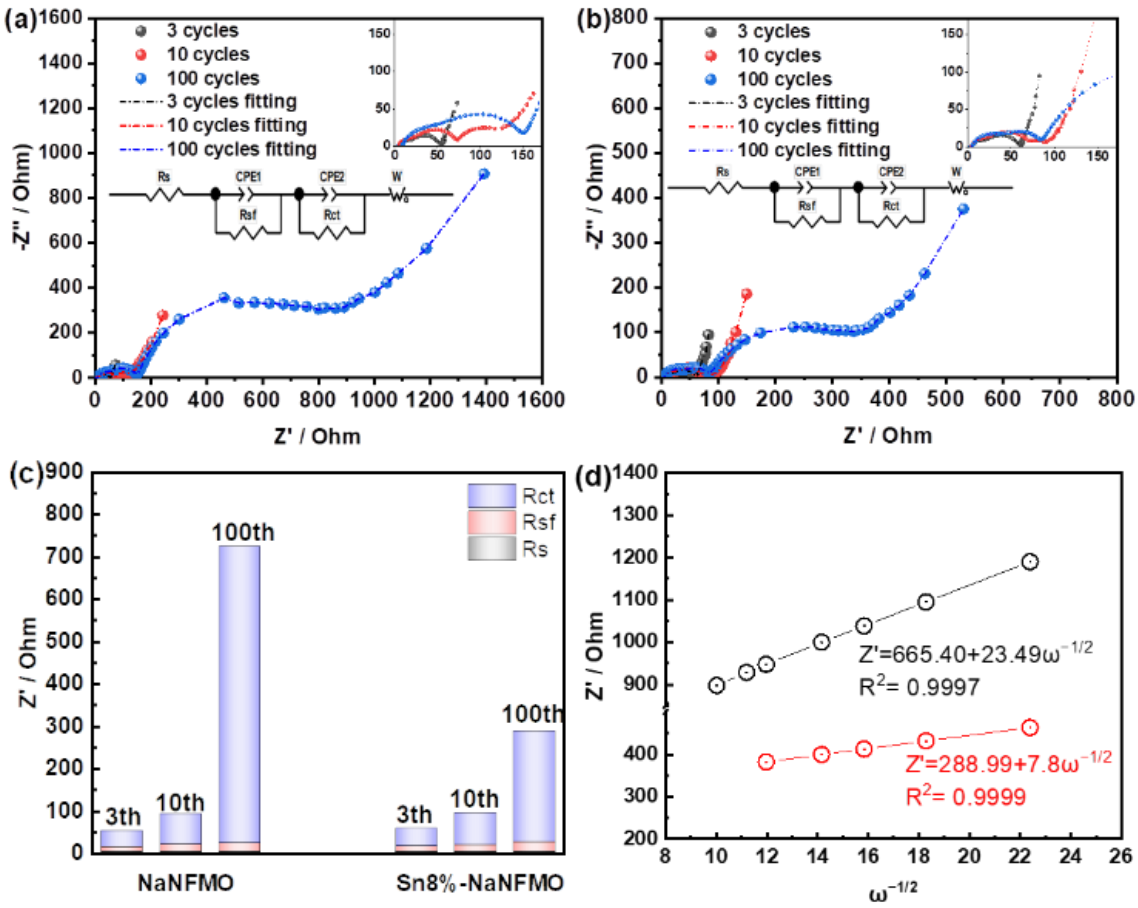


Figure 4.10 Nyquist plots of (a) NaNFMO and (b) Sn8%-NaNFMO after different cycles. (c) Comparison of fitted impedance for NaNFMO and Sn8%-NaNFMO. (d) Liner fitting of Z' vs. $\omega^{-0.5}$ in the low-frequency region for NaNFMO and Sn8%-NaNFMO samples after 100 cycles.

4.3.3 Mechanism investigation

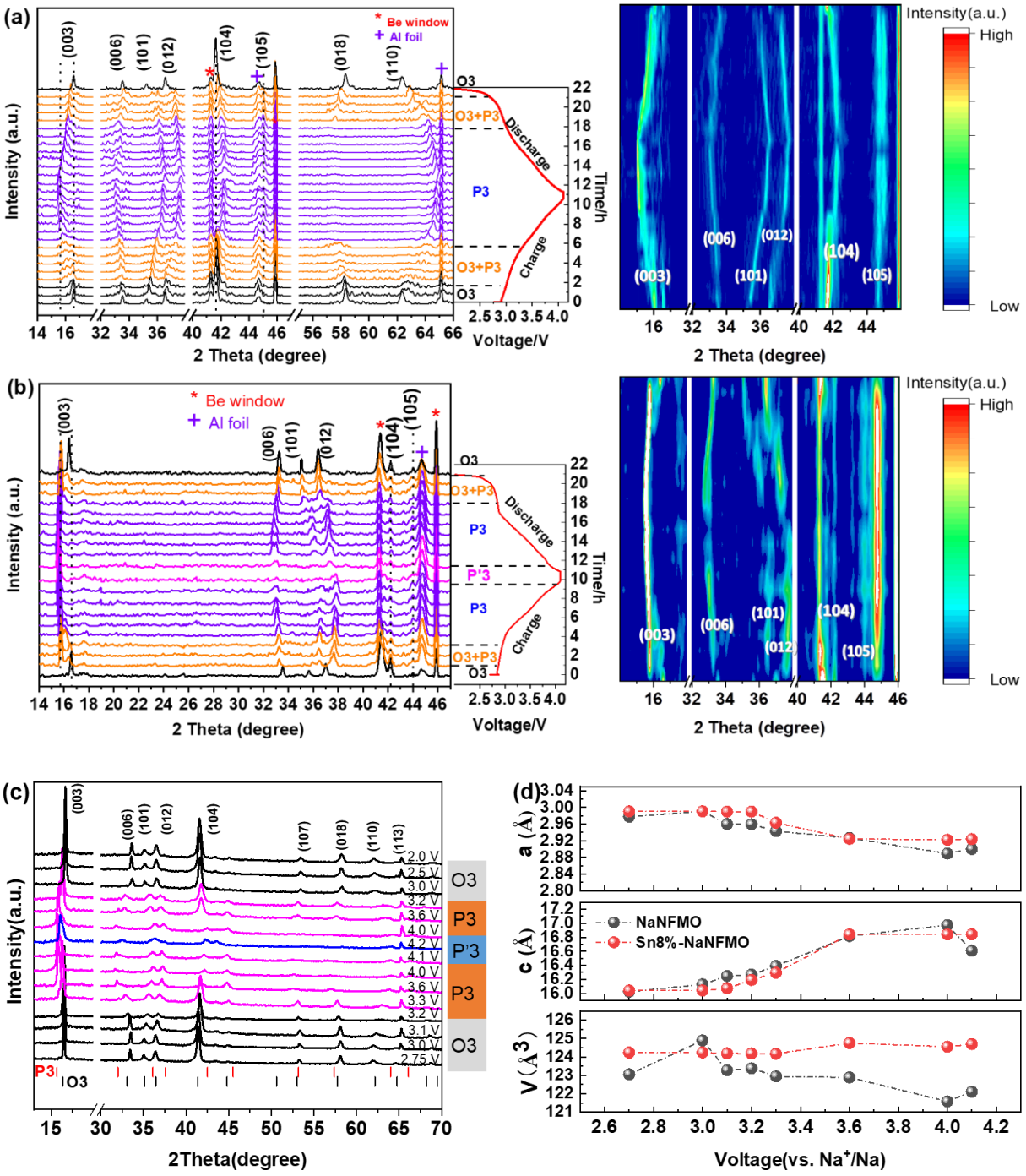


Figure 4.11 Operando XRD patterns and corresponding 2D contour maps showing the evolution of the main characteristic peaks for (a) Sn8%-NaNFMO and (b) NaNFMO cathodes during the first charge/discharge process between 2.0 V and 4.1 V at 0.1 C. (c) EX-situ XRD patterns during the first charge/discharge of Sn8%-NaNFMO electrodes between 2.0 V and 4.2 V at 0.1 C. (d) Lattice parameters a, c and V evolution during charge process.

To gain insight into the effects of Sn modification on structural evolution upon Na^+ extraction/insertion, operando XRD analysis was performed for NaNFMO and Sn8%-NaNFMO electrodes during the first cycle in the voltage range of 2.0-4.1 V (*vs* Na^+/Na) at 0.1C. Figure 4.11 shows the corresponding XRD patterns collected at various charge and discharge depths in Na half-cells. Generally, this peak variation is in good agreement with the previous report, demonstrating an $O3_{hex}$→$P3_{hex}$→($P'3_{mon}$)→$P3_{hex}$→$O3_{hex}$ sequence during cycling.[3, 29] Upon initial charging, (003), (006), and (018) peaks shift to lower angles, while (101), (012), (104), and (110) peaks shift to higher angles for both samples, indicating the increase of c-axis and decrease of a-axis in the O3 phase. When charging to 3.2 V (*vs* Na^+/Na), NaNFMO sample experiences the first phase transition from hexagonal O3 to hexagonal P3 phase, which was evident from the fact that the (003) peak shift from 16.5° to 16.0° and a significant decrease in peak intensity of (104), as well as the appearance of (105) peak. In contrast, the O3 phase of Sn8%-NaNFMO remains until 3.3 V, indicating that the phase transitions from hexagonal O3 to hexagonal P3 was delayed by the Sn modification, which was consistent with the dQ/dV curve. Significant differences between the two cathodes were observed when it came to the end of the charge state. With further charging to 4.0 V (*vs* Na^+/Na), the peak profile of the P3 phase becomes asymmetrical for NaNFMO, accompanied by the disappearance of $(006)_{Hex.P3}$ and $(105)_{Hex.P3}$ peaks. Such peak changing indicates structural deterioration, which can be assigned to the monoclinic P'3 phase with a distorted lattice observed in previous literature.[54] In contrast, the $(006)_{Hex.P3}$ and $(105)_{Hex.P3}$ peaks in P3 phase still remain for Sn8%-NaNFMO until further charging to 4.2 V (*vs* Na^+/Na) as shown in Figure 4.11c, indicating that the unfavourable high voltage phase transformation was suppressed. Upon discharge, all of the peaks can shift back to the initial positions, indicating a reversible process in the first cycle. The evolution of lattice parameters was derived by Rietveld refinement and reported in Figure4.11d.

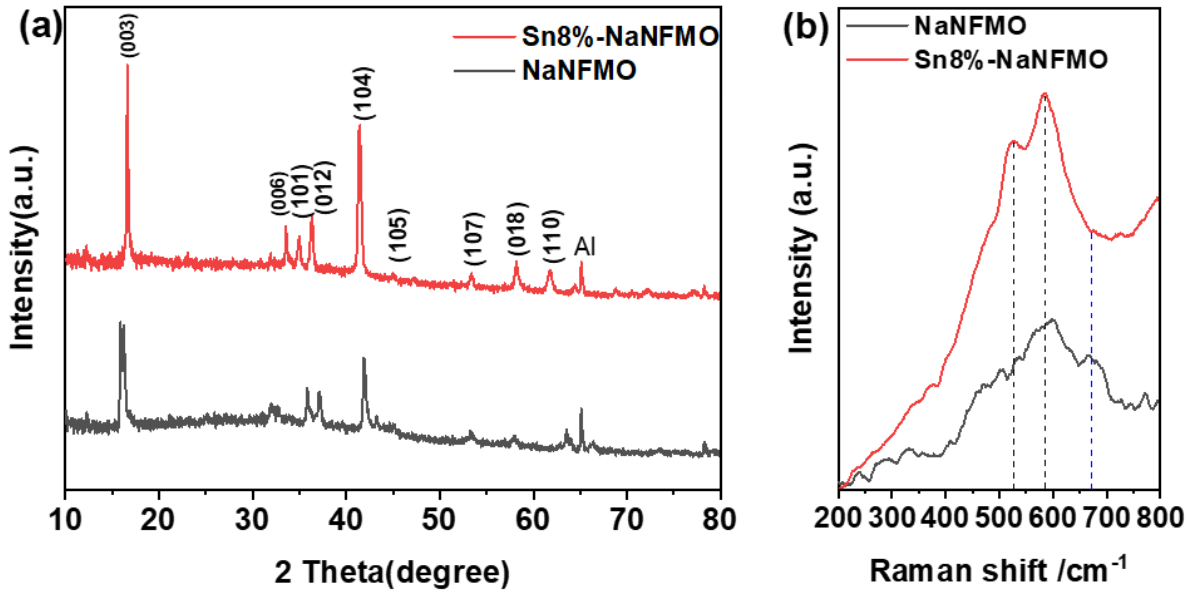


Figure 4.12 (a) XRD patterns and (b) Raman spectra of NaNFMO and Sn8%-NaNFMO after 100cycles.

Post-mortem analyses were conducted to examine the improved structural stability of Sn8%-NaNFMO cathode. Figure 4.12a shows the XRD patterns of the pristine and 8%Sn modified cathode after 100 cycles. The data for NaNFMO shows a significant reduction in peak intensity along with evidence for some peak splitting (particularly for the (003) reflection) indicative of significant structural changes. This is further shown in the Raman data with the emergence of the characteristic peak of spinel-like structure around 660 cm^{-1}, [78] as shown in Figure 4.12b**.** In contrast, the positions and intensities of the XRD and Raman peaks of Sn8%-NaNFMO were well maintained.

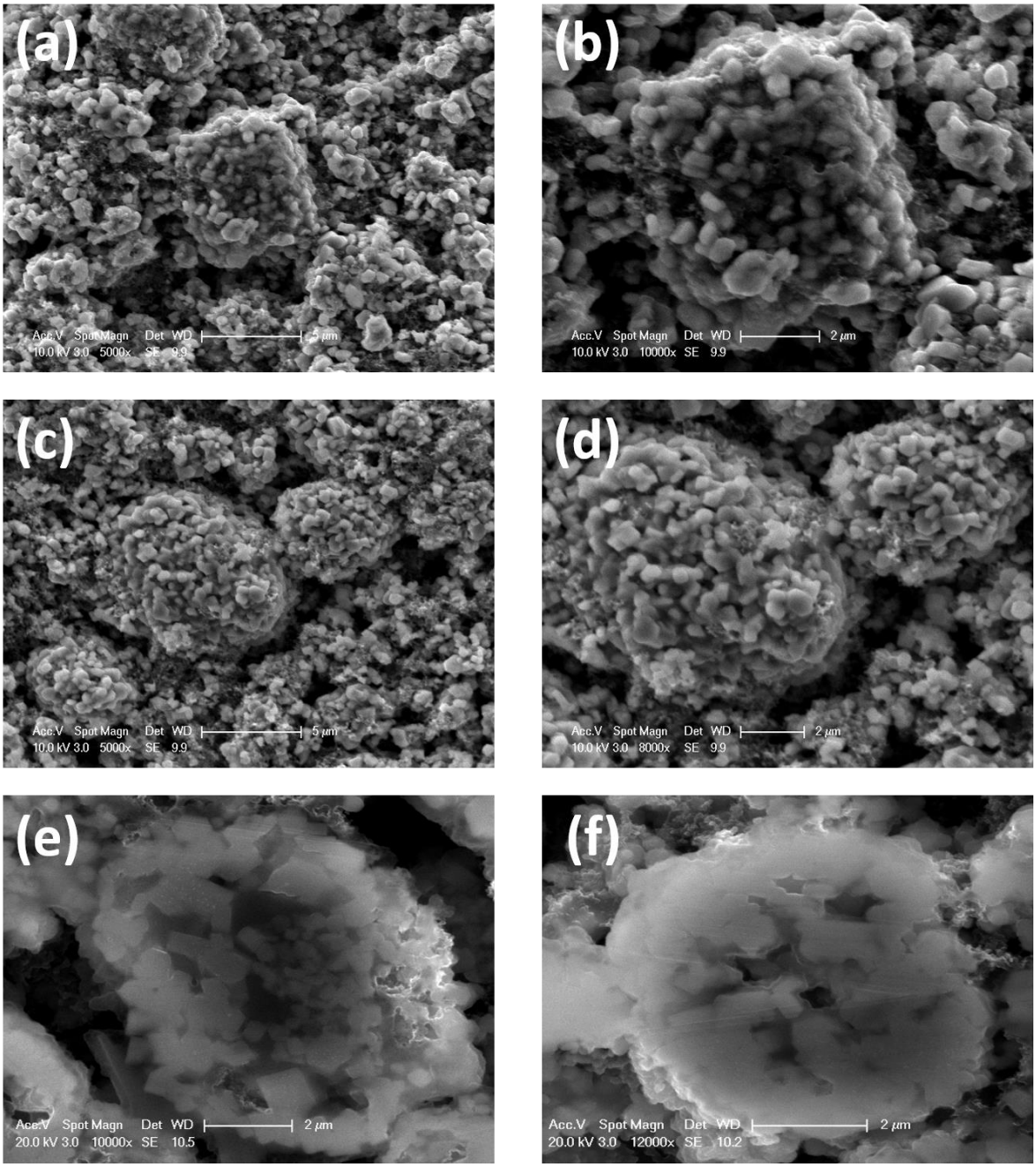


Figure 4.13 SEM images of NaNFMO (a, b) and Sn8%-NaNFMO (c, d) after 150 cycles. Cross-section images of NaNFMO (e) and Sn8%-NaNFMO (f) after 150 cycles.

The morphology of the cathodes after 150 cycles under 0.5C were observed by SEM. As shown in Figure 4.13, although no immediate difference was observed, at a closer inspection of the particles from the nondoped sample (Figure 4.13 b,e) surface degradation is observed. Particularly in Figure 4.13 e, the porous particle shows an interface grown into the middle of the sample, while Figure 4.13 b shows a “glue”-type surface coating. In the Sn8% cathode

(Figure 4.13 f), there are still open central particle pores that are not filled by this cathode interface growth, and Figure 4.13 d shows less apparent surface degradation on the particles. These results indicate the enhanced structural and surface stability during long-term cycling on Sn incorporation.

4.4 Conclusion

The successfully synthesized novel, low-cost Sn modified O3-type cathode material (Sn8%-NaNFMO) has been shown to exhibit both good structure stability and electrochemical properties via an industrially feasible co-precipitation method. The influence of Sn modification of $Na[Ni_{1/3}Fe_{1/3}Mn_{1/3}]O_2$ on the crystal structure and electrochemical properties has been investigated for the first time, and the mechanism was discussed preliminarily. XRD test and refinement indicated that Sn modified sample kept the same O3 type crystal structure of the pristine $Na[Ni_{1/3}Fe_{1/3}Mn_{1/3}]O_2$ with enlarged d-spacing of the Na^+ layer. Electrochemical analyses demonstrated that Sn modification was effective in suppressing the phase transformation and thus improving the structure stability significantly, leading to a highly improved Na storage behavior in terms of average voltage, rate capability, and cycling stability. As a result, the 8%Sn modified NaNFMO cathode exhibited its optimized cycling performance by an almost doubled capacity retention increase after 150 cycles in the wide voltage range of 2.0-4.1 V (*vs* Na^+/Na). This work demonstrates that controlled Sn modification is a practical and efficient strategy for stabilizing O3-type layered structures for sodium-ion batteries.

Table 4-2 Summary of the refined parameters and the R factors.

	NaNFM	Sn1%-	Sn3%-	Sn5%-	Sn8%-	Sn10%-
Sn Occupancy	0.0000	0.0099	0.0291	0.0476	0.0741	0.0909
TM	0.3333	0.3300	0.3236	0.3175	0.3086	0.3030
Na	1.0000	0.9901	0.9709	0.9524	0.9259	0.9091
Rwp/%	2.34	1.98	2.22	3.32	2.58	2.47
Rp/%	1.75	1.56	1.71	2.52	1.96	1.91
Chi^2	1.7290	1.59	1.416	0.6448	1.71	1.442
a(Å)	2.97732(22)	2.98597(9)	2.98897(8)	2.98895(8)	2.99471(10)	2.99267(10)
c(Å)	16.0395(17)	16.0103(7)	16.0480(8)	16.0782(8)	16.1379(12)	16.1681(12)
c/a	5.3872	5.3619	5.3692	5.3792	5.3883	5.3888
V($Å^3$)	123.132(25)	123.624(10)	124.163(10)	124.395(11)	125.339(14)	125.403(13)
z for 6c site	0.23396(23)	0.23009(16)	0.23404(17)	0.23488(17)	0.23780(22)	0.23626(22)
Na layer(Å)	3.1878(27)	3.3059(17)	3.1869(10)	3.1659(16)	3.0834(16)	3.1390(14)
TMO_2(Å)	2.1587(19)	2.0309(13)	2.1624(10)	2.1935(11)	2.2959(18)	2.2504(17)
Na-O(Å)	2.3442(25)	2.3884(18)	2.3488(19)	2.3417(18)	2.3165(23)	2.3343 (24)
TM-O(Å)	2.0298(20)	2.0007(13)	2.0364(14)	2.0444(15)	2.0754(19)	2.0619(19)

Table 4-3 Summary of the further refined parameters and the R factors considering the sodium vacancy.

	NaNFM	Sn1%-	Sn3%-	Sn5%-	Sn8%-	Sn10%-
Sn Occupancy	0.0000	0.0759	0.0178	0.0156	0.0331	0.0908
TM Occupancy	0.3333	0.3080	0.3277	0.3281	0.3223	0.3089
Na Occupancy	1.0000	0.9241	0.9831	0.9844	0.9669	0.9092
Rwp/%	2.46	1.93	2.15	3.30	2.57	2.47
Rp/%	1.85	1.53	1.67	2.50	1.96	1.91
Chi^2	1.9110	1.506	1.321	0.6366	1.692	1.442
a(Å)	2.9775(2)	2.98594(9)	2.98897(8)	2.98899(8)	2.99473(10)	2.99267(10)
c(Å)	16.040(2)	16.0102(7)	16.0480(8)	16.0783(9)	16.1377(12)	16.1681(12)
c/a	5.3872	5.3619	5.3691	5.3792	5.3887	5.4026
V(Å^3)	123.152(3)	123.620(10)	124.163(10)	124.400(10)	125.339(14)	125.403(13)
z for 6c site	0.23396(23)	0.23145(18)	0.23372(20)	0.23405(19)	0.23658(27)	0.23625(24)
Na layer(Å)	3.1876(21)	3.2630(11)	3.1975(14)	3.1929(21)	3.1217(12)	3.1387(14)
TMO$_2$(Å)	2.1589(10)	2.0738(13)	2.1519(24)	2.1665(32)	2.2575(17)	2.2506(11)
Na-O(Å)	2.3281(29)	2.3734(20)	2.3524(21)	2.3509(21)	2.3293(29)	2.3342(26)
TM-O(Å)	2.0428(23)	2.0118(15)	2.0336(17)	2.0375(16)	2.0648(24)	2.0620(21)

Table 4-4 Summary of cell parameters used for GITT calculation

			NaNFM	Sn8%-NaNFMO
τ	the applied current time interval	min	90	90
M_{AM}	atomic weight of active material	g mol^{-1}	111.48	116.46
V_M	the molar volume of active material	cm^3 mol^{-1}	23.32	24.36
m_{AM}	mass of active material	mg	6.78	6.86
L	the thickness of the electrode	um	29	30
S	the electrode surface area	cm^2	16.34	16.56

4.5 References

1. Kim, D.; Lee, E.; Slater, M.; Lu, W.; Rood, S.; Johnson, C. S., Layered $Na[Ni_{1/3}Fe_{1/3}Mn_{1/3}]O_2$ cathodes for Na-ion battery application. *Electrochemistry Communications* **2012,** 18, 66-69.
2. Wang, H.; Liao, X.-Z.; Yang, Y.; Yan, X.; He, Y.-S.; Ma, Z.-F., Large-Scale Synthesis of $NaNi_{1/3}Fe_{1/3}Mn_{1/3}O_2$ as High Performance Cathode Materials for Sodium Ion Batteries. *Journal of The Electrochemical Society* **2016,** 163, (3), A565-A570.
3. Xie, Y.; Wang, H.; Xu, G.; Wang, J.; Sheng, H.; Chen, Z.; Ren, Y.; Sun, C.-J.; Wen, J.; Wang, J.; Miller, D. J.; Lu, J.; Amine, K.; Ma, Z.-F., In Operando XRD and TXM Study on the Metastable Structure Change of $NaNi_{1/3}Fe_{1/3}Mn_{1/3}O_2$ under Electrochemical Sodium-Ion Intercalation. *Advanced Energy Materials* **2016,** 6, (24).
4. Deng, C.; Gabriel, E.; Skinner, P.; Lee, S.; Barnes, P.; Ma, C.; Gim, J.; Lau, M. L.; Lee, E.; Xiong, H., Origins of Irreversibility in Layered $NaNi_xFe_yMn_zO_2$ Cathode Materials for Sodium Ion Batteries. *ACS Appl Mater Interfaces* **2020,** 12, (46), 51397-51408.
5. Jeong, M.; Lee, H.; Yoon, J.; Yoon, W.-S., O3-type $NaNi_{1/3}Fe_{1/3}Mn_{1/3}O_2$ layered cathode for Na-ion batteries: Structural evolution and redox mechanism upon Na (de) intercalation. *Journal of Power Sources* **2019,** 439.
6. Guo, S.; Li, Q.; Liu, P.; Chen, M.; Zhou, H., Environmentally stable interface of layered oxide cathodes for sodium-ion batteries. *Nature Communications* **2017,** 8, (1).
7. Mu, L.; Feng, X.; Kou, R.; Zhang, Y.; Guo, H.; Tian, C.; Sun, C.-J.; Du, X.-W.; Nordlund, D.; Xin, H. L.; Lin, F., Deciphering the Cathode-Electrolyte Interfacial Chemistry in Sodium Layered Cathode Materials. *Advanced Energy Materials* **2018,** 8, (34).
8. Song, X.; Meng, T.; Deng, Y.; Gao, A.; Nan, J.; Shu, D.; Yi, F., The effects of the functional electrolyte additive on the cathode material $Na_{0.76}Ni_{0.3}Fe_{0.4}Mn_{0.3}O_2$ for sodium-ion batteries. *Electrochimica Acta* **2018,** 281, 370-377.
9. Hwang, J.-Y.; Myung, S.-T.; Choi, J. U.; Yoon, C. S.; Yashiro, H.; Sun, Y.-K., Resolving the degradation pathways of the O3-type layered oxide cathode surface through the nano-scale aluminum oxide coating for high-energy density sodium-ion batteries. *Journal of Materials Chemistry A* **2017,** 5, (45), 23671-23680.
10. Song, T.; Kendrick, E., Recent progress on strategies to improve the high-voltage stability of layered-oxide cathode materials for sodium-ion batteries. *Journal of Physics: Materials* **2021,** 4, (3).
11. Chen, T.; Guo, J.; Zhuo, Y.; Hu, H.; Liu, W.; Liu, F.; Liu, P.; Yan, J.; Liu, K., An inactive metal supported oxide cathode material with high rate capability for sodium ion batteries. *Energy Storage Materials* **2019,** 20, 263-268.
12. Zhang, C.; Gao, R.; Zheng, L.; Hao, Y.; Liu, X., New Insights into the Roles of Mg in Improving the Rate Capability and Cycling Stability of O3-$NaMn_{0.48}Ni_{0.2}Fe_{0.3}Mg_{0.02}O_2$ for Sodium-Ion Batteries. *ACS Appl Mater Interfaces* **2018,** 10, (13), 10819-10827.
13. Yao, H.-R.; Wang, P.-F.; Wang, Y.; Yu, X.; Yin, Y.-X.; Guo, Y.-G., Excellent Comprehensive Performance of Na-Based Layered Oxide Benefiting from the Synergetic Contributions of Multimetal Ions. *Advanced Energy Materials* **2017,** 7, (15).
14. Sun, X.; Jin, Y.; Zhang, C.-Y.; Wen, J.-W.; Shao, Y.; Zang, Y.; Chen, C.-H., $Na[Ni_{0.4}Fe_{0.2}Mn_{0.4-x}Ti_x]O_2$: a cathode of high capacity and superior cyclability for Na-ion batteries. *J. Mater. Chem. A* **2014,** 2, (41), 17268-17271.
15. Yu, T.-Y.; Hwang, J.-Y.; Bae, I. T.; Jung, H.-G.; Sun, Y.-K., High-performance Ti-doped O3-type $Na[Ti_x(Ni_{0.6}Co_{0.2}Mn_{0.2})_{1-x}]O_2$ cathodes for practical sodium-ion batteries. *Journal of Power Sources* **2019,** 422, 1-8.
16. Hwang, T.; Lee, J. H.; Choi, S. H.; Oh, R. G.; Kim, D.; Cho, M.; Cho, W.; Park, M. S., Critical Role of Titanium in O3-Type Layered Cathode Materials for Sodium-Ion Batteries. *ACS Appl Mater Interfaces* **2019,** 11, (34), 30894-30901.

17. Leng, M.; Bi, J.; Wang, W.; Xing, Z.; Yan, W.; Gao, X.; Wang, J.; Liu, R., Superior electrochemical performance of O3-type $NaN_{i0.5-x}Mn_{0.3}Ti_{0.2}Zr_xO_2$ cathode material for sodium-ion batteries from Ti and Zr substitution of the transition metals. *Journal of Alloys and Compounds* **2020,** 816.
18. Zhao, Y.; Xia, M.; Hu, X.; Zhao, Z.; Wang, Y.; Lv, Z., Effects of Sn doping on the structural and electrochemical properties of $Li_{1.2}Ni_{0.2}Mn_{0.8}O_2$ Li-rich cathode materials. *Electrochimica Acta* **2015,** 174, 1167-1174.
19. Wang, P. F.; Xin, H.; Zuo, T. T.; Li, Q.; Yang, X.; Yin, Y. X.; Gao, X.; Yu, X.; Guo, Y. G., An Abnormal 3.7 Volt O3-Type Sodium-Ion Battery Cathode. *Angew Chem Int Ed Engl* **2018,** 57, (27), 8178-8183.
20. Sathiya, M.; Jacquet, Q.; Doublet, M.-L.; Karakulina, O. M.; Hadermann, J.; Tarascon, J.-M., A Chemical Approach to Raise Cell Voltage and Suppress Phase Transition in O3 Sodium Layered Oxide Electrodes. *Advanced Energy Materials* **2018,** 8, (11).
21. Rong, X.; Qi, X.; Lu, Y.; Wang, Y.; Li, Y.; Jiang, L.; Yang, K.; Gao, F.; Huang, X.; Chen, L.; Hu, Y.-S., A new Tin-based O3-$Na_{0.9}[Ni_{0.45-x/2}Mn_xSn_{0.55-x/2}]O_2$ as sodium-ion battery cathode. *Journal of Energy Chemistry* **2019,** 31, 132-137.
22. Rong, X.; Gao, F.; Ding, F.; Lu, Y.; Yang, K.; Li, H.; Huang, X.; Chen, L.; Hu, Y.-S., Triple effects of Sn-substitution on $Na_{0.67}Ni_{0.33}Mn_{0.67}O_2$. *Journal of Materials Science & Technology* **2019,** 35, (7), 1250-1254.
23. Li, J.; Risthaus, T.; Wang, J.; Zhou, D.; He, X.; Ehteshami, N.; Murzin, V.; Friesen, A.; Liu, H.; Hou, X.; Diehl, M.; Paillard, E.; Winter, M.; Li, J., The effect of Sn substitution on the structure and oxygen activity of $Na_{0.67}Ni_{0.33}Mn_{0.67}O_2$ cathode materials for sodium ion batteries. *Journal of Power Sources* **2020,** 449.
24. Smith, K.; Treacher, J.; Ledwoch, D.; Adamson, P.; Kendrick, E. Novel High Energy Density Sodium Layered Oxide Cathode Materials : From Material to Cells. *ECS Transactions* **2017**, 75, 13-24.
25. Kendrick, E.; Gruar, R. Layered oxide materials for batteries. U.S. Patent US20170222224A12017.
26. Kendrick, E.; Gruar, R. *Tin-containing compounds*. PCT, WO2015177568A1.2015, p11.
27. Yu, Y.; Ning, D.; Li, Q.; Franz, A.; Zheng, L.; Zhang, N.; Ren, G.; Schumacher, G.; Liu, X., Revealing the anionic redox chemistry in O3-type layered oxide cathode for sodium-ion batteries. *Energy Storage Materials* **2021,** 38, 130-140.
28. Yu, J.; Yu, H.; Zhou, L.; Cheng, Q.; Jiang, H., Trace Ti/Mg co-doped O3-type layered oxide cathodes with enhanced kinetics and stability for sodium-ion batteries. *Appl. Surf. Sci.* **2024,** 649.
29. Yao, H. R.; Lv, W. J.; Yin, Y. X.; Ye, H.; Wu, X. W.; Wang, Y.; Gong, Y.; Li, Q.; Yu, X.; Gu, L.; Huang, Z.; Guo, Y. G., Suppression of Monoclinic Phase Transitions of O3-Type Cathodes Based on Electronic Delocalization for Na-Ion Batteries. *ACS Appl Mater Interfaces* **2019,** 11, (25), 22067-22073.
30. Wang, P.-F.; You, Y.; Yin, Y.-X.; Guo, Y.-G., Layered Oxide Cathodes for Sodium-Ion Batteries: Phase Transition, Air Stability, and Performance. *Advanced Energy Materials* **2018,** 8, (8).
31. Wang, Y.; Xiao, R.; Hu, Y. S.; Avdeev, M.; Chen, L., P2-$Na_{0.6}[Cr_{0.6}Ti_{0.4}]O_2$ cation-disordered electrode for high-rate symmetric rechargeable sodium-ion batteries. *Nat Commun* **2015,** 6, 6954.
32. Yao, H. R.; Wang, P. F.; Gong, Y.; Zhang, J.; Yu, X.; Gu, L.; OuYang, C.; Yin, Y. X.; Hu, E.; Yang, X. Q.; Stavitski, E.; Guo, Y. G.; Wan, L. J., Designing Air-Stable O3-Type Cathode Materials by Combined Structure Modulation for Na-Ion Batteries. *J Am Chem Soc* **2017,** 139, (25), 8440-8443.
33. Wang, P. F.; You, Y.; Yin, Y. X.; Wang, Y. S.; Wan, L. J.; Gu, L.; Guo, Y. G., Suppressing the P2-O2 Phase Transition of $Na_{0.67}Mn_{0.67}Ni_{0.33}O_2$ by Magnesium Substitution for Improved Sodium-Ion Batteries. *Angew Chem Int Ed Engl* **2016,** 55, (26), 7445-9.
34. Liu, D.; Fan, X.; Li, Z.; Liu, T.; Sun, M.; Qian, C.; Ling, M.; Liu, Y.; Liang, C., A cation/anion co-doped $Li_{1.12}Na_{0.08}Ni_{0.2}Mn_{0.6}O_{1.95}F_{0.05}$ cathode for lithium ion batteries. *Nano Energy* **2019,** 58, 786-796.
35. Xie, M.; Luo, R.; Lu, J.; Chen, R.; Wu, F.; Wang, X.; Zhan, C.; Wu, H.; Albishri, H. M.; Al-Bogami, A. S.; El-Hady, D. A.; Amine, K., Synthesis-microstructure-performance relationship of layered transition metal oxides as cathode for rechargeable sodium batteries prepared by high-temperature calcination. *ACS Appl Mater Interfaces* **2014,** 6, (19), 17176-83.

36. Hu, R.; Ouyang, Y.; Liang, T.; Wang, H.; Liu, J.; Chen, J.; Yang, C.; Yang, L.; Zhu, M., Stabilizing the Nanostructure of SnO_2 Anodes by Transition Metals: A Route to Achieve High Initial Coulombic Efficiency and Stable Capacities for Lithium Storage. *Adv Mater* **2017,** 29, (13).
37. Roberts, S.; Chen, L.; Kishore, B.; Dancer, C. E. J.; Simmons, M. J. H.; Kendrick, E., Mechanism of gelation in high nickel content cathode slurries for sodium-ion batteries. *J Colloid Interface Sci* **2022,** 627, 427-437.
38. Moulder, J. F.; Stickle, W. F.; Sobol, P. E.; Bomben, K. D. Handbook of X-ray Photoelectron Spectroscopy; Physical Electronics, Inc, **1992**.
39. Alburquenque, D.; Troncoso, L.; Denardin, J. C.; Butera, A.; Padmasree, K. D.; Ortiz, J.; Herrera, F.; Marco, J. F.; Gautier, J. L., Structural and physicochemical properties of nickel manganite $NiMn_2O_4$-δsynthesized by sol-gel and ultra sound assisted methods. *Journal of Alloys and Compounds* **2016,** 672, 307-316.
40. Alburquenque, D.; Denardin, J. C.; Troncoso, L.; Marco, J. F.; Gautier, J. L., Substitution effects on the bulk and surface properties of (Li,Ni)Mn_2O4. *Ionics* **2017,** 24, (4), 977-987.
41. Alburquenque, D.; Márquez, P.; Troncoso, L.; Pereira, A.; Celis, F.; Sánchez-Arenillas, M.; Marco, J. F.; Gautier, J. L.; Escrig, J., $LiM_{0.5}Mn_{1.5}O_{4-\delta}$ (M = Co or Fe) spinels with a high oxidation state obtained by ultrasound-assisted thermal decomposition of nitrates. Characterization and physicochemical properties. *J. Solid State Chem.* **2020,** 284.
42. Yamashita, T.; Hayes, P., Analysis of XPS spectra of Fe^{2+} and Fe^{3+} ions in oxide materials. *Appl. Surf. Sci.* **2008,** 254, (8), 2441-2449.
43. Baez, D. F.; Pardo, H.; Laborda, I.; Marco, J. F.; Yanez, C.; Bollo, S., Reduced Graphene Oxides: Influence of the Reduction Method on the Electrocatalytic Effect towards Nucleic Acid Oxidation. *Nanomaterials (Basel)* **2017,** 7, (7).
44. Hirsh, H.; Olguin, M.; Chung, H.; Li, Y.; Bai, S.; Feng, D.; Wang, D.; Zhang, M.; Meng, Y. S., Meso-Structure Controlled Synthesis of Sodium Iron-Manganese Oxides Cathode for Low-Cost Na-Ion Batteries. *Journal of The Electrochemical Society* **2019,** 166, (12), A2528-A2535.
45. López, G. P.; Castner, D. G.; Ratner, B. D., XPS O 1s binding energies for polymers containing hydroxyl, ether, ketone and ester groups. *Surf. Interface Anal.* **1991,** 17, (5), 267-272.
46. Marco, J. F.; Gancedo, J. R.; Ortiz, J.; Gautier, J. L., Characterization of the spinel-related oxides $Ni_xCo_{3-x}O_4$ (x=0.3,1.3,1.8) prepared by spray pyrolysis at 350 °C. *Appl. Surf. Sci.* **2004,** 227, (1-4), 175-186.
47. Meskinis, S.; Vasiliauskas, A.; Andrulevicius, M.; Peckus, D.; Tamulevicius, S.; Viskontas, K., Diamond Like Carbon Films Containing Si: Structure and Nonlinear Optical Properties. *Materials (Basel)* **2020,** 13, (4).
48. Liu, S.; Feng, X.; Wang, X.; Shen, X.; Hu, E.; Xiao, R.; Yu, R.; Yang, H.; Song, N.; Wang, Z.; Yang, X.; Chen, L., Another Strategy, Detouring Potential Decay by Fast Completion of Cation Mixing. *Advanced Energy Materials* **2018,** 8, (15).
49. Zeng, Y.; Li, X.; Wang, J.; Sougrati, M. T.; Huang, Y.; Zhang, T.; Liu, B., In situ/operando Mössbauer spectroscopy for probing heterogeneous catalysis. *Chem Catalysis* **2021**.
50. Tripathi, A.; Rudola, A.; Gajjela, S. R.; Xi, S.; Balaya, P., Developing an O3 type layered oxide cathode and its application in 18650 commercial type Na-ion batteries. *Journal of Materials Chemistry A* **2019,** 7, (45), 25944-25960.
51. Weppner, W.; Huggins, R. A. Electrochemical investigation of the chemical diffusion, partial ionic conductivities, and other kinetic parameters in Li_3Sb and Li_3Bi. *J. Solid State Chem.* **1977**, 22, 297−308.
52. Qiu, X. Y.; Zhuang, Q. C.; Zhang, Q. Q.; Cao, R.; Ying, P. Z.; Qiang, Y. H.; Sun, S. G., Electrochemical and electronic properties of $LiCoO_2$ cathode investigated by galvanostatic cycling and EIS. *Phys Chem Chem Phys* **2012,** 14, (8), 2617-30.
53. Tatara, R.; Karayaylali, P.; Yu, Y.; Zhang, Y.; Giordano, L.; Maglia, F.; Jung, R.; Schmidt, J. P.; Lund, I.; Shao-Horn, Y., The Effect of Electrode-Electrolyte Interface on the Electrochemical Impedance

Spectra for Positive Electrode in Li-Ion Battery. *Journal of The Electrochemical Society* **2018,** 166, (3), A5090-A5098.
54. Wang, Q.; Mariyappan, S.; Vergnet, J.; Abakumov, A. M.; Rousse, G.; Rabuel, F.; Chakir, M.; Tarascon, J. M., Reaching the Energy Density Limit of Layered O3- $NaNi_{0.5}Mn_{0.5}O_2$ Electrodes via Dual Cu and Ti Substitution. *Advanced Energy Materials* **2019,** 9, (36).

Chapter 5 Informed synthesis and particle design of $NaNi_{1/3}Fe_{1/3}Mn_{1/3}O_2$ cathode materials for sodium-ion batteries

This work has been published in ***Chemical Engineering Journal Advances*** **16 (2023) 100572**
(Tengfei Song, Qiyao Zhang, Yongxiu Chen, Pengcheng Zhu, and Emma Kendrick)

DOI: 0.1016/j.ceja.2023.100572

Submitted: 23/06/2023

Accepted: 04/11/2023

Author contribution: T.F. conceived and designed the research, performed the experiments, conducted the data analysis, and drafted the manuscript. I would like to acknowledge Qiyao Zhang' contribution through an MSc project carried out under my supervision[1].

5.1 Introduction

Cobalt-free O3-type layered $NaNi_{1/3}Fe_{1/3}Mn_{1/3}O_2$ is one of the most promising cathode materials for SIBs because of its high theoretical capacity, good reversibility, usage of abundant raw materials, and flexible synthesis process[2]. Several methods have been reported in the synthesis of NaNFM cathode including solid-state[3, 4], oxalate coprecipitation[5], and hydroxide coprecipitation methods[6-8]. However, to our knowledge, few studies have systematically investigated the impacts of synthesis conditions on the particle physical properties and effects upon electrochemical performance.

Hydroxide co-precipitation is widely used in industry for the synthesis of cathode materials due to its intimate mixing of the precursor ionic components. The synthesis process involves the precipitation of metal hydroxides from a salt solution, and the subsequent formation, growth, and maturation of these particles, as well as agglomeration and fragmentation in the reactor. The properties of synthesized metal hydroxide ($TM(OH)_2$), such as morphology, size distribution, and tap density are significantly dependent on synthetic conditions. This is attributed to the complex competition between precipitation and complexation reactions as well as many conjugated input parameters; including temperature, pH, stirring speed, feeding concentration, feeding rate, residence time, and amount of chelating agent [9]. The precursor hydroxide particles are then milled and mixed with the alkali hydroxide or carbonate and fired. The control of the co-precipitation variables is critical to optimize the properties of the hydroxide intermediate products and the resulting fired active material, which ultimately affects the final performance properties of the cells. A detailed understanding of how process variables affect the physical and electrochemical properties is critical to designing materials with the desired characteristics.

Considerable efforts have been dedicated to enhancing the synthesis conditions with the goal of achieving uniformly dispersed spherical particles in lithium-ion batteries. For example, Lee *et al.*[10] conducted a study to determine the optimal conditions for producing spherical $(Ni_{1/3}Co_{1/3}Mn_{1/3})(OH)_2$ by controlling factors such as pH, stirring speed, and the quantity of chelating agent. Noh *et al.*[11] optimized the process conditions of $Ni_{0.6}Co_{0.2}Mn_{0.2}(OH)_2$ precursor, aiming to improve their performance at high rates and elevated temperatures. Liang *et al.*[9] focused on optimizing the process conditions for high tap-density and morphology of

$Ni_{0.6}Co_{0.2}Mn_{0.2}(OH)_2$ precursor. Dense and spherical hydroxides with a tap density of 1.94 g cm^{-3} were obtained. However, these endeavors were predominantly conducted through time-consuming trial and error or single-factor experiments (OFAT), which not only fail to identify the crucial factors influencing the output results but also risk overlooking the optimal settings for these factors.

To streamline the optimization process for new materials, there have been attempts to quantify the impact of synthesis variables on the desired outcome. Barai *et al.*[12] developed a comprehensive multi-scale computational model to simulate particle evolution during the co-precipitation process. This model enables the prediction of final particle size and size distribution based upon pH and ammonia content. Similarly, Para *et al.*[13], conducted a trial where they employed a population balance model to simulate the initial stages of particle formation during co-precipitation. However, constructing and validating these models requires substantial data and experiments to minimize discrepancies between experimental and simulated values and advanced statistics is necessary for accurate simulations.

In the existing literature, there has been a lack of emphasis on applying the Design of Experiments (DoE) methodology for the investigation and optimization of battery material synthesis. DoE is an effective problem-solving approach that allows for the identification of key factors and their effects by conducting a minimal number of experiments with multiple variable parameters. It enables simultaneous adjustments of multiple factors to be made. Aside from discerning the primary factor effects, DoE can also facilitate the detection of interactions among these factors and provide statistical models to predict output results.

In this work, the Design of Experiments (DoE) methodology is used, for the first time, in the synthesis of $NaNi_{1/3}Fe_{1/3}Mn_{1/3}O_2$, specifically aiming to establish the relationship between input variables and the outcome of the precursor preparation step. Based on prior knowledge, the pH level, chelating agent quantity, and stirring rate were recognized as key factors which influence the physicochemical properties of both intermediate and final powders[9]. Experimental procedures were conducted in a 5 L reactor, and the physical and electrochemical properties of the obtained samples were characterized to ascertain the impact of synthesis conditions, and, ultimately to identify the optimal synthesis parameters. Minitab Statistical Software was employed to facilitate the experimental design and data analysis processes. The effects of the input variables on the output response were assessed and an optimized synthesis condition

proposed. An improved understanding of how the synthesis conditions influence particle properties and ultimate electrochemical performance is also discussed.

The objectives of this study are:

(1) To establish a systematic engineering research methodology for identifying the critical parameters for optimizing the co-precipitation process to maximize performance. The outcomes of this study will provide a statistical model for predicting synthesis parameters to produce uniformly distributed particles. The goal is to minimize surface side reactions, enhance tap density, and prolong lifetime.
(2) To establish a connection between the synthesis parameters and the morphology as well as the electrochemical properties.

5.2 Experimental and methods

5.2.1 Experimental design and analysis

In this study, three synthesis factors, pH, the molar ratio of NH_4OH /$TMSO_4$(TM=Ni, Fe, Mn), and stirring speed (rpm) are selected as the input variables with a low and high level based on a 2^k (level factor) full factorial design matrix. The range of synthesis factors was selected based on a literature review and preliminary trial experiments. Specifically, a stirring speed of around 400-1000 rpm has been reported in the co-precipitation method[9, 10, 14, 15]. Therefore, 400 rpm was chosen as the low level, and 800 rpm was selected as the high level due to being the highest speed at which our reactor can operate stably without violent vibration. Regarding pH, values of 10 and 10.5 have been reported for the synthesis of Fe-containing materials[16-18]. Thus, a pH of 10 was chosen as the low level, and a slightly higher value of 11 was selected as the high level to examine the boundary condition. Setting the range for the NH_4OH chelating agent proved challenging, as the amount of NH_4OH chelating agent is often undisclosed in the literature, with phrases like "appropriate amount of NH_4OH " commonly used[19]. A value of 0.83 has been reported[17], so we selected 0.83 NH_4OH as a baseline in our preliminary trial experiments. We found that increasing the amount of NH_4OH is beneficial for achieving a spherical morphology until reaching 1.2, beyond which it leads to incomplete precipitation of some metal ions.

To assess the curvature of the fitted model, three additional replications of the central points (current parameters) were included. The temperature, metal sulfate and alkali concentration, metal sulfate feed flow rate, and residence time were held constant at optimal values determined from previous experiments across the DoE matrix. As a result, a design matrix consisting of a total of 11 experiments was generated using Minitab, as depicted in Figure 5.1 and Table 5.1.

The various responses of interest in this study include morphology, tap density (g/cm^3), particle size (um), particle distribution, structural properties, crystallite size, initial formation capacity ($mAh\ g^{-1}$) and cycling performance. Particle distribution was quantified as (D90 – D10)/D50 while the crystal structural was represented by the x-ray diffraction peak intensity ratio I003/I104, a commonly used indicator of cation mixing degree[20, 21]. The capacity retention after cycling under 0.5 C for 50 cycles was selected as the major output response.

The contribution of individual factors and their interactions to the response is evaluated by the ANOVA (Analysis of variance). The confidence level was set to 95% (α=0.05), corresponding to probability values (hereafter p-value) < 0.05. The p-value (probability value) was used to determine whether a factor or interaction is significant or not during the data fitting process. Specifically, factors with a p-value greater than 0.05 were considered statistically insignificant and were excluded from the regression model. The regression model considers both linear (Eq.5-1) and second-order polynomial (Eq.5-2) relationships between input factors ($x_i,\ i=1,2,3$) and output response (Y) depends on the quality of the fitting:

$$Y = \beta_0 + \sum_{i=1}^{3} \beta_i x_i + \sum \sum_{i<j}^{3} \beta_{ij} x_i x_j \quad (5\text{-}1)$$

$$Y = \beta_0 + \sum_{i=1}^{3} \beta_i x_i + \sum_{i=1}^{3} \beta_{ii} x_i^2 + \sum \sum_{i<j}^{3} \beta_{ij} x_i x_j \quad (5\text{-}2)$$

Where β_0 is the constant, $\beta_i, \beta_{ij}, \beta_{ii}$ are the regression coefficients of linear effect, 2-Way interactive effect, and quadratic effect, respectively.

Correlation coefficient (R^2) and predicted R^2 (R^2_{pred}) obtained from ANOVA were used as accuracy metrics to describe the reliability of fit and predictive capabilities of the regression models. The closer R^2 to 1 refers to a better fit and prediction performance.

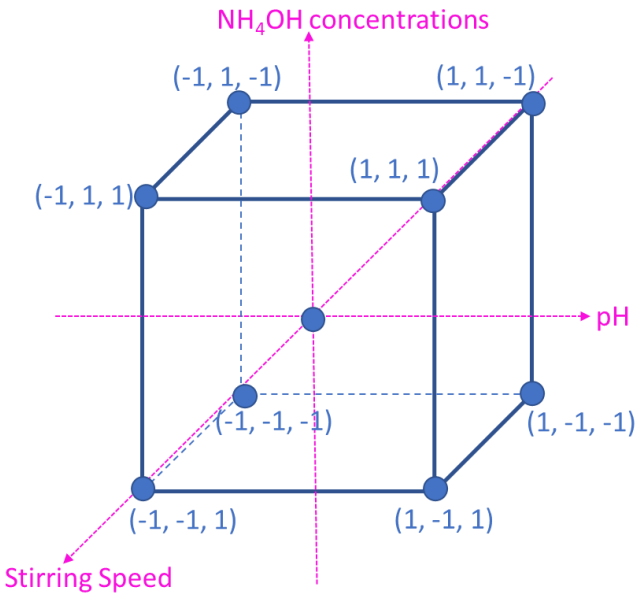


Figure 5.1 Design matrix with three operating conditions.

Table 5-1 Experimental design matrix for the $Ni_{1/3}Fe_{1/3}Mn_{1/3}(OH)_2$ co-precipitation reactions with different pH, ammonium hydroxide quantity and stirring speed.

DOE No.	Uncoded			Coded		
	x_1 pH	x_2 NH_4OH/TM	x_3 Stirring speed (rpm)	x_1 pH	x_2 NH_4OH/TM	x_3 Stirring speed (rpm)
1	10.0	0.8	400	-1	-1	-1
2	11.0	0.8	400	1	-1	-1
3	10.0	1.2	400	-1	1	-1
4	11.0	1.2	400	1	1	-1
5	10.0	0.8	800	-1	-1	1
6	11.0	0.8	800	1	-1	1
7	10.0	1.2	800	-1	1	1
8	11.0	1.2	800	1	1	1
9	10.5	1.0	600	0	0	0

10	10.5	1.0	600	0	0	0
11	10.5	1.0	600	0	0	0

Note: The design as shown is a non-randomised design (standard order). Central points are mixed with the other runs so that the Center Points are true "replicates" thus adding degrees of freedom.

5.2.2 Material synthesis

The synthesis method for $[Ni_{1/3}Fe_{1/3}Mn_{1/3}](OH)_2$ precursor and $Na[Ni_{1/3}Fe_{1/3}Mn_{1/3}]O_2$ have been described detail in **Chapter 3.1.1**.

In brief, a 2 M (1L) mixed metal aqueous solution consisting of $NiSO_4 \cdot 6H_2O$, $FeSO_4 \cdot 7H_2O$, and $MnSO_4 \cdot H_2O$ (molar ratio of Ni^{2+}: Fe^{2+}: Mn^{2+} =1: 1: 1) and 1 L of the NaOH:NH_4OH mixture is pumped into a 5L stirred tank at 1 mL min^{-1}. Stirring is performed at various rpm with a four-finned baffle. The pH is carefully controlled to the required value by adjusting the NaOH pumping rate. A schematic diagram depicting the process is illustrated in Figure 5.2.

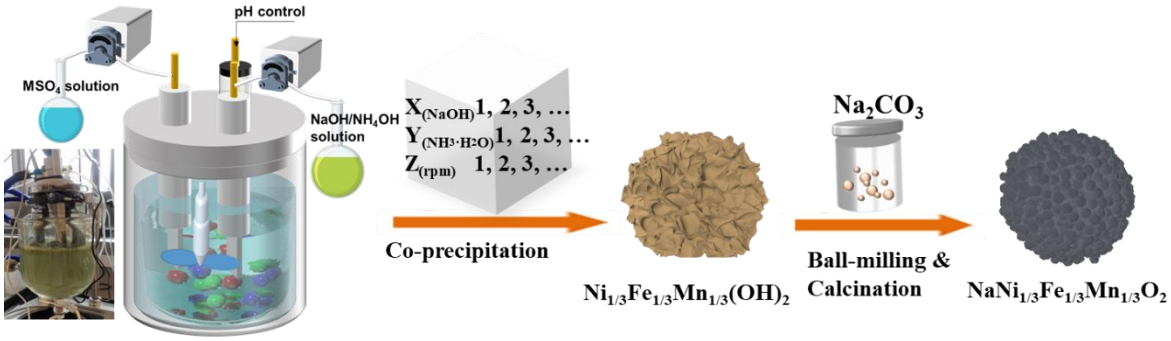


Figure 5.2 Illustration of the synthesis and optimization process.

5.2.3 Analytical techniques

The structural characteristics of the as-prepared powder materials is examined by X-ray diffraction (XRD, Proto, Cu Kα, λ = 1.54056 Å). The data is recorded at a degree step of 0.03° between 10-100° at 30 KV and 20 mA, and Rietveld refinement performed using GSAS-I to acquire lattice parameters. Scanning electron microscopy (SEM, Zeiss EVO15) operated at 10 KV, 15 pA, was performed to investigate particle morphology. Tap densities are measured using an autotap analyzer (Quantachrome) with 1000 times vibration. A laser particle size

analyzer (Sympatec, HELOS) with a wavelength of 635 nm is used to examine the particle size and distribution of the final powders. Each sample is measured three times and averaged.

The electrochemical characterizations are evaluated in CR2032 coin-type half-cells. Cycling were performed at C/2 CC-CV (C/20 current cut off limit) charge and C/2 discharge on a BCS battery test system within the voltage range of 2.0-4.1 V vs Na^+/Na at room temperature. Details about the cell making and testing setting, can be found on **Chapter 3**.

5.3 Results and discussion

5.3.1 Physical properties

A series of eleven syntheses were performed, each synthesis, including washing, filtering, drying, firing, and processing, takes approximately one week to complete. The obtained powders are handled and processed exclusively in glove box conditions to minimize any surface degradation of the materials, and the physical attributes of the materials are compared. A summary of the key results is provided in Table 5.2.

Table 5-2 Summary of experimental design and measured physical response results.

DOE No.	Synthesis conditions			Response				
	pH	NH_4OH/ TM	Stirring speed (rpm)	Particle size D50 (um)	Size distribution	Tap density (g/cm^3)	Crystallite size (nm)	I003/I104
1	10.0	0.8	400	2.00	1.71	0.98	53.894	0.82
2	11.0	0.8	400	3.18	2.14	1.10	49.002	0.88
3	10.0	1.2	400	2.42	1.73	1.17	61.798	0.90
4	11.0	1.2	400	11.43	3.13	1.38	57.546	0.73
5	10.0	0.8	800	1.68	1.57	1.08	42.467	1.03
6	11.0	0.8	800	3.06	1.80	1.15	39.305	1.02
7	10.0	1.2	800	2.76	1.49	1.29	46.120	1.07
8	11.0	1.2	800	12.64	2.47	1.55	45.160	1.03
9	10.5	1.0	600	2.14	1.79	1.13	51.974	0.87
10	10.5	1.0	600	2.06	1.67	1.21	55.898	0.92
11	10.5	1.0	600	2.43	1.54	1.26	51.070	0.85

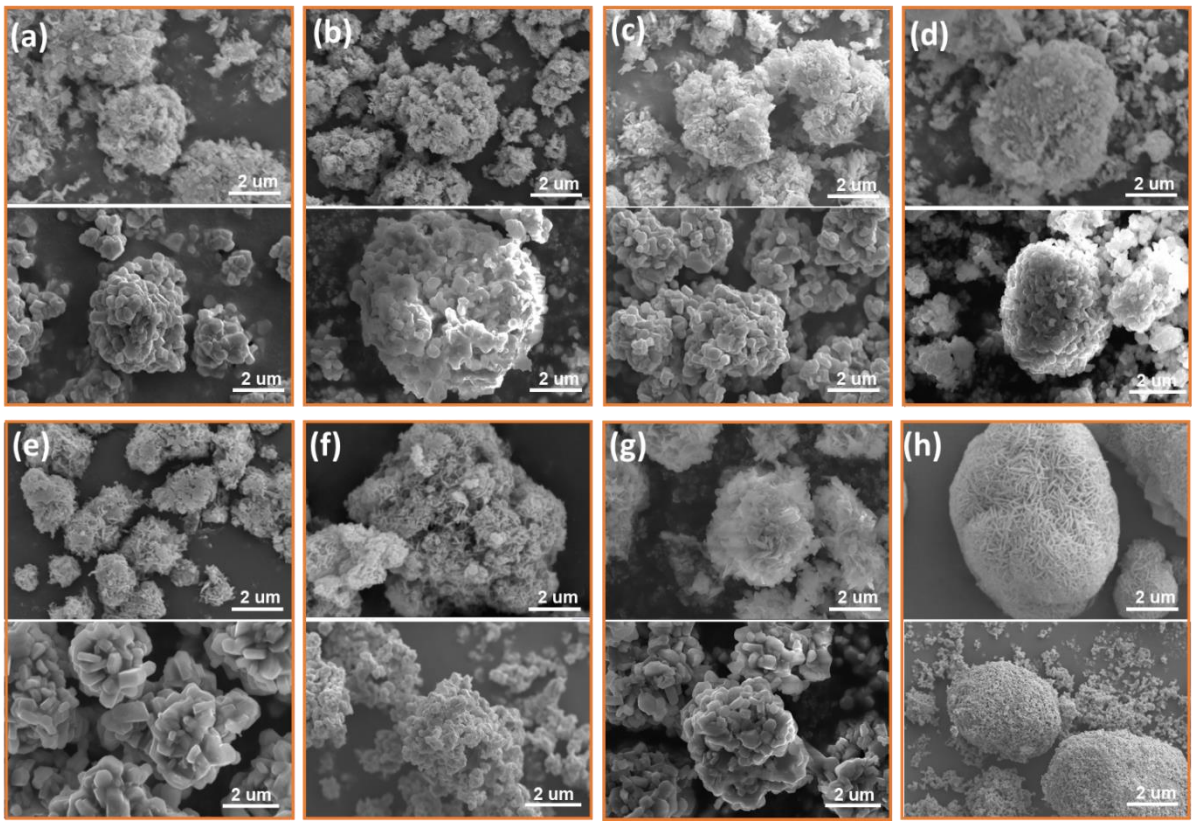


Figure 5.3 SEM images of the as-prepared hydroxide precursors (top) and final layered oxide particles (bottom) prepared at DoE1 (a), DoE2 (b), DoE3 (c), DoE4 (d), DoE5 (e), DoE6 (f), DoE7 (g), and DoE8 (h).

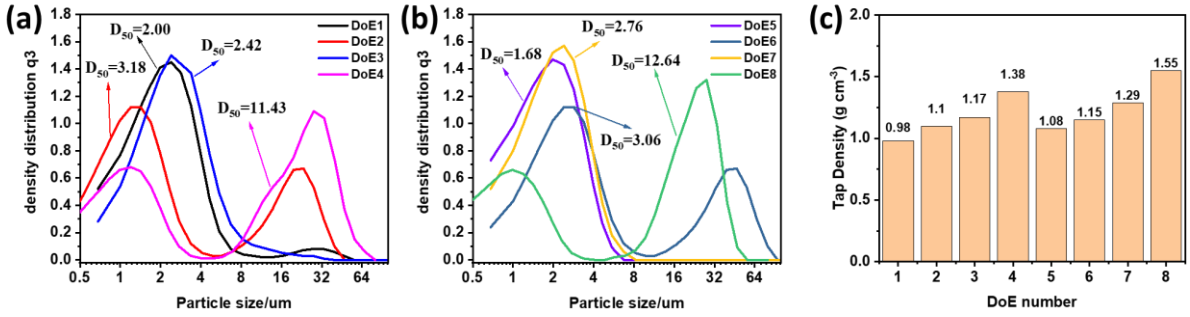


Figure 5.4 Particle size distribution (a,b) and tap density (c) of the synthesized final particles.

Figure 5.3 displays the SEM images of the synthesized layered oxide NaNFMO particles and their corresponding precursors. For clear comparison, the particle size distributions and tap density values of the final particles are shown in Figure 5.4. When the pH is set to 10, the obtained precursors exhibit a lamellar-like morphology (Figure 5.3a, c, e, g). After sodiation, the secondary particles undergo a transformation into quasi-spherical morphologies composed of randomly stacked primary particles with an average diameter of around 400 nm. In contrast,

when the pH is increased to 11, the precursors adopt a needle-like shape (Figure 5.3b, d, f, h), and the size of the primary particles reduces to approximately 200 nm after sodiation. Moreover, at higher pH values, the particle morphology becomes less uniform, and significant agglomeration with numerous fine particles can be observed. This is also reflected in the particle size distribution diagram, where two peaks are evident (Figure 5.4a, b). These small and immature grains may originate from the direct formation of hydroxide precipitates without coordination with ammonia during the initial stages in a strong alkali environment. The irregular morphology and broad particle size distribution at high pH values are unfavourable for rapid Na^+ diffusion processes and are expected to exacerbate side reactions between particles and electrolyte, leading to accelerated capacity loss during cycling. In addition, samples synthesized at high pH tend to exhibit higher tap densities (Figure 5.4c). This can be attributed to the fact that smaller particles can fill the voids among larger ones when mixing particles with different sizes.

The concentration of NH_4OH also plays a crucial role in determining the properties of the particles. Previous studies have demonstrated that a higher concentration of NH_4OH is advantageous for achieving densely packed secondary particles [10, 22]. Figure 5.3 illustrates that, with increased NH_4OH concentration, the secondary particles exhibit a more spherical shape with densely packed primary grains. Additionally, it is evident that the secondary particles grow, as indicated by the increase in D50 values from 1.68 to 2.76 μm and 3.06 to 12.64 μm for DoE 5-8. To provide a visual representation of this process, a schematic illustration is presented in Figure 5.5.

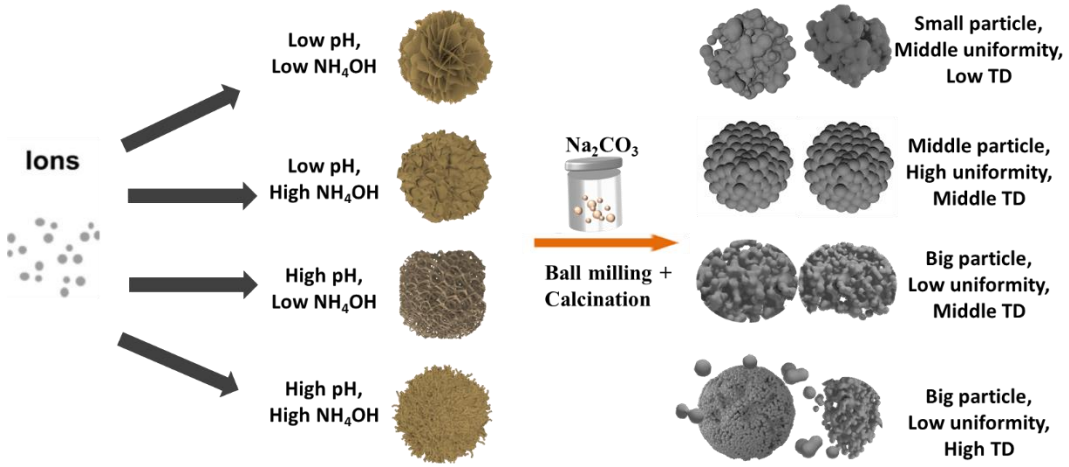


Figure 5.5 Schematic illustration of effects of synthetic factors on the precursor morphology and the physical properties of the final particles.

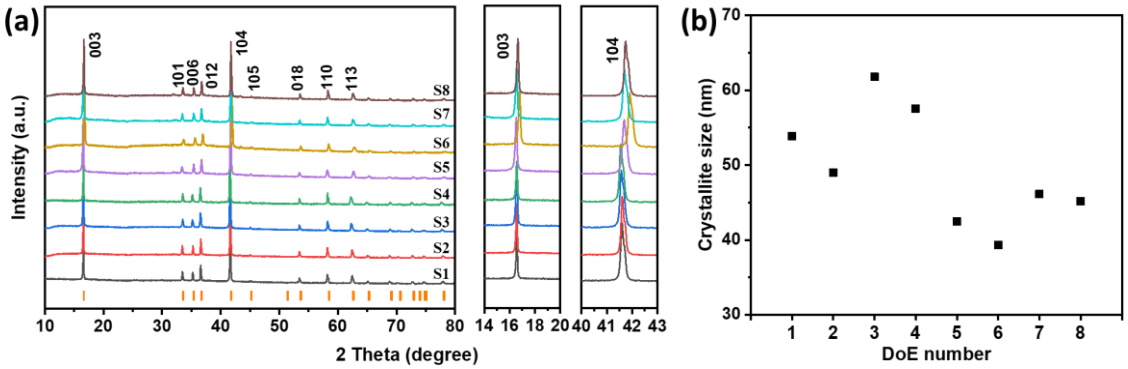


Figure 5.6 (a) XRD patterns of NaNFMO samples obtained under different conditions. (b) Crystallite size calculated from 003 and 104 peaks.

The XRD patterns (Fig. 5.6a) demonstrate the formation of single-phase materials in all cases, with indexing matching to a hexagonal O3-type α-$NaFeO_2$ structure (R-3m space group). However, upon closer examination of the (003) and (104) reflections, it can be observed that the diffraction peaks shift towards higher angles as the pH value increases. This shift indicates a contraction of the interplanar spacing (c-axis). Rietveld refinements were conducted by using the GSAS software (Figure 5.7), and the calculated lattice parameters are provided in Figure 5.8 and Table 5-3. As shown in Figure 5.8, samples prepared by DoE 4 and DoE 6 exhibit the smallest values for lattice c and d003 spacing, which may lead to sluggish sodium ion diffusion and a decrease in electrochemical performance.

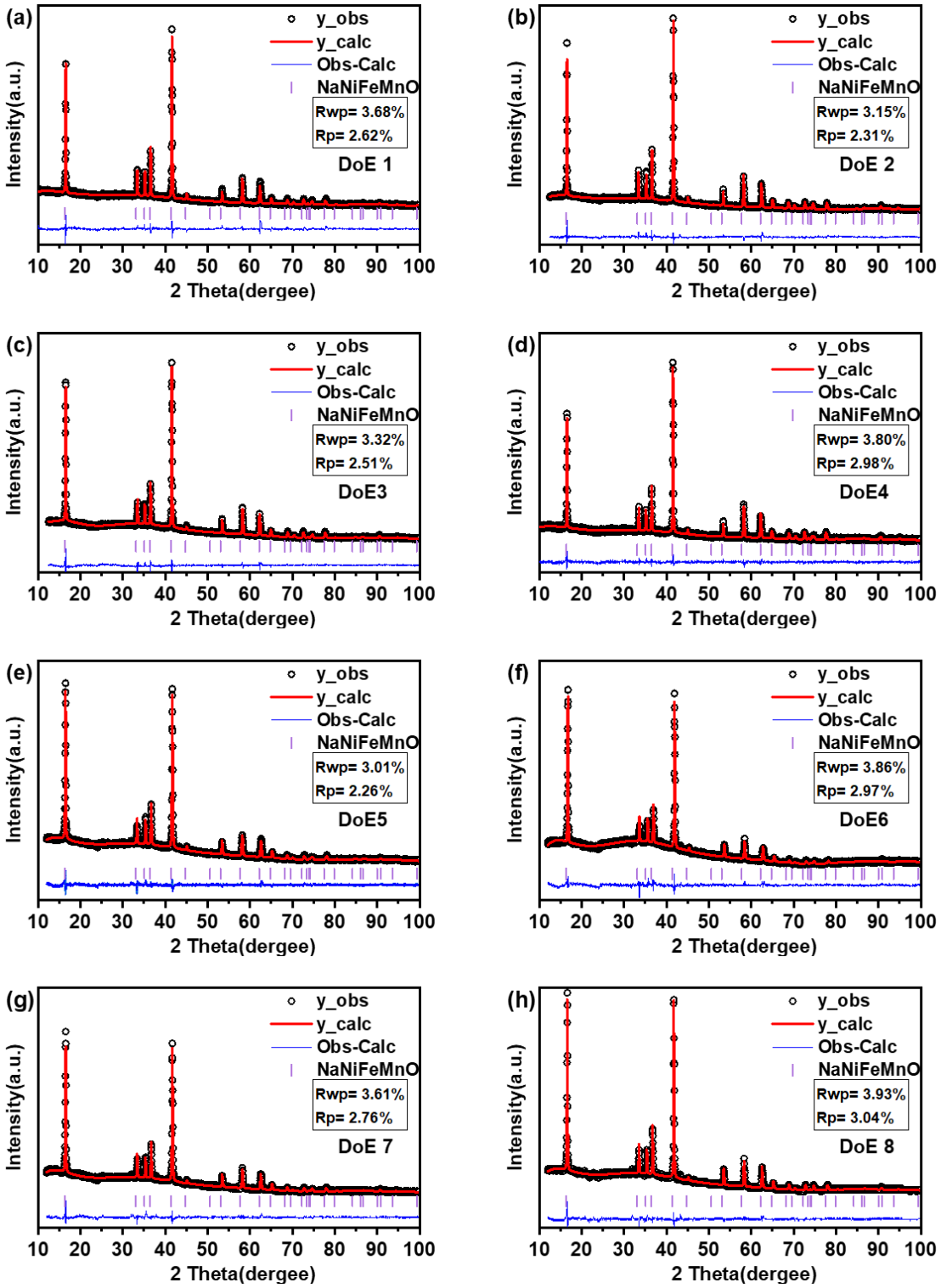


Figure 5.7 Detailed Rietveld refinements of XRD pattern of the as-prepared cathode powdered materials

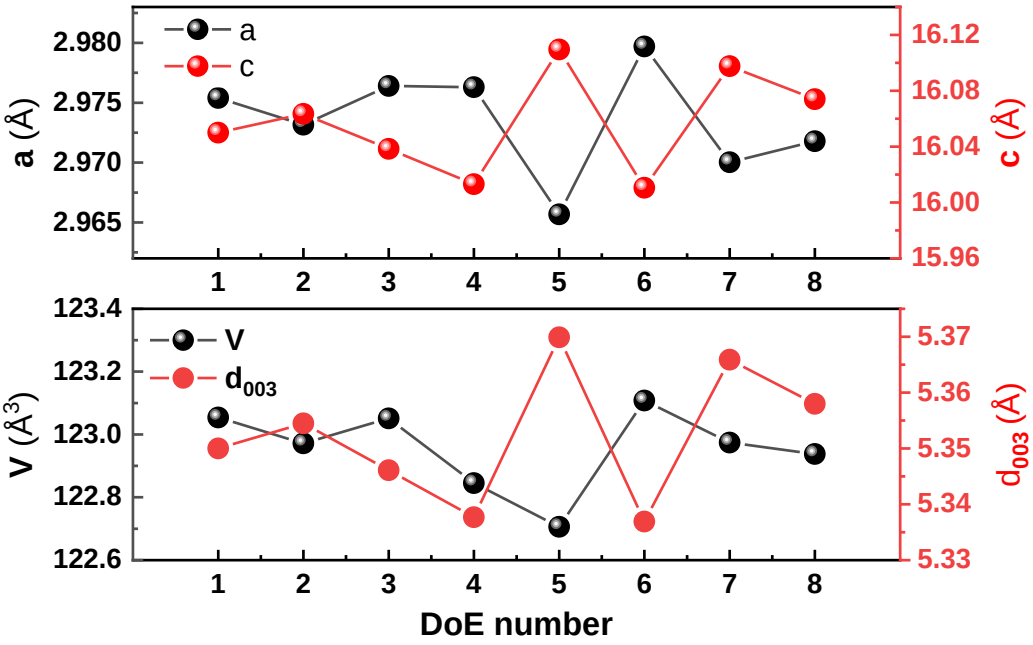


Figure 5.8 Variation of lattice parameters and the lattice spacing d003 value as a function of DoE number.

Table 5-3 Summary of the refined parameters and the R factors.

	a(Å)	c(Å)	V(Å^3)	d(003)/(Å)	Rwp/%	Rp/%	Chi^2
DoE 1	2.97540(10)	16.0500(8)	123.054(11)	5.3500	3.68	2.62	6.166
DoE 2	2.97316(8)	16.0635(6)	122.972(8)	5.3545	3.15	2.31	5.407
DoE 3	2.97644(8)	16.0384(9)	123.051(10)	5.3461	3.66	2.86	2.892
DoE 4	2.97630(5)	16.0131(6)	122.845(5)	5.3377	3.32	2.51	6.033
DoE 5	2.97232(10)	16.1153(14)	123.299(16)	5.3718	3.86	2.97	4.361
DoE 6	2.97971(8)	16.0105(9)	123.108(10)	5.3369	3.80	2.98	2.838
DoE 7	2.97003(9)	16.0976(11)	122.974(13)	5.3659	3.61	2.76	2.220
DoE 8	2.97178(8)	16.0739(10)	122.938(11)	5.3580	3.93	3.04	2.218

Additionally, an increase in the stirring speed, as seen in DOE5-8, leads to broadening of the diffraction peaks, indicating a decrease in crystallinity. The average crystal sizes for all samples were determined using the well-established Scherrer equation.

$$D=k\lambda/\beta\cos\theta \qquad (5\text{-}3)$$

Where K is a constant related to crystallite shape, normally taken as 0.94, λ is the X-ray wavelength in nanometer (nm), β is the peak width of the diffraction peak profile at half maximum height (FWHM) and θ is half the diffraction angle[23]. The calculation results show that the average crystal sizes decreased after increasing the stirring speed (Fig. 5.6b), which suggests that faster stirring may alter the surface properties, growth kinetics, and final morphology of NaNFMO.

5.3.2 Electrochemical properties

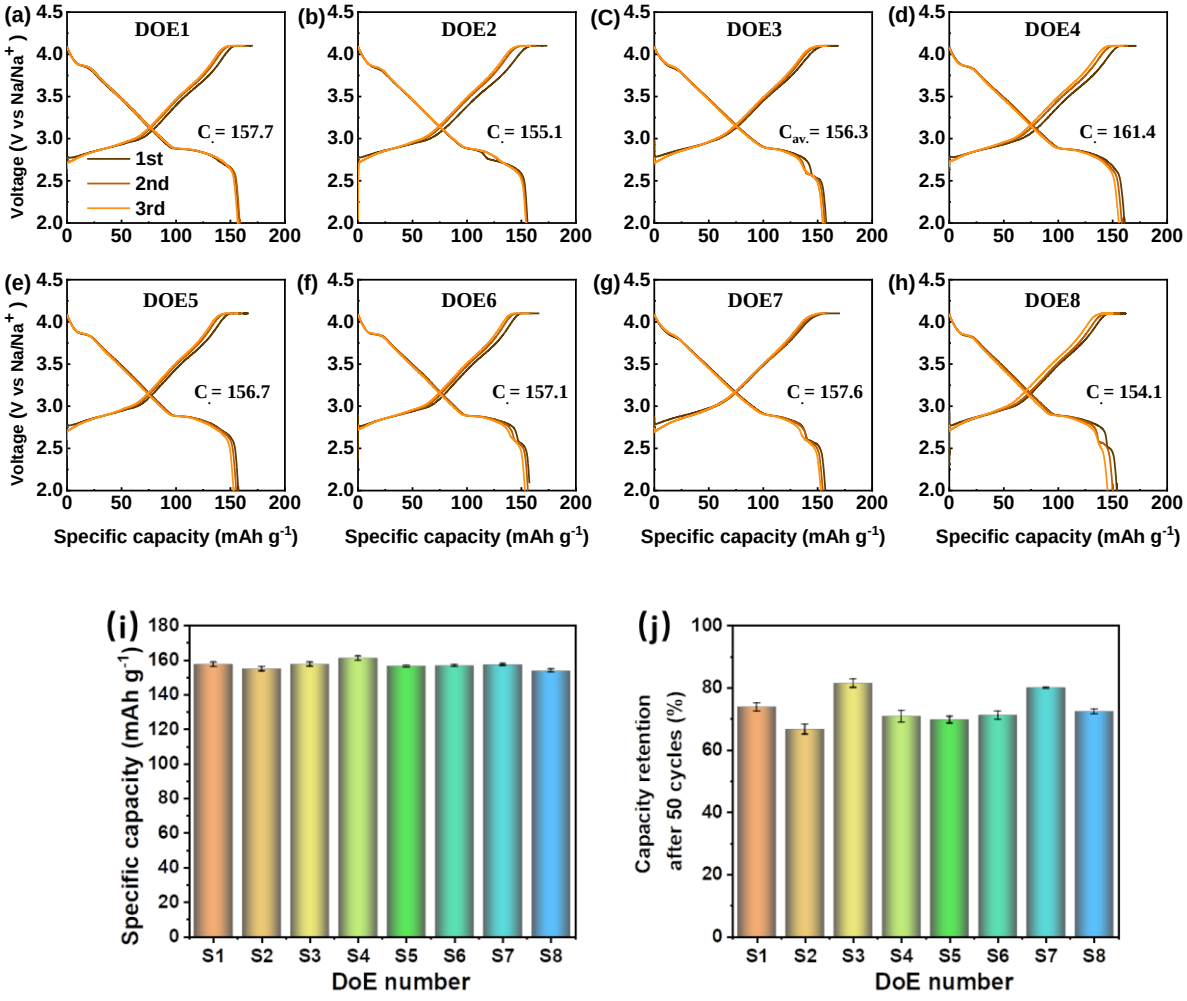


Figure 5.9 (a-h) Charge and discharge curves of the initial 3 formation cycles for the synthesized materials. Comparison of the formation capacity (i) and capacity retention after 50 cycles (j) for the as-synthesized materials.

The formation charge/discharge curves and the corresponding formation capacity (the 1st cycle) of the prepared cells with a current density of 15 mA g^{-1} (0.1C) are shown in Fig 5.9a-i. The formation capacity varies slightly between 154.1 and 161.3 mAh g^{-1} with input parameters, and sample 8 synthesized pH=11, NH_4OH /$TMSO_4$=1.2, 800rpm shows the lowest initial capacity.

By contrast, significant variations were observed in terms of capacity retentions after 50 cycles at 0.5 C as shown in Figure 5.9j. Samples synthesized at lower pH value (10) tend to show better cycling performance than the ones synthesized at pH=11, and samples synthesized at pH=10, NH_4OH /$TMSO_4$=1.2 (S3, S7) give the highest capacity retentions. In addition, the significant difference in the vertical error bars is worth noting. Samples synthesized at low stirring speeds showed larger error bars in terms of both initial capacity and cycling stability, which may originate from the inhomogeneous distribution of the particles as shown in Fig 5.3-4. Therefore, higher stirring speed is preferred in terms of homogeneity.

O3-type layered oxides typically suffer from irreversible structural evolution upon Na^+ extraction /insertion process, which affects the cycling stability. Figure 5.10 gives the calculated dQ/dV *vs*. voltage plots from the first 3 cycles, where the plateau around 3.0 V (*vs.* Na^+/Na) is related to the reversible phase transition from O3 to P3, and plateaux around 4.0 V (*vs.* Na^+/Na) is associated with the irreversible phase conversion of P3-P3' [24]. However, the cycling stability is not fully explained by crystal structure only, as shown in Figure 5.11, where the capacity retention is poorly related to either the capacity contribution from the different phases (A/B) or I003/I104, as indicated by the R^2. The weak relationship between cycling performance and structural properties indicates that capacity degradation is the result of a combination of intrinsic structural decay and extrinsic interface decay, which is closely related to the physical properties of the particles.

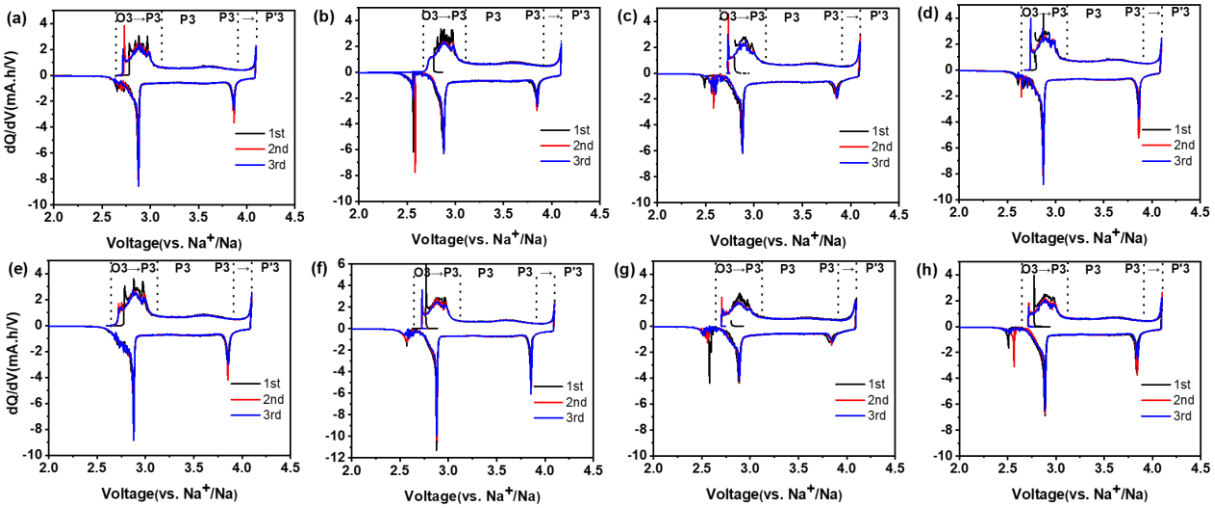


Figure 5.10 Comparison of differential capacity (dQ/dV) curves of the first 3 cycles. The peak around 3.0 V (*vs*. Na^+/Na) is named as Peak A, and the peak around 4.0 V (*vs*. Na^+/Na) is named as Peak B. The intensity ratios of peak B to peak A were calculated and used in Figure 5.11.

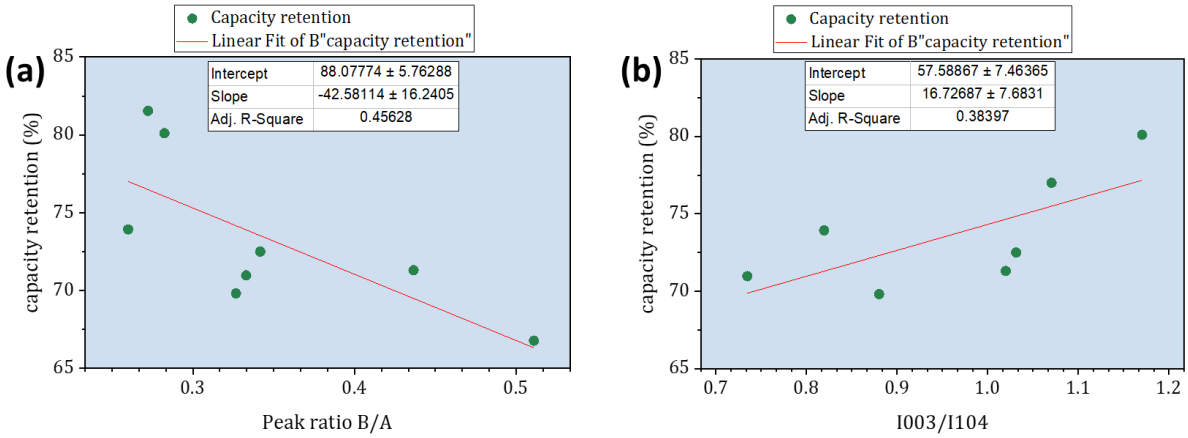


Figure 5.11 Linear fitting between the capacity retention and the peak ratio B/A(a) and I003/I104(b).

5.3.3 Response analysis and results of ANOVA

To quantify the impact of synthesis inputs on the physical and electrochemical outputs, factorial regressions were conducted to identify significant factors, determine coefficient effects, and generate regression equations using forward selection based on p-values (<0.05).

Figure 5.12 presents the Pareto chart illustrating the effective parameters for the regression models. The fitting results, including coded coefficients and corresponding confidence values, for the selected responses are presented in Table 5-4. Strong correlations were observed between input factors and particle size (D50), as evidenced by high R^2 and R^2_{pred} values. The

R^2 values for tap density, crystallite size, and capacity retention were also notably high (around 0.95), although the R^2_{pred} values slightly decreased to around 0.9. Nevertheless, these values remain above the critical threshold of 0.8, indicating that the models can still be used for prediction [25]. Conversely, the correlation function for I003/104 showed less reliability, as indicated by the lower R^2_{pred} value. In addition, the influence of synthesis inputs on particle distribution and formation capacity was not clear and therefore they were not considered further in the analysis.

Based on the findings presented in Figure 5.12 and Table 5-4, it was determined that both the pH and NH_4OH amount are significant operating parameters that have an impact on particle size (D50) and capacity retention. In contrast, the influence of stirring speed is relatively less pronounced within the constrained operating region. However, the interaction effects of pH with NH_4OH or stirring speed were found to be significant. Additionally, both tap density and crystallite size were found to be influenced by all three parameters. Notably, NH_4OH concentration exhibited the most significant influence on tap density, whereas stirring speed had the strongest impact on crystallite size.

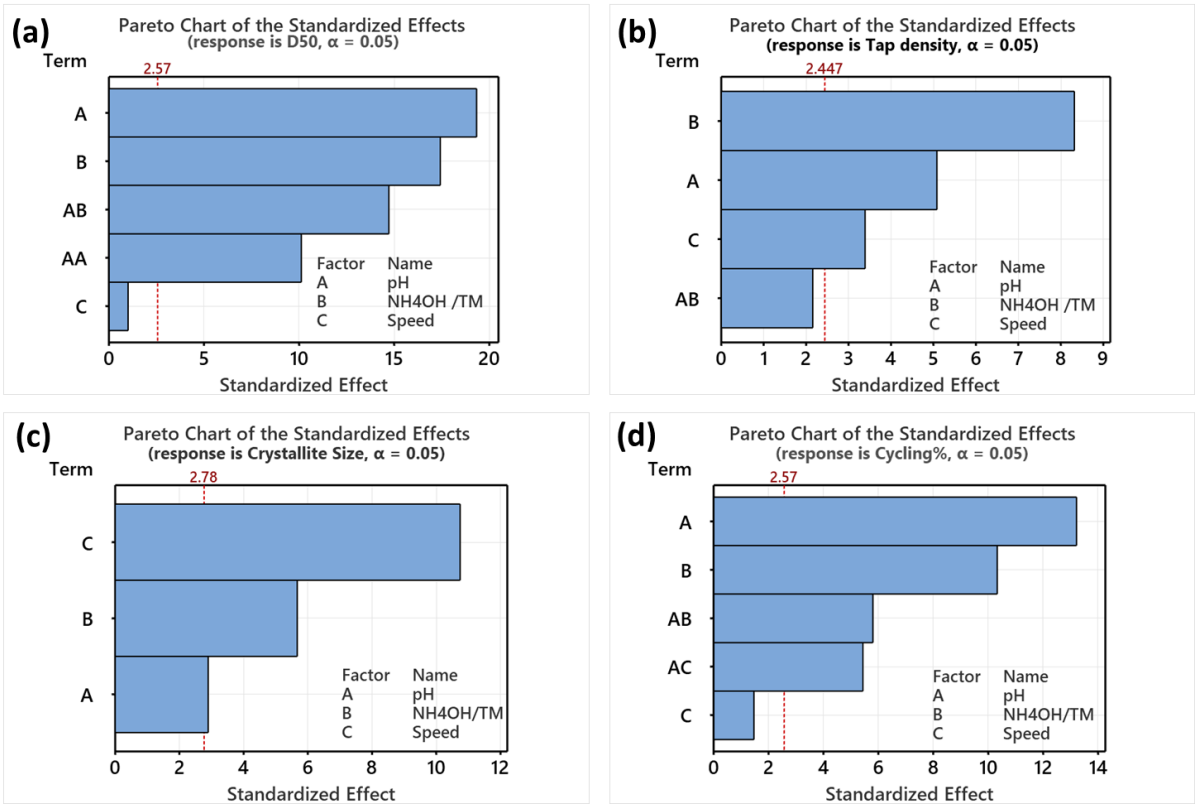


Figure 5.12 Pareto charts of effective parameters for the regression model (a) Particle size D50, (b) Tap Density, (c) Crystallite Size, and (d) Capacity Retention.

Table 5-4 Summary of fitted models with coded coefficients and corresponding confidence levels for the prediction of the selected responses (β_1 for pH, β_2 for NH_4OH/TM, β_3 for speed).

	Response				
Coefficients (in Coded Units	**Particle size D50**	**Tap density**	**Crystallize size**	**I003/I104**	**Capacity retention**
β_0	2.210	1.2091	49.412	0.9358	73.494
β_1	2.681	0.0825	-1.658	--	-3.354
β_2	2.416	0.1350	3.245	--	2.621
β_3	0.139	0.0550	-6.148	0.1032	0.371
β_{12}	2.041	0.0350	--	--	-1.471
β_{13}	--	--	--	--	1.379
β_{23}	--	--	--	--	--
β_1^2	2.686	--	--	--	--
$\mathbf{R^2}$	0.9942	0.9488	0.9750	0.8298	0.9858
$\mathbf{R^2_{pred}}$	0.9643	0.8648	0.8999	0.6974	0.9101

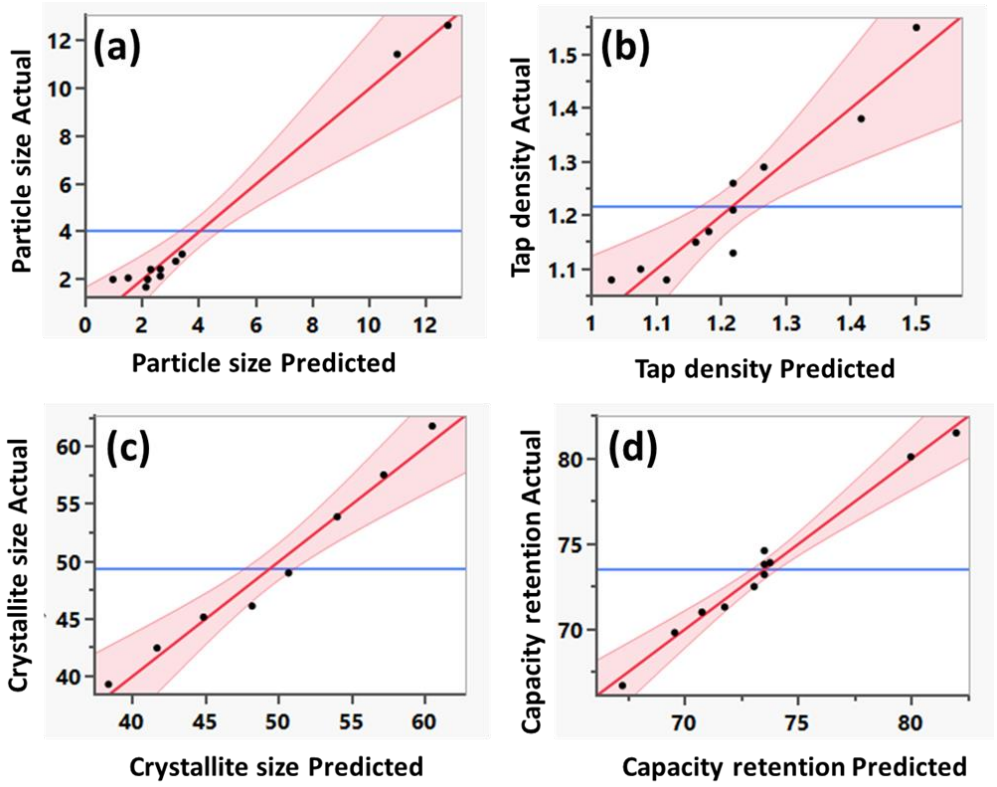


Figure 5.13 The distribution of the predicted versus actual values of the Particle size D50 (a), Tap Density (b), Crystallite Size (c), and Capacity Retention (d).

To assess the accuracy of the regression models, the comparison between the experimental results and the predicted values obtained from the fitted models is presented in Figure 5.13. The actual experimental values from the designed DoE runs are depicted as black dots, while the red straight line represents the ideal prediction. The graph demonstrates that the experimental values closely align with the prediction line and exhibit a normal distribution. This indicates that the fitted models accurately represent the selected responses.

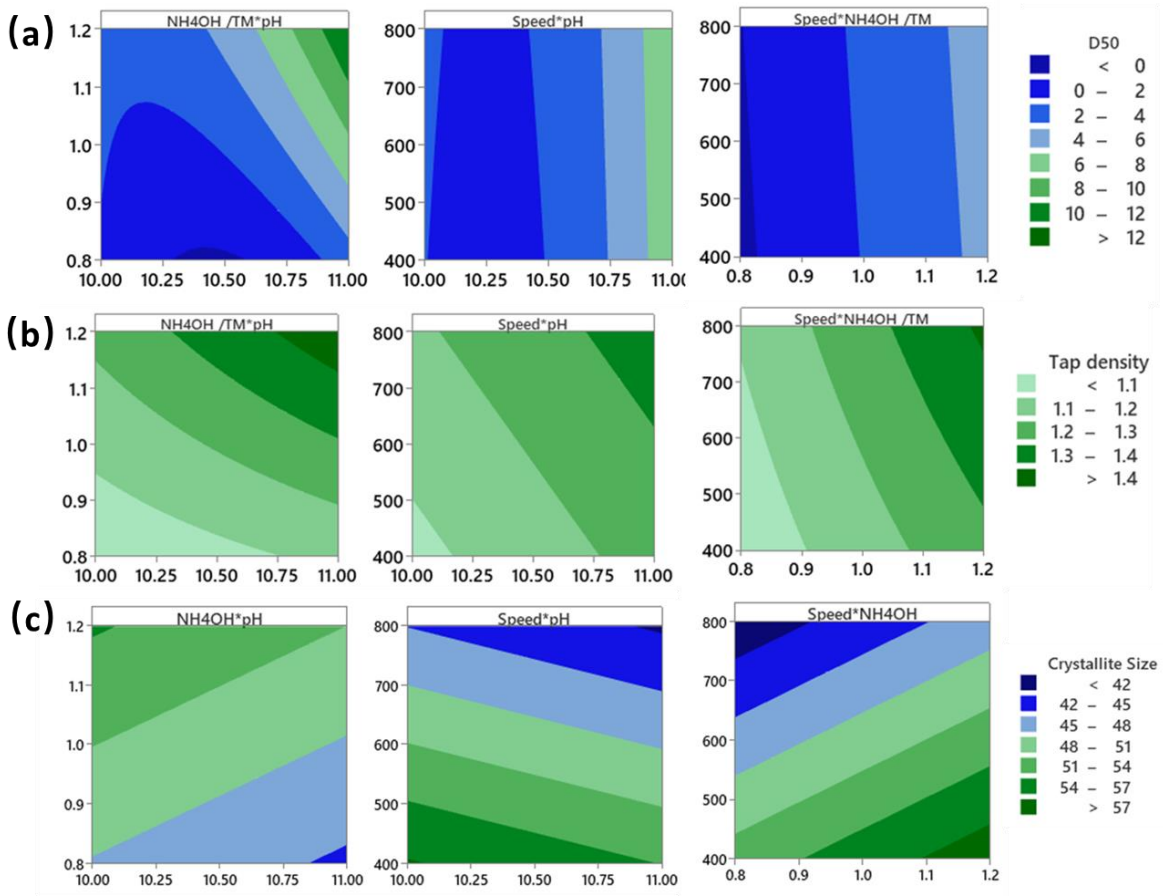


Figure 5.14 Contour plots of the relationship between input factors and output responses, (a) particle size D50, (b) tap density, and (c) crystallite size.

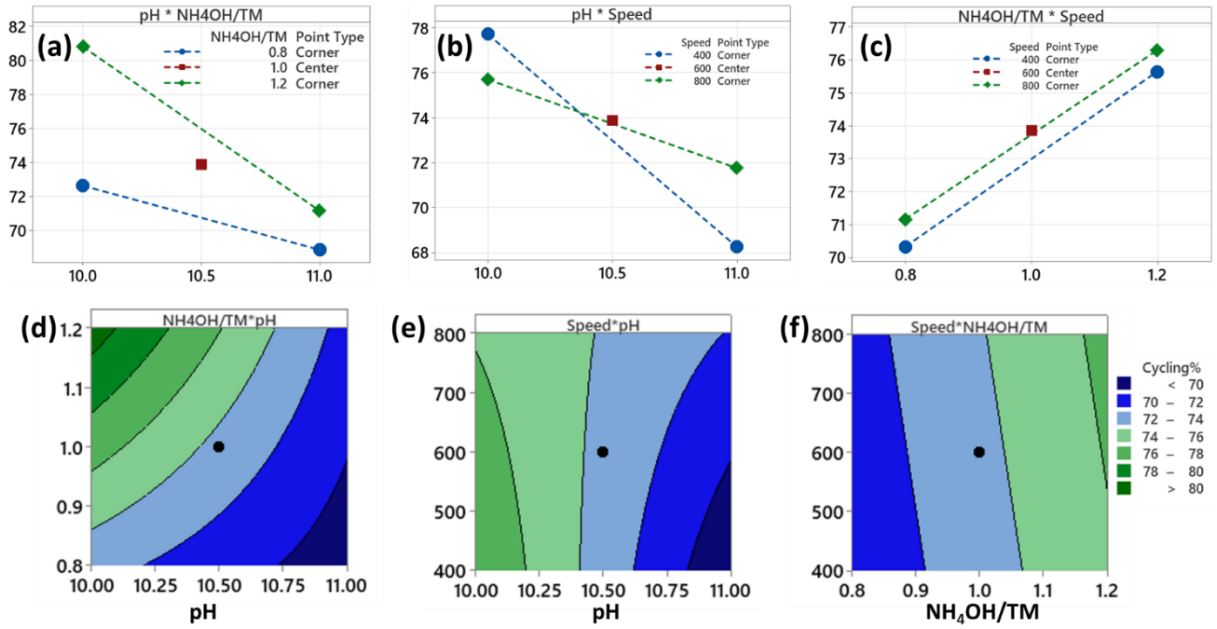


Figure 5.15 Interaction effect plots (a-c) and corresponding contour plots (d-f) for capacity retention.

To provide further information upon the impact of input factors on output responses, interaction contour plots depicting the relationship between factors and responses are presented in Figure 5.14 and Figure 5.15. Among the various output responses, capacity retention is chosen as a representative example for detailed discussion.

The interaction effect plots, and corresponding contour plots of the cycling performance are shown in Figure 5.15. These plots illustrate the relationship between pH and NH_4OH (Figure 5.15a, d), pH and speed (Figure 5.15b, e), and NH_4OH and speed (Figure 5.15c, f). By analyzing the interaction effects of different synthesis parameters on the cycling performance, optimal synthesis conditions can be determined. According to the ANOVA results presented in Table 5-4, the pH* NH_4OH interaction is identified as the most significant second-order interaction. When the pH value is increased from 10 to 11 at a high level of NH_4OH (green line in Fig. 5.15a), the cycling retention drops rapidly. However, the negative effect of pH is less pronounced at the low level of NH_4OH. The capacity retention decreases by 5.19% and 11.94% at the low and high levels of NH_4OH, respectively. The contour plot (Fig. 5.15d) reveals that the highest cycling retention is achieved within a narrow region, specifically for pH values ranging from 10.0 to 10.1 and NH_4OH levels ranging from 1.15 to 1.2.

The interaction of pH*speed is another important factor to consider. In Figure 5.15b, two lines intersect at around pH=10.4, indicating that below this pH value, materials produced with lower

stirring speed exhibit longer cycle life. This can be attributed to the decrease in solution supersaturation at low pH, which promotes particle growth rather than nucleation. Higher energy stirring, on the other hand, may crush the immature particles, negatively affecting particle growth. This observation is consistent with the samples from DoE1 and DoE5 shown in Figure 5.3a and e. In contrast, at higher pH, solution supersaturation increases, leading to higher nucleation rates. Higher energy stirring enhances the collision between primary particles, facilitating particle agglomeration and growth. The optimal pH*speed setting can be determined as 10.0≤pH≤10.2 and 400≤speed≤750, as depicted in the contour plot (Figure 5.15e).

The NH_4OH*speed interaction plots (Figure 5.15c, f) indicate that the cycling performance is not significantly influenced by the stirring speed. However, there is an increasing trend in better cycling performance as the level of NH_4OH is increased.

Based on the analysis above, the optimal conditions for achieving the highest cycling performance are: 10.0≤pH≤10.1, 1.15≤ NH_4OH/Metal ≤1.2, 400≤Speed≤750. Although the effect of stirring speed is less pronounced within the range studied, a higher stirring speed can lead to a narrower particle size distribution resulting in improved consistency in terms of initial capacity and cycling stability, as discussed earlier. Therefore, an intermediate value of speed (600 rpm) was chosen for the subsequent experiments.

5.4 Validation experiments

To validate the optimal synthetic conditions determined through the above analysis, a confirmatory experiment was conducted using the selected settings: pH= 10.1, NH_4OH/Metal ratio of 1.2, and stirring speed of 600 rpm.

Figure 5.16 shows the SEM images of $Ni_{1/3}Fe_{1/3}Mn_{1/3}(OH)_2$ and $NaNi_{1/3}Fe_{1/3}Mn_{1/3}O_2$ synthesized using optimal parameters. Throughout the process, the precursor was collected at various time intervals to monitor the growth of particle size and morphology. After 2 hours, secondary particles were observed, resulting from the agglomeration of loosely packed primary particles. Over time, the agglomerates became more compacted, and the particle sizes gradually increased. The particles also exhibited a more spherical shape with a smoother surface. After 24 hours, a flower-like secondary particle composed of lamellar primary particles, measuring approximately 400 nm in lateral dimension, was observed. In Figure 5.16 g the morphology of

$NaNi_{1/3}Fe_{1/3}Mn_{1/3}O_2$ after sodiation is shown. The lamellar primary particles transformed into thick plate shapes, and spherical second particles with a narrow size distribution were obtained, as shown in the particle size distribution diagram (Figure 5.16h). The relatively dense packing and uniform size distribution contribute to an improved tap density of 1.50 g cm^{-3}.

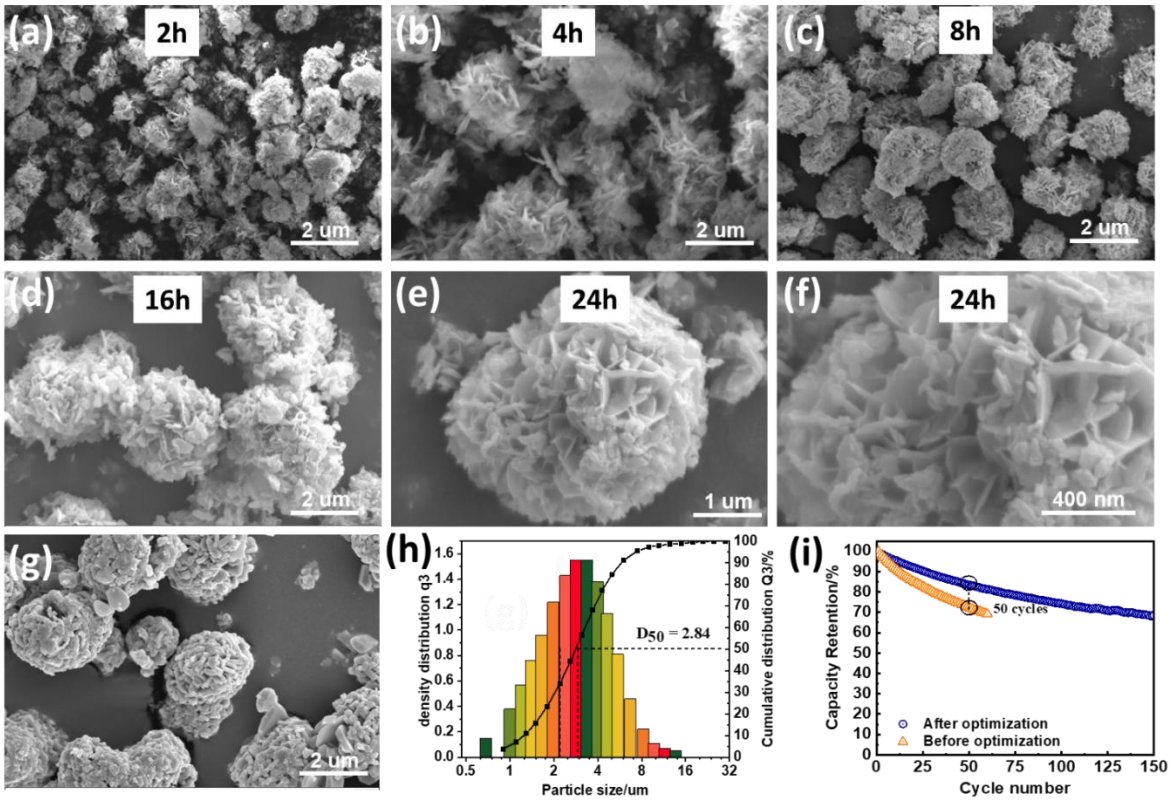


Figure 5.16 (a-f) SEM images of $Ni_{1/3}Fe_{1/3}Mn_{1/3}(OH)_2$ collected at different reaction time. SEM image (g) and Particle size distribution (h) of Na $Ni_{1/3}Fe_{1/3}Mn_{1/3}O_2$ synthesized under optimized conditions. (i) Comparison of cycling performance before and after optimization.

Figure 5.16i shows the cycling performance of optimized $NaNi_{1/3}Fe_{1/3}Mn_{1/3}O_2$. After 50 cycles at 0.5C, the capacity retention reaches 83.4%, which is higher compared to the sample synthesized using the central point parameters prior to optimization. Table 5-5 provides a summary comparison of the selected responses, including both experimental and predicted values obtained from the empirical models. The results demonstrate good agreement between the predicted and experimental values, with a deviation of less than 20% for all selected responses. The improved cycling performance, coupled with the validation of the empirical models, serves as evidence of the success achieved through the DoE optimization process.

Table 5-5 Comparison of experimental and predicted values for selected responses.

Response	Experimental value	Predicted value	Deviation
Particle size D50/um	2.8	2.6	7.7%
Tap density/ g cm^{-3}	1.5	1.3	15.4%
Crystallize size/nm	56.7	54.0	5.4%
Capacity retention/%	83.4	80.0	4.3%

It is important to acknowledge that this study focused on the investigation of three selected factors. However, further research is warranted to explore the influence of additional parameters such as residence time, feeding concentration, and feeding flow rate. Additionally, a subsequent experimental design within a smaller design space, utilizing the response surface method (RSM), would be beneficial for a more comprehensive evaluation of the effects of pH and NH_4OH, as well as their interactions on the physiochemical properties of $NaNi_{1/3}Fe_{1/3}Mn_{1/3}O_2$ cathode materials.

5.5 Conclusions

Sodium nickel iron manganese oxide ($NaNi_{1/3}Fe_{1/3}Mn_{1/3}O_2$) cathode materials for sodium-ion batteries were synthesized using a hydroxide coprecipitation process. The physical properties and electrochemical performance of the synthesized materials were investigated in relation to three process variables: pH, the molar ratio of NH_4OH/MSO_4, and stirring speed. A statistical experimental design method was employed to identify the key factors and develop regression models to predict the optimised synthesis conditions for long cycle life.

Four regression equations were derived to describe the relationship between the synthesis factors and the selected responses, D50 (particle size), tap density, crystallite size, and capacity retention. These equations provided valuable insights into how the synthesis conditions influence the physical properties of the particles and their electrochemical performance.

The analysis revealed that both pH and NH_4OH significantly affect all the selected responses. Higher pH values result in larger secondary particle sizes (D50) and higher tap densities, but lead to decreased crystallite sizes and particle uniformity, ultimately impacting the cycling performance. Higher NH_4OH concentration played a positive role in all the studied particle properties, contributing to improved uniformity and tap density. Stirring speed, while less pronounced overall, emerged as a significant factor for crystallite size. The interaction effects of pH with NH_4OH or stirring speed were also found to be significant in determining the final cycling performance.

Based on the experimental design method, the optimal synthesis conditions for achieving the best cycling performance were determined to be within the ranges of $10.0 \leq pH \leq 10.1$, $1.15 \leq NH_4OH/Metal \leq 1.2$, and $400 \leq Speed \leq 750$. A confirmatory experiment conducted under these optimized conditions results in particles with uniform size distribution and an improved tap density of 1.50 g cm^{-3}. This improvement in particle characteristics contributed to significantly improved cycle-life performance compared to the pre-optimization state. Whilst this study was performed with a sodium-ion Iron, manganese, nickel mixed oxide, the same principles can be utilised for other sodium and lithium-ion cathode materials.

This work shows that through careful optimisation of the synthesis conditions, we can inform the design of these layered oxide cathode materials and improve the performance properties including cycle life. This allows us to tailor the materials for high energy density and cycle life for stationary storage applications.

5.6 References

1. Zhang, Q. Y. Optimize the synthetic conditions of $NaNi_{1/3}Fe_{1/3}Mn_{1/3}O_2$ cathode material for high-capacity sodium-ion batteries via co-precipitation method. Master's Thesis, University of Birmingham, Birmingham, U.K., **2022**.
2. Kim, D.; Lee, E.; Slater, M.; Lu, W.; Rood, S.; Johnson, C. S., Layered $Na[Ni_{1/3}Fe_{1/3}Mn_{1/3}]O_2$ cathodes for Na-ion battery application. *Electrochemistry Communications* **2012,** 18, 66-69.
3. Yu, Y.; Ning, D.; Li, Q.; Franz, A.; Zheng, L.; Zhang, N.; Ren, G.; Schumacher, G.; Liu, X., Revealing the anionic redox chemistry in O3-type layered oxide cathode for sodium-ion batteries. *Energy Storage Materials* **2021,** 38, 130-140.
4. Zhang, Q.; Huang, Y.; Liu, Y.; Sun, S.; Wang, K.; Li, Y.; Li, X.; Han, J.; Huang, Y., F-doped O3-$NaNi_{1/3}Fe_{1/3}Mn_{1/3}O_2$ as high-performance cathode materials for sodium-ion batteries. *Science China Materials* **2017,** 60, (7), 629-636.
5. Jeong, M.; Lee, H.; Yoon, J.; Yoon, W.-S., O3-type $NaNi_{1/3}Fe_{1/3}Mn_{1/3}O_2$ layered cathode for Na-ion batteries: Structural evolution and redox mechanism upon Na (de) intercalation. *Journal of Power Sources* **2019,** 439.
6. Wang, H.; Liao, X.-Z.; Yang, Y.; Yan, X.; He, Y.-S.; Ma, Z.-F., Large-Scale Synthesis of $NaNi_{1/3}Fe_{1/3}Mn_{1/3}O_2$ as High Performance Cathode Materials for Sodium Ion Batteries. *Journal of The Electrochemical Society* **2016,** 163, (3), A565-A570.
7. Li, X.; Shen, X.; Zhao, J.; Yang, Y.; Zhang, Q.; Ding, F.; Han, M.; Xu, C.; Yang, C.; Liu, H.; Hu, Y. S., O3-$NaFe_{(1/3-x)}Ni_{1/3}Mn_{1/3}Al_xO_2$ Cathodes with Improved Air Stability for Na-Ion Batteries. *ACS Appl Mater Interfaces* **2021**.
8. Mu, L.; Rahman, M. M.; Zhang, Y.; Feng, X.; Du, X.-W.; Nordlund, D.; Lin, F., Surface transformation by a “cocktail” solvent enables stable cathode materials for sodium ion batteries. *Journal of Materials Chemistry A* **2018,** 6, (6), 2758-2766.
9. Liang, L.; Du, K.; Peng, Z.; Cao, Y.; Duan, J.; Jiang, J.; Hu, G., Co–precipitation synthesis of $Ni_{0.6}Co_{0.2}Mn_{0.2}(OH)_2$ precursor and characterization of $LiNi_{0.6}Co_{0.2}Mn_{0.2}O_2$ cathode material for secondary lithium batteries. *Electrochimica Acta* **2014,** 130, 82-89.
10. Lee, M. H.; Kang, Y. J.; Myung, S. T.; Sun, Y. K., Synthetic optimization of $Li[Ni_{1/3}Co_{1/3}Mn_{1/3}]O_2$ via co-precipitation. *Electrochimica Acta* **2004,** 50, (4), 939-948.
11. Noh, M.; Cho, J., Optimized Synthetic Conditions of $LiNi_{0.5}Co_{0.2}Mn_{0.3}O_2$ Cathode Materials for High Rate Lithium Batteries via Co-Precipitation Method. *Journal of The Electrochemical Society* **2012,** 160, (1), A105-A111.
12. Barai, P.; Feng, Z.; Kondo, H.; Srinivasan, V., Multiscale Computational Model for Particle Size Evolution during Coprecipitation of Li-Ion Battery Cathode Precursors. *J. Phys. Chem. B* **2019,** 123, (15), 3291-3303.
13. Para, M. L.; Alidoost, M.; Shiea, M.; Boccardo, G.; Buffo, A.; Barresi, A. A.; Marchisio, D., A modelling and experimental study on the co-precipitation of $Ni_{0.8}Mn_{0.1}Co_{0.1}(OH)_2$ as precursor for battery cathodes. *Chem. Eng. Sci.* **2022,** 254.
14. Li, J.; Camardese, J.; Glazier, S.; Dahn, J. R., Structural and Electrochemical Study of the Li–Mn–Ni Oxide System within the Layered Single Phase Region. *Chemistry of Materials* **2014,** 26, (24), 7059-7066.
15. Wang, D.; Belharouak, I.; Ortega, L. H.; Zhang, X.; Xu, R.; Zhou, D.; Zhou, G.; Amine, K., Synthesis of high capacity cathodes for lithium-ion batteries by morphology-tailored hydroxide co-precipitation. *Journal of Power Sources* **2015,** 274, 451-457.
16. Han, M. H.; Acebedo, B.; Gonzalo, E.; Fontecoba, P. S.; Clarke, S.; Saurel, D.; Rojo, T., Synthesis and Electrochemistry Study of P2- and O3-phase $Na_{2/3}Fe_{1/2}Mn_{1/2}O_2$. *Electrochimica Acta* **2015,** 182, 1029-1036.

17. Mu, L.; Feng, X.; Kou, R.; Zhang, Y.; Guo, H.; Tian, C.; Sun, C.-J.; Du, X.-W.; Nordlund, D.; Xin, H. L.; Lin, F., Deciphering the Cathode-Electrolyte Interfacial Chemistry in Sodium Layered Cathode Materials. *Advanced Energy Materials* **2018,** 8, (34).
18. Hong, N.; Li, J.; Guo, S.; Han, H.; Wang, H.; Hu, X.; Huang, J.; Zhang, B.; Hua, F.; Song, B.; Bugday, N.; Yasar, S.; Altin, S.; Deng, W.; Zou, G.; Hou, H.; Long, Z.; Ji, X., An in situ dual-modification strategy for O3-$NaNi_{1/3}Fe_{1/3}Mn_{1/3}O_2$ towards high-performance sodium-ion batteries. *Journal of Materials Chemistry A* **2023**.
19. Huang, Y.; Wang, Z.-x.; Li, X.-h.; Guo, H.-j.; Wang, J.-x., Synthesis of $Ni_{0.8}Co_{0.1}Mn_{0.1}(OH)_2$ precursor and electrochemical performance of $LiNi_{0.8}Co_{0.1}Mn_{0.1}O_2$ cathode material for lithium batteries. *Transactions of Nonferrous Metals Society of China* **2015,** 25, (7), 2253-2259.
20. Hwang, B. J.; Tsai, Y. W.; Carlier, D.; Ceder, G., A Combined Computational/Experimental Study on $LiNi_{1/3}Co_{1/3}Mn_{1/3}O_2$. *Chemistry of Materials* **2003,** 15, (19), 3676-3682.
21. Cai, X.; Zhang, N.; Wang, J.; Zhou, X.; Xu, F.; Ding, H.; Wang, P.; Song, L.; Huang, J.; Fu, X.; Cui, X.; Yang, C.; Li, S., Understanding mechanism of voltage decay and temperature sensitivity of Li-rich manganese-based cathode materials. *Materials & Design* **2023,** 225.
22. van Bommel, A.; Dahn, J. R., Analysis of the Growth Mechanism of Coprecipitated Spherical and Dense Nickel, Manganese, and Cobalt-Containing Hydroxides in the Presence of Aqueous Ammonia. *Chemistry of Materials* **2009,** 21, (8), 1500-1503.
23. Monshi, A.; Foroughi, M. R.; Monshi, M. R., Modified Scherrer Equation to Estimate More Accurately Nano-Crystallite Size Using XRD. *World Journal of Nano Science and Engineering* **2012,** 02, (03), 154-160.
24. Song, T.; Chen, L.; Gastol, D.; Dong, B.; Marco, J. F.; Berry, F.; Slater, P.; Reed, D.; Kendrick, E., High-Voltage Stabilization of O3-Type Layered Oxide for Sodium-Ion Batteries by Simultaneous Tin Dual Modification. *Chemistry of Materials* **2022**.
25. Myers, R. H.; Montgomery, D. C.; Anderson-Cook, C. M., *Response Surface Methodology: Process and Product Optimization Using Designed Experiments*. Wiley: 2011.

Chapter 6 Optimize areal capacity balance to maximize the lifetime of sodium-ion batteries

This work has been formatted into a paper and will be submitted to ***Journal of Power Sources*** (Tengfei Song, Yongxiu Chen, Lin Chen, and Emma Kendrick).

Author contribution: T.F. conceived and designed the research, performed the experiments, conducted the data analysis, and drafted the manuscript. Yongxiu Chen: Full cell voltage simulation, GITT calcuation. Lin Chen: Full cell making. Emma Kendrick: Lead supervision, conceptualisation, writing review& editing.

6.1 Introduction

In the past two decades, great efforts have been devoted to sodium-ion batteries (SIBs) research, with a wealth of promising new positive and negative materials being proposed. However, less attention has been paid to the full-cell design perspective. The cycle life not only depends on the reversibility of cathode and anode materials themselves, but is highly determined by the cell design parameters, such as electrode formulation, electrode thickness, electrode porosity, electrolyte composition, working voltage window, and capacity match between the cathode and anode.

N/P ratio (Negative/Positive), defined as the areal capacity ratio between the negative electrode (N) and positive cathode (P) is a simple yet critical parameter in designing full-cell with high performance[1-4]. In practical full cells, the designed N/P value should ensure that no Li/Na plating occurs over its entire life cycle within the set operating voltage range. It is worth mentioning that the N/P ratio is a dynamic value that varies with cycling and is influenced by the applied electrochemical conditions as well as the relative degradation rates of the positive and negative electrodes, rather than being a static value throughout the entire battery life. This change in capacity balance in a lithium-ion cell is reflected in the LLI (loss of lithium inventory) and LAM (loss of active material)[5]. More specifically, LLI occurs with SEI growth and lithium dendrites, whereas LAM occurs when electrode delamination or particle cracking leads to active particles being isolated. There has been no work looking at Loss of sodium inventory (LSI) or active material loss in sodium-ion batteries. A tutorial upon balancing a lithium-ion cell can be found here[6]. In this tutorial, the active mass is balanced between the negative and positive electrode, based on the reversible specific capacity after formation cycles are completed. This does not therefore take into consideration the loss of lithium inventory during the formation process, termed as first cycle losses (FCL), which for sodium-ion is significantly larger than for lithium-ion[7]. It should be noted that depending upon the precise operating conditions of the cell, due to the difference in the Kinetics (overpotential) observed at each independent electrode, the balance will change[8].

It is assumed that Li^+ plating will occur when the anode potential is below 0 V vs. Li/Li^+. Therefore, for a well-balanced lithium-ion full-cell, a typical value of 1.1 (10% redundancy on

the anode side) has been utilised in the LIBs to avoid Li-metal plating at all operating conditions, for safety considerations caused by the relatively faster degradation of the anode part and heterogeneous current density[3, 9]. This is in part true, however, there are examples where depending upon the play between kinetics and thermodynamics plating does not happen at low potentials, this has been observed particularly at high rate[10]. On the other hand, there is also a strong influence from the overpotentials observed at the interfaces induced by the growing SEI and high SEI film resistance, which promotes the likelihood of plating[11].

A number of publications have investigated the effects of negative/ positive capacity ratio on the coulombic efficiency, reversible capacity, cycling performance, discharge rate capability, fast charging, and Li plating in LIBs[12-18]. However, to the best of our knowledge, few studies have been conducted on the effects of N/P ratio on the electrochemical performance for sodium-ion full cells and the corresponding boundary condition of Na plating.

Two-electrode type cell has the advantage of easy assembling but has the limitation of not being able to monitor the potential of individual electrodes. In a three-electrode cell, a Na metal reference electrode (RE) is positioned at the edge of the cell, connected to both working and counter electrode, which helps to monitor the potential variations of both positive and negative electrode, respectively.

In this chapter, layered oxide/hard carbon full cell with N/P ratios of 0.8, 0.9, 1.0, 1.1 1.2 and 1.3 were investigated using three-electrode cells. The potential variations of both the positive and negative electrodes with different N/P ratios were obtained. The effects of N/P ratio on the material utilization, initial capacity, first coulombic efficiency, and cycling performance were investigated. The capacity fading mechanisms with different N/P ratios were explained by the potential shifting observed in the three-electrode cells.

6.2 Experimental

6.2.1 Materials preparation

An in-house made 8% Sn-modified $Na[Ni_{1/3}Fe_{1/3}Mn_{1/3}]O_2$ (named as Sn-NFM111 hereafter) was used as the cathode material. The synthesis and electrode preparation details have been described in Chapter 4.

A commercially available Hard carbon (Kuranode, Kuraray) was used in this work as the anode material. The negative electrode was prepared by mixing HC material, CMC (Bondwell™), and conductive additive (C45, Timcal) in a mass ratio of 90: 5: 5. CMC was pre-dispersed in deionized water to form a solution with 1.5% solid content. Mixing was processed in a Thinky ARE-250 planetary mixer. The mixed slurry was coated onto 16 um aluminium foil by Doctor-blade. The anode electrode was vacuum-dried at 120 °C for 24 h, followed by calendared to the desired thickness with a porosity of about 25%.

The mass loading of active materials on positive electrode was 7.70 mg cm^{-2} (equal to 1 mAh cm^{-2}), and the mass loading on negative electrode varies from 2.90 - 4.66 mg cm^{-2} (equal to 0.8 -1.3 mAh cm^{-2}). Detailed parameters of both electrodes with different N/P ratios are shown in Table 6.1.

Table 6-1 Details of Sn-NFM111 || Hard carbon full cells with different N/P ratios.

Cell	Positive (Ø18.0 mm)				Negative (Ø18.0 mm)				N/P
	Thickness/ um	Porosity/ %	Am loading (mg cm^{-2})	Areal capacity (mAh cm^{-2})	Thickness/ um	Porosity/ %	Am Loading (mg cm^{-2})	Areal capacity (mAh cm^{-2})	
1#	51.5	35.0	7.70	1.0	47	25.0	2.89	0.81	0.8
2#					50		3.21	0.90	0.9
3#					53		3.53	0.99	1.0
4#					58		3.96	1.11	1.1
5#					62		4.31	1.21	1.2
6#					65		4.66	1.31	1.3

Note: Am represents Active material. Defined reversible specific capacity: 130 mAh g^{-1} for Sn-NFM111 and 280 mAh g^{-1} for HC.

6.2.2 Electrochemical performance tests

Hard carbon|| Sn-NFM111 full cells were built in a three-electrode E-cell provided by EL-Cell GmbH. In which, high-purity sodium metal (Aldrich, 99%) was used as reference-electrode (RE), enable a high reliable result. 100 uL 1 M $NaPF_6$ in EC: DEC: FEC (12.6: 47.1: 35: 5.3 wt%) was used electrolyte. Glass fiber (Whatman^{TM}) was used as separator. The diameter for both cathode and anode is 18.0 mm.

The 3-electrode cells were evaluated by constant current charge/discharge procedure (CC-CV) on a Biologic VMP3 battery testing system. Two formation cycles were performed at 10 mA/g CC-CV (2 mA/g current cut off limit) charge and discharge, followed by cycled at 50 mA/g CC-CV (5 mA/g current cut off limit) charge and discharge between 1.5 and 4.1 V. Full cell voltages and positive/negative electrode potentials *vs.* Na^+/Na reference were recorded as a function of time.

Prior to full-cell evaluation, the capacity and cycling performance of both Sn-NFM111cathode material and hard carbon anode material were evaluated using 2325-type coin cell, in which Na metal (Aldrich, 99%) was used as counter electrode. The same formation and cycling procedure above were used. Sn-NFM111 positive half-cell was charged and discharged between 2.0 and 4.1 V vs. Na^+/Na, and hard carbon negative half-cell was discharged and charged between 0.01 and 2.0 V *vs.* Na^+/Na. Both E-cell and coin-cell were assembled in an argon-filled glovebox. All tests have been conducted at room temperature (25 °C).

6.3 Results and discussion

6.3.1 Active materials characterization

Initially, the physiochemical properties of the as-synthesized Sn-NFM111 cathode material and commercial HC anode material were characterized as a benchmark. SEM images of the cathode (Figure 6.1a) and anode (Figure 6.1b) materials are shown in Figure 6.1. The home-synthesized cathode material displays spheroidal morphology with an average particle size of 5 μm. The HC anode shows flat particles with an average particle size of 9 μm.

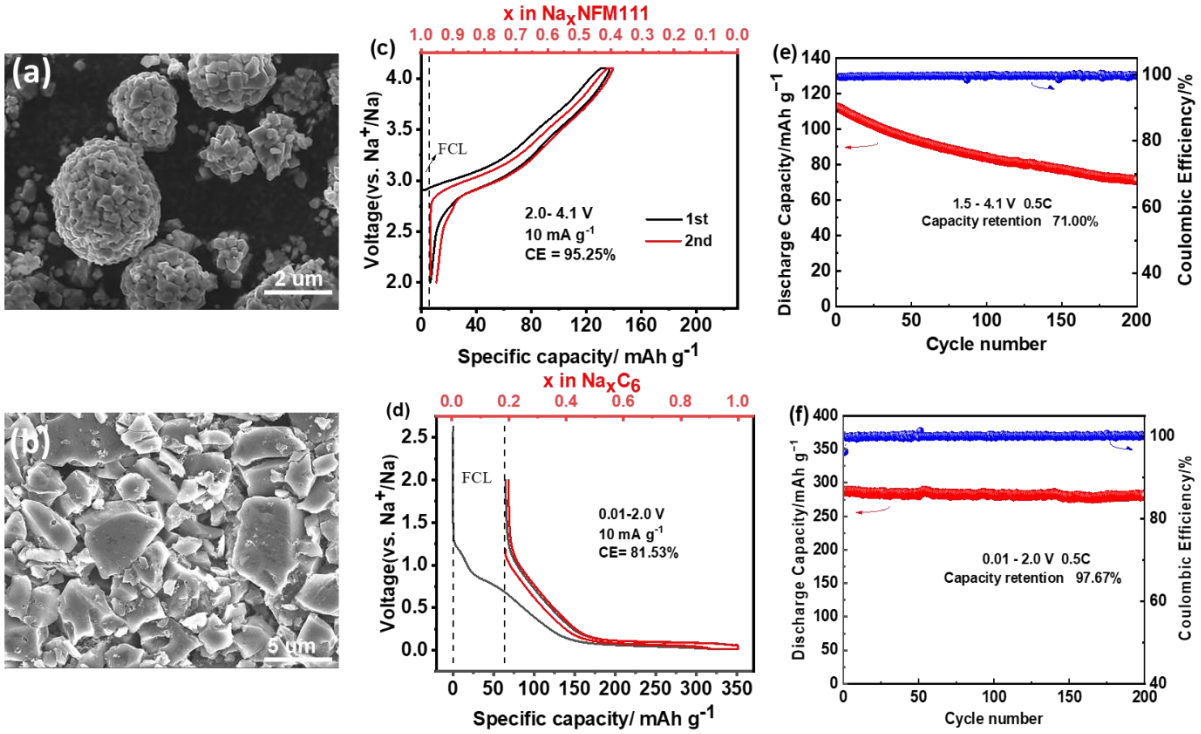


Figure 6.1 SEM images of (a) Sn-NFM111 cathode and (b) commercial HC anode material; Voltage profiles of (c) cathode material in the first 2 cycles at 10 mA g^{-1} and 2.0 – 4.1 V vs Na/Na^+ and (d) hard carbon anode material in the first 2 cycles at 10 mA g^{-1} and 0.01–2.0 V vs Na/Na^+; the cycling performance of (e) cathode and (f) anode material at 0.5 C. The areal capacities for both cathode and anode tested in half-cell are 1 mAh cm^{-2}.

The electrochemical performance was performed in half-cell setup. Figure 6.1c-f show the initial two formation voltage curves and cycling performance of the cathode and anode. The hard carbon anode shows a reversible capacity of ~280 mAh g^{-1} at a current density of 10 mA g^{-1} in the voltage range of 0.01-2.0 V vs. Na^+/Na, and the first cycle loss is around 18.5%. By contrast, the cathode material has a sloped voltage profile with a specific capacity of ~130 mAh g^{-1} and shows much higher Coulombic efficiency of 95.2% in the first charge/discharge process within 2.0 - 4.1 V *vs* Na^+/Na. However, the cycling stability of the positive electrode is lower than that of the negative electrode.

From the dQ dV curves of hard carbon (Figure 6.2), the sodiation plateau at around 50 mV which is quite close to 0 V *vs* Na^+/Na, which means that the anodic potential needs to be consciously controlled during the charging process to utilize as much the plateau capacity as possible, whilst avoid Na plating. This can be achieved by adjusting the N/P ratio.

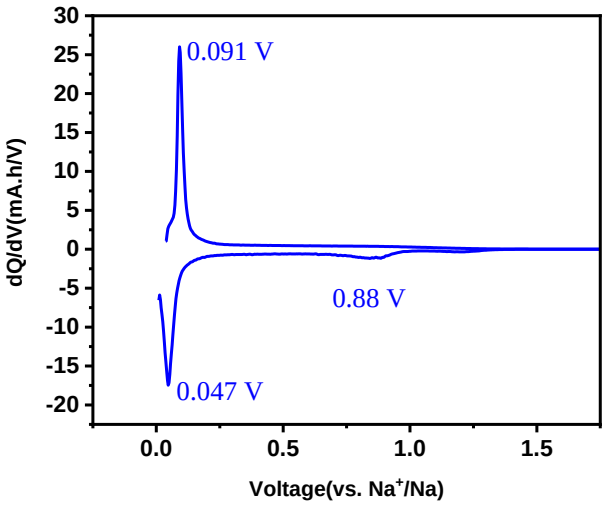


Figure 6.2 dQ/dV curves of hard carbon anode.

6.3.2 Formation with different areal capacity balances

Considering the first cycle loss (FCL) from EIS formation and structural collapse during the 1st formation cycle, area capacities of each electrode were calculated based on the reversible specific capacity of 2nd formation cycle obtained in the half cell. Full cells with different N/P ratios were obtained by varying the loading mass of the anode electrode with fixed cathode coating mass. The employed N/P ratios ranged from 0.8 to 1.3 at 0.1 intervals.

Figure 6.3a-b shows the voltage/potential profiles for the full cell and both electrodes during the first formation cycle at 0.1C (based on the positive electrode, the specific current of 1C was defined to be 150 mA g^{-1}). It is found that the cut-off potentials for both the positive and negative electrodes with an N/P of 1.3 are higher than those with an N/P of 0.8 at the end of charge, indicating the difference in electrode utilization under different N/P ratios. To reflect this trend more clearly, the cut-off potentials of the positive and negative electrodes at the end of charging (EOC) of different N/P ratios are summarized in Figure 6.3c and 6.3d. As shown in Figure 6.3c, at the EOC (4.1 V), the cut-off potentials of both the cathode and anode are rising with the increase of N/P ratio. As $V_{cell} = V_{cathode} - V_{anode}$, at lower N/P ratios, the anode is in a almost fully sodiated state while the cathode is not completely desodiated. N/P ratios lower than 0.9 lead to over sodiation of HC anode when the cell was fully charged. On the contrary, in case of higher N/P ratios, anode to be slightly capacity-excess than the cathode, only part of the HC was sodiated, resulting in a higher anode potential at EOC, consequently

the cathode potential was evaluated ($U_{cathode}$↑) to trigger the full-cell voltage cutoff. For example, the anode potential at EOC is -0.020 V for the cell with N/P ratio of 0.8, whereas it is 0.073 V for the cell with N/P ratio of 1.3. Consequently, the cathode potential at EOC must be 4.079 V and 4.173 V to reach the given full cell cut-off voltage of 4.1 V.

It should be noted that the sodium deposition potential of the cell with an NP ratio of 0.8 is lower than 0 V, which is attributed to the effect of cell polarization. It is assumed that Na^+ (or Li^+) plating will occur when the anode potential is below 0 V vs. Na/Na^+ (or Li/Li^+), which is thermodynamically correct, however the kinetics also are important. If there is no polarization or kinetic limitation, the Na (or Li) plating will occur when the NE/Na^+ (or NE/Li^+) potential reaches 0 V. However, the actual potential at which Na^+ (or Li^+) start plating varies with the charge current density, electrode thickness, particle size, and electrolyte properties due to the increase in polarization[10, 19-21].

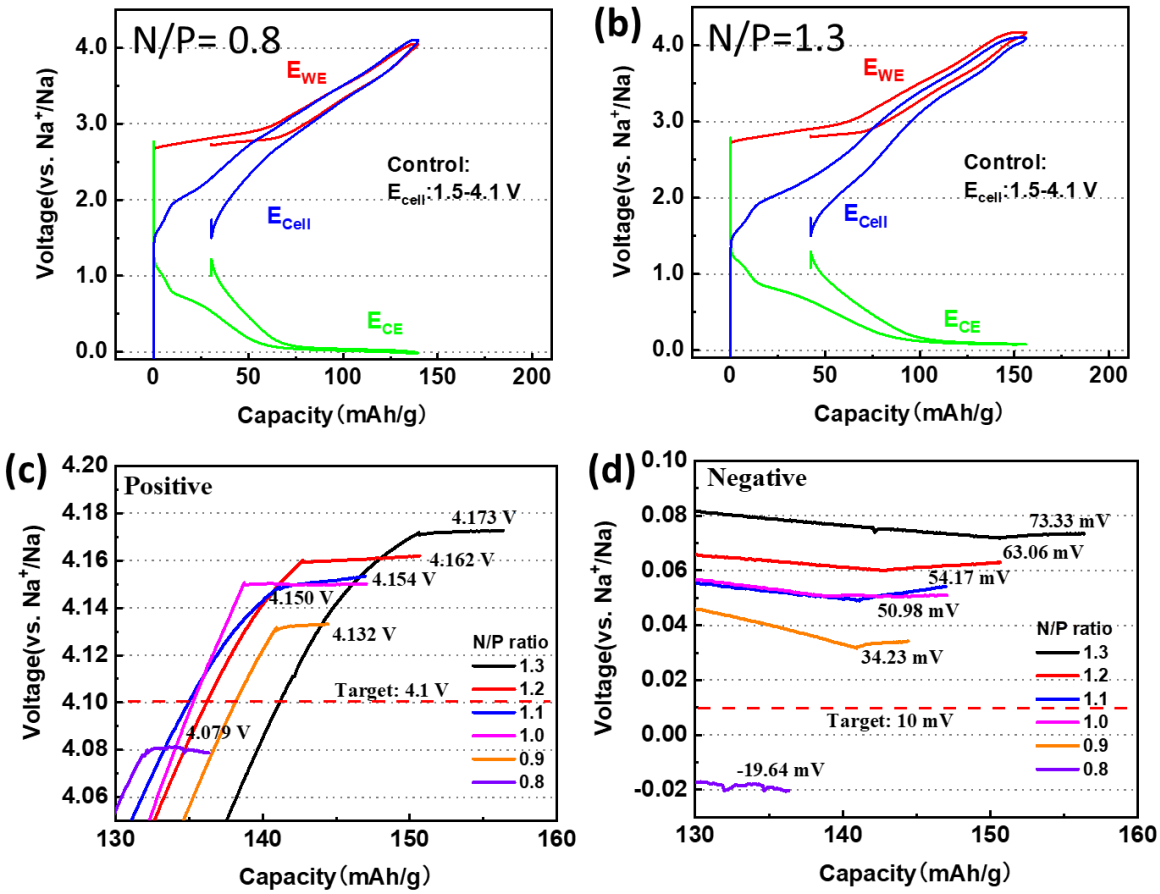


Figure 6.3 (a-b) First charge/discharge voltage/potential profile for the three-electrode cells within a controlled full cell voltage range of 1.5 – 4.1 V at 0.1C. Comparison of the end-off potentials of (c) cathode and (d) anode in the first charge process.

Although low depth of sodiation in the anode was guaranteed at a high N/P ratio, it resulted in over-desodiation of the cathode, thus may further lead to phase change of cathode and possible related electrolyte oxidation. As shown in Figure 6.4a, upon charging the positive electrode beyond 4.1 V (vs Na^+/Na), a new plateau appears on the voltage profile, reflected as a new pair of oxidation/reduction peaks (marked as an arrow) on the corresponding dQ/dV curve (see Figure 6.4b). It has been reported that the new peak above 4.1 V are associated with the irreversible phase transformation from hexagonal P3 into monoclinic P′3, which is unfavorable for the structure stability[22]. Furthermore, the kinetics behaviour of Na ion is also affected when the EOC potential of the positive electrode exceeds the critical value due to an inappropriate N/P ratio. Figure 6.4c shows the variation of Na^+ diffusion coefficient during de-sodiation and sodiation process. The Na diffusion coefficient decreases sharply when the charging potential exceeds 4.1 V, which may lead to significant polarization during cycling and, consequently, affect the utilization of sodium ions. Therefore, to maximize the lifetime of full cell, N/P ratio should be optimized to avoid overcharge of both positive and negative electrodes.

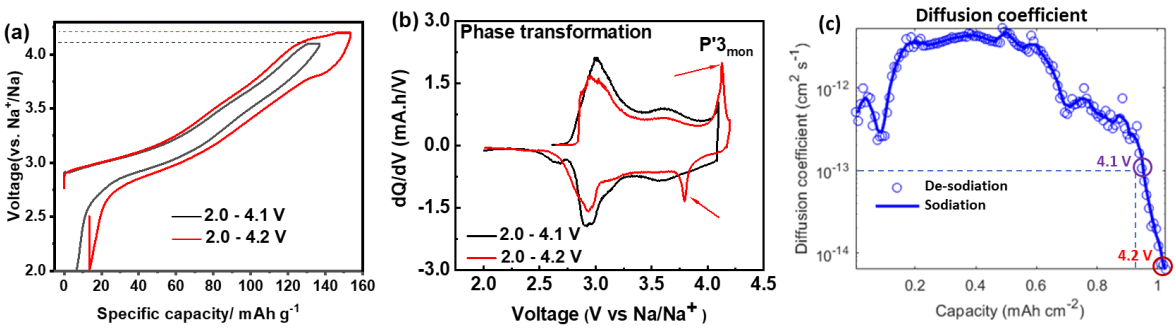


Figure 6.4 Comparison of (a) initial voltage profiles and (b) differential capacity (dQ/dV) curves of Sn-NFM111 when charged to different cut-off potentials. (c) GITT curves of Sn-NFM111 within voltage range of 2.0 – 4.2 V vs. Na^+/Na.

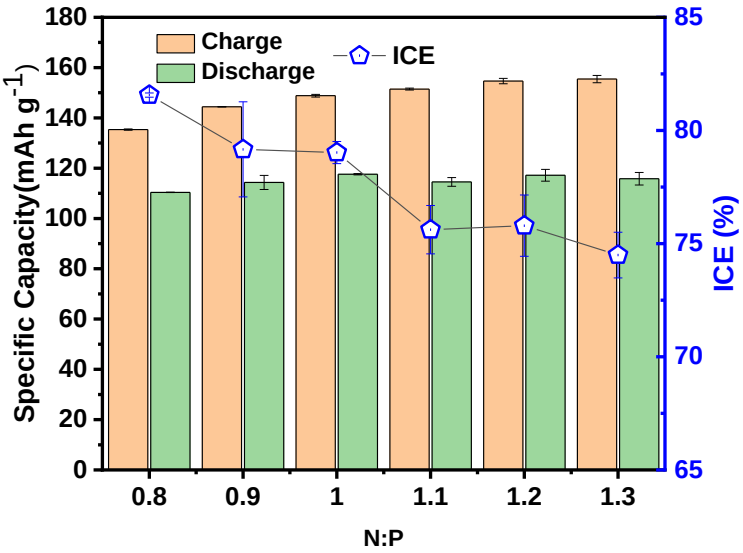


Figure 6.5 The variation of the first charge/discharge specific capacity (based on the weight of cathode material) and initial coulombic efficiency as a function of N/P ratio.

Figure 6.5 illustrates the relationship between the first charge/discharge specific capacity, ICE and the N/P ratios. With the N/P ratio gradually increasing from 0.8 to 1.3, the 1st charge specific capacity increases from 136.3 to 155.4 mAh g^{-1}. The increased charge capacity can be explained by the increased utilization of the cathode material caused by the shifting of the upper cut-off potential as discussed above. By contrast, the 1st discharge capacity does not show the same trend, which first increases from about 110.4 (N/P=0.8) to 117.6 mAh g^{-1} (N/P=1.1) and then gradually decreases till a stable level of about 115 mAh g^{-1}. Unlike the 1st charge capacity, the 1st discharge capacity is determined by the combination of the positive and negative electrodes as well as the formation of the SEI film, which can be expressed as follows: Reversible Na^+ = Na^+ extracted from cathode - Na^+ trapped in anode - Na^+ consumed in SEI/CEI formation. When the N/P ratio is less than 1.0, the positive electrode capacity is excessive relative to the negative electrode capacity, and the battery capacity is limited by the negative electrode capacity; as the N/P ratio increase (negative electrode capacity increase), more Na^+ can be inserted into the negative electrode instead of being consumed as Na deposition on the anode surface, therefore the 1st discharge capacity is increased. When the N/P ratio is higher than 1.0, the positive electrode capacity is insufficient relative to the negative electrode, and the battery capacity is limited by the positive electrode. For the ICE, which was the result of interplay between various factors, gradually decreased from approx. 81.6% to 74.5% with increasing the N/P, which implies that cells with higher N/P ratio experience a higher irreversible capacity

loss. This is consist with previous research in LIBs[1]. The increased irreversible Na^+ consumed to the formation of SEI (solid electrolyte interface) with increasing anode.

6.3.3 Cycling performance with different areal capacity balances

The full cell cycle life was also greatly influenced by the areal capacity balance of negative and positive electrode. Figure 6.6 shows the cycling performance of an average of 3 cells with various N/P ratios within a controlled full cell voltage range of 1.5 - 4.1 V at 0.5 C (based on the positive electrode, the specific current of 1C was defined to be 150 mA g^{-1}). It could be seen that increasing the N/P value leads to accelerated fading of cycling stability, except for the cells with N/P ratio of 0.8. The cells with the lowest N/P ratio of 0.8 exhibit the worst cycling stability, whereas cells with N/P ratio of 0.9 demonstrate the best cycling performance. Cell with N/P ratios ranging between 1.0 and 1.2 display similar cycling performance. After 200 cycles, the capacity retentions are 50.00, 70.65, 67.06, 67.23, 66.61, and 64.08%, for the cells with N/P ratio of 0.8, 0.9,1.0, 1.1, 1.2 and 1.3, respectively. Though N/P ratios equal to 0.8 and 1.3 performed the worse cycling stability than that of other ratios, they declined for different reasons, which will be discussed later. Cells with relatively low N/P ratios (N/P 0.9 and 1.0) show better cycling stability than those with a conventional high N/P ratio (⩾1.1), this phenomenon is completely opposite to what is generally acknowledged in graphite based LIBs[23].

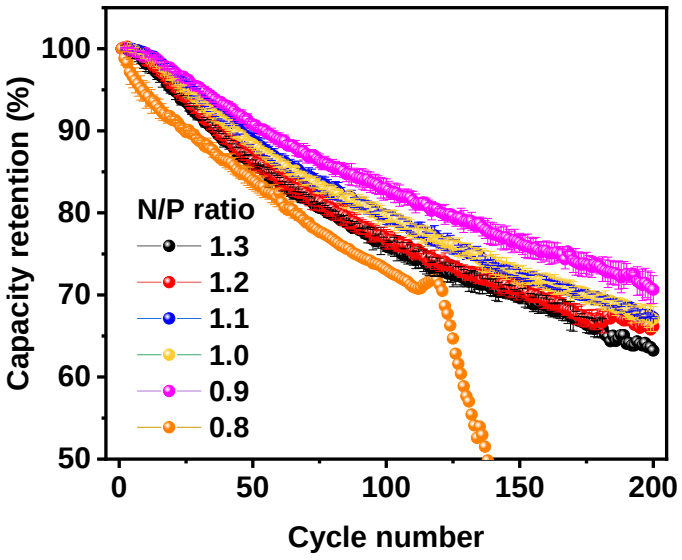


Figure 6.6 Cycling performance of cells with various N/P ratios within a controlled full cell voltage range of 1.5 – 4.1 V. Data were averaged from 3 cells for each condition.

6.3.4 Capacity fading mechanisms with different areal capacity balances

In order to understand the capacity fading mechanisms under different N/P ratios, cells with N/P value of 0.8, 1.0, and 1.3, were chose for detail study. After cycling, the cells were disassembled, and HC was washed in DMC and then examined by Scanning electron microscopy (SEM, Zeiss EVO15) operated at 10 KV, 15 pA to check the sodium plating. Figure 6.7 shows the morphology of HC electrode after cycling. Visual inspections were carried out before SEM. As shown in the optical images, visible Na plating was observed on the HC surface for cells with N/P ratio of 0.8, which clearly explains the poor cycling stability. This type of sodium deposition appears in SEM images as a layer of granular material, completely covering the surface of hard carbon particles, making the gaps between the hard carbon particles become less distinct as shown in Figure 6.7a. As the NP ratio increases, the surface of the hard carbon particles becomes cleaner, and the gaps between the particles become more pronounced.

Sodium deposition was also observed in the negative electrode of the cell with an N/P ratio of 1.0 after 200 cycles. However, it should be noted that this sodium deposition occurred mainly at the edge of the electrode, which was significantly different from that of the cell with an N/P ratio of 0.8. Even in the cell with an N/P ratio of 1.3, a slight edge sodium deposition can also be observed. The reason for this phenomenon is not entirely clear yet, which may be due to the uneven coating of the electrode, the uneven pressure during cell assembly, or the stress result from the repeated sodium ion insertion/desertion process, resulting in the occurrence of minor cracks in the negative electrode.

Although the degree of sodium deposition in the cell with an N/P ratio of 1.3 is much lower than that in the cell with an N/P ratio of 1.0, its cycling performance is worse than the N/P ratio of 1.0 cell. This suggests that the cycling performance of the full cell is not determined solely by the degree of sodium deposition in the negative electrode, but rather by a combination of the positive and negative electrodes. This is also confirmed by the analysis of the positive and negative potential shifts below (i.e., the degradation of the positive electrode at high N/P ratios is the main reason for the poor cycling performance of the cells).

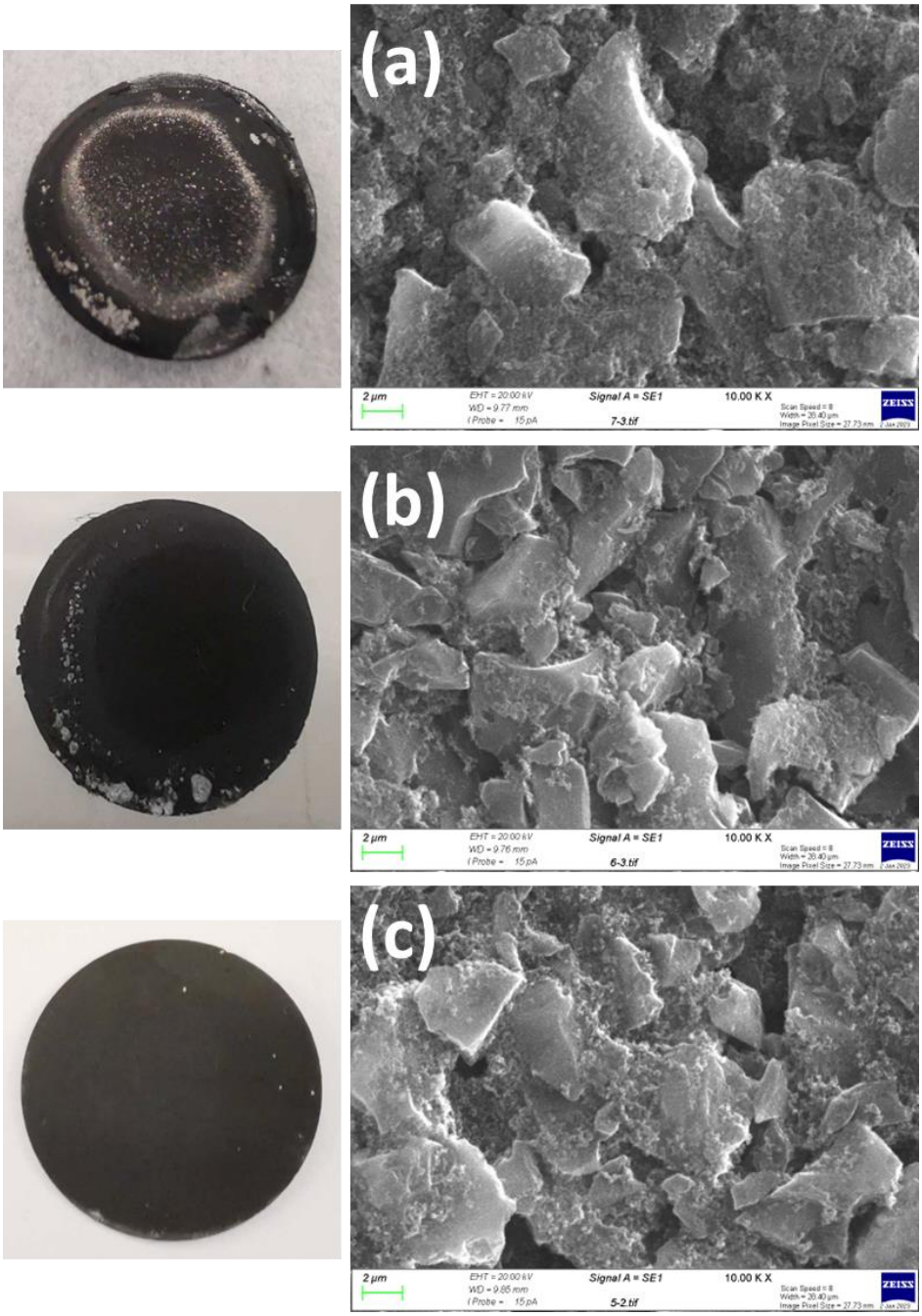


Figure 6.7 Optical image (left) and SEM images (right) of HC after cycling tests (a) N/P=0.8, (b) N/P= 1.0, and (c) N/P=1.3.

The variations of both cathode and anode voltage profiles upon cycling with Na RE. were obtained from the 3-electrode cell. As shown in Figure 6.8, the lower cut-off potential of the positive and the upper cut-off potential of the negative are shifting to lower potentials during cycling, resulting in narrowing of the negative electrode potential and broadening of the positive

electrode potential. Potentials shifting during cycling is widely observed in batteries. However, in LIBs, both the positive and negative cutoff potentials are moving to higher potentials at the end of charge and discharge[17].

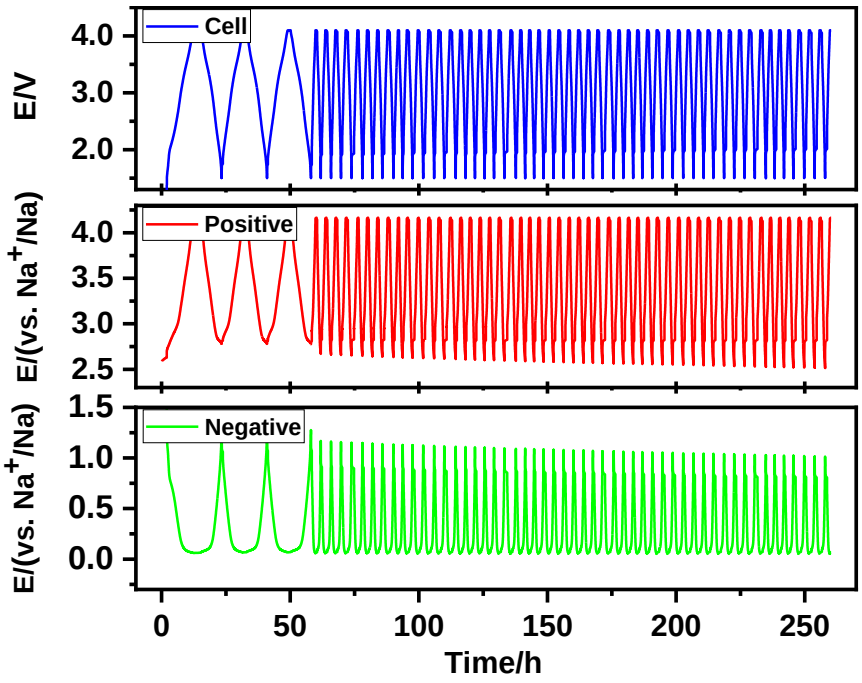


Figure 6.8 Cell voltage, together with the electrode potentials over time during cycling of Sn-NFM111 || Hard carbon cell with N/P ratio of 1.0 cycles between 1.5-4.1 V.

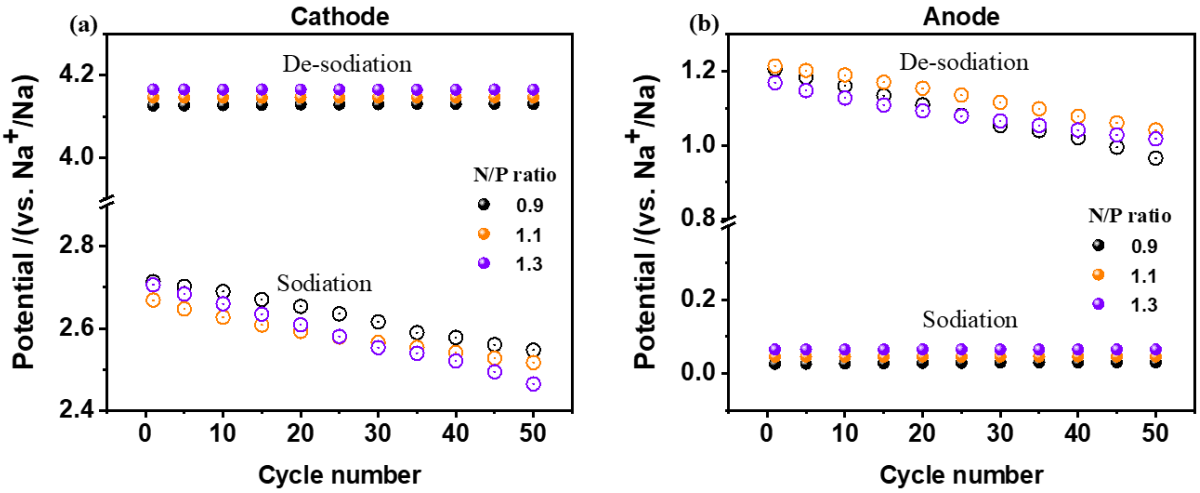


Figure 6.9 Variations of cathode and anode cut-off potentials while cycling with N/P ratios of 0.8, 1.0, and 1.3.

The evolution of EOC and EOD potentials for the cathode and anode with cycling are illustrated in Figure 6.9. The EOC potentials of both cathode and anode are relatively constant, no obvious

changes are observed during cycling. By contrast, the EOD potentials undergo much stronger shifting, namely decrease with cycling. The bottom (EOC) potential of the anode does not change significantly in its absolute value, indicating that a full state of sodiation is reached during every cycle. However, the upper (EOD) potential of the anode decreases upon cycling, indicating that not all Na^+ ions are removed from the anode as cycling progresses; some remain within the anode. Therefore, a loss of sodium inventory (LSI) occurs in the anode. On the cathode side, during discharge, a decrease in the low (EOD) potential is observed, indicating an over-sodiation process as cycling progresses. This suggests that we are likely losing active material on the sodium cathode side. This phenomenon occurs more rapidly with the 1.3 ratio. Therefore, the loss of cathode active material is likely attributed to the high voltage plateau above 4.1V, which increases resistance due to the sluggish kinetics for sodium ions, as discussed earlier.

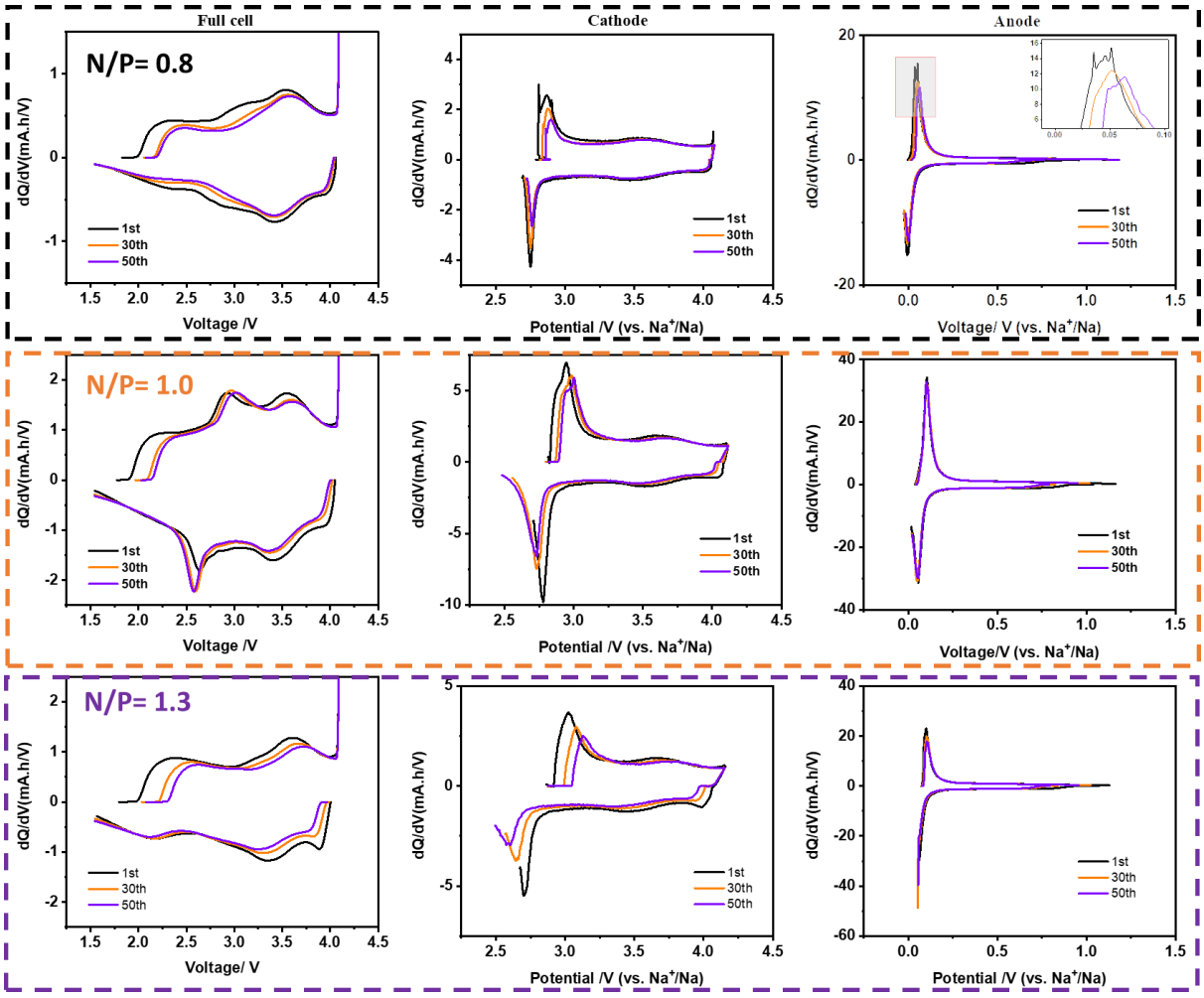


Figure 6.10 Differential voltage profiles of full cell, cathode, and anode of cells with N/P ratios of 0.8, 1.0, and 1.3.

More details can be found from the dQ/dV curves. As shown in Figure 6.10, peaks shift can be observed for all full cells, indicating an increase in cell resistance over time. However, when the dQ/dV of the full cell is dissected into each electrode, we can identify the specific electrode contributing to the increase in resistance.

For a cell with an N/P of 0.8, the positive electrode showed almost no polarisation during discharge over 50 cycles, whereas the negative electrode showed severe polarisation. This suggests that the degradation of the cell with low N/P ratio is dominated by negative-driven side reaction. By contrast, the positive electrode of cell with N/P ratio of 1.3 exhibits severe polarisation with cycling, which implies that the degradation of the cell with high N/P ratio is dominated by cathode-driven side reaction. As mentioned above, the cycling stability of layered cathode is sensitive to the upper cut-off potential (Na^+ extraction ratio). A higher upper potential can trigger irreversible structural changes and increase the risk of electrolyte oxidation, which can explain the accelerated degradation of cells under high N/P ratios.

6.4 Conclusion

The areal capacity balance has a major impact on the electrochemical performance of batteries. In this chapter, the cycling performance of Sn-$NaNi_{1/3}Fe_{1/3}Mn_{1/3}O_2$ || Hard carbon full cells with various N/P ratios were evaluated. The failure mechanisms under different N/P levels were preliminary discussed. A clear positive correlation was observed between first charge capacity and N/P ratio, and a negative correlation was observed between Coulomb efficiency and N/P ratio, while first discharge capacity was influenced by multiple factors. A higher N/P ratio results in an increased cathode cut-off potential at the end of de-sodiation, inducing phase change and sluggish kinetics for sodium ions. Consequently, active material losing occurs on the sodium cathode side, which is responsible for the accelerated degradation of the full cell. In contrast, a loss of sodium inventory through plating occurs in the anode side when the N/P ratio is too low. Rational guidelines are derived from the study based on 3-electrode cells, from which knowledge can be built and transferred to full pouch cell.

6.5 References

1. Chen, Z.; Zhang, L.; Wu, X.; Song, K.; Ren, B.; Li, T.; Zhang, S., Effect of N/P ratios on the performance of $LiNi_{0.8}Co_{0.15}Al_{0.05}O_2||SiO_x$ /Graphite lithium-ion batteries. *Journal of Power Sources* **2019,** 439.
2. Jeon, I.; Hong, W. G.; Yoon, S.; Choi, Y.; Kim, H. J.; Kim, J. P., Safety, high-performing and effects of the N/P ratio of a solid lithium ion battery using PEGDME based polymer electrolytes. *Heliyon* **2023,** 9, (2), e13292.
3. Xue, R.; Huang, H.; Li, G.; Chen, L., Effect of cathodeanode mass ratio in lithium-ion secondary cells. *Journal of Power Sources* **1995,** 55, (1), 111-114.
4. Wu, X.; Song, K.; Zhang, X.; Hu, N.; Li, L.; Li, W.; Zhang, L.; Zhang, H., Safety Issues in Lithium Ion Batteries: Materials and Cell Design. *Frontiers in Energy Research* **2019,** 7.
5. Attia, P. M.; Bills, A.; Brosa Planella, F.; Dechent, P.; dos Reis, G.; Dubarry, M.; Gasper, P.; Gilchrist, R.; Greenbank, S.; Howey, D.; Liu, O.; Khoo, E.; Preger, Y.; Soni, A.; Sripad, S.; Stefanopoulou, A. G.; Sulzer, V., Review—"Knees" in Lithium-Ion Battery Aging Trajectories. *Journal of The Electrochemical Society* **2022,** 169, (6).
6. Kasnatscheew, J.; Placke, T.; Streipert, B.; Rothermel, S.; Wagner, R.; Meister, P.; Laskovic, I. C.; Winter, M., A Tutorial into Practical Capacity and Mass Balancing of Lithium Ion Batteries. *Journal of The Electrochemical Society* **2017,** 164, (12), A2479-A2486.
7. Roberts, S.; Kendrick, E., The re-emergence of sodium ion batteries: testing, processing, and manufacturability. *Nanotechnol Sci Appl* **2018,** 11, 23-33.
8. Chen, Y.; Key, J.; O'Regan, K.; Song, T.; Han, Y.; Kendrick, E., Revealing the rate-limiting electrode of lithium batteries at high rates and mass loadings. *Chemical Engineering Journal* **2022,** 450.
9. Kim, C.-S.; Jeong, K. M.; Kim, K.; Yi, C.-W., Effects of Capacity Ratios between Anode and Cathode on Electrochemical Properties for Lithium Polymer Batteries. *Electrochimica Acta* **2015,** 155, 431-436.
10. Lain, M. J.; Kendrick, E., Understanding the limitations of lithium ion batteries at high rates. *Journal of Power Sources* **2021,** 493.
11. Janakiraman, U.; Garrick, T. R.; Fortier, M. E., Review—Lithium Plating Detection Methods in Li-Ion Batteries. *Journal of The Electrochemical Society* **2020,** 167, (16).
12. Song, B. F.; Dhanabalan, A.; Biswal, S. L., Evaluating the capacity ratio and prelithiation strategies for extending cyclability in porous silicon composite anodes and lithium iron phosphate cathodes for high capacity lithium-ion batteries. *Journal of Energy Storage* **2020,** 28.
13. Luo, M.; F. Rodrigues, M.-T.; Shaw, L. L.; Abraham, D. P., Examining Effects of Negative to Positive Capacity Ratio in Three-Electrode Lithium-Ion Cells with Layered Oxide Cathode and Si Anode. *ACS Applied Energy Materials* **2022,** 5, (5), 5513-5518.
14. Mu, G.; Agrawal, S.; Sittisomwong, P.; Bai, P., Impacts of negative to positive capacities ratios on the performance of next-generation lithium-ion batteries. *Electrochimica Acta* **2022,** 406.
15. Niri, M. F.; Apachitei, G.; Lain, M.; Copley, M.; Marco, J., Machine learning for investigating the relative importance of electrodes' N:P areal capacity ratio in the manufacturing of lithium-ion battery cells. *Journal of Power Sources* **2022,** 549.
16. Yourey, W.; Fu, Y.; Li, N.; Battaglia, V.; Tong, W., Design Considerations for Fast Charging Lithium Ion Cells for NMC/MCMB Electrode Pairs. *Batteries* **2021,** 7, (1).
17. Klett, M.; Gilbert, J. A.; Trask, S. E.; Polzin, B. J.; Jansen, A. N.; Dees, D. W.; Abraham, D. P., Electrode Behavior RE-Visited: Monitoring Potential Windows, Capacity Loss, and Impedance Changes in $Li_{1.03}(Ni_{0.5}Co_{0.2}Mn_{0.3})_{0.97}O_2$/Silicon-Graphite Full Cells. *Journal of The Electrochemical Society* **2016,** 163, (6), A875-A887.
18. Baasner, A.; Reuter, F.; Seidel, M.; Krause, A.; Pflug, E.; Härtel, P.; Dörfler, S.; Abendroth, T.; Althues, H.; Kaskel, S., The Role of Balancing Nanostructured Silicon Anodes and NMC Cathodes in

Lithium-Ion Full-Cells with High Volumetric Energy Density. *Journal of The Electrochemical Society* **2020,** 167, (2).
19. Teng, J.; Tang, X.; Tang, M.; Wu, Q.; Li, J., Failure mechanism and voltage regulation strategy of low N/P ratio lithium iron phosphate battery. *Journal of Energy Storage* **2022,** 51.
20. Hedman, J.; Mogensen, R.; Younesi, R.; Björefors, F., Fiber Optic Sensors for Detection of Sodium Plating in Sodium-Ion Batteries. *ACS Applied Energy Materials* **2022,** 5, (5), 6219-6227.
21. Smart, M. C.; Ratnakumar, B. V., Effects of Electrolyte Composition on Lithium Plating in Lithium-Ion Cells. *Journal of The Electrochemical Society* **2011,** 158, (4), A379-A389.
22. Song, T.; Chen, L.; Gastol, D.; Dong, B.; Marco, J. F.; Berry, F.; Slater, P.; Reed, D.; Kendrick, E., High-Voltage Stabilization of O3-Type Layered Oxide for Sodium-Ion Batteries by Simultaneous Tin Dual Modification. *Chemistry of Materials* **2022**.
23. Abe, Y.; Kumagai, S., Effect of negative/positive capacity ratio on the rate and cycling performances of $LiFePO_4$/graphite lithium-ion batteries. *Journal of Energy Storage* **2018,** 19, 96-102.

Chapter 7 Conclusions and Outlook

7.1 Conclusions

Sodium-ion batteries (SIBs) have emerged as one promising alternative to LIBs in global energy strategies. To promote the commercialization of SIBs in the energy storage sector, considerable efforts have been devoted to enhancing SIBs' energy density and cycling durability, particularly in developing new cathode materials. This thesis focuses on the investigation of cobalt-free O3-type layered oxide $NaNi_{1/3}Fe_{1/3}Mn_{1/3}O_2$, employing synergistic engineering strategies spanning from the crystal structure to the full cell level, with the aim of extending cycle longevity. The results also highlighted the necessity of combining multiple optimization strategies for developing SIBs with competitive electrochemical performance.

In Chapter 4, the doping strategy was investigated by incorporating Sn into the crystal structure. The influence of Sn doping amount on the structure, phase transitions, surface composition, and electrochemical properties has been investigated, and the mechanism was studied through an extensive analysis by in situ XRD, HRTEM, FIB-SEM, XPS, and Mössbauer spectroscopy. It was found that the Sn^{4+} dopant with a larger radius increased the lattice parameters and enhanced the binding energy between Na and O while maintaining the α-$NaFeO_2$ structure, which contributed to the suppressed irreversible phase transition under the voltage region above 4.1 V. Furthermore, simultaneous stabilization of bulk structure and interface was achieved when the doping amount reached 8%. As a result, the 8%Sn-modified NaNFMO exhibited optimized cycling performance with 70% capacity retention after 150 cycles in the voltage range of 1.5−4.1 V *vs.* Na/Na^+, which is an almost doubled capacity retention increase compared to the pristine. This work also provides an industrially feasible strategy to simultaneously stabilize the bulk structure and interface for layered cathodes via precise control of the Sn doping amount.

Apart from the crystal structure, the cycle life of NaNFMO electrode is influenced by the morphology, particle size, and size distribution of the active material. Chapter 5 refined the precursor synthesis process and probed how the synthesis conditions (pH, molar ratio of ammonia/metal precursor salt, and stirring speed) impact the physical properties and ultimate electrochemical performance of the materials. By merging Design of Experiments (DoE) with regression analysis, visual mathematical connections between the synthesis conditions and

material properties were established, thus realizing the improvement of material properties through fine-tuning synthetic conditions.

Statistical analysis indicates that both physical and electrochemical properties are mainly controlled through pH and NH_4OH amounts, while the effects of stirring speed are less pronounced. The optimal conditions for yielding the best cycling performance were derived from regression equations, which were $10.0 \leq pH \leq 10.1$, $1.15 \leq NH_4OH/Metal \leq 1.2$, $400 \leq Speed \leq 750$. The enhanced cycling stability was attributed to the improved particle characteristics, i.e., particle homogeneity, sphericity, and compacted density.

The final chapter focused on optimizing the full-cell design parameters of 8%Sn-$NaNi_{1/3}Fe_{1/3}Mn_{1/3}O_2$ || Hard carbon towards maximizing the full-cell performance. 3-electrode cells were used to evaluate the effect of mass balance (N/P ratio) and working voltage window on the electrochemical performance of the full cell. The degradation mechanisms were understood by exploring the potential behaviors, material utilization, state-of-charge shifting, and impedance increase during cycling. The results showed that full cells with a lower N/P ratio exhibit higher Coulombic efficiency and improved capacity retention, and cells with an N/P ratio of 0.9 demonstrated the best cycling performance. Measurements of end-off charge (EOC) potentials indicated that increasing the N/P ratio triggered an elevated cathode potential at the EOC, inducing phase changes and structural degradation. This, in turn, accelerates the deterioration of the entire cell. This work highlights the importance of mass balance in developing practical SIBs and offers a tutorial upon balancing a sodium-ion cell.

7.2 Outlook

In this study, a range of investigations involving doping, surface modification, morphology engineering, and full-cell design have been made to obtain Ni/Fe/Mn basal oxides with improved electrochemical properties as promising cathode materials for sodium-ion batteries.

Though many interesting findings were discovered and a great improvement in cycle life was achieved, a considerable number of further works are required to promote the commercialization of SIBs.

Firstly, future research could focus on synthesis process optimization. In Chapter 5, the synthesis study focused on the investigation of three selected factors (pH, amount of cheating agent, and stirring speed). However, further research is warranted to explore the influence of additional parameters such as residence time, feeding concentration, and feeding flow rate. Additionally, a more precise experimental design by utilizing the response surface method (RSM) rather than a two-level full factorial experimental design (2^k) would be beneficial for a more comprehensive evaluation of the effects of parameters, as well as their interactions on the physiochemical properties of the precursor $Ni_{1/3}Fe_{1/3}Mn_{1/3}(OH)_2$ and $NaNi_{1/3}Fe_{1/3}Mn_{1/3}O_2$ cathode materials. These results would help to understand the growing processes of particles, thus achieving the informed synthesis and particle design of layered oxide cathode materials with improved particle properties including cycle life.

The final physicochemical properties of layered oxides are also affected by the calcination process, i.e. firing temperature, time, atmosphere (air, N_2 or O_2), and even mineraliser additives. This can also be done through a design of experiments method to produce materials with controlled Na amount, secondary particle size, and preferred crystallite orientation.

Second, regarding the inherent shortcoming of multiple phase transition of O3 layered oxides during Na^+ extraction and insertion, and doping strategy has been proven to be effective in stabilizing the higher voltage phase transitions. However, there are lack of fundamental disciplines for screening dopants. Therefore, it is necessary to further investigate the doping-enhancing-structure stability mechanism. This work can be carried out in collaboration with modelers and in conjunction with advanced characterization techniques to provide a deep understanding of the relationships between the composition, structure, and electrochemical performance.

Third, it is necessary to improve the air stability of O3-type layered oxide either by structure regulation or novel surface coating. In this work, doping integrated coating by Sn was introduced to improve the surface stability, synthesized by dry mixing the $Ni_{1/3}Fe_{1/3}Mn_{1/3}(OH)_2$ precursor with SnO_2 nanoparticles, generating Sn/Na/O composite layer less than 10 nm. This approach, while simple and easy to implement, faces challenges in generating a homogeneous surface protection film. Further research should focus on novel coating approaches to create a homogeneous and robust coating layer to suppress side reactions with H_2O/CO_2 in moist air.

Last, but not least, for full-cell development, further research is needed to investigate the changes in Na^+ stoichiometry during formation and cycling. This will help us better understand the observed results in terms of areal capacity balances from a stoichiometry perspective. Additionally, a methodology is required to predict the stoichiometry limits of the positive and negative electrodes under different areal capacity balances. This would streamline the optimization process for full-cell development, reducing development time.